THE UNIVERSITY
of ADELAIDE

Two-Higgs-Doublet Models

A Global Study

Filip Rajec

December 4, 2020

A thesis submitted towards the degree of
Doctor In Philosophy
The Faculty of Physical Sciences
The University of Adelaide

Disclaimer

I certify that this work contains no material which has been accepted for the award of any other degree or diploma in my name, in any university or other tertiary institution and, to the best of my knowledge and belief, contains no material previously published or written by another person, except where due reference has been made in the text. In addition, I certify that no part of this work will, in the future, be used in a submission in my name, for any other degree or diploma in any university or other tertiary institution without the prior approval of the University of Adelaide and where applicable, any partner institution responsible for the joint-award of this degree.

I give permission for the digital version of my thesis to be made available on the web, via the Universitys digital research repository, the Library Search and also through web search engines, unless permission has been granted by the University to restrict access for a period of time.

I acknowledge the support I have received for my research through the provision of an Australian Government Research Training Program Scholarship.

SIGNED: _____ _____

DATE: _____

Acknowledgements

I want to start by acknowledging and thanking my supervisors Anthony G. Williams & Martin White. You have both been incredibly generous with your time & expertise throughout my postgraduate journey. Tony, you have taught me to know when to step back and look at the bigger picture, turning what seemed like an impossible challenge into something I could not only progress in but excel in. This has fundamentally improved the quality and creativity of almost everything I approach. Martin, you have been a beacon of guidance and always given the right dose of calculated advice. You've taught me the balance of critical analysis and action necessary to solve problems of all shapes and sizes.

I am thankful to all of those I have had the pleasure to work alongside. These include A. Beniwal, J. Herrero-Garcia, M. Nebot, W. Su & A. Scaffidi. Each of you has provided me with the rich guidance and understanding I've needed over these past years. I would also like extend this thank you to members of the GAMBIT community, in particular, P. Scott, A. Kvellestad, J. McKay and P. Athron. I would like to acknowledge the supercomputer facilities that have been used in the production of this work: Pheonix (University of Adelaide) and Marconi (Cineca, Italy).

To my fellow postgrad students, you've all been a hoot. Thank you for your help, love, support & of course for the times at the pub.

Thank you, S. Santucci, S. Johnson, M. Odlum & the staff in the physical sciences office for all your incredible work behind the scenes. More broadly, I want to thank the University of Adelaide and all the excellent student services, particularly for backing me through health difficulties. Indeed, I am very grateful for the opportunity & support I have been privileged with to do my postgraduate studies.

Last but certainly not least I want to say to my mum, dad, sister, my *babkas'* and my close friends, I have been blessed to have to such an abundance of support over the years. You know how thankful I am for each of you & I always will be.

Abstract

We look at global scans of the parameter space of Two-Higgs-Doublet Models (2HDMs).

Our first study is a Bayesian analysis of the Yukawa Z_2-aligned 2HDMs: the type-I, type-II, type-X (lepton-specific) and type-Y (flipped) models. Incorporated into these analyses are the theoretical constraints: perturbativity checks, the stability of the potential and the unitarity of the scattering matrix (up to NLO). The generic potential couplings are run up to 1 TeV, stability and perturbativity are then rechecked at this upper bound. We also calculate loop corrections to the scalar masses and check that they do not grow too large. Next, we apply experimental constraints. These include Higgs signals and searches matched to the latest data from LEP, the Tevatron and the LHC. As well as fits onto the electroweak precision parameters and an array of flavour processes, notably the radiative B decays and the R_K and R_K^* anomalies.

Our second study is a frequentist analysis of the most general 2HDM (or type-III model), searching for limits on flavour changing quark decays. The most general 2HDM introduces flavour-changing currents (FCC). We apply a subset of the theoretical and the experimental bounds described above (at tree-level) and work with a restricted Yukawa sector. The restricted Yukawa sector allows FCC only between fermions and then only between the second and third generation. The flavour analysis focuses on the discrepancy in the B_s^0-meson mass splitting with the Standard Model (SM) and leads us to explore how this process may be better fit by a 2HDM.

Detailed Contents

Figures

Tables

1 Introduction

The two-Higgs-doublet model (2HDM) is a natural extension to the Standard Models (SMs) scalar sector that introduces new spin-0 particles. The 2HDM, in general, allows for flavour changing currents (FCC) at tree-level. However, as these are constrained by experiment, Z_2 symmetry is applied to the 2HDM to forbid such processes. The different application of Z_2 symmetry, or the alignment of the Yukawa sector, leads to four conventional types of 2HDMs: type-I, type-II, lepton-specific (type-X) and flipped (type-Y).

In this thesis, we will use modern global scanning techniques on the four types of flavour aligned 2HDMs by extending the open-source code `GAMBIT`. Additionally, we carry out similar standalone scans on the general 2HDM with FCC to identify upper bounds on interesting flavour changing decays of the Higgs boson. All models we scan over are CP-conserving, and we perform our analysis on the flavour aligned models at two-loop-level where possible.

We begin in Chapter 2 by describing the SM, with a focus on the Higgs mechanism, the SM Higgs production and decay pathways and also give a brief introduction to effective field theory.

In Chapter 3, we introduce the 2HDM and focus on its theory. We define the various forms of the scalar potential, and give details about symmetries and transformations, the structure of the vacuum and the resultant spectrum of particles. We also look at the form of the scattering amplitudes. This chapter delivers a checklist of theoretical requirements for use in our global scans, including ensuring a stable potential and unitary S-matrix.

In Chapter 4, we turn our attention to the phenomenology of the 2HDM. We introduce the Higgs basis and the Yukawa sector of the 2HDM including the aligned models arising from Z_2 alignment in the Yukawa sector. This leads us to describe the modifications to existing decay processes as well as newly introduced decays of the 2HDM. Next we present a discussion of flavour physics using an effective theory approach. We focus on radiative B decays ($\mathrm{BR}(b \to s\gamma)$) and the B^0-meson mass-splitting ($\Delta M_{B_s^0}$) flavour processes. These two processes motivate us as they provide constraints on the interesting decays $h \to bs$ and $t \to ch$, which are highly suppressed in the SM and as such may provide a fingerprint for the 2HDM at future colliders. Closing this chapter, we write about the electroweak precision parameters and their adaptation to the 2HDM. Decays, flavour processes

and the electroweak precision parameters from this chapter provide us with more constraints to apply within our global scans.

In Chapter 5, we detail our global scan techniques and also introduce GAMBIT and our standalone global scan code. We detail the statistics, and scanning algorithms necessary to transform the constraints into likelihoods and in turn map out the model parameter spaces. We walk through the necessary steps taken to implement the Z_2-symmetric models into GAMBIT and provide some starting steps for getting 2HDM global scans running with the source code. We describe all likelihoods used in our GAMBIT scan and give details about the spectrum generation. We finish by turning our attention to the general type-III model with FCC and explain the scanning method and likelihoods used in this case.

Chapter 6 presents *preliminary* results from the GAMBIT scans of CP-conserving 2HDM with soft Z_2-breaking. We present each of the four Z_2 Yukawa aligned models (type-I, type-II, lepton-specific and flipped) and explain the bounds, best-fit points and shapes of distributions for interesting parameters. Our results are presented as 1D and 2D profile likelihood distributions.

Chapter 7 presents results from the standalone scans of CP-conserving general 2HDM (type-III). This model includes extra off-diagonal Yukawa's beyond those of the SM that give rise to the FCC. For our FC decay processes we want to investigate ($h \to bs$ and $t \to ch$) we are only interested in the off-diagonal Yukawa's between the second- and third-generation.[1] We place upper bounds on these processes to see if evidence of a 2HDM may potentially be detected at higher energy colliders. Our results are presented as 2D posterior likelihood distributions.

1: We, therefore, fix the all other off-diagonal Yukawa's to zero.

PART I: BACKGROUND READING

The Standard Model: Origins of the Higgs Scalar Boson

2

The field of physics, consisting of experimental, phenomenological and theoretical research, aims to explain the properties of matter and energy. Such features prove captivating and elegant at all scales. From the grand structures and motions of celestial bodies, right down to the scale of the most fundamental building blocks of our universe. The description and categorisation of these fundamental building blocks are encapsulated in the Standard Model of Particle Physics (SM). We refer to these fundamental building blocks as particles, using a representation with which we are all familiar. These particles are, in fact, point-like fluctuations of their constituent fields. The SM is not only a catalogue of these particle properties, such as their masses and their interactions but a quantitative theory that allows us to explain the mathematical origins of the properties. This chapter aims to introduce the framework of the SM. Particular interest will be put on the Higgs boson, and the mechanism by which particles acquire their fundamental mass.

2.1 A Quick Introduction to the SM

Particles of the SM At the quantum level (tiny scales) particles fall into states of discrete energy. The statistical distribution in equilibrium of the particles in these states is given by either the Fermi-Dirac or the Bose-Einstein distribution. The distribution a particle will join depends on a fundamental property of the particle known as its spin. From this property, we may separate the particles described by the SM into two groups: elementary fermions (Fermi-Dirac distributed) and elementary bosons (Bose-Einstein distributed). The elementary fermion group is further broken down into quarks and leptons. There are six quarks and six leptons (excluding anti-matter partners). The lepton group contains three families: the electron and electron neutrino, the muon and muon neutrino and the tau and tau neutrino. Similarly, the quark group is described by three families, the up, down quarks, the charm, strange quarks and the top and bottom quarks. Here, the families are ordered respectively according to increasing mass. In the SM, neutrinos are considered to be massless.[3] The elementary boson group consists of: the photon (mediator of the electromagnetic force), the Z and $W^{\pm}$ bosons (mediators of the electroweak force), the gluons (mediators of the strong force) and the Higgs boson (provider of fundamental mass in the SM). At this point, it is good to

3: Experimentally; neutrinos are observed to have a small mass (see chapter 15, Ref. [1]).

pause and refer to a diagram that summarises the above. Refer to Figure 2.1 for a pictorial representation of the particles of the SM grouped by the forces.

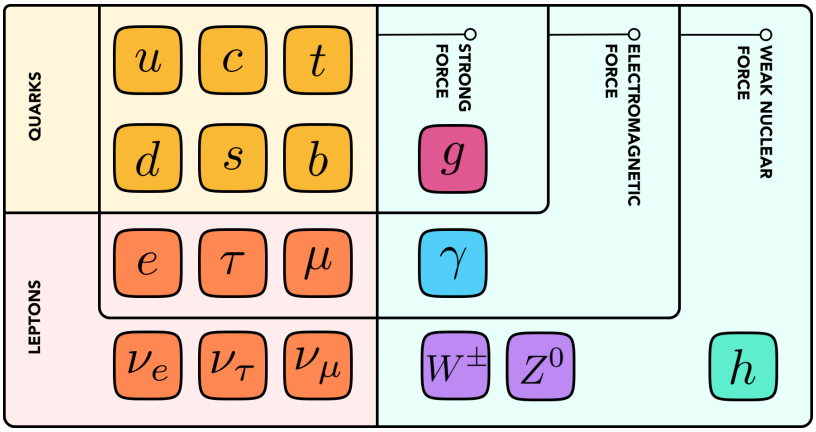

Figure 2.1: Particles and Forces of the SM

4: The force of gravity is not included in the SM. The gravitational force is the weakest of all four with strength 10^{-41} compared to that of the strong force. The gravitational force has an infinite range; however, to date, we have not been able to discover the mediator particle or source of the interaction at a quantum level. The hypothetical graviton is accepted as the force-carrying particle for gravity. Gravity acts on all particles of the SM.

Interactions in the SM There are three forces in the SM[4] each carried by a mediator particle. The mediator particles are all bosons with interactions restricted to a particular set of fermions (and bosons). As such, not all fermions experience each of the forces. Each force has a unique strength and range. Strengths of forces are defined by the strength in which the mediator particles couple during interaction (coupling constant). The strongest of the forces is the suitably named strong force; it has a short-range. Gluons carry the strong force, and can only interact with other gluons and quarks. The strong force is responsible for holding quarks together in stable hadrons, which can either be composed of an even number of quarks (mesons) or an odd pair of quarks (baryons). Quarks have never experimentally been observed on their own. The next force is the electromagnetic force, which is 1/60 the strength of the strong force, with an infinite range. The electromagnetic force is carried by the photon and is felt by all charged particles, namely, the quarks and the charged leptons (electron, tau and muon). Famously, the electromagnetic force keeps the electron in orbit around the nucleus of an atom. Third, and a factor or 10^{-4} the strength of the electromagnetic force*, is the weak nuclear force. The weak nuclear force is mediated by the Z, W^+ and W^- bosons. As the name suggests, the weak nuclear force takes part in radioactive decay. Again, refer to Figure 2.1 for a pictorial representation of the mediator particles, forces, leptons and quarks.

The Higgs boson Up until now, we have not mentioned the Higgs boson. The Higgs boson is part of the electroweak sector but not a

* at the scale of 2 GeV

mediator of the forces described above. The Higgs boson exists to provide the particles with fundamental masses. The other mediator particles interact with other particles based upon their properties (such as charge or spin), whereas the interaction with the Higgs boson gives the other particles the property of mass. For example, an electron carries a charge before taking part in an electromagnetic interaction, but does not carry a fundamental mass until it interacts with the Higgs.

The SM without the Higgs boson has cannot explain the origin of particle masses. The details of this problem and how constructing a solution leads to the necessary existence of the Higgs boson is covered in sections 2.3 and 2.4.

2.2 A Quantum Field Theory Introduction to the SM

Quantum field theory (QFT) is the framework of particle physics. It is the quantisation of the familiar classical field theory, which, for example, can be used to model matter in a gravitational field. The dynamics of a QFT are encapsulated by a Lagrangian density $\mathscr{L}$ [5] (onward referred to as just the Lagrangian). To accurately describe nature, we must ensure that our Lagrangian respects two transformation properties - these being Lorentz and gauge invariance.

5: The Lagrangian density integrates over space to give the Lagrangian itself

$$L = \int \mathscr{L} d^3x. \tag{2.1}$$

Lorentz Transformations Lorentz transformations allow us to compare physics between two frames of reference in space-time all the while taking relativistic effects into account. The space-time coordinate x^μ transforms under Lorentz transformations according to

$$x^\mu \to (x')^\mu = \Lambda^\mu_\nu x^\nu, \tag{2.2}$$

where Λ^μ_ν is a four-by-four transformation matrix that may include both relativistic boosts and rotations in spatial directions as well as a time dilation transformation. We require that our Lagrangian is invariant (it does not change) under such Lorentz space-time transformations. In a field representation (where $\phi(x)$ is a scalar field) we expect that the transformation,

$$\phi(x) \to \phi'(x) = \phi(\Lambda^{-1}x), \tag{2.3}$$

leaves our Lagrangian invariant. The Lorentz transformation is global, that is Λ^μ_ν is independent of space-time coordinate x^μ.

Gauge Transformations Unlike Lorentz transformations which are independent of space-time, gauge transformations are local and as such depend on x^μ. This dependence on space-time in the transformation results in the appearance of additional terms picked up by derivative operators. Such extra terms must be cancelled to ensure gauge invariance. As a taste of what is to come, the process that leads these additional terms to cancel introduces new field operators leading to new bosons in the SM.

Before gauge transformations, the Lorentz invariant field Lagrangian of a free Dirac field (spin-half) ψ is given as

$$\mathscr{L} = \overline{\psi}(i\gamma^\mu \partial_\mu - m)\psi, \tag{2.4}$$

where m is the mass of the field.

Imposing gauge invariance on the Lagrangian, we find that we can construct the theories discussed below.

QED QED is the most successful of all theories in the sense that it allows matching calculations to observables with incredible accuracy. QED is a theory of the electromagnetic interaction. Making our Lagrangian of Eq. (2.4) gauge invariant under the Abelian group $U(1)$ we find the appearance of a massless field, the photon. This process is detailed in section 2.3.2.

The Electroweak Theory Moving from the $U(1)$ symmetry describing QED to the non-Abelian group combination $SU(2) \times U(1)$, our Lagrangian produces four massless bosons. After the introduction of the Higgs boson through spontaneous symmetry breaking (see section 2.3.2) we find that these bosons become three massive vector bosons ($Z^0, W^\pm$) and a massless photon. In this way, the weak nuclear force and the electromagnetic force belong to a single framework known as the Electroweak Theory.

QCD QCD is a theory of the strong interaction. QCD appears under the imposition of gauge invariance under the non-Abelian $SU(3)$ group. This group introduces eight new fields which correspond to the eight colour charged gluons.

Gauge Group of the SM The SM which describes all these forces is hence a Lorentz invariant QFT that respects the $SU(3) \times SU(2) \times U(1)$ gauge symmetry group.

2.3 Electroweak Theory and the Higgs Mechanism

The need for the scalar field, which we have come to know as the Higgs field originated from two inconsistencies within the SM. The first of these being the inability to formulate bosonic and fermionic mass terms without a Higgs scalar term. Within the formulation of the SM, it was recognised that neither gauge boson mass terms nor fermion mass terms respect the SM gauge symmetry. The addition of the Higgs field to these terms brings gauge invariance, this process will be shown later. In the meantime, let us look the the second problem which involves unitarity violation in the four-point scatterings of Fermi's Theory [2] [3].

2.3.1 Unitarity Violation in Fermi's Theory

Let us begin, by considering the weak force mediated interaction of a neutrino-muon pair going to a neutrino-electron pair

$$\bar{\nu}_\mu + \mu^- \rightarrow \bar{\nu}_e + e^-. \tag{2.5}$$

This process is shown in Figure 2.2.

We aim to calculate the strength of coupling at the vertex of this interaction. For such a vertex to occur the particles must meet and scatter off of one another. We describe the scattering using the classical idea of an area in which these particles interact. Such an area is known as the scattering cross-section.

Fermi's theory describes this process as a four-point interaction, with form

$$G_F(\bar{\psi}\psi)(\bar{\psi}\psi), \tag{2.6}$$

where G_F is known as the Fermi coupling. The overall dimension of the vertex is required to be 4, and using the fact that ψ has dimension

$$\psi = [M]^{3/2}, \tag{2.7}$$

our coupling constant must then have dimension

$$G_F = [M]^{-2}. \tag{2.8}$$

The dimension of the cross-section, is given to be

$$\sigma = [M]^{-2}. \tag{2.9}$$

Since $\sigma \sim G_F^2$, to preserve dimensionality we must multiply σ by a term of dimension $[M]^2$.

$$\sigma \sim G_F^2 E^2, \tag{2.10}$$

where E is the centre of mass-energy for the interaction. Using partial wave expansion, the cross-section for a spin-less particle may be written in the form [4] [6]

$$\sigma \leq \frac{4\pi}{k^2} \sum_{l=0}^{\infty} (2l+1), \tag{2.11}$$

with k is the momentum in the centre of mass frame. We see that in Eq. (2.11) the cross-section will always decrease as the energy increases. This statement directly contradicts the form of Eq. (2.10) forming the essence of the unitarity violation of the weak force.

6: There is a $\sin^2 \delta_l$ term (where δ_l is a real angle associated with the amplitude) which we may ignore by rewriting the cross-section as an inequality.

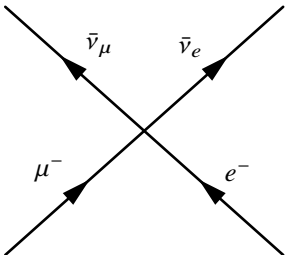

Figure 2.2: The four point Fermi interaction: $\bar{\nu}_\mu + \mu^- \rightarrow \bar{\nu}_e + e^-$.

To aid our situation, we can UV-complete the interaction, as shown in Figure 2.3. UV completing means that we add a mediator particle that only appears on-shell (physically) at high energies. In our UV-completed vertex of Figure 2.3 the mediator is the W boson.

At each vertex we have

$$(\bar{\psi}\psi)W. \tag{2.12}$$

Vector boson fields have mass dimensionality

$$W = [M]^1, \tag{2.13}$$

and, our cross-section goes like $\sim g^2$, with $g = [M]^0$. Hence, we need to divide it by a term of dimension $[M]^2$ to satisfy dimensionality. Upon division

$$\sigma \sim \frac{g^2}{E^2}, \tag{2.14}$$

which evidently decreases with increasing energy, preserving unitarity.

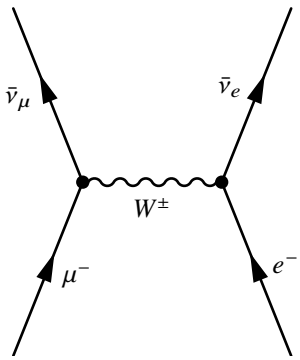

Figure 2.3: The $W^\pm$ boson mediated four-point interaction: $\bar{\nu}_\mu + \mu^- \rightarrow \bar{\nu}_e + e^-$.

The UV-completed interaction is experimentally observed to hold only over small ranges which has the profound implication that the W boson must be a massive particle.

2.3.2 Electroweak Symmetry Breaking

The Higgs in the SM arises from an aspect known as the Higgs Mechanism, which is responsible for electroweak symmetry breaking (EWSB).

Goldstone's theorem is an important precursor to EWSB. It says that for a continuous global symmetry of our theory having symmetry generator Q, if Q annihilates the ground state ($Q|0\rangle = 0$), it leads to

the appearance of a massive particle. Otherwise, if Q does not annihilate the ground state ($Q|0\rangle \neq 0$) then we have the appearance of a massless state, known as a Goldstone Boson.

Spontaneous symmetry breaking occurs when a symmetry present in our theory is broken by the ground state. EWSB is the occurrence of this in the electroweak sector.

We will work towards being able to apply spontaneous symmetry breaking to a model invariant under local $SU(2) \times U(1)$ symmetry as present in the electroweak theory. We find that the EWSB process is responsible for the appearance and unification of the weak and electromagnetic forces of the SM.

The Global $U(1)$ Group Model Consider the Goldstone Model Lagrangian [3], [5], [6] describing a complex scalar ϕ field

$$\mathcal{L} = (\partial_\mu \phi^\dagger)(\partial^\mu \phi) + \mu^2(\phi^\dagger \phi) - \frac{1}{4}\lambda(\phi^\dagger \phi)^2, \tag{2.15}$$

with

$$\phi = \frac{1}{\sqrt{2}}(\phi_1 - i\phi_2). \tag{2.16}$$

Eq. (2.15) respects a global $U(1)$ symmetry, under which the field ϕ transforms

$$\phi \longrightarrow \phi' = \exp(-i\alpha)\phi, \tag{2.17}$$

where α is a constant phase. Such a transformation, as can easily be shown, leaves the Lagrangian invariant.

A Lagrangian for the field contains a kinetic T and potential term V

$$\mathcal{L} = T(\phi) - V(\phi), \tag{2.18}$$

where T contains terms that go like $\partial_\mu(\partial_\mu \phi \partial^\mu \phi)$ and

$$V = -\mu^2(\phi^\dagger \phi) + \frac{1}{4}\lambda(\phi^\dagger \phi)^2. \tag{2.19}$$

The mass term in the Lagrangian is the term quadratic in the field operators, this will from the above appear in the potential V. The quadratic term in V has coefficient $-\mu^2$. Conventionally the mass term has the form $+\frac{m^2}{2}(\phi^\dagger \phi)$, which gives us a mass term of $m_\phi = \sqrt{-2\mu}$. Then the mass term associated with our complex Goldstone Lagrangian is imaginary, resulting in a negative mass squared.

To produce a positive mass spectrum of particles, we need to examine the potential term in the Lagrangian. The crucial step is to find the

minimum of our potential. The minimum can be found by solving

$$\frac{\partial V}{\partial(\phi^\dagger\phi)} = 0. \tag{2.20}$$

For our potential the minimum occurs on the circle

$$\phi_{1,\min}^2 + \phi_{2,\min}^2 = \frac{4\mu^2}{\lambda} \equiv v^2. \tag{2.21}$$

This circle represents a degenerate set of minimum solutions and we are free to choose a particular solution. A simple solution, where one of the components is chosen zero, is $\phi_{1,\min} = v$ and $\phi_{2,\min} = 0$. Substituting the real and imaginary solution components into Eq. (2.16), we get the solution $\phi_{\min} = \frac{v}{\sqrt{2}}$. We call this chosen minimum energy the vacuum state or ground state.

A graphical discussion of the points discussed so far proves useful. Plotting the potential function against ϕ_1 and ϕ_2, we find a Mexican hat result, shown in Figure 2.4.

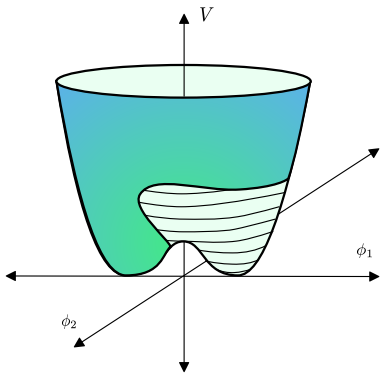

Figure 2.4: The SM Higgs potential function. The z-axis is the potential function, while the x and y-axes are the fields ϕ_1 and ϕ_2.

Figure 2.4 shows that we have two sets of extrema, a circle of global *minimum* surrounding a local *maximum*. Initially, to respect the symmetries of the Lagrangian, the potential sits at the local maximum, where $\phi_1 = \phi_2 = 0$. This is meta-stable point, but we have a 'safer' region, the stable points along the circle of minima. This is precisely the circle described by our vacuum state.

This process of moving to our global minimum has altered a symmetry of the system. Notice that at the local maximum our system was symmetric under rotations about the potential axis, V. However, after moving to a solution on the circle of minima, such a symmetry is no longer present. This change in the system symmetry state is what we mean by spontaneous symmetry breaking. As we shall see later the symmetries of this global minimum are different to that of the original Lagrangian.

In a quantum theory, the system will oscillate around the classical minimum. As such, we next cast our attention to small oscillations about our newly defined vacuum state. We may express our complete set of vacuum states in polar form

$$\phi(x) = \frac{1}{\sqrt{2}}(v \pm h(x)) \exp\left(\frac{i\theta(x)}{v}\right). \tag{2.22}$$

This is just the equation of the minimum potential circle, with a perturbation $h(x)$ to the radial term, corresponding to an oscillation around the minimum.

Substituting this form into the Goldstone Lagrangian Eq. (2.15) gives

$$\mathcal{L}_G = (\partial_\mu h)(\partial^\mu h) - \mu^2 h^2 + \frac{1}{2}(\partial_\mu \theta)(\partial^\mu \theta) + ..., \tag{2.23}$$

where the ellipsis represent higher dimension interaction terms. The appearance of the negative sign associated with the mass term here comes from a cancellation when expanding the dimension four term in the Lagrangian (keeping in mind that v is defined as in Eq. (2.21)).

We now have a massive field h with mass $\sqrt{2}\mu$, and a massless field θ. Spontaneous symmetry breaking has reduced our initial complex scalar field to a pair of fields, one massive, one massless. The massless field is, in fact, a Goldstone mode. By Goldstone's Theorem, it was guaranteed to make an appearance if symmetry was broken and here it is in the form of θ.

The Local $U(1)$ Model Next consider a local $U(1)$ transformation

$$\phi \longrightarrow \phi' = \exp(-i\alpha(x))\phi. \tag{2.24}$$

Under such a transformation, our Goldstone Lagrangian Eq. (2.15) is no longer invariant as we pick up $\partial\alpha(x)$ terms. To retain invariance, we introduce a massless field A^μ and the covariant derivative

$$D^\mu = \partial^\mu + iqA^\mu, \tag{2.25}$$

where A^μ transforms as

$$A^\mu \longrightarrow A'^\mu = A^\mu + \frac{1}{q}\partial^\mu \alpha(x). \tag{2.26}$$

Our Goldstone Lagrangian becomes

$$\mathcal{L} = [(\partial_\mu + iqA_\mu)\phi]^\dagger[(\partial^\mu + iqA^\mu)\phi] - \frac{1}{4}F_{\mu\nu}F^{\mu\nu} + \mu^2(\phi^\dagger\phi) - \frac{1}{4}\lambda(\phi^\dagger\phi)^2, \tag{2.27}$$

where we have included the kinetic energy term $F_{\mu\nu}F^{\mu\nu}$ for the massless field. Identically to the global case, we break the symmetry of the theory and express ϕ in its polar form Eq. (2.22). Now, we can exploit a crucial feature attributed to local symmetries. Start by performing a gauge transformation on ϕ

$$\phi(x) \longrightarrow \phi(x)' = \exp\big[-i\alpha(x)\big]\frac{1}{\sqrt{2}}\big(v \pm h(x)\big)\exp\left(\frac{i\theta(x)}{v}\right), \tag{2.28}$$

and selecting

$$\alpha(x) = \frac{\theta(x)}{v}, \tag{2.29}$$

we conveniently get

$$\phi' = \frac{1}{\sqrt{2}}(v \pm h(x)). \tag{2.30}$$

Our θ field has gone. We say the θ field has been 'gauged-away'.We are always free to choose an α that gauges-away our massless mode under such a local symmetry. To investigate what is happening on the particle front let us substitute this new form into our Goldstone Lagrangian

$$\begin{aligned}\mathscr{L} = &-\frac{1}{4}(\partial_\mu A_\nu - \partial_\nu A_u)(\partial^\mu A^\nu - \partial^\nu A^\mu) + \frac{1}{2}q^2v^2A_\mu A^\mu \\ &+ \frac{1}{2}\partial_\mu h \partial^\mu h - \mu^2 h^2 + \dots ,\end{aligned} \tag{2.31}$$

again the ellipsis represent higher dimensional terms.

From the Lagrangian, we see that both of our fields are now massive. The previously massless gauge field A 'swallows' the Goldstone field θ through the local gauge transformation. This disappearance of the θ field contributes a longitudinal polarisation state to the vector field, through which A becomes massive.

The Electroweak Non-Abelian $SU(2) \times U(1)$ Model Let us now extend to a Lagrangian that respects the electroweak local $SU(2) \times U(1)$ symmetry. The $SU(2)$ group brings with it an extra three degrees of freedom. To accommodate for these degrees of freedom, we promote ϕ to a complex doublet of four real scalar fields

$$\phi = \begin{pmatrix} \phi^+ \\ \phi^o \end{pmatrix} = \begin{pmatrix} \phi_1 + i\phi_2 \\ \phi_3 + i\phi_4 \end{pmatrix}. \tag{2.32}$$

ϕ transforms according to the SU(2) gauge transformation

$$\phi \longrightarrow \phi' = \exp(-i\boldsymbol{\alpha}\cdot\boldsymbol{\tau}/2)\phi. \tag{2.33}$$

as well as the $U(1)$ symmetry transformation of Eq. (2.17). Here, $\boldsymbol{\tau}$ are the Pauli-spin matrices[7] and $\boldsymbol{\alpha}$ is a vector consisting of gauge parameters. After spontaneous symmetry breaking the vacuum state acquires an expectation value

$$\langle 0|\phi_1^2 + \phi_2^2 + \phi_3^2 + \phi_4^2|0\rangle = v^2. \tag{2.34}$$

One solution to this vacuum state follows

$$\phi = \frac{1}{\sqrt{2}}\begin{pmatrix} 0 \\ v \end{pmatrix}. \tag{2.35}$$

This choice of solution is convenient to make when describing the "Glashow-Weinberg-Salam" (GWS) Model [7] for the description of electroweak interactions and also the standard choice in the unitary gauge.[8]

The solution to the vacuum state above mixes the third component

7: The Pauli-spin matrices generate a representation of $SU(2)$.

8: The unitary gauge is a choice of gauge transformations for our scalar fields such that Goldstone bosons disappear from the theory.

of the $SU(2)$ symmetry with $U(1)$ symmetry, resulting in symmetry generators, $\tau_1, \tau_2, I + \tau_3, I - \tau_3$.

The symmetries $\tau_1, \tau_2, I - \tau_3$ do not annihilate the ground state[9] and due to Goldstone's theorem these give three Goldstone bosons. However, the symmetry $I + \tau_3$ does annihilate the ground state

$$(I + \tau_3) \begin{pmatrix} 0 \\ \frac{v}{\sqrt{2}} \end{pmatrix} = 0. \tag{2.36}$$

In turn, we have the appearance of a massive state. Regardless of the solution we choose for our ground state, an unbroken symmetry will arise. Hence, breaking symmetry under these conditions results in three massless Goldstone bosons, one for each broken symmetry, as opposed to the four we expect under complete symmetry breaking.

Each of the three broken symmetries will generate massless bosons which will then become extra polarisation states of the W^+, W^- and Z bosons, giving them mass. The unbroken symmetry will remain, and so a single massless photon appears in the final theory. Among the remnants, we will also have a massive scalar field, the Higgs field

$$\phi = \begin{pmatrix} \phi^+ \\ \phi^o \end{pmatrix} = \frac{1}{\sqrt{2}} \begin{pmatrix} 0 \\ v + h(x) \end{pmatrix}, \tag{2.37}$$

where v is known as the vacuum expectation value (VEV) and has value $v \sim 246$ GeV.

This leaves us with precisely what we see in the electroweak sector: three massive bosons and a massless photon. We have spontaneously broken $SU(2) \times U(1)$ symmetry to a $U(1)$ symmetry. Counting degrees of freedom, we began with four real scalar ϕ fields with four degrees of freedom in total. We also had four massless gauge fields, each with two polarisation states. Initially, this amounts to twelve degrees of freedom in total.

Three symmetries are broken and, as a result, we get three Goldstone bosons. These bosons are then 'swallowed' by three gauge bosons giving them an extra polarisation state.

After symmetry breaking, we have three massive vector fields $W^\pm, Z$, a massless vector field A and one massive scalar field h. Counting the final degrees of freedom we find, as expected, that there is an equal amount before and after symmetry breaking has been performed. This is summarised in Table 2.1.

The appropriate Lagrangian is

$$\mathcal{L} = [D_\mu \phi]^\dagger [D^\mu \phi] - \frac{1}{4} \boldsymbol{F}_{\mu\nu} \boldsymbol{F}^{\mu\nu} - \frac{1}{4} G_{\mu\nu} G^{\mu\nu} + \mu^2 (\phi^\dagger \phi) - \frac{1}{4} \lambda (\phi^\dagger \phi)^2, \tag{2.38}$$

9: A key feature was that $Q|\phi_0\rangle \neq 0$, for a broken symmetry Q acting on the vacuum state ϕ_0.

with derivative operator

$$D^\mu \phi = (\partial^\mu + ig\boldsymbol{\tau} \cdot \boldsymbol{W}^\mu/2 + ig' B^\mu/2)\phi, \tag{2.39}$$

where $\boldsymbol{F}^{\mu\nu}$ and $G^{\mu\nu}$ are the kinetic terms for the gauge fields $\boldsymbol{W}^\mu$ and B^μ, respectively

$$\begin{aligned} \boldsymbol{F}^{\mu\nu} &= \partial^\mu \boldsymbol{W}^\nu - \partial^\nu \boldsymbol{W}^\mu - g\boldsymbol{W}^\mu \times \boldsymbol{W}^\nu, \\ G^{\mu\nu} &= \partial^\mu B^\nu - \partial^\nu B^\mu. \end{aligned} \tag{2.40}$$

The gauge field $\boldsymbol{W}^\mu$ transforms under $SU(2)$, while B^μ transforms under $U(1)_Y$. We have also introduced the gauge couplings g and g' for the $\boldsymbol{W}^\nu$ and B^ν fields, respectively.

Gauge Boson Spectrum The $W^\pm$ bosons are described in terms of the W_1 and W_2 fields via the linear combination

$$W^\pm = \frac{1}{\sqrt{2}}(W_1 \pm iW_2). \tag{2.41}$$

It becomes more complicated for the Z boson and the photon, which stem from the W_3 and B gauge fields. After EWSB, we find that the associated Lagrangian mixes the gauge fields, and so the resulting mass matrix is not diagonal. We aim to diagonalise this mass matrix bringing our fields into a physical basis. The term that involves this mixing may be written in a matrix form

$$\frac{1}{8}v^2 \begin{pmatrix} W_{3\mu}, B_\mu \end{pmatrix} \begin{pmatrix} g^2 & -gg' \\ -gg' & (g')^2 \end{pmatrix} \begin{pmatrix} W_{3\mu} \\ B_\mu \end{pmatrix}. \tag{2.42}$$

Solving the eigenvalue equation, we may diagonalise the interaction matrix

$$M_{W_3 B} = \frac{1}{8}v^2 \begin{pmatrix} g^2 + (g')^2 & 0 \\ 0 & 0 \end{pmatrix}. \tag{2.43}$$

The diagonal interaction matrix now has the masses for the Z bosons and the photon along the diagonal.

We can describe this mixing through a more elegant approach by making use of the Weinberg angle. By convention we define

$$c_{\theta_W} = \frac{g}{\sqrt{g^2 + (g')^2}}, \; s_{\theta_W} = \frac{g'}{\sqrt{g^2 + (g')^2}}. \tag{2.44}$$

An orthogonal rotation through the Weinberg angle relates our W_3 and B fields to their physical states

$$\begin{pmatrix} Z^\mu \\ A^\mu \end{pmatrix} = \begin{pmatrix} c_{\theta_W} & s_{\theta_W} \\ -s_{\theta_W} & c_{\theta_W} \end{pmatrix} \begin{pmatrix} W_3^\mu \\ B^\mu \end{pmatrix}. \tag{2.45}$$

Expanding out the quadratic derivative operator term of the Lagrangian and rotating through the Weinberg angle, we have

$$(D_\mu\phi)^\dagger(D^\mu\phi) = \frac{1}{2}(v+h)\left[\frac{g^2W_\mu^- W^{\mu+}}{2} + \partial_\mu\partial^\mu + \frac{g^2Z_\mu Z^\mu}{4c_{\theta_W}}\right](v+h). \quad (2.46)$$

At this point we may read off masses* and couplings directly

$$m_W = \frac{gv}{2}, \quad m_Z = \frac{m_W}{c_{\theta_W}}, \quad (2.47)$$

$$g_{hWW} = igm_W g^{\mu\nu}, \quad g_{hhWW} = \frac{i2m_W^2}{v^2}g^{\mu\nu}, \quad (2.48)$$

$$g_{hZZ} = \frac{ig}{c_{\theta_W}}m_Z g^{\mu\nu}, \quad g_{hZZ} = \frac{ig^2}{2c_{\theta_W}^2}g^{\mu\nu}. \quad (2.49)$$

By the Weinberg angle we may express the masses of $W^\pm$ and Z vector bosons as

$$m_W = \frac{vg'}{2t_{\theta_W}}, \quad m_Z = \frac{v}{2g's_{\theta_W}}. \quad (2.50)$$

This leads to the useful relationship

$$\frac{m_W}{m_Z} = c_{\theta_W}. \quad (2.51)$$

We see that if $\theta_W \to 0$ then $m_W \to m_Z$, so the Weinberg angle relates the mass difference between the charged W bosons and the neutral Z boson. This mixing may be represented as

$$\rho = \frac{m_W^2}{m_Z^2 c_{\theta_W}^2}, \quad (2.52)$$

which at tree-level equals one but deviates when incorporating self-energy corrections $\Pi_{WW}^{\mu\nu}$ and $\Pi_{ZZ}^{\mu\nu}$. Later we will see that the ρ parameter comes in useful when searching for new physics (NP) in the electroweak sector.

2.4 Fermions

Fermions (spin-half) particles were discovered to have mass as early as 1923 when the oil drop experiment [8] was used to measure the electron charge. This need for fermion mass motivates us to extend the Higgs mechanism to spin-half particles.

Field	DOF	No.
Before EWSB		
W	2	3
B	2	1
ϕ	1	4
After EWSB		
$W^\pm, Z$	3	3
A	2	1
h	1	1

Table 2.1: Fields and degrees of freedom (DOF) before and after Electroweak Symmetry Breaking (EWSB) has occurred.

* The mass of the $W^\pm$ boson is defined as twice the mass that would be result using the general $\frac{1}{2}m^2\psi$ prescription. This is because the $W^\pm$ particle is in fact defined as a linear combination of the W^1 and W^2 particles and the physical mass eigenstate of $W^\pm$ needs to be multiplied by two to account for this.

Later, in 1956, it was shown fermions cannot be massless according to electroweak theory as they violate parity under interactions with the weak force [9] [10]. We discuss why this is so, and introduce the concept of left- and right-handed particles in the following.

2.4.1 Chiral Symmetry

Fermions are divided into two groups, left-handed and right-handed, based on properties known as helicity and chirality.

The projection of a particle's spin onto the direction of momentum defines a particle's helicity. A particle can either have left- or right-handed helicity[10] . As the direction any massive particle is travelling in is entirely dependent on the frame of reference of the observer, we can always find two frames in which a massive particle has opposite vectors of motion, hence, opposite helicities. To avoid this kind of frame dependence, we introduce a concept known as chirality. Chirality also assigns particles a handiness (left or right-handed) depending on their spin and direction of travel. However, chirality is Lorentz invariant. Massless particles must by this definition have the same helicity and chirality. It is not possible to find a frame in which their direction of motion is reversed as this would require a boost larger than c.

10: by definition a clockwise spin in the direction a particle is travelling is left-handed.

In the Dirac representation, the chirality operator is the γ_5 matrix with eigenvalues $-1, +1$ for left-handed and right-handed chiral classification, respectively. In order to extract left or right-handed components of a particle's wave function ψ we use the projection operators

$$\psi_L = P_L\psi = \frac{1-\gamma_5}{2}\psi, \quad \psi_R = P_R\psi = \frac{1+\gamma_5}{2}\psi, \tag{2.53}$$

where $\psi = \psi_L + \psi_R$.

Now, this is interesting to us as weak interactions have been observed [10] to treat left- and right-handed fermions differently. In particular, $W^{\pm}$ bosons interact only with left-chiral fermion doublets; they violate parity. The outcome of this is that fermions must be able to exist as both left- and right-handed states. Leading to the requirement that fermions must have a mass because, as discussed, massless particles are restricted to a single chirality.

2.4.2 Fermions and Flavour

Left-handed fermions are grouped in $SU(2)$ doublets, whereas right-handed fermions are grouped into $SU(2)$ singlets. Particles within each $SU(2)$ doublet are referred to as a family.

Fermion Families

Left-Handed Lepton Doublets

$$l_L^1 = \begin{pmatrix} \nu_e \\ e^- \end{pmatrix}_L, \quad l_L^2 = \begin{pmatrix} \nu_\mu \\ \mu^- \end{pmatrix}_L, \quad l_L^3 = \begin{pmatrix} \nu_\tau \\ \tau^- \end{pmatrix}_L. \tag{2.54}$$

Right-Handed Lepton Singlets

$$e_R, \quad \mu_R, \quad \tau_R, \quad \{\nu_{eR}, \quad \nu_{\mu R}, \quad \nu_{\tau R}\}. \tag{2.55}$$

Left-Handed Quark Doublets

$$q_L^1 = \begin{pmatrix} u \\ d \end{pmatrix}_L, \quad q_L^2 = \begin{pmatrix} s \\ c \end{pmatrix}_L, \quad q_L^3 = \begin{pmatrix} t \\ b \end{pmatrix}_L. \tag{2.56}$$

Right-Handed Quark Singlets

$$u_R, \quad d_R, \quad s_R, \quad c_R, \quad t_R, \quad b_R. \tag{2.57}$$

Notice that the right-handed neutrinos are in curly-braces. Until recently right-handed neutrinos were not thought to exist. As such the neutrinos could not change chirality and had to be massless. Recently oscillations between neutrino families have been observed [11] which are only possible if both left and right-handed neutrinos are present. Measurements have put a small upper limit on the total mass of the three neutrinos. By not included right-handed neutrinos above, we are assuming a massless neutrino theory.

2.4.3 Weak Isospin and Hypercharge of Fermions

Weak isospin and weak hypercharge are quantum numbers that together describe the electroweak interaction. Weak isospin is one of the three generators associated with $SU(2)$, while weak hypercharge is the generator associated with $U(1)$. We denote the magnitude of

weak isospin as T. Usually, we are only interested in the third component of weak isospin T_3, which is conserved by all forces.

Left-handed fermions have quantum numbers $T = 1/2$ and $T_3 = \pm 1/2$ [11] , whereas right-handed fermions possess a quantum number of $T = 0$ for each T. Charged $W^{\pm}$ bosons only interact with particles that have a non-zero T_3 quantum number. Hence they only interact with left-handed fermions. Upon interaction, charged $W^{\pm}$ bosons will raise or lower the value of T_3 of a fermion by an integer value. This interaction causes the particles to change flavour within their doublet. To include right-handed counterparts, we introduce the concept of weak hypercharge. Weak hypercharge is associated with the B field and takes into account both right- and left-handed fermions. We denote weak hypercharge by Y and together with the third component of weak isospin T_3 we construct a particles charge via the Gell-Mann-Nishijima Formula

$$Q = T_3 + Y/2. \tag{2.60}$$

To complete our picture of weak isospin and hypercharge, we give the values associated with these quantum numbers as well as the resultant charge in Table 2.2.

11: The sign of $T_3 = \pm 1/2$ depends on the fermions position in the doublet structure

$$T_3 = \frac{1}{2}\begin{pmatrix} 1 & 0 \\ 0 & -1 \end{pmatrix}, \tag{2.58}$$

such that, for the example of the up-down quark doublet

$$T_3 \begin{pmatrix} u \\ d \end{pmatrix}_L = \left(+\frac{1}{2}u_L\right) + \left(-\frac{1}{2}d_L\right). \tag{2.59}$$

Particle	T_3	Y	Q
$l^i_{\nu L}$	1/2	-1	0
$l^i_{\nu R}$	0	0	0
l^i_L	-1/2	-1	-1
l^i_R	0	-2	-1
u^i_L	1/2	1/3	2/3
u^i_R	0	4/3	2/3
d^i_L	-1/2	1/3	-1/3
d^i_R	0	-2/3	-1/3

Table 2.2: Quantum numbers of the left and right-handed SM fermions. Each of the fermions is summed over the families $i = 1, 2, 3$.

2.4.4 Yukawa Lagrangian

Earlier, we mentioned that fermions needed to be massive (except neutrinos). A mass term for a fermion would have the form

$$\bar{\psi}_L m \psi_R. \tag{2.61}$$

However, this form is not gauge invariant under $SU(2)$ and $U(1)$ transformations as the chiral left- and right-handed components transform differently. Introduction of the ϕ field is required to regain gauge invariance, such that mass terms can be generated. The Lagrangian which then describes the fermion mass generation is known as the Yukawa Lagrangian and is given by

$$\mathcal{L}_{\text{Yukawa}} = -\sum_{i,j=1}^{3}\left[Y_u^{ij}\overline{u}^i_L\tilde{\phi}u^j_R + Y_d^{ij}\overline{d}^i_L\phi d^j_R + Y_l^{ij}\overline{l}^i_L\phi l^j_R + [\text{H.c.}]\right], \tag{2.62}$$

where the sum is over the three families of particles and we have not included the mass terms for neutrinos. The Y terms are Yukawa matrices which quantify masses and possibly interaction strengths between members of a family. To correctly represent an up quark mass we have also defined

$$\tilde{\phi} = -i\tau_2\phi^* = \frac{1}{\sqrt{2}}\begin{pmatrix} v+h \\ 0 \end{pmatrix}. \tag{2.63}$$

Lepton Sector Expanding out the leptonic piece of the Yukawa

$$\mathscr{L}_{\text{leptons}} = \sum_{i,j=1}^{3} \left[-G_l^{ij} \begin{pmatrix} \overline{l_\nu}, \bar{l} \end{pmatrix}_L^i \begin{pmatrix} \phi^+ \\ \phi^o \end{pmatrix} e_R^j \right] + [\text{H.c.}] \,. \tag{2.64}$$

The sum is over the three lepton families. Breaking symmetry in the usual way and substituting in the GWS choice for the scalar field we are left with a Lagrangian for the Higgs-lepton coupling[12]

$$\mathscr{L}_{\text{leptons}} = \sum_{i,j=1}^{3} \left[-m_l^{ij} (\bar{l}^i l^j) - \frac{m_l^{ij}}{v} (\bar{l}^i l^j) h \right], \tag{2.66}$$

where

$$m_l^{ij} = \frac{Y_l^{ij} v}{\sqrt{2}}. \tag{2.67}$$

The piece of the Lagrangian Eq. (2.66) after EWSB gives us a lepton mass term and a three-point Higgs-lepton interaction. The mass m_l^{ij} is a 3×3 matrix[13] . We are in what is known as the interaction basis (or weak basis). As the mass matrix is diagonal already, we can easily read off the masses for our leptons, and the interaction basis is equivalent to the mass basis.

12: Note that for fermion ψ we have

$$\overline{\psi}_L \psi_R + \overline{\psi}_R \psi_L = \overline{\psi} \psi. \tag{2.65}$$

13: As we are working in a theory where the neutrinos are massless, it is always possible to obtain a diagonal mass matrix.

Quark Sector The Higgs-quark interactions are

$$\mathscr{L}_{\text{quarks}} = -\sum_{i,j=1}^{3} \left[G_d^{ij} \bar{q_L}^i \phi d_R^j - G_u^{ij} \bar{q_L}^i \tilde{\phi} u_R^j \right] + [\text{H.c.}] \,, \tag{2.68}$$

with the summation $i, j = 1, 2, 3$ over the three quark families.

The quark Lagrangian after EWSB is

$$\mathscr{L}_{\text{quarks}} = \sum_{i,j=1}^{3} \left[-m_d^{ij} \bar{d}^i d^j \left(1 + \frac{h}{v}\right) - m_u^{ij} \bar{u}^i u^i \left(1 + \frac{h}{v}\right) \right], \tag{2.69}$$

where we define

$$m_d^{ij} = \frac{Y_d^{ij} v}{\sqrt{2}}, \quad m_u^{ij} = \frac{Y_u^{ij} v}{\sqrt{2}}. \tag{2.70}$$

There exist interactions among different quark families. As a result, the mass matrices in this interaction basis are not diagonal and to determine physical mass values we need to move to a mass basis in which the matrices are diagonal. This change in basis is characterised by the unitary T and S matrices[14] , which are chosen such that they diagonalise mass matrix m_ψ

$$M_\psi^{ij} = (S_\psi^{ij})^\dagger m_\psi^{ij} T_\psi^{ij}, \tag{2.71}$$

for $\psi = u, c, t, d, s, b$. Rotated to the mass basis the quark Lagrangian

14: S originates from transforming left-handed components, and T originates from transforming right-handed components.

Eq. (2.69) becomes

$$\mathscr{L}_{\text{quarks}} = \sum_{i,j=1}^{3} \left[-M_d^{ij} \bar{d}'^i d'^j \left(1 + \frac{h}{v}\right) - M_u^{ij} \bar{u}'^i u'^i \left(1 + \frac{h}{v}\right) \right]. \tag{2.72}$$

The transformations through S and T also need to be applied to other terms involving fermions in the Lagrangian. One such term is that describing quark self-energies and interactions with gauge bosons

$$\begin{aligned}\mathscr{L}_{\text{K,quarks}} = \bar{q_L}\gamma^\mu(\partial_u + ig\boldsymbol{\tau}\cdot\boldsymbol{W}_\mu/2 + ig'B_\mu/2)q_L + \bar{u_R}\gamma^\mu(\partial_u + ig'B_\mu/2)u_R \\ + \bar{d_R}\gamma^\mu(\partial_u + ig'B_\mu/2)d_R.\end{aligned} \tag{2.73}$$

Expanding, terms associated with the neutral gauge fields (W_3 and B) are of the form

$$\bar{u_L^i}[\text{field}]u_L^j \ , \ \bar{d_L^i}[\text{field}]d_L^j \ \ldots . \tag{2.74}$$

Moving to the mass basis leaves these unchanged. Terms associated with the charged gauge fields ($W^\pm$) take on the form

$$\bar{u_L^i}[\text{field}]d_L^j \ , \ \bar{d_L^i}[\text{field}]u_L^j \ \ldots . \tag{2.75}$$

As these mix quark flavours, moving into the mass basis will give rise to an important component of the electroweak theory, the Cabibbo-Kobayashi-Maskawa (CKM) Matrix [12]. The basis transformation,

$$\bar{u}_L'^i (S_u^{ij})^\dagger [\text{field}] (S_d^{ij}) d_L^i, \tag{2.76}$$

defines the CKM matrix, which is unitary

$$V_{\text{CKM}} = (S_u^{ij})^\dagger (S_d^{ij}). \tag{2.77}$$

The CKM matrix describes flavour-changing (FC) interactions among quarks. The result is that a quark can change its flavour through interaction with a $W^\pm$ particle. For example, a down-quark can become an up-quark through the emission of a W boson, as shown in Figure 2.5. This kind of flavour-changing process is known as a flavour-changing charged current (FCCC), as the flavour is changed by a charged particle. FCCCs will flip fermions to the other member of the doublet-structure (change their charge Q by one), which may not necessarily be within their own family. Alternatively, if the FC process happens through a neutral particle, and the fermion charge does not changed, we get flavour-changing neutral currents (FCNC). There are no FCNC in the SM at tree-level. However, they may be constructed at one-loop, as shown in Figure 2.6. By experimental observation, it was shown that FC processes are significantly suppressed in the SM, even at one loop. This suppression was explained by Sheldon L. Glashow, John Iliopoulos and Luciano Maiani and is known as the GIM mechanism.

At loop-level, cancellations between diagrams of quarks with similar mass (namely the charm and up quark) lead to the occurrence of such a suppression. The CKM matrix governs the FC properties of the W-boson.

The CKM Matrix is given explicitly as

$$V_{\text{CKM}} = \begin{pmatrix} V_{ud} & V_{us} & V_{ub} \\ V_{cd} & V_{cs} & V_{cb} \\ V_{tb} & V_{cs} & V_{tb} \end{pmatrix}. \tag{2.78}$$

To see the significance of terms in the CKM, we may approximate it as

$$V_{\text{CKM}} = \begin{pmatrix} 1 & \Lambda & \Lambda^3 \\ \Lambda & 1 & \Lambda^2 \\ \Lambda^3 & \Lambda^2 & 1 \end{pmatrix}. \tag{2.79}$$

where $\Lambda \backsim 0.2$. As such, processes proportional to terms of power two or more in Λ are negligible in the SM. The complex values of the CKM parameters may be found in Appendix F. An alternate method to parameterise the values of the CKM matrix is known as the Wolfenstein parameterisation

$$V_{\text{CKM}} = \begin{pmatrix} 1-\lambda^2/2 & \lambda & A\lambda^3(\rho - i\eta) \\ -\lambda & 1-\lambda^2/2 & A\lambda^2 \\ A\lambda^3(1-\rho-i\eta) & -A\lambda^2 & 1 \end{pmatrix}, \tag{2.80}$$

where the matrix contains higher corrections but we have included terms of up to order λ^3. In the Wolfenstein parameterisation we have values given in Appendix F.1.

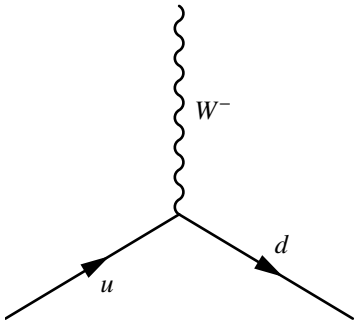

Figure 2.5: The W^- mediated flavour-changing quark interaction.

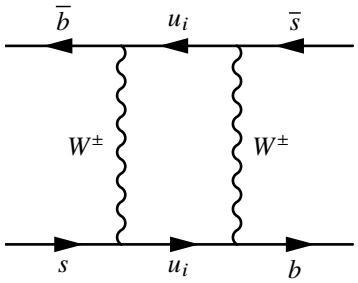

Figure 2.6: Meson mixing in the SM. This diagram shows a box (one-loop-level) diagram of B_s^0 meson mixing.

2.4.5 The Fundamental Couplings in the SM

We have seen that we can extract coupling terms by expanding the Lagrangian. There are three fundamental couplings in the SM that describe the strength of the interactions. These fundamental parameters are the fine structure constant α (electromagnetic interactions), the strong coupling constant α_S (strong QCD interactions) and the Fermi constant G_F (weak interactions). The couplings are energy-dependant, and we discuss the determination of each coupling individually below. We follow the review [13] (specifically sections 9, 10 and 66) and where not explicitly stated we use the values and numerical results presented in the review.

Fine Structure Constant (α): The fine structure constant α is the dimensionless fundamental parameter describing the electromagnetic interaction between elementary charged particles. In QED this is the

coupling of the photon and the electron. The parameter α depends on the energy scale of the electron and is generally stated in the Thomson limit, in which the energy of the photon is much less than that of the particle ($q^2 \sim 0$)

$$\alpha^{-1}(0) = \left(\frac{e^2}{4\pi}\right)^{-1} = 137.036, \tag{2.81}$$

where e is the positron electric charge. Quoted is the experimentally observed value of e from measurement of the $e^{\pm}$ anomalous magnetic moment [14]. At higher energy levels we must incorporate corrections to the vacuum polarization function of the photon, and we may write α at energy q^2 as

$$\alpha(q^2) = \frac{\alpha(0)}{1 - \Delta\alpha(q^2)}, \tag{2.82}$$

with

$$\Delta\alpha(q^2) = \Pi_{\gamma\gamma}(0) - \Pi_{\gamma\gamma}(q^2). \tag{2.83}$$

At the energy of the Z boson and in the $\overline{\text{MS}}$ renormalisation scheme

$$\hat{\alpha}^{-1}(m_Z^2)^{(5)} = 127.916 \pm 0.015. \tag{2.84}$$

We use the convention that parameters with a hat are evaluated in the $\overline{\text{MS}}$ renormalisation scheme [15] [16]. The superscript signifies that the calculation has been carried out to 5-loop order. We may relate this scheme to the on-shell parameter via

$$\Delta\hat{\alpha}(m_Z^2) - \Delta\alpha(m_Z^2) = 0.007127(2). \tag{2.85}$$

Fermi Constant (G_F): The strength of weak interactions is governed by the weak coupling parameter Fermi's constant G_F. Fermi's constant may be derived from the muon lifetime formula

$$\frac{1}{\tau_\mu} = \frac{G_F^2 m_\mu^2}{192\pi^3}\left(1 + \Delta q\right). \tag{2.86}$$

Δq contains higher order QED corrections, expressed as a power series expansion in the renormalised fine-structure constant (at the muon energy)

$$\hat{\alpha}^{-1}(m_\mu) = 135.901. \tag{2.87}$$

See for example Ref. [17] or Ref. [13] for the full expansion. The latest value of Fermi's constant has been evaluated to be

$$G_F = 1.1663787(6) \times 10^{-5}\ \text{GeV}^{-2}. \tag{2.88}$$

The Fermi constant may be related to the electroweak coupling constant g and the Higgs VEV v through the relations

$$G_F = \frac{g^2}{4\sqrt{2}m_W^2} = \frac{1}{(\sqrt{2}v)^{1/2}}. \tag{2.89}$$

Strong Coupling Constant: (α_S)**:** The strong interaction is governed by the QCD coupling α_s. The QCD coupling is dependent the on the energy of the interaction μ and satisfies the renormalisation Group Equation[15] (RGE)

15: An equation that describes the energy evolution of the coupling.

$$\beta(\alpha_s) = \mu^2 \frac{\partial \alpha_s(\mu)}{\partial \log(\mu)} = -(b_0\alpha_s^2 + b_1\alpha_s^3 + b_2\alpha_s^4 + ...). \tag{2.90}$$

In the RGE b_0, b_1, b_2 are the one, two and three-loop β-function coefficients respectively and the ellipses represent further loop corrections that may be applied. The beta-function coefficients depend on the number of flavours (as well as colour-factors C_F, C_A and T_R). The one-loop beta function coefficient is

$$b_0 = \frac{11C_A - 4n_f T_R}{12\pi} = \frac{33 - 2n_f}{12\pi}. \tag{2.91}$$

The remaining beta function coefficients may be found in the review Ref. [13]. One can then solve this analytically at one-loop-level, in the case where the number of flavours is constant. The one-loop equation becomes

$$\alpha_s(\mu) = \left(b_0 \log \frac{\mu^2}{\Lambda^2}\right)^{-1} \tag{2.92}$$

with Λ the scale where perturbativity of α_s breaks down. An analytical solution up to four-loops is presented in the reference. In our numerical analysis we calculate α_s to two-loops unless otherwise specified.[16]

16: Note that α_s is always normalised in the $\overline{MS}$ scheme.

Experimentally, at the mass of the Z boson, we have the strong coupling constant

$$\alpha_s(m_Z) = 0.1181(11). \tag{2.93}$$

With this as a starting point, we may run to another energy scale with two loop accuracy using

$$\alpha_s(\mu) = \frac{\alpha_s(m_Z)}{v(\mu)}\left[1 - \frac{\beta_1}{\beta_0}\frac{\alpha_s(m_Z)}{4\pi}\frac{\ln v(\mu)}{v(\mu)}\right], \tag{2.94}$$

where

$$v(\mu) = 1 - \beta_0 \frac{\alpha_s(m_Z)}{2\pi} \ln \frac{m_Z}{\mu}. \tag{2.95}$$

Here $\beta_0 = \frac{23}{3}$ and $\beta_1 = \frac{116}{3}$ are the beta function coefficients (with the π terms written explicitly outside of the functions and the number of flavours taken constant).

2.4.5.1 Running of the Fermion Masses

The masses of the fermions constitute fundamental parameters of the SM. The position of a fermion propagator pole is known as its pole

mass - this definition is close to its physical mass. Otherwise, akin to couplings, masses run with the energy of the theory and we must also define the running masses. The relationship between the pole mass and the running mass at the energy of the pole mass is (in the $\overline{MS}$ scheme)

$$\begin{aligned}\overline{m}_q(m_q) =& m_q\Bigg[1-\frac{4}{3}\frac{\alpha_s(m_q)}{\pi}+(1.0414N_f-14.3323)\left(\frac{\alpha_s(m_q)}{\pi}\right)^2 \\ &+(-0.65269N_f^2+26.9239N_f-198.7068\left(\frac{\alpha_s(m_q)}{\pi}\right)^3\Bigg],\end{aligned} \tag{2.96}$$

with N_f the number of flavours in the theory considered. The relation is to three-loop order in α_s. The $\overline{MS}$ mass can then be run via the RGE

$$\mu^2\frac{d\overline{m}(\mu)}{d\mu^2}=-\gamma(\alpha_s(\mu))\overline{m}(\mu). \tag{2.97}$$

Here we introduce γ the anomalous dimension, it can be found to four-loops in the review.

Running fermion masses will be used in our numerical analysis, especially when matching flavour physics processes at their occurring energy scales.

2.5 Production & Decays of the SM Higgs Bosons

The Higgs scalar particle interacts with all fermions and bosons of the SM. In this section, we would like to find expressions for the decay processes that possess a non-negligible contribution to the total SM Higgs boson width. Each of the processes discussed in this section are known as the visible Higgs decays; that is, they involve only known particles of the SM. The experimentally measured Higgs boson has a mass of $m_h \sim 125$ GeV, and as such, some decays are kinematically forbidden in the SM. Kinematically forbidden decays occur when the on-shell mass of the final state is greater than that of the SM-Higgs. In this section we just state the particle decay widths. In Appendix A we introduce the methods that are used to calculate the decay widths and derive two- and three-body Lorentz invariant phase space. We then also in this Appendix apply these foundations and calculate $h \to ff$ and $h \to WX$ processes as examples.

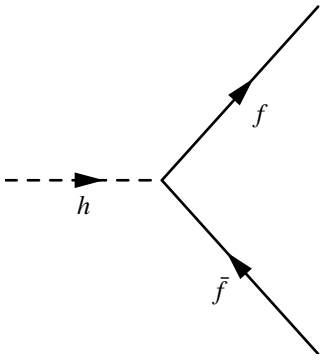

Figure 2.7: The $h \to f\,\bar{f}$ decay.

Higgs to Fermion Decay ($h \to ff$) The process is shown in Figure 2.7. We state the tree-level width below (see Appendix A for the derivation).

$h \to f\bar{f}$ Decay Width

$$\Gamma(h \to f\bar{f}) = \frac{N_c G_F m_h m_f^2}{4\sqrt{2}\pi} [1 - x_f]^{\frac{3}{2}}. \tag{2.98}$$

We have included the colour factor, $N_c = 3$ for quarks and $N_c = 1$ for leptons, in the expression and we define

$$x_i = \frac{4m_i^2}{m_h^2}. \tag{2.99}$$

There are non-negligible NLO and NNLO corrections due to gluons when the decay involves two quarks. These corrections to the width are given by

$$\Gamma = \Gamma_0 \left[1 + 5.67 \frac{\alpha_s(m_h)}{\pi} + (35.94 - 1.36 N_f) \frac{\alpha_s(m_h)}{\pi^2} \right], \tag{2.100}$$

where Γ_0 is the tree-level width.

The Higgs to W decay ($h \to W^+W^-$) The Higgs scalar may decay to two charged vector bosons $W^\pm$. This is kinematically forbidden in the SM as $m_h < 2m_{W^\pm}$. In a model where the scalar is heavier than the combined mass of two $W^\pm$ bosons, the decay width is stated below [18].

$h \to W^+W^-$ Decay Width ($m_h > 2m_{W^\pm}$)

$$\Gamma(h \to W^+W^-) = \frac{G_F m_h^3 \sqrt{1 - x_W}}{8\sqrt{2}\pi} \left[1 - x_W + \frac{3}{4} x_W^2 \right]. \tag{2.101}$$

This decay is still, however, significant in the SM Higgs phenomenology as one of the W bosons may be off-shell (virtual) and then decay into X and $\overline{X}$ components in a way such that $m_h \geq (m_{W^\pm} + 2(m_X))$ holds, the process is shown in Figure 2.8.

Derivation for this process is presented in Appendix A and we state the final width here.

$h \to WX$ Decay Width ($m_{W^\pm} < m_h < 2m_{W^\pm}$)

$$\Gamma(h \to W^\pm X) = \frac{3G_F^2 m_W^4 m_h}{16\pi^3} F_{VX}(\epsilon_W). \tag{2.102}$$

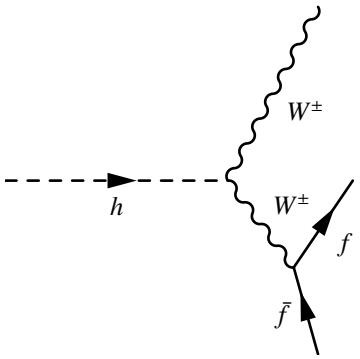

Figure 2.8: The $h \to W^\pm X$ decay process. X in this case represents the two-fermion final state $\overline{f}f$.

We define

$$F_{VX}(\epsilon) = \frac{3(1-8\epsilon^2+20\epsilon^4)}{\sqrt{4\epsilon^2-1}}\arccos\left(\frac{3\epsilon^2-1}{2\epsilon^3}\right) - (1-\epsilon^2)\left(\frac{47}{2}\epsilon^2 - \frac{13}{2} + \frac{1}{\epsilon^2}\right) - 3(1-6\epsilon^2+4\epsilon^4)\ln\epsilon, \tag{2.103}$$

and

$$\epsilon_i = \frac{m_i}{m_h} = \frac{\sqrt{x_i}}{2}. \tag{2.104}$$

The Higgs to Z decay $(h \to ZZ)$ $(m_h > 2m_Z)$ Identical to the $W^\pm$ decay, but with half the number of final states, the Higgs to Z boson decay is given below.

$h \to ZZ$ Decay Width

$$\Gamma(h \to ZZ) = \frac{G_F m_h^3 \sqrt{1-x_Z}}{16\sqrt{2}\pi}\left[1 - x_Z + \frac{3}{4}x_Z^2\right]. \tag{2.105}$$

Finding an expression for three-body decay of $h \to ZX$ follows a similar process to the Higgs to WX boson decay detailed above [19] and is given below.

$h \to ZX$ Decay Width $(m_Z < m_h < 2m_Z)$

$$\Gamma(h \to ZX) = \frac{G_F^2 m_W^4 m_h}{64\pi^3 c_{\theta_W}^4}\left[7 - \frac{40}{3}s_{\theta_W}^2 + \frac{160}{9}s_{\theta_W}^4\right]F_{VX}(\epsilon_Z). \tag{2.106}$$

The Higgs to Photon Decay: $h \to \gamma\gamma$ decay The decay, although having a negligible contribution to the overall SM Higgs branching ratio, is fundamental to the discovery of the Higgs due to its clean signal at colliders. As the photon does not interact directly with the Higgs, these decays must happen indirectly through a loop that joins the initial and final states. Figure 2.9 shows a fermion-loop contribution to the process. Additionally, the $W^\pm$ particles contribute to the loop, as the photon interacts with all charged particles.

The decay width is given below [20].

$h \to \gamma\gamma$ Decay Width

$$\Gamma(h \to \gamma\gamma) = \frac{G_F \alpha^2 m_h^3}{128\sqrt{2}\pi^3} \left| F_W(x_W) + \sum_{\text{fermions}} N_c Q_f^2 F_f(x_f) \right|^2. \tag{2.107}$$

In the decay, Q_f is the charge of the fermion. The form factor contains contributions from the charged bosons $W^\pm$ and the fermions[17]

$$\begin{aligned} F_W(x) &= -[2 + 3x + 3x(2-x)f(x)], \\ F_f(x) &= 2x[1 + (1-x)f(x)], \end{aligned} \tag{2.108}$$

with function

$$f(x) = \begin{cases} \arcsin^2(x^{-1/2}) & \text{if } x \geq 1, \\ \frac{-1}{4}\left[\ln\frac{1+\sqrt{1-x}}{1-\sqrt{1-x}} - i\pi\right] & \text{if } x < 1. \end{cases}$$

The conditional covers the off-shell top quark contribution within the loop.

17: The scalar and pseudo-scalar parts are implicit in the F_f function. Pseudo-scalar terms are those that change sign under parity inversion.

The Higgs to Gluon Decay: $h \to gg$ Another important decay channel is the Higgs to gluon-gluon decay. Again, as the gluons do not directly interact with the Higgs, we must sum over all loop contributions. In this case, the loop contributions are only from quarks.

The $h \to gg$ is given below [20].

$h \to gg$ Decay Width

$$\Gamma(h \to gg) = \frac{G_F \alpha_s m_h^3}{36\sqrt{2}\pi^3} \left| \sum_{\text{quarks}} F_q(x_q) \right|^2. \tag{2.109}$$

In this decay α_s is evaluated at $m_h/2$ and

$$F_q(x) = \frac{4}{3} F_f(x). \tag{2.110}$$

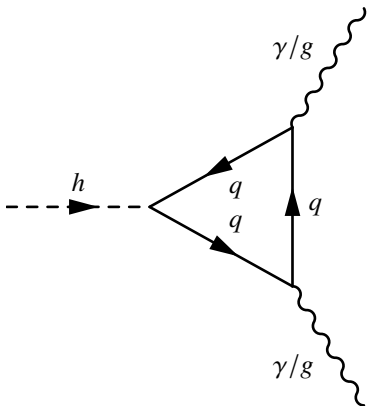

Figure 2.9: The $h \to gg/\gamma\gamma$ decay process which happens via a quark loop.

2.5.1 The Decay Spectrum

Although a Higgs-like resonance has been detected at ~ 125 GeV, it is illuminating to survey the SM branching ratios of a scalar particle for

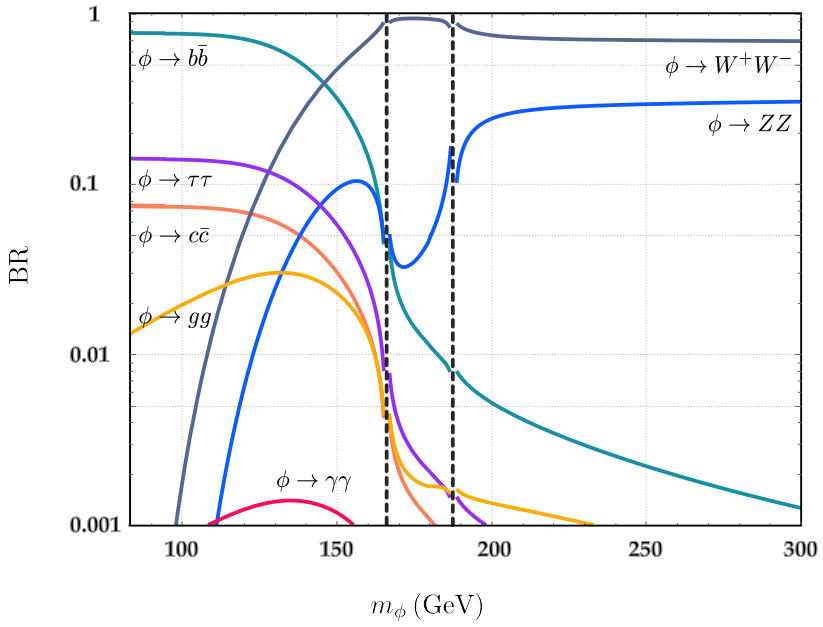

Figure 2.10: The scalar decay branching ratios for $m_W < m_h < 300$ GeV. We see two discontinuities at $2m_W$ and $2m_Z$ (black dashed lines), which occur due to a lack of higher-order corrections to the W and Z propagators. Above 300 GeV the decays of the scalar are dominated by the $\phi \to WW$ and $\phi \to ZZ$ decays.

masses $m_W < m_\phi < 1$ TeV. The formula for the branching ratio of a process is given by

$$\mathrm{BR}(\phi \to X) = \frac{\Gamma_X}{\Gamma_\phi}, \tag{2.111}$$

where Γ_X is the width of a process with final state X and Γ_ϕ is the total scalar width, the sum of all the process widths that contribute to the decay of ϕ. We present the branching ratios of the scalar decays in Figure 2.10. The two most predominant decays are $h \to b\bar{b}$ and $h \to W^+W^-$ as these particles interact with the Higgs most readily. The decay widths of the fermions and the massive bosons go as m_i^2, where m_i is the mass of the respective fermion or boson. As a result, the decays with the highest probability of incidence will be those corresponding to the particles with the most considerable mass. This observation agrees nicely with the underlying principle that the Higgs boson was introduced to give particles mass. We expect particles that interact more often with the Higgs boson to have a larger mass.

Of course, the massless particles; the photon and the gluon, do not interact with the Higgs directly. As discussed, they must interact through a particle loop. There is a large disparity between the $h \to gg$ and $h \to \gamma\gamma$ decay channels. The gluon loop is restricted to the quarks, whereas the photon loop has all fermions as well as charged bosons as contributors. We can explain this disparity by examining the couplings

$$\frac{\Gamma(h \to gg)}{\Gamma(h \to \gamma\gamma)} \approx 3.6\left(\frac{\alpha_S}{\alpha}\right)^2 \frac{|F_g|^2}{|F_\gamma|^2}, \tag{2.112}$$

where we have simplified the form factor components into F_g and F_γ for the gluon and photon processes respectively. The main offender here is the $(\alpha_S/\alpha)^2$ factor, which contributes a factor of ~ 250 causing the wide separation we see between the photon and gluon channels. Essentially, this is a result of the strong interaction (associated with α_S) being of much greater strength than the electromagnetic interaction (associated with α).

We may match experimental observations of Higgs decays from particle collider data with those predicted by Figure 2.10. Any discrepancies would suggest deviations from our SM Higgs, opening up the possibility for physics beyond the SM. We see that a Higgs boson at the mass 125 GeV is very attractive as it provides us with an opportunity to probe many different decay channels.

2.5.2 Higgs Production Channels

A critical component of measurements we make (at colliders) involves the production cross-section of our Higgs states. The measured quantity - the signal strength - is defined according to

$$\mu_{XY} = \sigma_X \Gamma_Y, \tag{2.113}$$

where X is our production channel and Y represents our decay channel. For our Higgs, four main production channels exist, and we will discuss each mechanism in order of respective cross-section size. We will skip the theoretical framework. But note, production widths are found in the same way as decay widths.

Since partons (quarks or gluons) are involved in the initial state, we need information about the position and momentum distribution of such partons within their parent hadron. We get such information from parton distribution functions (PDFs). In this case, the production cross-section is a convolution of the parton-level cross-section we predict with the PDF. Note, that the PDFs are collider-dependant.

Gluon-Gluon Fusion A reversal of the Higgs to gluon-gluon decay in the time direction leads to the gluon-gluon fusion production mechanism $\sigma(gg \to H)$. Gluon-gluon fusion has the largest cross-section of the production channels at the LHC[18] . We show the process in Figure 2.11. The production cross-section is related to the $h \to gg$ decay, with relationship

18: This is said in the context of collider observations.

$$\sigma(gg \to h) = \frac{1}{16\pi}\Gamma(h \to gg)\delta(s - m_h^2), \tag{2.114}$$

which, as expected, is just the difference between the initial state phase spaces of the processes of the two processes

$$\frac{\Gamma(h \to gg)}{\sigma(gg \to h)} = \frac{\int dQ_1}{\int dQ_2}. \tag{2.115}$$

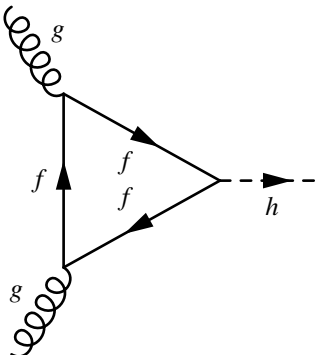

Figure 2.11: The gluon-gluon fusion Higgs production process.

Other Production Channels The second most prominent decay channel at the LHC is vector-boson fusion, this is shown in Figure 2.12. Other production channels known as Higgs-strahlung (also known as $W^{\pm}$ and Z^0 associated production) and top-top/bottom-bottom fusion are shown in Figure 2.13 and Figure 2.14 respectively.

2.6 Effective Field Theory

Most particle interactions, especially loop-processes, involve exchanges between particles that differ over several orders of magnitude in energy. In the SM we work up to the top mass $m_t \sim 170\text{GeV}$.

Generally, when we are solving a physical process, we like to restrict ourselves to magnitudes at which our process occurs. We approximate away effects that happen at different magnitudes.

If then for a particle interaction we are only interested in the physics below a given scale M are we safe to ignore all states with mass $m > M$? The answer is no, as these states may appear off-shell and must be considered. What we may do, however, is create an effective theory. An effective field theory (EFT) is one in which we encode all the physics of heavier states $m > M$ into the vertices of the theory itself.

Let us discuss how this is done.

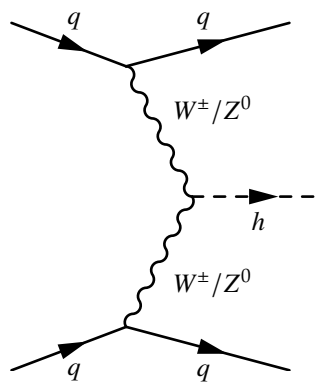

Figure 2.12: The vector-boson fusion Higgs production process.

2.6.1 Constructing an EFT

The creation of an EFT at the energy M occurs by matching the physics at this energy. The matched expressions are then used as the starting point for the effective theory which no longer includes states at or above energy M. The effects of particles at or above our matching energy of M become implicit in the matched theory and have a simpler form than if included in full.

The true benefit of an EFT is in the simplicity of matched terms. This simplified starting point allows us to calculate otherwise complicated interactions.

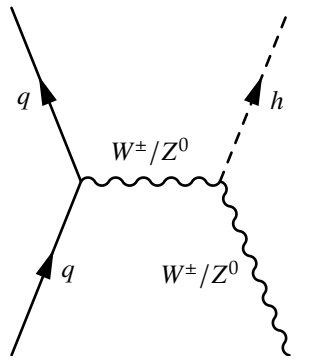

Figure 2.13: The Higgs-strahlung Higgs production process.

We have indeed already seen an example of an EFT. In section 2.3.1 we spoke about the Fermi four-point interaction. This is a four-point vertex that is UV-completed by a $W^{\pm}$ boson. However, before the discovery of the $W^{\pm}$ boson, it was just thought of as a point-like interaction, an effective interaction. In the effective Fermi theory what we do is work at $m < m_W$ such that all particles with $m \geq m_W$ are encoded in the vertex a priori.

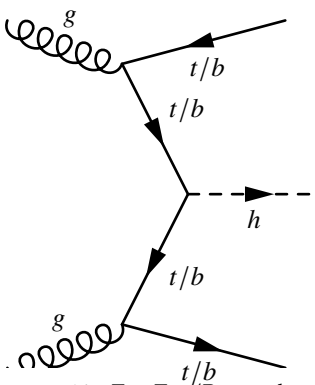

Figure 2.14: Top-Top/Bottom-bottom Fusion Higgs production process.

Following [21], building an EFT follows two steps power counting and matching. When building an EFT, power counting lets us decide to what order in the Lagrangian we want to keep terms up to and matching is the process of extracting the coefficients from those terms.

More formally: When calculating an interaction we find that it expands out in terms of $(1/M)^n$, where M is the energy of the state we are integrating out of our EFT and n is the mass dimension of the corresponding operator. Keeping only the non-negligible terms, we must decide how large we want to allow n; in other words, up to what dimension operators do we want to include. This process of choosing the power of $(1/M)$ is called power-counting. Next, we construct an effective Lagrangian that contains each operator that we have kept, with unknown coefficients. The theories we wish to UV-complete are then matched at $\mu = M$, and we find these unknown coefficients in our effective theory, making it ready to use.

Taking the UV-completed Fermi interaction as an example, if we Taylor expand out the W-propagator in powers of $\frac{p^2}{m^2}$ and keep only the leading term, we get precisely the point-like interaction. If we choose to keep terms of larger powers in $\frac{p^2}{m^2}$ we may build a more accurate effective theory.

We may write an effective version of our complete Lagrangian for m_W the heaviest state in our theory as

$$\mathscr{L}_{\text{eff}} = \mathscr{L}^{m<m_W}_{\text{QED}\times\text{QCD}} + \sum_i C_i(\mu) O_i(\mu), \tag{2.116}$$

where $\mathscr{L}^{m<m_W}_{\text{QED}\times\text{QCD}}$ encodes all physics below m_W and $\sum_i C_i(\mu)O_i(\mu)$ encodes all physics at or above m_W. Here μ is the energy scale at which we evaluate the elements, with $C(\mu)$ the Wilson coefficients of the theory and $O(\mu)$ the operators. These operators represent the in and out states involved in a process, or put more succinctly, they represent the current. The Wilson coefficients $C(\mu)$ contain the couplings for a corresponding operator (current) obtained by matching the effective theory.

Let us define the effective Hamiltonian as

$$\mathscr{H}^{BSM,\text{eff}} = -\lambda_c^{ab}\frac{4G_F}{\sqrt{2}}\sum_i C_i^{(0)}(\mu)\, O_i^{(0)}(\mu). \tag{2.117}$$

The factor $-\lambda_c^{ab}\frac{4G_F}{\sqrt{2}}$ is conventional and is due to the appearance of a potential $W^\pm$ boson, the CKM factor λ_c^{ab} is defined as

$$\lambda_q = V_{cb}^{\text{CKM}*}V_{ca}^{\text{CKM}}. \tag{2.118}$$

Here we write $C^{(0)}$ and $O^{(0)}$ both as bare quantities that require renormalisation. Renormalised quantities may be related to bare quantities via matrices as shown

$$O_i^{(0)} = \hat{Z}_{ji}^O O_j, \tag{2.119}$$

$$C_i^{(0)} = \hat{Z}_{ij}^C O_j. \tag{2.120}$$

To match our theoretical calculations with phenomenological observables, we need to run the Wilson coefficients down to the observable scale μ_f. We do this using the RGE

$$\frac{d}{d\ln\mu}C_i(\mu) = \gamma_{ji}C_j(\mu) \tag{2.121}$$

where γ_{ij} is the anomalous dimension matrix (ADM). Notice that the ADM has no explicit dependence on the energy scale.

We may find the ADM through making use of the fact that one-loop divergences must be cancelled by counter-terms when performing the renormalisation. This condition leads to the equation,

$$\begin{aligned}\gamma^T = \frac{\alpha_s}{4\pi}\left[-2\hat{A}^s - 2\delta\hat{Z}^{O,s}\right] + \frac{\alpha_{\text{em}}}{4\pi}\left[-2\hat{A}^{\text{em}} - 2\delta\hat{Z}^{O,\text{em}}\right] \\ + \mathcal{O}(\alpha_s^2, \alpha_{\text{em}}^2, \alpha_s\alpha_{\text{em}}).\end{aligned} \tag{2.122}$$

In this equation $\hat{A}^i$ are the one-loop divergences of bare amplitudes.

A full discussion of the derivation of the ADM, as well as the form of $\delta\hat{Z}^O$ can be found in [22]. The ADM may be used to build the evolution operator matrix $\hat{U}$, giving the running in vector notation, which we find useful when working with many operators and Wilson coefficients

$$\vec{C}(\mu) = \hat{U}(\mu,\mu_0)\vec{C}(\mu_0). \tag{2.123}$$

After the RG evolution, we have an amplitude that matches the scale of experimental observations.
We may find some mixing between the Wilson coefficients as the dominant interactions change with the running of energy. This is evident

from equation (2.121) when the ADM is non-diagonal.

This RGE may be solved, and the matrix can be found using the publicly available `Mathematica` code `DSixTools` [23][22].

Theory of the Two-Higgs-Doublet Model

3

The SM has a single $SU(2)$ doublet which when combined with the transfer of degrees of freedom within electroweak theory leaves us with a single scalar particle - the Higgs boson. There is no reason to assume that the model realised in nature is as such. The natural extension to the SM Higgs scalar sector is adding a second Higgs doublet field, which results in a spectrum of new particles and interactions. Models with a second Higgs doublet are suitably named two-Higgs-doublet models (2HDMs).

The following two chapters are intended to be a review of the 2HDMs key features. We approach this with the angle of building valid 2HDMs and observing how this would alter the SM. We intend to provide a self-contained toolbox for performing 2HDM global fits here. Running the risk of 'disrupting the flow', the explanations and proofs in this chapter use a variety of methods. Rest assured, that where the most straightforward method is not presented, we have good reason in hopes of getting across essential insights into the 2HDM.

We begin this chapter by looking at the most general form of the 2HDM potential and exploring the different notations in which it is presented throughout the literature.

The 2HDM provides a rich structure of phenomena relating to CP-symmetries. We explore the possibility of CP-violation in the potential and find it may occur explicitly like in the SM, as well as spontaneously in the vacuum. Additionally, we find that CP may be softly broken in the 2HDM potential, which is not possible in the SM.

While investigating CP related phenomena, we simultaneously construct the most general vacuum of an N-Higgs Doublet. This allows us to explain the different forms of VEVs that the 2HDM may attain. We perform EWSB with each different set of VEVs to present a general method in which we may extract the physical spectrum of the theory.

Further, we provide a more in-depth analysis of the 2HDM vacuum to prove a set of useful claims. Such claims allow us to make predictions about the model and place constraints on the global parameter space by ensuring the stability of our potential and our vacuum.

3.1 Defining The Scalar Potential

The scalar potential gives the spectrum of scalar particles as well as interactions. We define the most general scalar potential for the 2HDM and explore the different notations which have become useful in investigating the theory and phenomenology of the 2HDM.

The field doublets in the 2HDM are Φ_1 and Φ_2.

Scalar Doublets in the 2HDM

$$\Phi_1 = \begin{pmatrix} \phi_1 + i\phi_2 \\ \phi_5 + i\phi_7 \end{pmatrix}, \quad \Phi_2 = \begin{pmatrix} \phi_3 + i\phi_4 \\ \phi_6 + i\phi_8 \end{pmatrix}. \tag{3.1}$$

The extra doublet Φ_2 shares all the same quantum numbers with Φ_1.

We would like to construct a Higgs potential that is both renormalisable and gauge invariant. [20]

20: As an introduction for the reader and for convenient reference we state the most commonly studied phenomenological forms of the 2HDM potential here. Section 3.2.4 explains the symmetry classes that are applied to the potentials to get them to their different forms.

General Potential The most general $SU(2) \times U(1)$ potential we can construct is given below.

General Scalar Potential of 2HDM

$$\begin{aligned} V =& m_{11}^2 \Phi_1^\dagger \Phi_1 + m_{22}^2 \Phi_2^\dagger \Phi_2 - (m_{12}^2 \Phi_1^\dagger \Phi_2 + [\text{H.c.}]) \\ &+ \frac{1}{2}\lambda_1 (\Phi_1^\dagger \Phi_1)^2 + \frac{1}{2}\lambda_2 (\Phi_2^\dagger \Phi_2)^2 \\ &+ \lambda_3 (\Phi_1^\dagger \Phi_1)(\Phi_2^\dagger \Phi_2) + \lambda_4 (\Phi_1^\dagger \Phi_2)(\Phi_2^\dagger \Phi_1) \\ &+ \left[\frac{1}{2}\lambda_5 (\Phi_1^\dagger \Phi_2)^2 + \lambda_6 (\Phi_1^\dagger \Phi_1)(\Phi_1^\dagger \Phi_2) + \lambda_7 (\Phi_2^\dagger \Phi_2)(\Phi_1^\dagger \Phi_2) + \text{H.c} \right]. \end{aligned} \tag{3.2}$$

This potential has a total of 14 free parameters classified in Table 3.1. As the potential contains complex couplings this potential breaks CP and is known as the general CP-violating potential.

Real	Complex
m_{11}	m_{12}
m_{22}	λ_5
λ_1	λ_6
λ_2	λ_7
λ_3	
λ_4	

Table 3.1: Classification of the general CP-violating 2HDM potential parameters.

General CP-conserving Potential To preserve CP, we impose certain symmetries onto the potential to remove the complex terms. CP-violation of this kind is known as explicit. It can be shown that if all terms in the Higgs potential are real, then the potential conserves CP explicitly. The general CP-conserving potential is, hence, the same as Eq. (3.2) but with all couplings real. This form of the potential has ten

free parameters. *We will use a CP-conserving potential for our results in chapters 6 and 7.*

Z_2-symmetric Potential Commonly a Z_2 ($\Phi_1 \to \Phi_1$ and $\Phi_2 \to -\Phi_2$) symmetry is imposed upon our potential. The result is a simpler form of our potential, with $\lambda_6 = \lambda_7 = 0$ and all remaining couplings real. We keep $m_{12}^2 \neq 0$ as a soft Z_2-symmetry breaking term. This form of the potential has 8 free parameters. A Z_2-conserving potential is also automatically CP-conserving. *We will use a Z_2-conserving potential for our results in chapter 6.*

CP-violation may also occur in the vacuum itself. When the potential has been evaluated at this VEV, the resultant vacuum may be CP-violating. We refer to this as spontaneous CP breaking.

In section 3.2.3, we construct the most general potential that explicitly respects CP-symmetry. In section 3.3, we start with this explicit CP-conserving potential and derive the simplest form of the vacuum that spontaneously conserves CP.

In our numerical analyses, we will not consider CP-violation in the potential - all parameters in the potential are taken real. Making this selection is equivalent to imposing a CP1 symmetry (of the GCP-symmetry class), more information is forthcoming in section 3.2.4. We will nevertheless continue to discuss the possibility of CP-violation in the potential as well as CP-violation in the vacuum solution as both have interesting phenomenological effects within the 2HDM.

In addition, there are three useful alternative notations in which we may represent the potential. Each notation simplifies different types of calculations as well as shedding a different light on relationships between parameters in the potential.

Alternative Form I: Symmetries and Basis Transformations This notation is useful for the investigation of symmetries as well as basis transformations of the potential. We can express the potential via a summation, making clever use of indices.

General Scalar Potential of 2HDM: Symmetries and Basis Transforms

$$V = \sum_{a,b=1}^{2} Y_{ab}\Phi_a^\dagger\Phi_b + \frac{1}{2}\sum_{a,b,c,d=1}^{2} Z_{ab,cd}(\Phi_a^\dagger\Phi_b)(\Phi_c^\dagger\Phi_d), \qquad (3.3)$$

In the above[21]

$$Z_{ab,cd} = Z_{cd,ab}. \tag{3.6}$$

Alternative Form II: Vacuum and Spectrum Generation Using this notation, it is easiest to examine the vacuum of the theory as well as to construct mass matrices in the particle spectrum generation. Let us introduce a basis of Hermitian operators,

$$\begin{aligned} x_1 &\equiv \Phi_1^\dagger \Phi_1, \\ x_2 &\equiv \Phi_2^\dagger \Phi_2, \\ x_3 &\equiv \frac{1}{2}(\Phi_1^\dagger \Phi_2 + \Phi_2^\dagger \Phi_1) = \mathrm{Re}(\Phi_1^\dagger \Phi_2), \\ x_4 &\equiv -\frac{i}{2}(\Phi_1^\dagger \Phi_2 - \Phi_2^\dagger \Phi_1) = \mathrm{Im}(\Phi_1^\dagger \Phi_2). \end{aligned} \tag{3.7}$$

Notice

$$x_3 + x_4 = (\Phi_1^\dagger \Phi_2), \tag{3.8}$$

with x_4 imaginary

$$(x_3 + x_4)^\dagger = (x_3 - x_4). \tag{3.9}$$

The most general potential then has the form

$$\begin{aligned} V = {} & a_1 x_1 + a_2 x_2 + \left[\frac{1}{2} a_3 (x_3 + x_4) + [\mathrm{H.c.}]\right] + b_{11} x_1^2 + b_{22} x_2^2 \\ & + b_{12} x_1 x_2 + \frac{1}{2}(b_{33} - b_{44})(x_3^2 - x_4^2) \\ & + \left[\frac{1}{4}(b_{33} + b_{44})(x_3 + x_4)^2 + \frac{1}{2} b_{13} x_1 (x_3 + x_4) + \frac{1}{2} b_{23} x_2 (x_3 + x_4) + [\mathrm{H.c.}]\right]. \end{aligned} \tag{3.10}$$

Here $a_3, (b_{33} + b_{44}), b_{13}$ and b_{23} are complex. We have used the Hermicity of the operators interchangeably to simplify the appearance. Introducing

$$X = \begin{pmatrix} x_1 \\ x_2 \\ x_3 \\ x_4 \end{pmatrix} = \begin{pmatrix} \phi_1^2 + \phi_2^2 + \phi_5^2 + \phi_7^2 \\ \phi_3^2 + \phi_4^2 + \phi_6^2 + \phi_8^2 \\ \phi_1\phi_3 + \phi_2\phi_4 + \phi_5\phi_6 + \phi_7\phi_8 \\ \phi_1\phi_4 - \phi_2\phi_3 + \phi_5\phi_8 - \phi_6\phi_7 \end{pmatrix}, \quad A = \begin{pmatrix} a_1 \\ a_2 \\ Re(a_3) \\ Im(a_3) \end{pmatrix},$$

$$B = \begin{pmatrix} 2b_{11} & b_{12} & Re(b_{13}) & Im(b_{13}) \\ b_{12} & 2b_{22} & Re(b_{23}) & Im(b_{23}) \\ Re(b_{13}) & Re(b_{23}) & 2b_{33} & Im(b_{33} + b_{44}) \\ Im(b_{13}) & Im(b_{23}) & Im(b_{33} + b_{44}) & 2b_{44} \end{pmatrix}. \tag{3.11}$$

We may rewrite the potential as

$$V = A^T X + \frac{1}{2} X^T B X. \tag{3.12}$$

21: By hermicity of the potential ($V^\dagger = V$),

$$Y_{ab} = Y_{ba}^*, \tag{3.4}$$

$$Z_{ab,cd} = Z_{ba,dc}^*. \tag{3.5}$$

More simply, the general potential with real couplings can be expressed as[22]

General Scalar Potential of 2HDM: Vacuum and Spectrum Generation

$$V = a_1x_1 + a_2x_2 + a_3x_3 + b_{11}x_1^2 + b_{22}x_2^2 + b_{33}x_3^2 + b_{44}x_4^2 + b_{12}x_1x_2 + b_{13}x_1x_3 + b_{23}x_2x_3. \tag{3.14}$$

In this case

$$A = \begin{pmatrix} a_1 \\ a_2 \\ a_3 \\ 0 \end{pmatrix}, \quad B = \begin{pmatrix} 2b_{11} & b_{12} & b_{13} & 0 \\ b_{12} & 2b_{22} & b_{23} & 0 \\ b_{13} & b_{23} & 2b_{33} & 0 \\ 0 & 0 & 0 & 2b_{44} \end{pmatrix}. \tag{3.15}$$

Setting $b_{13} = b_{23} = 0$ recovers a completely CP-conserving form for the potential.

Alternative Form III: Vacuum Structure There exists an alternative method to investigate the vacuum phenomenology. This method introduces a basis of gauge-invariant bi-linear field operators

$$\begin{aligned} r_0 &\equiv \Phi_1^\dagger\Phi_1 + \Phi_2^\dagger\Phi_2, \\ r_1 &\equiv -(\Phi_1^\dagger\Phi_2 + \Phi_2^\dagger\Phi_1) = -2\mathrm{Re}(\Phi_1^\dagger\Phi_2), \\ r_2 &\equiv i(\Phi_1^\dagger\Phi_2 - \Phi_2^\dagger\Phi_1) = -2\mathrm{Im}(\Phi_1^\dagger\Phi_2), \\ r_3 &\equiv -(\Phi_1^\dagger\Phi_1 - \Phi_2^\dagger\Phi_2), \end{aligned} \tag{3.16}$$

which together create the covariant four-vector $r_\mu = (r_0, -r_i)$ which lives in Minkowski space. Such a comparison may seem unusual at first but in fact the 2HDM potential exhibits a Minkowski structure.

General Scalar Potential of 2HDM: Vacuum Structure

$$V = -M_\mu r^\mu + \frac{1}{2}\Lambda_{\mu\nu}r^\mu r^\nu. \tag{3.17}$$

For the most general 2HDM potential we may identify the $M_{\mu\nu}$ vector

$$M_\mu = (M_0, M_i) = \left(-\frac{1}{2}(m_{11}^2 + m_{22}^2),\ \mathrm{Re}(m_{12}^2),\ \mathrm{Im}(m_{12}^2),\ \frac{1}{2}(m_{22}^2 - m_{11}^2)\right). \tag{3.18}$$

22: Relations to the potential notation of 3.2

$$\begin{aligned} &a_1 = m_{11}^2, a_2 = m_{22}^2, a_3 = -2m_{12}^2, \\ &b_{11} = \frac{1}{2}\lambda_1,\ b_{22} = \frac{1}{2}\lambda_2,\ b_{12} = \lambda_3, \\ &b_{33} = \lambda_5 + \lambda_4,\ b_{44} = \lambda_5 - \lambda_4 \\ &b_{13} = 2\lambda_6,\ b_{23} = 2\lambda_7. \end{aligned} \tag{3.13}$$

We use the Minkowski metric in this parameterisation

$$M^\mu = (M_0, -M_i). \tag{3.19}$$

The tensor is

$$\Lambda_{\mu\nu} = \frac{1}{2}\begin{pmatrix} \frac{\lambda_1+\lambda_2}{2}+\lambda_3 & \mathrm{Re}(\lambda_6+\lambda_7) & -\mathrm{Im}(\lambda_6+\lambda_7) & \frac{\lambda_1-\lambda_2}{2} \\ \mathrm{Re}(\lambda_6+\lambda_7) & \lambda_4+\mathrm{Re}(\lambda_5) & -\mathrm{Im}(\lambda_5) & \mathrm{Re}(\lambda_6-\lambda_7) \\ -\mathrm{Im}(\lambda_6+\lambda_7) & -\mathrm{Im}(\lambda_5) & \lambda_4-\mathrm{Re}(\lambda_5) & -\mathrm{Im}(\lambda_6-\lambda_7) \\ \frac{\lambda_1-\lambda_2}{2} & \mathrm{Re}(\lambda_6-\lambda_7) & -\mathrm{Im}(\lambda_6-\lambda_7) & \frac{\lambda_1+\lambda_2}{2}-\lambda_3 \end{pmatrix}. \tag{3.20}$$

Upon inspection of the bi-linears defined in Eq. (3.16) we must have

$$\begin{aligned} r_0 &\geq 0, \\ r^\mu r_\mu &\geq 0. \end{aligned} \tag{3.21}$$

The second of these conditions is a result of the Cauchy-Schwartz inequality. As such, all four-vectors r_μ must lie either within or on the forward light-cone LC^+. In fact, the apex of the cone when $\Phi_1 = \Phi_2 = 0$ corresponds to a symmetric EWSB solution. The four vectors r_μ that make up the rest of the surface correspond to neutral vacuum solutions, and those inside the forward light-cone correspond to charge-breaking (and CP-breaking) vacuum solutions.

3.1.1 Running of the 2HDM potential couplings

Our couplings of the 2HDM potential run with energy according to the renormalisation Group Equations

$$\frac{d\lambda}{d\ln\mu^2} = \sum_l h^l \beta^l_\lambda, \tag{3.22}$$

where l is the number of corrections we want to work with, for example, if we work to NLO at which $l = 2$. The beta functions for the running for both the generic couplings and the Minkowski metric form may be found in Ref. [24].

3.2 Basis, Higgs Family and GCP-transformations

The physics of a theory remains the same as long as the symmetries of the theory are preserved. By the physics of a theory, we mean quantities such as observable masses, physical interaction strengths and more. We can always perform a global basis transformation on the two-Higgs field doublets, which will preserve all symmetries and

thus will not alter the physics. The global basis transformation U is applied to both Higgs doublets as

$$\Phi'_a = \sum_{b=1}^{2} U_{ab}\Phi_b, \tag{3.23}$$

where U is a unitary matrix.

3.2.1 Higgs Family Transformations

A nice group of the unitary basis transformation is known as Higgs Family (HF) symmetries [25]. It is defined by

$$\Phi_a \xrightarrow{HF} \sum_{b=1}^{2} S_{ab}\Phi_b, \tag{3.24}$$

with S a unitary matrix. HF symmetries leave the form of the potential given in Eq. (3.3) unchanged, that is they leave the values of Y_{ab} and $Z_{ab,cd}$ unchanged. This is not the case with other basis transformations. Under any basis change U the HF-transformation may be related through

$$S' = USU^{\dagger}. \tag{3.25}$$

We find that most of the desirable symmetries to apply, for example Z_2 symmetry, belong to the HF category.

3.2.2 General CP-transformation

In a single scalar field theory with the field defined by Φ, the CP-transformation is

$$\Phi \xrightarrow{CP} \Phi^*. \tag{3.26}$$

The above is just the form of a charge conjugation transformation as parity is always conserved in a scalar theory. Hence, a charge-transformation is equivalent to a CP-transformation in this case. The natural extension of the single CP-transformation to a case where there are two fields would be

$$\begin{aligned} \Phi_1 &\xrightarrow{CP} \Phi_1^*, \\ \Phi_2 &\xrightarrow{CP} \Phi_2^*. \end{aligned} \tag{3.27}$$

If another basis transformation U introduces complex terms, we will find that the CP-transformation is not closed in the transformed basis. To preserve the CP-transformation under any global basis transformations, we also need to transform the CP-transformation itself. We introduce a general CP-transformation, or a GCP-transformation, with

the definition

$$\Phi_a \xrightarrow{GCP} \sum_{b=1}^{2} X_{ab}\Phi_b^*. \tag{3.28}$$

X is an arbitrary unitary matrix which is defined such that it allows us to preserve the nature of the CP-transformation. Every time we change the basis, we need to redefine X. In a basis transformed by U, X becomes X'[23] via

$$X' = UXU^T. \tag{3.30}$$

23: It can be proved that X' can always be written in the form

$$X' = \begin{pmatrix} c_\theta & s_\theta \\ -s_\theta & c_\theta \end{pmatrix}. \tag{3.29}$$

3.2.3 Explicit CP Invariance of the Potential

As we have previously stated, we want our potential to conserve CP explicitly. We need to ensure that our potential is invariant under a GCP-transformation. Let us select the hypercharge transformation

$$\Phi_i \xrightarrow{GCP} e^{iY_i\alpha_i}\Phi_i^*. \tag{3.31}$$

To simplify the analysis consider how each of the basis operators of the potential x_i defined in Eq. (3.7) transform individually

$$\begin{aligned} x_1 = \Phi_1^\dagger\Phi_1 &\xrightarrow{GCP} (e^{-i\alpha_1})(e^{i\alpha_1})(\Phi_1^\dagger\Phi_1)^\dagger, \\ &= \Phi_1^\dagger\Phi_1 = x_1. \end{aligned} \tag{3.32}$$

Similarly, x_2 is invariant under a GCP interaction. The operators x_3 and x_4 contain mixed Φ_1 and Φ_2 terms and as a result, the exponential functions that appear after the GCP-transformation will contain both α_1 and α_2. Now, α_i is an arbitrary parameter so we are free to choose $\alpha_1 = \alpha_2$ such that the combination $e^{i(\alpha_1-\alpha_2)} = 1$. Then

$$\begin{aligned} x_3 &= \frac{1}{2}(\Phi_1^\dagger\Phi_2 + \Phi_2^\dagger\Phi_1) \\ &\xrightarrow{GCP} \frac{1}{2}[(e^{-i\alpha_1})(e^{i\alpha_2})(\Phi_1^\dagger\Phi_2)^\dagger + (e^{i\alpha_1})(e^{-i\alpha_2})(\Phi_2^\dagger\Phi_1)^\dagger], \\ &= \frac{1}{2}[\Phi_2^\dagger\Phi_1 + \Phi_1^\dagger\Phi_2] = x_3. \end{aligned} \tag{3.33}$$

Finally, x_4 transforms as

$$\begin{aligned} x_4 &= -\frac{i}{2}(\Phi_1^\dagger\Phi_2 - \Phi_2^\dagger\Phi_1) \\ &\xrightarrow{GCP} -\frac{i}{2}[(e^{-i\alpha_1})(e^{i\alpha_2})(\Phi_1^\dagger\Phi_2)^\dagger - (e^{i\alpha_1})(e^{-i\alpha_2})(\Phi_2^\dagger\Phi_1)^\dagger], \\ &= -\frac{i}{2}[\Phi_2^\dagger\Phi_1 - \Phi_1^\dagger\Phi_2] = -x_4 \end{aligned} \tag{3.34}$$

As x_4 changes sign under a GCP-transformation it is not invariant, but

$$\begin{aligned} x_4x_4 &\xrightarrow{GCP} (-x_4)(-x_4) \\ &= x_4x_4. \end{aligned} \tag{3.35}$$

Terms linear in x_4 will need to vanish if we choose the potential to obey GCP invariance. The general potential of Eq. (3.10) then reduces to

$$\begin{aligned} V = {} & a_1 x_1 + a_2 x_2 + a_3 x_3 + b_{11} x_1^2 + b_{22} x_2^2 \\ & + b_{12} x_1 x_2 + b_{33} x_3^2 + b_{44} x_4^2 + b_{13} x_1 x_3 + b_{23} x_2 x_3 . \end{aligned} \tag{3.36}$$

which is exactly the form we anticipated in Eq. (3.14) when taking all couplings of the potential real.

In this case, x_4 is a soft symmetry breaking term and is often included. Soft symmetry breaking terms are easy to find in the 2HDM, unlike the SM where they do not appear.[24]

24: There are two types of symmetry breaking that may occur. Hard symmetry breaking occurs when the term of dimension four does not respect the considered symmetry. Hard symmetry breaking causes some difficulties when it comes to the renormalisation of the theory. Soft symmetry, on the other hand, occurs when the term of dimension two do not respect the symmetry. Soft symmetry breaking does not affect the renormalisation of the theory.

3.2.4 Classes of Symmetry

So far, we have studied two types of transformations; basis transformations (of which the HF transformations are a particularly useful subgroup) and GCP-transformations. Both transformation types leave the kinetic terms of the potential unchanged. It has been shown in [26] that any combination of HF and GCP-symmetries imposed on the potential belongs to one of six distinct classes. Potentials within the same class will yield the same physical observables. Basis transformations can never cross from one class to another. In other words, basis transformations leave the physical observables of the theory invariant. Here we list each of the symmetry classes by stating their field transformation matrix.

Table 3.2: The restrictions each symmetry class places onto the parameters of the potential. This Table is adopted from [27]. Fields with no entries are unconstrained.

Symmetry Class	m_{11}^2	m_{22}^2	m_{12}^2	λ_1	λ_2	λ_3	λ_4	λ_5	λ_6	λ_7
Z_2			0						0	0
$U(1)$			0					0	0	0
$SU(2)$		m_{11}^2	0		λ_1		$\lambda_1 - \lambda_3$	0	0	0
CP1			real					real	real	real
CP2		m_{11}^2	0		λ_1					$-\lambda_6$
CP3		m_{11}^2	0		λ_1			$\lambda_1 - \lambda_3 - \lambda_4$ (real)	0	0

Symmetry Class Transformations

1. Class I: Z_2

$$S = \begin{pmatrix} 1 & 0 \\ 0 & -1 \end{pmatrix}. \tag{3.37}$$

2. Class II: $U(1)$

$$S = \begin{pmatrix} e^{-i\xi} & 0 \\ 0 & e^{i\xi} \end{pmatrix}. \tag{3.38}$$

3. Class III: $SU(2)$

$$S = \begin{pmatrix} e^{-i\xi} c_\theta & e^{-i\psi} s_\theta \\ -e^{i\psi} s_\theta & e^{i\xi} c_\theta \end{pmatrix}. \tag{3.39}$$

4. Class IV: CP1

$$X = \begin{pmatrix} 1 & 0 \\ 0 & 1 \end{pmatrix}. \tag{3.40}$$

5. Class V: CP2

$$X = \begin{pmatrix} 0 & 1 \\ -1 & 0 \end{pmatrix}. \tag{3.41}$$

6. Class VI: CP3

$$X = \begin{pmatrix} c_\theta & s_\theta \\ -s_\theta & c_\theta \end{pmatrix}. \tag{3.42}$$

The restrictions each of these classes have on the parameters of the potential is shown in the Table 3.2. We derive these restrictions for the $U(1)$ HF-symmetry and a GCP-transformation in Appendix C.

As touched on previously $SU(2)$ provides the greatest restriction, reducing the number of free parameters in the potential to three. In our numerical analysis, we always apply at least the $CP1$ symmetry class, in which all terms are real.

The most commonly imposed symmetry is Z_2, which removes the CP-violating potential terms entirely. The soft breaking term m_{12}^2 is often kept but assumed real.

Z_2 serves another purpose, and that is providing restrictions on the Yukawa sector of the 2HDM. The 2HDM allows for flavour-changing (FC) interactions. Leptons (e_L) and quarks (u_L, d_L) can change to another particle in their family (or between families in the case of the latter) upon interaction with a scalar. FC occurs as both of the scalar doublets couples to each particle field. A discussion of FC in the 2HDM follows in section 4.4.

We often want to avoid any FC at tree-level, to coincide with the lack of observation of such processes. A way to achieve this is through imposing a Z_2-symmetry on each family of the Yukawa sector. Imposing this leads to the four common types of 2HDMs which are discussed further in section 4.2.

3.3 The Vacuum Structure

There still exists the possibility of CP-violation in the vacuum itself. Before we embark on finding the form of such a vacuum let us sidestep and explore the general forms that the vacuum may attain in a 2HDM. In the SM the vacuum is described by a single doublet. The VEV for the SM Higgs field is given by;

$$\langle \Phi \rangle = \begin{pmatrix} v_1 + iv_2 \\ v_3 + iv_4 \end{pmatrix}, \tag{3.43}$$

where $v_1, ..., v_4$ are real numbers. We may always perform $SU(2)$ and $U(1)$ gauge transformations on our Φ field as our SM Lagrangian is $SU(2) \times U(1)$ invariant. Introduce a $SU(2) \times U(1)$ transformation M such that after spontaneous symmetry breaking

$$\langle M\Phi \rangle = \begin{pmatrix} 0 \\ v \end{pmatrix}, \tag{3.44}$$

where v is real. [25] The basis defined by the transformation M is known as the unitary basis.

25: The form of Eq. (3.44) preserves $U(1)$ charge symmetry as well as CP-symmetry.

3.3.1 The Vacuum of The 2HDM

Let us extend this to the case where we have two Higgs doublet fields. The result is as anticipated two VEVs, each corresponding to a scalar field doublet. Each Higgs field simultaneously acquires a VEV.

Analogous to the SM, we strive to perform basis transformations on our fields Φ_1 and Φ_2 to simplify the form of the VEVs after SSB. For two doublets, basis transformations alone do not ensure that the VEVs respect $U(1)$ charge symmetry or CP-symmetry. Hence, we have the

possibility of VEVs that produce $U(1)$ charge breaking or CP breaking vacua. [26]

26: Normal minima are defined as those that preserve $U(1)$ charge as well as CP - an example is the SM VEV of Eq. (3.44).

Applying the $U(1)$ charge operator $(Q)^*$ to the VEV doublets (i=1,2)

$$Q\langle\Phi_i\rangle = \begin{pmatrix} v_i^u \\ 0 \end{pmatrix} \tag{3.48}$$

tells us that for a non-zero upper component of the VEV, the $U(1)$ charge operator is broken by the VEV.

The work of Ref. [28] investigates different combinations of minima in a N-Higgs doublet models to find the simplest form of the VEVs that are attainable.

From this work we give below the most general form our set of VEVs can attain in the 2HDM.

General minimum

$$\langle\Phi_1\rangle = \frac{1}{\sqrt{2}}\begin{pmatrix} \alpha \\ v_1 \end{pmatrix}, \quad \langle\Phi_2\rangle = \frac{1}{\sqrt{2}}\begin{pmatrix} 0 \\ v_2 e^{i\theta} \end{pmatrix}. \tag{3.49}$$

It is possible that the potential may attain more than one minimum in the 2HDM, and as such we may simultaneously have more than one set of VEVs satisfying the potential. As discussed in Ref. [28], there exist different types of minima. The 2HDM potential may attain three possible distinct minima.

The $U(1)$ charge breaking (CB) minimum

$$\langle\Phi_1\rangle = \frac{1}{\sqrt{2}}\begin{pmatrix} \alpha \\ v_1 \end{pmatrix}, \quad \langle\Phi_2\rangle = \frac{1}{\sqrt{2}}\begin{pmatrix} 0 \\ v_2 \end{pmatrix}, \tag{3.50}$$

where v_1, v_2 and α are real parameters.

* The $U(1)$ charge operator Q is defined by the Gell-Mann-Nishijima formula

$$Q = I_3 + \frac{1}{2}Y, \tag{3.45}$$

where I_3 is the third component of isospin given by $\frac{1}{2}\tau_3$ and Y is hypercharge. From this

$$Q = \frac{1}{2}\begin{pmatrix} Y+1 & 0 \\ 0 & Y-1 \end{pmatrix}. \tag{3.46}$$

By convention we set $Y = 1$ for each Higgs-doublet

$$Q = \begin{pmatrix} 1 & 0 \\ 0 & 0 \end{pmatrix}. \tag{3.47}$$

The CP-violating (CPV) minimum

$$\langle \Phi_1 \rangle = \frac{1}{\sqrt{2}} \begin{pmatrix} 0 \\ v_1 \end{pmatrix}, \quad \langle \Phi_2 \rangle = \frac{1}{\sqrt{2}} \begin{pmatrix} 0 \\ v_2 e^{i\theta} \end{pmatrix}, \tag{3.51}$$

where θ is real.

The normal minimum

$$\langle \Phi_1 \rangle = \frac{1}{\sqrt{2}} \begin{pmatrix} 0 \\ v_1 \end{pmatrix}, \quad \langle \Phi_2 \rangle = \frac{1}{\sqrt{2}} \begin{pmatrix} 0 \\ v_2 \end{pmatrix}. \tag{3.52}$$

Notice that we do not have a minimum that is simultaneously $U(1)$ charge-breaking and CP-breaking, like in the most general form Eq. (3.49). We will prove in the next section that this kind of minimum cannot exist in the 2HDM.

The mixing of v_1 and v_2 with respect to the electroweak VEV solution v is given by the angle β, such that

$$v_1 = v c_\beta, \quad v_2 = v s_\beta. \tag{3.53}$$

This mixing may then be given as a ratio and results in the 2HDM parameter t_β.

Mixing of v_1 and v_2

$$t_\beta = \frac{v_2}{v_1}. \tag{3.54}$$

The stationary points of a Higgs potential are found by differentiating the potential with respect to each field, then evaluating at the respective VEVs

$$\left. \frac{\partial V}{\partial \phi_i} \right|_{\Phi_a = \langle \Phi_a \rangle} = 0, \tag{3.55}$$

for $i = 1, .., 8$ and $a = 1, 2$. In the 2HDM this produces eight equations with eight unknowns. There are two unknowns for a normal minimum, three unknowns for a charge- and CP-breaking minima.

We see that there is the possibility of CP-violation occurring in the vacuum itself. We call this spontaneous CP-violation. There are two ways in which we may avoid spontaneous CP-violation.

1. Impose invariance under Z_2-symmetry, with $\Phi_2 \to -\Phi_2$. Under a Z_2-symmetry, $\langle \Phi_2 \rangle \to -\langle \Phi_2 \rangle$ which eliminates any terms linear in Φ_2 which may otherwise violate CP-symmetry spontaneously.

2. Impose invariance under a global symmetry, with $\Phi_2 \to e^{i\eta}\Phi_2$. The addition of a global symmetry results in the lower component transforming as $v_2 e^{\theta} \to v_2 e^{i(\theta+\eta)}$, we may then rotate away the CP-breaking term by setting $\theta = -\eta$.

In both these cases, Φ_1 remains unchanged.

Let us impose each of these symmetries onto the potential with explicit CP-invariance Eq. (3.14). Under Z_2-symmetry Eq. (3.14) becomes

$$\begin{aligned} V = {} & a_1 x_1 + a_2 x_2 + b_{11} x_1^2 + b_{22} x_2^2 + b_{33} x_3^2 + b_{44} x_4^2 \\ & + b_{12} x_1 x_2. \end{aligned} \tag{3.56}$$

In the case where we demand a global symmetry ($\Phi_2 \to e^{i\eta}\Phi_2$) it is clear that x_1 and x_2 are invariant under the global symmetry, x_3 and x_4 are transformed as

$$\begin{aligned} x_3 = \frac{1}{2}(\Phi_1^\dagger \Phi_2 + \Phi_2^\dagger \Phi_1) \to \frac{1}{2}[(e^{i\eta})\Phi_1^\dagger \Phi_2 + (e^{-i\eta})\Phi_2^\dagger \Phi_1], \\ \neq x_3, \end{aligned} \tag{3.57}$$

with

$$\begin{aligned} x_3 x_3 = \frac{1}{4}(\Phi_1^\dagger \Phi_2 + \Phi_2^\dagger \Phi_1)^2 \to \frac{1}{4}[(e^{i\eta})\Phi_1^\dagger \Phi_2 + (e^{-i\eta})\Phi_2^\dagger \Phi_1]^2, \\ \neq x_3 x_3. \end{aligned} \tag{3.58}$$

Similarly, x_4 and x_4^2 do not transform invariantly under this global symmetry. Consider the combination $x_3^2 + x_4^2$ obtained by setting $b_{33} = b_{44}$ in the potential

$$\begin{aligned} x_3^2 + x_4^2 \to {} & \frac{1}{2}[(e^{i\eta})(e^{-i\eta})\Phi_1^\dagger \Phi_2 \Phi_2^\dagger \Phi_1 + (e^{-i\eta})(e^{i\eta})\Phi_2^\dagger \Phi_1 \Phi_1^\dagger \Phi_2], \\ = {} & x_3^2 + x_4^2. \end{aligned} \tag{3.59}$$

The explicitly and spontaneously CP-conserving potential with a global symmetry is then

$$\begin{aligned} V = {} & a_1 x_1 + a_2 x_2 + b_{11} x_1^2 + b_{22} x_2^2 + b_{33}(x_3^2 + x_4^2) \\ & + b_{12} x_1 x_2. \end{aligned} \tag{3.60}$$

Goldstone's Theorem states that for each continuous global symmetry that does not annihilate the ground state, we have the appearance of a Goldstone boson. In other words, certain symmetries that remain invariant at the VEV will result in massless particles.

The VEV for the potential above is, of course, invariant under CP-symmetry as this was the basis in which we defined it. However, it is also invariant under our introduced symmetry $\Phi_2 \to e^{i\eta}\Phi_2$ at the ground state, as we have shown above. This $U(1)$ symmetry is both

continuous and global, which means that it will result in the appearance of an additional massless boson in our theory. An additional massless boson is not desirable, so we aim to break this symmetry and rid ourselves of this massless mode. We need to introduce a soft symmetry breaking term.

Consider the operator x_3. We know that this term breaks the $U(1)$ global symmetry that we have introduced, let us check if it preserves CP-symmetry at the vacuum state

$$\begin{aligned}\langle x_3\rangle &= \frac{1}{2}(\langle\Phi_1\rangle^\dagger\langle\Phi_2\rangle + \langle\Phi_2\rangle^\dagger\langle\Phi_1\rangle),\\ &= \frac{1}{2}[v_1^\dagger v_2 e^{i\theta} + v_2^\dagger v_1 e^{-i\theta}],\\ &\xrightarrow{CP} \frac{1}{2}[e^{i(\alpha_2-\alpha_1)}v_1 v_2^\dagger e^{-i\theta} + e^{i(\alpha_1-\alpha_2)}v_2 v_1^\dagger e^{i\theta}],\\ &= \langle x_3\rangle.\end{aligned} \tag{3.61}$$

Then to avoid the appearance of a Goldstone Boson we reintroduce the $-a_3^2x_3^2$ term. This will maintain CP-invariance but break the $\Phi_2 \to e^{i\eta}\Phi_2$ symmetry. Our final potential is

$$\begin{aligned}V = a_1x_1 + a_2x_2 - a_3x_3 + b_{11}x_1^2 + b_{22}x_2^2 + b_{33}(x_3^2 + x_4^2)\\ + b_{12}x_1x_2,\end{aligned} \tag{3.62}$$

which in our most general potential notation is

$$\begin{aligned}V =& m_{11}^2\Phi_1^\dagger\Phi_1 + m_{22}^2\Phi_2^\dagger\Phi_2 - (m_{12}^2\Phi_1^\dagger\Phi_2 + [\text{H.c.}])\\ &+\frac{1}{2}\lambda_1(\Phi_1^\dagger\Phi_1)^2 + \frac{1}{2}\lambda_2(\Phi_2^\dagger\Phi_2)^2\\ &+ \lambda_3(\Phi_1^\dagger\Phi_1)(\Phi_2^\dagger\Phi_2) + \lambda_4(\Phi_1^\dagger\Phi_2)(\Phi_2^\dagger\Phi_1) + \frac{1}{2}\lambda_5(\Phi_1^\dagger\Phi_2)^2,\end{aligned} \tag{3.63}$$

with λ_5 real. We may arrive at this same potential choice and protection from a CP-violating minimum if we apply a Z_2-symmetry and then return the soft-breaking term by hand.

3.4 The Particle Spectrum of the 2HDM Potential

3.4.1 Physical Particle Spectrum of the 2HDM Potential

We have seen that mass terms may be extracted using

$$m_\varphi^2 = \left.\frac{\partial^2 V}{(\partial\phi)^2}\right|_{\text{VEV}}, \tag{3.64}$$

where φ is the quantum fluctuation of the field ϕ which we are differentiating with respect to. In our case, we have multiple fields, so we will need to perform multiple differentiations. The masses of the scalar particles corresponding to fluctuations of each of the fields are then encoded in the matrix[27]

$$M^2 = \left.\frac{\partial^2 V}{\partial\phi_i \partial\phi_j}\right|_{\Phi_a=\langle\Phi_a\rangle}. \tag{3.65}$$

27: In the 2HDM we have eight real field operators ϕ_i. So M^2 must be an 8×8 matrix.

Notice that unless M^2 is purely diagonal, mass terms with field mixing will be present. The appearance of such mixed terms means that we cannot directly read off the physical mass terms from M^2. A basis with such mixed states is known as the interaction basis. To rotate away the mixed terms, we must diagonalise M^2 into the mass basis.

Reading off the field-doublets introduced in Eq. (3.1) along with the knowledge that the charge operator Q extracts the upper doublet components, the fields ϕ_1, ϕ_2, ϕ_3 and ϕ_4 result in charged scalars. The real lower components of the doublets ϕ_5 and ϕ_6 then give neutral CP-even scalar particles, while the imaginary lower components ϕ_7 and ϕ_8 give neutral CP-odd (pseudo-scalar) particles.

From these identifications we know how to read the masses off our 8×8 mass matrix. We should next observe that for $|i-j|>4$

$$M^2 = \left.\frac{\partial^2 V}{\partial\phi_i \partial\phi_j}\right|_{\Phi_a=\langle\Phi_a\rangle} = 0. \tag{3.66}$$

This means that our mass matrix has the block-diagonal structure

$$M^2 = \begin{bmatrix} M_\pm^2 & 0_4 \\ 0_4 & M_0^2 \end{bmatrix}, \tag{3.67}$$

where $M_\pm$ and M_0 are 4×4 matrices that encode the charged and neutral masses respectively and 0_4 is a 4×4 zero matrix.

Let us introduce a new notation for perturbations around our normal minimum solution Eq. (3.52)

$$\Phi_1 = \frac{1}{\sqrt{2}}\begin{pmatrix} \sqrt{2}\varphi_{1+} \\ v_1 + n_1 \end{pmatrix}, \qquad \Phi_2 = \frac{1}{\sqrt{2}}\begin{pmatrix} \sqrt{2}\varphi_{2+} \\ v_2 + n_2 \end{pmatrix}, \tag{3.68}$$

where

$$n_i = h_i + i z_i. \tag{3.69}$$

This parameterisation is conventional as clearly reveals our spectrum of scalar particles.[28]

We can relate our interaction basis to our mass basis via rotation matrices, parameterised by mixing angles α and β.

28: The bottom components $(h_1, h_2 = \phi_5, \phi_6)$ and $(z_1, z_2 = \phi_7, \phi_8)$. The top components are charged field operators which correspond to linear combinations of the former upper field components

$$\phi_{1+} = \frac{1}{\sqrt{2}}(\phi_1 + i\phi_2), \tag{3.70}$$

$$\phi_{2+} = \frac{1}{\sqrt{2}}(\phi_3 + i\phi_4), \tag{3.71}$$

The 4×4 matrix $M_{\pm}^2$ has degeneracy among the positively and negatively charged particles so we can describe the entire rotation into the physical basis via the below.

Charged Higgs Rotation

$$\begin{pmatrix} c_\beta & s_\beta \\ -s_\beta & c_\beta \end{pmatrix} \begin{pmatrix} \varphi_{1+} \\ \varphi_{2+} \end{pmatrix} = \begin{pmatrix} G^+ \\ H^+ \end{pmatrix}. \tag{3.72}$$

Or simply

$$R^\dagger(\beta)\varphi^+ = H^+, \tag{3.73}$$

where $R(\theta)$ is the usual rotation matrix. We may easily make all the particles negatively charged in Eq. (3.72) by taking the Hermitian conjugates.

When we have a normal minimum the neutral mass matrix M_0^2 is further block diagonal into 2×2 blocks and there is no mass-mixing between the scalar and pseudoscalar. As such we can easily progress considering only these 2×2 blocks.

Perturbations around the real CP-even fields may be rotated into their physical basis through α as below.

CP-even Higgs Rotation

$$\begin{pmatrix} c_\alpha & s_\alpha \\ -s_\alpha & c_\alpha \end{pmatrix} \begin{pmatrix} h_1 \\ h_2 \end{pmatrix} = \begin{pmatrix} H^0 \\ h^0 \end{pmatrix}. \tag{3.74}$$

Or simply

$$R^\dagger(\alpha)\varphi_R = H^0. \tag{3.75}$$

The real scalar fields (h_1, h_2) rotate into two physical scalar Higgs bosons H^0 and h^0. With this definition notice that $\alpha = \frac{\pi}{2} \pm n\pi$ for integer n identifies h_1 with h^0, while $\alpha = \pm n\pi$ identifies h_1 with H^0.

Finally, the perturbations around the imaginary fields are rotated into their physical basis by the angle β as below.

CP-odd Higgs Rotation

$$\begin{pmatrix} c_\beta & s_\beta \\ -s_\beta & c_\beta \end{pmatrix} \begin{pmatrix} \varphi_{1I} \\ \varphi_{2I} \end{pmatrix} = \begin{pmatrix} G^0 \\ A^0 \end{pmatrix}. \tag{3.76}$$

Or simply

$$R(\beta)^\dagger \varphi_I = A^0. \tag{3.77}$$

The imaginary scalar fields (z_1, z_2) rotate into a physical pseudo-scalar particle A^0 and massless pseudo-scalar Goldstone Boson G^0. We get five massive scalar particles and three massless Goldstone particles. As in the SM Higgs theory, the three massless Goldstone particles are 'swallowed' by the gauge bosons $(W^{\pm}, Z)$ to become extra polarisation states of the gauge bosons.

Label the interaction eigenstates column vector H_I and mass eigenstates column vector H_M. As we have seen the orthogonal rotation matrix R performs this rotation

$$R^{\dagger} H_I = H_M. \tag{3.78}$$

The rotation between the interaction and mass matrices is also done by the rotation matrix. Label our interaction matrix M_I, the physical mass matrix M_P, then

$$R^{\dagger} M_I R = M_P. \tag{3.79}$$

These two equations Eq. (3.78) and Eq. (3.79) may be combined to show that the two bases are equivalent

$$\begin{aligned} H_M^{\dagger} M_P H_M &= (RH_I)^{\dagger}(RM_I R^{\dagger})(RH_I), \\ &= H_I^{\dagger} M_I H_I. \end{aligned} \tag{3.80}$$

Matrices related by an invertible rotation matrix such as Eq. (3.79) are known as similar. [29] We may say more about similar matrices, following the discussion in [29] we see

$$\begin{aligned} R(M_I - \lambda I)R^{-1} &= RM_I R^{-1} - R\lambda I R^{-1}, \\ &= M_P - \lambda I. \end{aligned} \tag{3.81}$$

29: We say $M_I \sim M_P$ to denote that the interaction and physical mass matrices are similar.

We show that the characteristic equations for the interaction mass matrix and physical mass matrix are equivalent

$$\begin{aligned} \det(M_P - \lambda I) &= \det(R(M_I - \lambda I)R^{-1}), \\ &= \det(R)\det(M_I - \lambda I)\det(R^{-1}), \\ &= \det(M_I - \lambda I). \end{aligned} \tag{3.82}$$

This is satisfied for any orthogonal matrix R even if the determinant is not one. Equivalent characteristic equations yield the same eigenvalues. Hence, any two similar matrices will have identical eigenvalues. Eigenvalues of our interaction and physical mass matrices are the same. A more powerful result of this is that any basis change of the form Eq. (3.79) invoked by an invertible matrix will preserve the eigenvalues of the 'original' matrix. As such, a suitable basis change cannot change the physical (observable) masses of our system of particles.

An orthogonal rotation matrix R is constructed from the eigenvectors corresponding to the eigenvalues that we find when we solve the characteristic polynomial. [30]

30: If we define eigenvectors γ_1 and γ_2 then the corresponding rotation matrix is

$$O = \begin{pmatrix} \gamma_1^T \\ \gamma_2^T \end{pmatrix}. \tag{3.83}$$

Which we may express as the corresponding rotation matrices for $\theta = \alpha, \beta$ via

$$\gamma_1 = \begin{pmatrix} c_\theta \\ s_\theta \end{pmatrix}, \quad \gamma_2 = \begin{pmatrix} -s_\theta \\ c_\theta \end{pmatrix}. \tag{3.84}$$

3.4.2 Scalar Masses and SM-limits of the 2HDM

Taking for granted that we have a normal minimum solution the most natural way to extract scalar mass terms is to expand the potential in field-perturbations like those given in Eq. (3.52). Using the rotations of Eqs. (3.72), (3.74) and Eq. (3.76) we get the more illuminating (in a physical sense) form of the vacuum perturbations

$$\begin{aligned} \Phi_1 &= \frac{1}{\sqrt{2}} \begin{pmatrix} \sqrt{2}(G^+ c_\beta - H^+ s_\beta) \\ v_1 c_\beta + (-h^0 s_\alpha + H^0 c_\alpha) + i(G^0 c_\beta - A^0 s_\beta) \end{pmatrix}, \\ \Phi_2 &= \frac{1}{\sqrt{2}} \begin{pmatrix} \sqrt{2}(G^+ s_\beta + H^+ c_\beta) \\ v_2 s_\beta + (h^0 c_\alpha + H^0 s_\alpha) + i(G^0 s_\beta + A^0 c_\beta) \end{pmatrix}. \end{aligned} \tag{3.85}$$

Upon substitution of these fields into the scalar potential we may extract the bi-linear mass terms. Starting with the pseudo-scalar mass

$$m_A^2 = \frac{m_{12}^2}{s_\beta c_\beta} - \frac{v^2}{2}(2\lambda_5 + \lambda_6 \cot\beta + \lambda_7 t_\beta). \tag{3.86}$$

Rather conveniently, we may write all remaining scalar masses in terms of m_A^2. The charged scalar particle mass is given by

$$m_{H^\pm}^2 = \frac{m_{12}^2}{s_\beta c_\beta} - \frac{v^2}{2}(\lambda_4 + \lambda_5) = m_A^2 + \frac{v^2}{2}(\lambda_5 - \lambda_4). \tag{3.87}$$

Finally, the CP-even scalar particle mass matrix is easier left in its interaction state with components

$$\begin{aligned} \mathcal{M}_{11}^2 &= m_A^2 s_\beta^2 + v^2(\lambda_1 c_\beta^2 + 2\lambda_6 s_\beta c_\beta + \lambda_5 s_\beta^2), \\ \mathcal{M}_{22}^2 &= m_A^2 c_\beta^2 + v^2(\lambda_2 s_\beta^2 + 2\lambda_7 s_\beta c_\beta + \lambda_5 c_\beta^2), \\ \mathcal{M}_{12}^2 &= \mathcal{M}_{21}^2 = -m_A^2 s_\beta c_\beta + v^2((\lambda_3 + \lambda_4) s_\beta c_\beta + \lambda_6 c_\beta^2 + \lambda_7 s_\beta^2). \end{aligned} \tag{3.88}$$

Using the standard eigenvalue prescription to rotate this into the physical state

$$m_{h^0,H^0}^2 = \frac{1}{2}\left(\mathcal{M}_{11}^2 + \mathcal{M}_{22}^2 \pm \sqrt{(\mathcal{M}_{11}^2 - \mathcal{M}_{22}^2)^2 + 4(\mathcal{M}_{12}^2)^2}\right). \tag{3.89}$$

The mixing angle α satisfies

$$\begin{aligned} s_{2\alpha} &= \frac{2\mathcal{M}_{12}^2}{\sqrt{(\mathcal{M}_{11}^2 - \mathcal{M}_{22}^2)^2 + 4(\mathcal{M}_{12}^2)^2}}, \\ c_{2\alpha} &= \frac{\mathcal{M}_{11}^2 - \mathcal{M}_{22}^2}{\sqrt{(\mathcal{M}_{11}^2 - \mathcal{M}_{22}^2)^2 + 4(\mathcal{M}_{12}^2)^2}}. \end{aligned} \tag{3.90}$$

Consider imposing a Z_2-symmetry and setting $\lambda_3 = \lambda_4 = \lambda_5 = 0$ (restricting mixing in $\mathcal{M}_{12}$). In this limit, the scalar masses are reduced to the forms

$$m_A^2 = m_{H^\pm}^2 = \frac{m_{12}^2}{s_\beta c_\beta}, \tag{3.91}$$

and CP-even

$$\begin{aligned} m_h^2 &= \frac{m_{12}^2}{t_\beta} + v^2 s_\beta^2 \lambda_2, \\ m_H^2 &= m_{12}^2 t_\beta + v^2 c_\beta^2 \lambda_1. \end{aligned} \tag{3.92}$$

This limit is useful for intuitively studying the forms of m_h and m_H as we shall see later. Further, completely removing any mixing between h_1 and h_2 physical states, we impose $m_{12}^2 = 0$ and scalar masses become $m_h^2 = v^2 s_\beta^2 \lambda_2$, $m_H^2 = v^2 c_\beta^2 \lambda_1$ and $m_{H^\pm}^2 = m_A = 0$. We see that we recover the SM in the limit that $\beta \to \infty$, or as $v_1 \to v$ and $v_2 \to 0$. In this case the second doublet is completely decoupled from the first.

It is enough to take $v_1 = v$ and $v_2 = 0$ and $m_{12}^2 = 0$ (with a Z_2-symmetry) to get decoupling behaviour between the doublets. This kind of scenario leads to the inert model. In this scenario, one neutral scalar decouples from the gauge bosons and depending on theory, the fermions as well. Such behaviour leads to the identification of the decoupled scalar as a potential dark matter candidate. The inert model has been discussed in the literature, we will not consider it in this research.

3.5 Phenomenology and Stability of the 2HDM Vacuum

As a potential can attain multiple minima simultaneously, we are left wondering how each of these compares to one other. The idea of multiple minima leaves us with an interesting question. Say the physical Higgs field has a vacuum that corresponds to the normal vacuum $v = \sqrt{v_1^2 + v_2^2}$. Is there a deeper minimum? That is to say, is it possible for the vacuum to either drop to or quantum tunnel to lower minimum. Such tunnelling would spell disaster in the physical world. We assume that our vacuum is stable against tunnelling, that the physical minimum is indeed the deepest minima.

In the 2HDM, we make three useful claims [30].

Vacuum Lemmas

1. If the normal minimum exists in combination with a CB minimum, it is always a global minimum.
2. A $U(1)$ charge breaking minimum cannot exist simultaneously with a CP breaking minimum as a solution to the same potential.
3. Any $U(1)$ charge breaking or CP breaking stationary points that exist simultaneously with a normal minimum are necessarily saddle points.

Putting (2) and (3) together we can make the final statement:

4. Minima of different natures cannot coexist as solutions to the same potential in the 2HDM.

We prove each of the above claims in Appendix D.

3.5.1 Stability of the Vacuum

It is crucial to examine the stability of the potential. We have shown in the Appendix the remarkable result that minima of different natures may not co-exist in the 2HDM. However, we have not considered the case where there are multiple vacuum solutions of the same type. A situation like this is troubling as it means we may not be at the global minimum, causing possible tunnelling to a 'deeper' minimum solution. A realised minimum which is not global is known as meta-stable. For the case of CB and CP-breaking minimum solutions, we may only have a single solution to the minimisation conditions, so in this case, we need not worry about tunnelling. For normal vacua, however, in the 2HDM, there may be more than one solution to the minimisation conditions. We must verify that the solution we observe is indeed not a meta-stable minimum.

We begin first by ensuring our potential solution does indeed satisfy the minimum condition of being bounded from below. Calculations bounding the potential from below and checking for meta-stability are carried out at tree-level.

3.5.1.1 Bounded from Below

There are several methods in which we may find the conditions that bound our potential from below, as there exist several choices in which we may parameterise our potential. Bounded from below means that

there does not exist a direction in field-space (Φ_i) in which our potential tends to negative infinity. In other words, the existence of a 'deepest' vacuum solution is guaranteed.

We will demonstrate two methods by which we can find the necessary conditions for our potential to be bounded from below.

Method 1: Radial Potential Parameterisation An approach to check if our potential is bounded from below is to parameterise the fields using radial components and extend those radial components to the potential boundaries as discussed in Appendix A of [31]. Begin by writing the doublets using the radial parameterisation as

$$\begin{aligned} \Phi_1^\dagger \Phi_1 &= r^2 c_\gamma^2, \\ \Phi_2^\dagger \Phi_2 &= r^2 s_\gamma^2, \\ \Phi_2^\dagger \Phi_1 &= \rho e^{i\theta} r^2 c_\gamma s_\gamma, \end{aligned} \tag{3.93}$$

where $r \geq 0$, $\gamma \in [0, \pi/2]$, $\rho \in [0,1]$ and $\theta \in [0, \pi/2)$. In this parameterisation the potential may be separated into terms proportional to r^2 and r^4. If we write the potential as $V = V_2 + V_4$, where V_4 represents terms proportional to r^4, then bounded from below conditions translate to $V_4 > 0$ for all points within the bounds defined above.

Method 2: Minkowski-space-time Parameterisation Another method which gives us conditions on the couplings of our potential and is extendable to investigating the meta-stability of the potential is an investigation of the vacuum structure in the Minkowski-space formulation of the potential, see Eq. (3.17). Our potential is bounded from below if the tensor $\Lambda_{\mu\nu}$ is positive-definite on the future light-cone. A positive-definite tensor $\Lambda_{\mu\nu}$ translates to three conditions [26]

- $\Lambda_{\mu\nu}$ is diagonalisable by a Lorentz group $SO(1,3)$ transformation.[31] The diagonalised matrix has $\{\Lambda_0, \Lambda_1, \Lambda_2, \Lambda_3\}$ across its diagonal.
- $\Lambda_0 > 0$ and real.
- $\Lambda_0 > \Lambda_k$, for $i = 1, 2, 3$.

31: This is equivalent to saying that our respective eigenvectors V^i make up an $SO(1,3)$ transformation matrix. This requires the first-eigenvector to be time-like ($|V^0|^2 = 1$) and the latter three-eigenvectors to be space-like ($|V^k|^2 = -1$ for $k = 1, 2, 3$).

In the case of a CP-conserving potential, the $\Lambda_{\mu\nu}$ matrix (Eq. (3.20)) has the form

$$\Lambda_{\mu\nu} = \frac{1}{2} \begin{pmatrix} \lambda_3 + \frac{\lambda_1+\lambda_2}{2} & \lambda_6 + \lambda_7 & 0 & \frac{\lambda_1-\lambda_2}{2} \\ \lambda_6 + \lambda_7 & \lambda_4 + \lambda_5 & 0 & \lambda_6 - \lambda_7 \\ 0 & 0 & \lambda_4 - \lambda_5 & 0 \\ \frac{\lambda_1-\lambda_2}{2} & \lambda_6 - \lambda_7 & 0 & -\lambda_3 + \frac{\lambda_1+\lambda_2}{2} \end{pmatrix}. \tag{3.94}$$

This is diagonalisable if the eigenvalue equation can be solved for $\Lambda_\mu^\nu = g^{\nu\nu}\Lambda_{\mu\nu}$. This may be done numerically, however, the conditions become too complicated to express here.

For the simpler case of a Z_2-symmetry when $\lambda_6 = \lambda_7 = 0$, our matrix $\Lambda_{\mu\nu}$ after a $SO(1,3)$ rotation is reduced to

$$\Lambda_{\mu\nu} = \frac{1}{2}\begin{pmatrix} \lambda_3 + \sqrt{\lambda_1\lambda_2} & 0 & 0 & 0 \\ 0 & \lambda_4 + \lambda_5 & 0 & 0 \\ 0 & 0 & \lambda_4 - \lambda_5 & 0 \\ 0 & 0 & 0 & -\lambda_3 + \sqrt{\lambda_1\lambda_2} \end{pmatrix}. \tag{3.95}$$

The conditions for a positive-definite tensor Λ^{μ}_{ν}, hence a potential bounded from below reduce to the stability conditions given below.

Stability Conditions (Z_2-symmetric model)

$$\lambda_1 > 0, \ \lambda_2 > 0, \tag{3.96}$$

$$\lambda_3 + \sqrt{\lambda_1\lambda_2} > 0, \tag{3.97}$$

$$\lambda_3 + \lambda_4 + \lambda_5 + \sqrt{\lambda_1\lambda_2} > 0. \tag{3.98}$$

The first two conditions Eq. (3.96) arise as the $SO(1,3)$ rotation requires the equality $\lambda_1 + \lambda_2 > |\lambda_1 - \lambda_2|$. The third Eq. (3.97) comes from the eigenvalue $\Lambda_0 > 0$ and the final condition Eq. (3.98) comes from a combination of the eigenvalues Λ_k for $k = 1, 2, 3$. [32]

32: Note these eigenvalues are read off $\Lambda^{\nu}_{\mu} = g^{\nu\nu}\Lambda_{\mu\nu}$, which effects the sign of Λ_k.

In the radial parameterisation, consider the case where $\gamma = 0, \pi/2$ and $\rho = 0$, this gives us the stability conditions of Eq. (3.96) and Eq. (3.97). For $\lambda_6 = \lambda_7$ we may extract Eq. (3.98).

3.5.1.2 Meta-stability of the Vacuum Solution

Meta-stability of the potential is a continuation of the bounded from below argument using the Minkowski-space-time parameterisation of the potential, see Eq. (3.17). We follow Ref. [32].

This argument applies to both the tensor specifying the CP-conserving potential Eq. (3.94) and the tensors specifying the Z_2 potential Eq. (3.95). Indeed it can be extended to the tensor of the general potential or to those with other symmetry classes imposed.

It has been shown [26], [33] that there may exist at most two normal minima solutions in the 2HDM.

Call the matrix that diagonalises the tensor R

$$R^{-1}\Lambda R = \text{diag}(\Lambda_0, \Lambda_1, \Lambda_2, \Lambda_3), \tag{3.99}$$

where $\Lambda_{(a)}$ are the eigenvalues and $\Lambda = \Lambda^{\nu}_{\mu}$.

Introduce the notation for the VEV solutions rotated into the diagonal basis of the tensor

$$\hat{M}_\mu = R^T M_\mu \Big|_{\text{VEV}}, \quad \hat{r}_\mu = R^T r_\mu \Big|_{\text{VEV}}, \tag{3.100}$$

where $|_{\text{VEV}}$ means evaluated at the VEV. Note that for a CP-conserving potential and CP-conserving minimum solution, $\hat{M}_2 = \hat{r}_2 = 0$.

Appendix A of [32] shows that a necessary condition for two minimum solutions is $\hat{M}_0 > 0$. The case where $\hat{M}_0 < 0$ and $\hat{M}_\mu \hat{M}^\mu < 0$ implies one normal minimum solution which guarantees that we have a global minimum, and we are done. If $\hat{M}_\mu \hat{M}^\mu \geq 0$ then we have no EWSB due to a trivial solution.

The condition

$$\hat{M}_0 > 0, \tag{3.101}$$

is necessary for two solutions, but so is the requirement that we are in the so-called asteroid curve, discussed in Appendix B of [32]. The asteroid curve condition for any CP-conserving model is

$$x^{3/2} + y^{3/2} \leq 1, \tag{3.102}$$

with

$$x = \frac{\hat{M}_1(\Lambda_0 - \Lambda_3)}{\hat{M}_0(\Lambda_3 - \Lambda_1)}, \quad y = \frac{\hat{M}_3(\Lambda_0 - \Lambda_1)}{\hat{M}_0(\Lambda_3 - \Lambda_1)}. \tag{3.103}$$

Hence, if both Eq. (3.101) and Eq. (3.103) are simultaneously satisfied, then we have two normal minima[33] .

33: Technically, we have at least two normal minima, but then we may only have a maximum of two normal minima coexisting in the 2HDM.

At this stage, we are at risk of a deeper solution to our electroweak vacuum $v \sim 246$ GeV. A vacuum that is at risk of tunnelling to a deeper vacuum solution is known as meta-stable or a panic vacuum. Appendix C in [32] shows how to calculate the conditions for the existence of a panic vacuum. The necessary and sufficient condition that our electroweak vacuum is the global minimum is given by

$$D = \hat{M}_1 \hat{M}_3 \hat{r}_1 \hat{r}_3 > 0. \tag{3.104}$$

D is known as the discriminant in this case.

We may quantify the above to the softly-broken Z_2-symmetry, represented by the tensor in Eq. (3.95). First and foremost, we need to determine if our potential does indeed have more than one normal minimum solution. The two conditions for this are given below [32].

Multiple Normal Vacuua Condition I: $\hat{M}_0 > 0$ (Z_2-symmetric model)

$$m_{11}^2 + k^2 m_{22}^2 < 0, \tag{3.105}$$

where

$$k = \left(\frac{\lambda_1}{\lambda_2}\right)^{1/4}. \tag{3.106}$$

Multiple Normal Vacuua Condition II: Astroid Curve (Z_2- conserving model)

$$x^{2/3} + y^{2/3} \leq 1, \tag{3.107}$$

where

$$x = \frac{4km_{12}^2}{m_{11}^2 + k^2 m_{22}^2} \frac{\sqrt{\lambda_1\lambda_2}}{\lambda_{345} - \sqrt{\lambda_1\lambda_2}}, \tag{3.108}$$

and

$$y = \frac{m_{11}^2 - k^2 m_{22}^2}{m_{11}^2 + k^2 m_{22}^2} \frac{\sqrt{\lambda_1\lambda_2} + \lambda_{345}}{\sqrt{\lambda_1\lambda_2} + \lambda_{345}}. \tag{3.109}$$

Note that $\lambda_{345} = \lambda_3 + \lambda_4 + \lambda_5$.

Next, to discern the case where we may have a meta-stable vacuum solution we have the discriminant condition

Vacuum Meta-stability Discriminant (Z_2-symmetric Potential)

$$D = m_{12}^2(m_{11}^2 - k^2 m_{22}^2)(t_\beta - k) > 0. \tag{3.110}$$

3.6 Scattering in the 2HDM

The scattering matrix of a system relates the initial and final states of a process. If we call the initial state ψ_{in} and the final state ψ_{out} then the scattering matrix S is defined such that

$$\psi_{\text{out}} = S\psi_{\text{in}}. \tag{3.111}$$

It is a requirement for the conservation of probability current that the S matrix be unitary $SS^\dagger = I$. This requirement becomes useful when taking into account the partial-wave analysis. Separation of the scattering matrix into the identity and the transfer matrix $S = I + iT$, leads to the unitarity relation $i(T^\dagger - T) = T^\dagger T$, which after placing between initial and final states leads to the optical theorem

$$\sigma = \frac{16\pi}{s} \sum_{l=0}^{\infty} (2l+1)\mathrm{Im}(a_l), \tag{3.112}$$

where s is the direction of the scattering and a_l is the partial wave with spin l. Following [34], the total cross section for a $\phi_1, \phi_2 \to \phi_3, \phi_4$ process is

$$\sigma = \frac{16\pi}{s} \sum_{l=0}^{\infty} (2l+1)|a_l|^2. \tag{3.113}$$

Together Eq. (3.112) and Eq. (3.113) give us the condition

$$|a_l|^2 = \mathrm{Im}(a_l), \tag{3.114}$$

for all l. Then writing $a_l = x + iy$ this becomes

$$x^2 + y^2 = y, \tag{3.115}$$

which is the equation of a circle with all points lying within $x < 1/2$ or

$$\mathrm{Re}(a_l) < \frac{1}{2}. \tag{3.116}$$

The partial wave amplitude may be written

$$a_l(s) = \frac{1}{32\pi} \int_{-1}^{1} d(c_\theta) P_l(c_\theta) \mathcal{M}(s,t,u), \tag{3.117}$$

Then the first of these s-wave amplitudes has the form

$$a_0(s) = \frac{1}{16\pi} [C_{\phi_i\phi_j \to \phi_k\phi_l} + C_{h \to \phi_i\phi_j}], \tag{3.118}$$

where C_X represents the coupling from a process of type X. We carry out the calculations at high energy. In the high energy limit, we only need to consider s-wave channel four-point scattering processes, corresponding to quartic couplings in the potential. Considering only four-point couplings we may re-phase the unitarity limit Eq. (3.116) to

$$|C_{\phi_i\phi_j \to \phi_k\phi_l}| \leq 8\pi. \tag{3.119}$$

Notice that such a limit is less restrictive than a standard perturbativity factor limit of 4π.

Calculating the couplings in the mass basis is rather involved, and it is more convenient to do it in the Higgs basis or before EWSB by

substituting the non-physical field doublet perturbations of Eq. 3.68 into the potential.[34] The calculation of couplings in the Higgs basis is delayed until the following chapter.

34: This approach is valid as the scattering matrix in this parameterisation is related to the physical basis (after EWSB) by a unitarity transformation. As such, it is enough the ensure the unitarity of either of these scattering matrices.

The elements of the scattering matrix for the two-to-two particle scatterings are classified based upon quantum numbers of the interactions of interest.

We have categorised the fields based upon the quantum numbers in Table 3.3. In Ref. [34] they calculate all possible scattering states such that we get a 22×22 matrix with block-diagonal elements defined by in and out states

$$\begin{aligned}
\mathcal{M}_1 &= (\phi_1^+\phi_2^-, \phi_2^+\phi_1^-, h_1 z_1, h_2 z_1, z_1 z_2, h_1 h_2), \\
\mathcal{M}_2 &= (\phi_1^+\phi_1^-, \phi_2^+\phi_2^-, \frac{z_1 z_1}{\sqrt{2}}, \frac{z_2 z_2}{\sqrt{2}}, \frac{h_1 h_1}{\sqrt{2}}, \frac{h_2 h_2}{\sqrt{2}}), \\
\mathcal{M}_3 &= (h_1 z_1, h_2 z_2), \\
\mathcal{M}_4 &= (h_1\phi_1^+, h_2\phi_1^+, z_1\phi_1^+, z_2\phi_2^+, h_1\phi_2^+, h_2\phi_2^+, z_1\phi_2^+, z_2\phi_2^+).
\end{aligned} \tag{3.120}$$

See the reference for the evaluated matrices and corresponding eigenvalues.

There is another method which gives us fewer eigenvalues to solve. In Ref. [35] they observe that under a re-phasing λ_5, CP is conserved at high energies. Then from this, they find that they can calculate the two-particle scattering before EWSB in terms of n_i, rather than h_i and z_i separately. Next, they categorise each set of combinations we may make from the doublets ϕ_1 and ϕ_2 by quantum number in their equations (4) and (5). In their other work Ref. [36] they expand these doublet combinations in the fields ϕ_i^+ and n_i before EWSB as shown in Table 3.4. Then finally, from these sets of two-particle states, they calculate the corresponding tree-level matrices.

	Z_2	Y	σ	σ_z
ϕ_1^+	+1	+1	+1/2	+1/2
ϕ_2^+	-1	+1	+1/2	+1/2
n_1	+1	+1	+1/2	-1/2
n_2	-1	+1	+1/2	-1/2

Table 3.3: The quantum numbers of the fields before EWSB.

Table 3.4: The doublet field scattering pairs before EWSB categorised by quantum numbers, taken from Ref. [36].

		$Y=1$		$Y=0$	
σ	σ_z	Z_2 even	Z_2 odd	Z_2 even	Z_2 odd
1	1	$\begin{pmatrix}\phi_1^+\phi_1^+\\ \phi_2^+\phi_2^+\end{pmatrix}$	$\phi_1^+\phi_2^+$	$\begin{pmatrix}\phi_1^+ n_1^*\\ \phi_2^+ n_2^*\end{pmatrix}$	$\begin{pmatrix}\phi_1^+ n_2^*\\ \phi_2^+ n_1^*\end{pmatrix}$
	0	$\begin{pmatrix}\phi_1^+ n_1\\ \phi_2^+ n_2\end{pmatrix}$	$\frac{\phi_1^+ n_2 + \phi_2^+ n_1}{\sqrt{2}}$	$\begin{pmatrix}\frac{\phi_1^+\phi_1^- - n_1 n_1^*}{\sqrt{2}}\\ \frac{\phi_2^+\phi_2^- - n_2 n_2^*}{\sqrt{2}}\end{pmatrix}$	$\begin{pmatrix}\frac{\phi_1^+\phi_2^- - n_1 n_2^*}{\sqrt{2}}\\ \frac{\phi_2^+\phi_1^- - n_2 n_1^*}{\sqrt{2}}\end{pmatrix}$
	-1	$\begin{pmatrix}n_1 n_1\\ n_2 n_2\end{pmatrix}$	$n_1 n_2$	$\begin{pmatrix}\phi_1^- n_1\\ \phi_2^- n_2\end{pmatrix}$	$\begin{pmatrix}\phi_1^- n_2\\ \phi_2^- n_1\end{pmatrix}$
0	0	absent	$\frac{\phi_1^+ n_2 - \phi_2^+ n_1}{\sqrt{2}}$	$\begin{pmatrix}\frac{\phi_1^+\phi_1^- + n_1 n_1^*}{\sqrt{2}}\\ \frac{\phi_2^+\phi_2^- + n_2 n_2^*}{\sqrt{2}}\end{pmatrix}$	$\begin{pmatrix}\frac{\phi_1^+\phi_2^- + n_1 n_2^*}{\sqrt{2}}\\ \frac{\phi_2^+\phi_1^- + n_2 n_1^*}{\sqrt{2}}\end{pmatrix}$

The scattering matrix has a block-diagonal structure due to the groupings by quantum numbers. For the general 2HDM the scattering amplitudes are written following the designation of Table 3.4 as [35] (see also [37, 38]).

$$\Lambda_{11}^{\mathrm{LO}} = \begin{pmatrix} \lambda_1 & \lambda_5 & \sqrt{2}\lambda_6 \\ \lambda_5^* & \lambda_2 & \sqrt{2}\lambda_7^* \\ \sqrt{2}\lambda_6 & \sqrt{2}\lambda_7 & \lambda_3+\lambda_4 \end{pmatrix}, \tag{3.121}$$

and

$$\Lambda_{10}^{\mathrm{LO}} = (\lambda_3 - \lambda_4), \tag{3.122}$$

and

$$\Lambda_{01}^{\mathrm{LO}} = \begin{pmatrix} \lambda_1 & \lambda_4 & \lambda_6 & \lambda_6^* \\ \lambda_4 & \lambda_2 & \lambda_7 & \lambda_7^* \\ \lambda_6^* & \lambda_7^* & \lambda_3 & \lambda_5^* \\ \lambda_6 & \lambda_7 & \lambda_5 & \lambda_3 \end{pmatrix}, \tag{3.123}$$

and

$$\Lambda_{00}^{\mathrm{LO}} = \begin{pmatrix} \lambda_3 & 2\lambda_3+\lambda_4 & 3\lambda_6 & 3\lambda_6^* \\ 2\lambda_3+\lambda_4 & 3\lambda_2 & 3\lambda_7 & 3\lambda_7^* \\ 3\lambda_6^* & 3\lambda_7^* & \lambda_3+2\lambda_4 & 3\lambda_5^* \\ 3\lambda_6 & 3\lambda_7 & 3\lambda_5 & \lambda_3+2\lambda_4 \end{pmatrix}. \tag{3.124}$$

The notation of these eigenvalues is $\mathrm{eig}(\Lambda_{Y\sigma}^{Z_2})$ the unitarity bound becomes

$$|\mathrm{eig}(\Lambda_i)| \leq \frac{1}{8\pi}. \tag{3.125}$$

We may analytically give eigenvalues for a Z_2-symmetric model, here we write them in the form of scattering amplitudes such that the unitarity limit condition of Eq. (3.116) applies. Similarly, the notation of these eigenvalues is $a_{Y\sigma\pm}^{Z_2}$.

Tree-Level Scattering Amplitudes Eigenvalues (Z_2- symmetric model)

$$
\begin{aligned}
a_{11\pm}^{\text{LO,even}} &= \frac{1}{32\pi}\left(\lambda_1+\lambda_2 \pm \sqrt{(\lambda_1-\lambda_2)^2+4\lambda_5^2}\right),\\
a_{01\pm}^{\text{LO,even}} &= \frac{1}{32\pi}\left(\lambda_1+\lambda_2 \pm \sqrt{(\lambda_1-\lambda_2)^2+4\lambda_4^2}\right),\\
a_{00\pm}^{\text{LO,even}} &= \frac{1}{32\pi}\left(3(\lambda_1+\lambda_2) \pm \sqrt{9(\lambda_1-\lambda_2)^2+4(2\lambda_3+\lambda_4)^2}\right),\\
a_{11}^{\text{LO,odd}} &= \frac{1}{16\pi}(\lambda_3+\lambda_4),\\
a_{10}^{\text{LO,odd}} &= \frac{1}{16\pi}(\lambda_3-\lambda_4),\\
a_{01\pm}^{\text{LO,odd}} &= \frac{1}{16\pi}(\lambda_3\pm\lambda_5),\\
a_{00\pm}^{\text{LO,odd}} &= \frac{1}{16\pi}(\lambda_3+2\lambda_4+3\lambda_5).
\end{aligned}
\tag{3.126}
$$

Moving to next-to-leading scattering, in the Z_2-symmetric model only block diagonal one-loop contributions to the scattering matrix are non-negligible. As such, the eigenvalues for the one-loop case may be expressed rather simply in terms of the matrix elements according to Ref. [39].

One-Loop-Level Scattering Amplitude Eigenavlues (Z_2- symmetric model)

$$
\begin{aligned}
a_{00\pm}^{\text{NLO,even}} &= \frac{1}{32\pi}\left(B_1+B_2 \pm \sqrt{(B_1-B_2)^2+4B_3^2}\right),\\
a_{00\pm}^{\text{NLO,odd}} &= \frac{1}{32\pi}\left(2B_4 \pm B_6\right),\\
a_{01\pm}^{\text{NLO,even}} &= \frac{1}{32\pi}\left(B_7+B_8 \pm \sqrt{(B_7-B_8)^2+4B_9^2}\right),\\
a_{01\pm}^{\text{NLO,odd}} &= \frac{1}{16\pi}(B_{13}\pm B_{15}),\\
a_{10}^{\text{NLO,odd}} &= \frac{1}{16\pi}B_{19},\\
a_{11\pm}^{\text{NLO,even}} &= \frac{1}{32\pi}\left(B_{20}+B_{21} \pm \sqrt{(B_{20}-B_{21})^2+4B_{22}^2}\right),\\
a_{11}^{\text{odd}} &= \frac{1}{16\pi}2B_{30}.
\end{aligned}
\tag{3.127}
$$

The B_i make up the block diagonal matrix elements and are given in their simple form in the Appendix of Ref. [39]. The form of B_i along with wave function corrections may be found in correspondingly labelled entries of the Appendix in Ref. [40]. B_i are also composed of

β functions for the λ terms, their complete form along with corrections from the gauge coupling parameters g_1, g_2, g_3 and the Yukawa couplings may be found in Refs. [41] and [42].

The constraint from one-loop unitarity is stronger and is given as

$$|a_0 - \frac{i}{2}| \leq \frac{1}{2}. \tag{3.128}$$

Phenomenology of the Two-Higgs-Doublet Model

4

Continuing on from the previous chapter which introduced the theory of the 2HDM we now discuss the phenomenology needed for our global fit.

Firstly in this chapter, we introduce the Higgs basis and detail why it is useful to work in. Next, we look at the Yukawa structure of the 2HDM and find that in the most general case, the scalars mediate FC interactions. Such interactions offer identifiable fingerprints in the search for scalars beyond the SM. We discuss an array of interesting flavour observables that offer such a fingerprint.

Finally, we introduce the electroweak oblique parameters and describe how they may be extended to a 2HDM.

4.1 The Higgs Basis

It is often more convenient and intuitive to move to the Higgs basis in which a non-trivial vacuum solution is identified with Φ_1. In the Higgs basis, it is easier to identify cases with SM-like scalar structure and more straightforward to expand the potential around the vacuum solution.

The Higgs basis is achieved through a transformation of the doublets in β [43]

$$\begin{pmatrix} H_1 \\ H_2 \end{pmatrix} = \begin{pmatrix} c_\beta & s_\beta \\ -s_\beta & c_\beta \end{pmatrix} \begin{pmatrix} \Phi_1 \\ \Phi_2 \end{pmatrix} . \tag{4.1}$$

This transformation means that the scalars A^0 and $H^\pm$ will be rotated into their mass eigenstate. In the Higgs basis, the doublets take the form

$$H_1 = \frac{1}{\sqrt{2}} \begin{pmatrix} \sqrt{2} G^+ \\ v + h_1' + i G^0 \end{pmatrix} , \qquad H_2 = \frac{1}{\sqrt{2}} \begin{pmatrix} \sqrt{2} H^+ \\ h_2' + i A^0 \end{pmatrix} , \tag{4.2}$$

where h_1' and h_2' are combinations of the CP-even neutral Higgs fields rotated in β, A^0 is a CP-odd neutral Higgs field, H^+ is a charged Higgs field, and G^+ and G^0 are the would-be Goldstone bosons. The most general potential (see e.g. Ref [43]) in the Higgs basis is*

* The transformation between the Higgs basis and generic basis is presented in Appendix A of [43].

General 2HDM Potential: Higgs Basis

$$
\begin{aligned}
V = {} & M_{11}^2 H_1^\dagger H_1 + M_{22}^2 H_2^\dagger H_2 - \left(M_{12}^2 H_2^\dagger H_1 + \text{H.}c. \right) + \frac{1}{2}\Lambda_1 \left(H_1^\dagger H_1 \right)^2 \\
& + \frac{1}{2}\Lambda_2 \left(H_2^\dagger H_2 \right)^2 + \Lambda_3 \left(H_1^\dagger H_1 \right) \left(H_2^\dagger H_2 \right) + \Lambda_4 \left(H_1^\dagger H_2 \right) \left(H_2^\dagger H_1 \right) \\
& + \left\{ \frac{1}{2}\Lambda_5 \left(H_1^\dagger H_2 \right)^2 + \left[\Lambda_6 \left(H_1^\dagger H_1 \right) + \Lambda_7 \left(H_2^\dagger H_2 \right) \right] H_1^\dagger H_2 + \text{H.}c. \right\} ,
\end{aligned}
$$

where Λ_i ($i = 1, 2, \ldots, 7$) are the quartic couplings and M_{ij}^2 are the bare mass-squared parameters. In general, Λ_5, Λ_6, Λ_7 and M_{12} can be complex. Note that one can choose Λ_5 to be real by redefining H_1 and H_2 [43].

Since only H_1 takes a VEV, differentiating Eq. (4.3) with respect to H_1 and H_2, gives the following minimisation conditions

$$
M_{11}^2 = -\frac{1}{2}\Lambda_1 v^2 , \qquad M_{12}^2 = \frac{1}{2}\Lambda_6 v^2 , \tag{4.3}
$$

which can be used to eliminate M_{11}^2 and M_{12}^2 as independent variables. Eq. (4.3) applies to both the real and imaginary parts. Inserting $\langle H_1 \rangle = (0, v/\sqrt{2})^T$ into Eq. (4.3), we obtain the squared mass of the charged scalar

$$
M_{H^+}^2 = M_{22}^2 + \frac{1}{2} v^2 \Lambda_3 , \tag{4.4}
$$

the mass matrix of the neutral CP-even scalar

$$
\mathcal{M}_h^2 = \begin{pmatrix} \Lambda_1 v^2 & \Lambda_6 v^2 \\ \Lambda_6 v^2 & m_A^2 + \Lambda_5 v^2 \end{pmatrix} , \tag{4.5}
$$

and the mass of the CP-odd scalar

$$
m_A^2 = M_{H^+}^2 - \frac{1}{2} v^2 \left(\Lambda_5 - \Lambda_4 \right) . \tag{4.6}
$$

Notice then that the $\{2,2\}$ element of the CP-even mass matrix is $m_A^2 + \Lambda_5 v^2 = M_{22}^2 + v^2 \Lambda_{345}$, where $\Lambda_{345} = \Lambda_3 + \Lambda_4 + \Lambda_5$. Extracting the CP-even mass eigenvalues

$$
m_{H,h}^2 \equiv \frac{1}{2} \left\{ m_A^2 + v^2 \left(\Lambda_1 + \Lambda_5 \right) \pm \sqrt{\left[m_A^2 + v^2 \left(\Lambda_5 - \Lambda_1 \right) \right]^2 + 4 v^4 \Lambda_6^2} \right\} . \tag{4.7}
$$

The CP-even physical Higgs states are related to the fields h_1' and h_2' via a negative rotation in α followed by a rotation in β, $R^T(\alpha) R(\beta) = R(\beta - \alpha)$, in matrix form

$$
\begin{pmatrix} H \\ h \end{pmatrix} = \begin{pmatrix} c_{\beta\alpha} & -s_{\beta\alpha} \\ s_{\beta\alpha} & c_{\beta\alpha} \end{pmatrix} \begin{pmatrix} h_1' \\ h_2' \end{pmatrix} , \tag{4.8}
$$

where we have define $c_{\beta\alpha}$ as $\cos(\beta - \alpha)$ and similarly for the sin term.

The angle $\beta - \alpha$ is important as in the limit $s_{\beta\alpha} = \pm 1$ we get $h_1' = h^0$, $h_2' = H^0$ and we recover Φ_1 as identically the SM scalar doublet. The alternative identification occurs when $h_1 = H^0, h_2 = h^0$, this is known as the hidden Higgs scenario, and the SM case corresponds to $s_{\beta\alpha} = 0$. A possible hidden Higgs scenario occurs if $m_H = 125$ GeV and identifies as the SM Higgs scalar while $m_h < 125$ GeV.

We may perform the rotation in the mass basis to write the masses in terms of $\beta - \alpha$

$$M_h^2 = R^T(\beta - \alpha)\mathcal{M}_h^2 R(\beta - \alpha), \tag{4.9}$$

where M_h^2 is the diagonal (physical) mass matrix. The off-diagonal entries M_h^2 being zero results in the relation

$$m_A^2 = v^2\left[(\Lambda_1 - \Lambda_5) + \frac{2\Lambda_6}{t_{2(\beta\alpha)}}\right]. \tag{4.10}$$

In the Higgs basis, it is easy to see the mixing between the CP-even scalars. The mixing of the CP-even physical eigenstates is controlled by the off-diagonal parameter in the CP-even mass matrix. If the off-diagonal parameters are small relative to the diagonal terms, then the mixing will be suppressed, and we have SM-like behaviour for the lighter CP-even state. This case is known as the alignment limit. We can see by looking at the form of Eq. (4.5) that the alignment limit is reached at low Λ_6 relative to the diagonal CP-even mass matrix entries.

Another way that we may recover the SM-like behaviour is by having one CP-even mass much larger than the other. The decoupling limit is reached when $m_A^2 + \Lambda_5 \gg \Lambda_1$. As the other heavy scalars are all set by m_{12}^2 (via m_A) then this condition separates the spectrum into a light SM-like state and much heavier extra scalar states as needed for the limit.

In the general 2HDM t_β is not a physical parameter (see [44] for a complete discussion into the significance of t_β). The physical parameter is $s_{\beta\alpha}$, which needs to be sufficiently close to one (i.e. the decoupling or alignment limit) to give rise to an adequately SM-like Higgs boson that obeys current observations [45]. It proves handy to find the physical angle $\beta - \alpha$ in terms of the scalar masses. From Eq. (4.10)

$$t_{2(\beta-\alpha)} = \frac{2v^2\Lambda_6}{m_A^2 + v^2(\Lambda_5 - \Lambda_1)}. \tag{4.11}$$

In the alignment limit $t_{2(\beta\alpha)}$ and thus Λ_6 approach zero, as mentioned.

Combining Eq. (4.7) with the above Eq. (4.11), we may show that

$$\begin{aligned} c_{2(\beta-\alpha)} &= -\frac{m_A^2 + v^2(\Lambda_5 - \Lambda_1)}{m_H^2 - m_h^2}, \\ s_{2(\beta-\alpha)} &= -\frac{2\Lambda_6 v^2}{m_H^2 - m_h^2}. \end{aligned} \tag{4.12}$$

We choose $c_{2(\beta-\alpha)}$ and $s_{2(\beta-\alpha)}$ negative, following convention that $s_{\beta\alpha} \to 1$ is the direction of the alignment limit. Choosing both positive corresponds to a rotation of $\frac{\pi}{2}$ in $(\beta-\alpha)$ leading to a redefinition of the alignment limit to $s_{\beta\alpha} \to 0$.

When recovering $\beta - \alpha$ from (4.11) it is guaranteed to lie on the interval $(-\frac{\pi}{2}, \frac{\pi}{2})$. The sign of $\beta - \alpha$ is dependant on (4.11).

The value of β always lies on the interval $(0, \frac{\pi}{2})$. If we calculate α using (4.11) we get an accessible region of $(-\frac{\pi}{2}, \pi)$. It is, however common to re-phase α by π (half-period) such that it lies on the interval $(-\frac{\pi}{2}, \frac{\pi}{2})$ if necessary. This will also re-phase $(\beta-\alpha)$ and flip the signs of $c_{\beta\alpha}$ and $s_{\beta\alpha}$ but leave the forms of (4.12) invariant. In our convention, the signs of $c_{\beta\alpha}$ and $s_{\beta\alpha}$ are retained if re-phasing is carried out, in other words, the signs are always obtained from Eq. (4.12), rather than the combination $(\beta-\alpha)$ itself.

4.1.1 Basis Independent Methods: Couplings of the Potential

The work of Ref. [44] uses a basis-independent treatment to examine the phenomenology of the 2HDM. Their methods allow for an elegant approach for extracting all cubic and quartic couplings of the scalar Higgs and Goldstone particles. Begin by defining the unit norm vectors as

$$\hat{v}_a = e^{i\eta} \begin{pmatrix} c_\beta \\ s_\beta e^{i\xi} \end{pmatrix}, \tag{4.13}$$

$$\hat{w}_a = \hat{v}_{\overline{a}}^* \epsilon_{ab} = e^{-i\eta} \begin{pmatrix} -s_\beta e^{-i\xi} \\ c_\beta \end{pmatrix}, \tag{4.14}$$

where ϵ_{ab} is the Levi-Civita tensor [36] and

$$\hat{v}_{\overline{a}}^* \hat{w}_a = 0. \tag{4.17}$$

Then the doublets in the Higgs basis are related to those in the generic basis via

$$\begin{aligned} H_1 &= \hat{v}_{\overline{a}}^* \Phi_a, \\ H_2 &= \hat{w}_{\overline{a}}^* \Phi_a. \end{aligned} \tag{4.18}$$

36: Defined by

$$\epsilon_{12} = \epsilon_{12} = -1, \tag{4.15}$$

and

$$\epsilon_{11} = \epsilon_{22} = 0. \tag{4.16}$$

We may also express the rotation between the generic and Higgs basis as

$$\hat{U} = \begin{pmatrix} \hat{v}_1^* & \hat{v}_2^* \\ \hat{w}_1^* & \hat{w}_2^* \end{pmatrix}. \tag{4.19}$$

Comparing the Higgs basis to the potential form introduced in Eq. (3.3),* beginning with the quadratic terms

$$M_{11}^2 = \mathrm{Tr}(YV), \quad M_{22}^2 = \mathrm{Tr}(YW), \quad M_{12}^2 = Y_{a\bar{b}}\hat{v}_{\bar{a}}^*\hat{w}_b, \tag{4.21}$$

where $V_{a\bar{b}} = \hat{v}_a\hat{v}_{\bar{b}}^*$ and $W_{a\bar{b}} = \hat{w}_a\hat{w}_{\bar{b}}^*$. The quartic term relations are shown in Table 4.1.

We may express a doublet field (following Appendix B of Ref. [44]) according to physical fields

$$\Phi_a = \begin{pmatrix} G^+\hat{v}_a + H^+\hat{w}_a \\ \frac{v}{\sqrt{2}}\hat{v}_a + \frac{1}{\sqrt{2}}\sum_{k=1}^{4}(q_{k1}\hat{v}_a + q_{k2}e^{-i\theta_{23}}\hat{w}_a)h_k \end{pmatrix}. \tag{4.22}$$

Then we may write the potential in terms of physical couplings, so we may read off cubic and quartic interaction terms directly from potentials given in equation (57) - (60) of Ref. [44], the couplings to vector bosons are stated in (64) - (67). The equations of the potential derived from the doublet (4.22) are in a basis independent form and as such the mixing angle needs to be defined specifically. We use the standard Higgs basis prescription of Eq. (4.8) for the CP-even mixing with a CP-conserving potential, which corresponds to Case I in the Appendix of [44]. The definitions necessary for this are

$$q_{kl} = \begin{pmatrix} s_{\beta\alpha} & \epsilon_6 c_{\beta\alpha} \\ -\epsilon_6 c_{\beta\alpha} & s_{\beta\alpha} \\ 0 & i \\ i & 0 \end{pmatrix}, \tag{4.23}$$

where $\epsilon_6 = \mathrm{sgn}(\Lambda_6)$. The term $e^{-i\theta_{23}} = \epsilon_6$ and there are also factors that come with each of the neutral physical Higgs states when reading off the couplings, these are shown here in brackets,

$$(+1)h^0, \quad (-\epsilon_6)H^0, \quad (\epsilon_6)A^0, \quad (+1)G^0. \tag{4.24}$$

Λ_1	$Z_{a\bar{b}c\bar{d}}V_{b\bar{a}}V_{d\bar{c}}$
Λ_2	$Z_{a\bar{b}c\bar{d}}W_{b\bar{a}}W_{d\bar{c}}$
Λ_3	$Z_{a\bar{b}c\bar{d}}V_{b\bar{a}}W_{d\bar{c}}$
Λ_4	$Z_{a\bar{b}c\bar{d}}V_{b\bar{c}}W_{d\bar{a}}$
Λ_5	$Z_{a\bar{b}c\bar{d}}\hat{v}_{\bar{a}}^*\hat{w}_b\hat{v}_{\bar{c}}^*\hat{w}_d$
Λ_6	$Z_{a\bar{b}c\bar{d}}\hat{v}_{\bar{a}}^*\hat{v}_b\hat{v}_{\bar{c}}^*\hat{w}_d$
Λ_7	$Z_{a\bar{b}c\bar{d}}\hat{v}_{\bar{a}}^*\hat{w}_b\hat{w}_{\bar{c}}^*\hat{w}_d$

Table 4.1: Relations between couplings of the Higgs basis and the tensor basis introduced in Eq. (3.3).

* Given here for convenience

$$V_H = Y_{ab}\Phi_a^\dagger\Phi_b + \frac{1}{2}Z_{abcd}(\Phi_a^\dagger\Phi_b)(\Phi_c^\dagger\Phi_d). \tag{4.20}$$

where the summation for $a, b, c, d = 1, 2$ is implicit.

4.2 The 2HDM Yukawa Sector

The most general Yukawa Lagrangian of the 2HDM reads

$$\begin{aligned} -\mathscr{L}_Y = &\overline{Q}\,(Y_u^{1\dagger}\tilde{\Phi}_1 + Y_u^{2\dagger}\tilde{\Phi}_2)u_{\mathrm{R}} + \overline{Q}\,(Y_d^{1\dagger}\Phi_1 + Y_d^{2\dagger}\Phi_2)d_{\mathrm{R}} + \\ &\overline{L}\,(Y_l^{1\dagger}\Phi_1 + Y_l^{2\dagger}\Phi_2)l_{\mathrm{R}} + \mathrm{H.}c.\,, \end{aligned} \tag{4.25}$$

where $Q = (u_{\mathrm{L}},\, d_{\mathrm{L}})^T$ and $u_{\mathrm{R}}, d_{\mathrm{R}}$, are the SU(2) quark doublets and singlets, respectively and $L = (e_{\mathrm{L}},\, \mu_{\mathrm{L}})^T$ and l_{R} are the SU(2) leptonic doublets and singlets, respectively.[37] Rotation into the Higgs basis presents us with a form which may more easily identify the Yukawa's with physical masses of the fermions

37: Note also that $\tilde{\Phi}_i = i\sigma_2\Phi_i^*$.

$$\begin{aligned} -\mathscr{L}_Y = &\overline{Q}\,(\kappa_u\tilde{H}_1 + \xi_u\tilde{H}_2)u_{\mathrm{R}} + \overline{Q}\,(\kappa_d H_1 + \xi_d H_2)d_{\mathrm{R}} + \\ &\overline{L}\,(\kappa_l H_1 + \xi_l H_2)l_{\mathrm{R}} + [\mathrm{H.c.}]\,, \end{aligned} \tag{4.26}$$

with the rotated Yukawa's

$$\begin{aligned} \kappa_f &= Y_f^1 c_\beta + Y_f^2 s_\beta, \\ \xi_f &= -Y_f^1 s_\beta + Y_f^2 c_\beta. \end{aligned} \tag{4.27}$$

There is always a basis in which we can identify κ_f as the diagonal fermion mass matrix

$$\kappa_f = \frac{\sqrt{2}\hat{M}_f}{v}, \tag{4.28}$$

where $\hat{M}_f = \mathrm{diag}(m_f)$ are the masses of the respective fermions. As we have two non-trivial Yukawa matrices, choosing κ_f purely-diagonal allows for the possibility of off-diagonal entries in ξ_f. Such entries lead to new FC interactions at tree-level and beyond. The absence of FC interactions in experimental observations thus calls for an adjustment to the general 2HDM. There are two ways in which we may naturally impose flavour conservation: an introduction of a symmetry or an alignment within the Yukawa sector.

If we rewrite the potentially flavour violating term matrix ξ with respect to κ, we may be able to spot patterns that will allow us to avoid flavour violation

$$\xi_f = \frac{Y_f^2}{c_\beta} - \kappa_f t_\beta. \tag{4.29}$$

Substituting either of the ξ or κ into the above will satisfy the equation. We may also reverse this in terms of Y_f^1

$$\xi_f = -\frac{Y_f^1}{s_\beta} + \kappa_f c t_\beta. \tag{4.30}$$

These relations forbid any off-diagonal terms in the Yukawa's. Imposing the restrictions by hand is known as aligning the Yukawa cou-

plings and is equivalent to setting

$$Y_f^1 \propto Y_f^2. \tag{4.31}$$

As such, with one of the above alignment conditions present, ensuring only a single Yukawa doesn't have any off-diagonal terms guarantees protection against FC completely.

An alternative method is through the introduction of Z_2^f symmetry. The symmetry will explicitly assign each fermion only one doublet with which to couple.

By convention, there are four models described by their Yukawa couplings, and they are listed in Table 4.2. The introduction of Z_2-symmetries within the Yukawa sector introduces relations of nature

$$\xi_f = k_f \kappa_f. \tag{4.32}$$

where k_f is a scaling factor, the scaling factors for respective models are given in Table 4.3.

The most discussed, the type-II 2HDM assigns Z_2^u-even to Φ_2, Z_2^d-even to Φ_1 and Z_2^l-even to Φ_1, leading to the terms

$$\begin{aligned} \xi_d &= -\kappa_d t_\beta, \\ \xi_e &= -\kappa_e t_\beta, \\ \xi_u &= \kappa_u c t_\beta. \end{aligned} \tag{4.33}$$

These may be derived in two ways. One method is directly from the form of the rotated Yukawa's (4.27) by setting either of the unrotated Yukawa's Y_f^1 or Y_f^2 to zero by the respective Z_2 symmetry present. The other method is from the alignment conditions of (4.29) and (4.30) by again setting the respective Yukawa to zero. The relationships between masses and unrotated Yukawa's in each model are then presented in Table 4.4.

The general type-III 2HDM does not impose any restrictions on the Yukawa's, and as such it allows for FC processes at tree-level. The type-III model is most easily and commonly studied in the Higgs basis.

Rotating the remaining fields (CP-even) into their physical basis and performing EWSB on Eq. (4.26) gives us a form from which we may

Type	Φ_1 (Z_2+)	Φ_2 (Z_2+)
I	$\times$	u, d, e
II	d, e	u
X (LS)	e	u, d
Y (flp.)	d	u, e

Table 4.2: Models of the 2HDM Yukawa sector. The general model couples to both the doublets. By convention there are four models that preserve flavour and are widely discussed.

Type	k_u	k_d	k_e
I	ct_β	ct_β	ct_β
II	ct_β	$-\mathrm{t}_\beta$	$-\mathrm{t}_\beta$
X (LS)	ct_β	ct_β	$-\mathrm{t}_\beta$
Y (flp.)	ct_β	$-\mathrm{t}_\beta$	ct_β

Table 4.3: The Yukawa coupling factors for the 2HDM in the Z_2-symmetric scheme.

Type	$\frac{\sqrt{2}M_u}{v}$	$\frac{\sqrt{2}M_d}{v}$	$\frac{\sqrt{2}M_e}{v}$
I	$Y_u^2 s_\beta$	$Y_d^2 s_\beta$	$Y_e^2 s_\beta$
II	$Y_u^2 s_\beta$	$Y_d^1 c_\beta$	$Y_e^1 c_\beta$
X (LS)	$Y_u^2 s_\beta$	$Y_d^2 s_\beta$	$Y_e^1 c_\beta$
Y (flp.)	$Y_u^2 s_\beta$	$Y_d^1 c_\beta$	$Y_e^2 s_\beta$

Table 4.4: Relationship between mass matrices and the Yukawa's in the generic basis.

read off the couplings of fermions and scalars

$$
\begin{aligned}
-\mathscr{L}_Y \;=\; & \overline{u}_b \left(V_{\mathrm{CKM},bc}\, \hat{\xi}^D_{ca} P_R - \hat{\xi}^{U*}_{cb}\, V_{\mathrm{CKM},ca} P_L \right) d_a\, H^+ \\
& + \overline{d}_b \left(\hat{\xi}^{D*}_{cb}\, V^*_{\mathrm{CKM},ac}\, P_L - V^*_{\mathrm{CKM},cb}\, \hat{\xi}^U_{ca} P_R \right) u_a\, H^- \\
& + \frac{h}{\sqrt{2}} \Bigg(\overline{d}_b \left[\left\{ \kappa^D_{ba} s_{\beta\alpha} + \hat{\xi}^D_{ba} c_{\beta\alpha} \right\} P_R + \left\{ \kappa^D_{ba} s_{\beta\alpha} + \hat{\xi}^{D*}_{ba} c_{\beta\alpha} \right\} P_L \right] d_a \\
& + \overline{u}_b \left[\left\{ \kappa^U_{ba} s_{\beta\alpha} + \hat{\xi}^U_{ba} c_{\beta\alpha} \right\} P_R + \left\{ \kappa^U_{ba} s_{\beta\alpha} + \hat{\xi}^{U*}_{ba} c_{\beta\alpha} \right\} P_L \right] u_a \Bigg) \\
& + \frac{H}{\sqrt{2}} \Bigg(\overline{d}_b \left[\left\{ \kappa^D_{ba} c_{\beta\alpha} - \hat{\xi}^D_{ba} s_{\beta\alpha} \right\} P_R + \left\{ \kappa^D_{ba} c_{\beta\alpha} - \hat{\xi}^{D*}_{ba} s_{\beta\alpha} \right\} P_L \right] d_a \\
& + \overline{u}_b \left[\left\{ \kappa^U_{ba} c_{\beta\alpha} - \hat{\xi}^U_{ba} s_{\beta\alpha} \right\} P_R + \left\{ \kappa^U_{ba} c_{\beta\alpha} - \hat{\xi}^{U*}_{ba} s_{\beta\alpha} \right\} P_L \right] u_a \Bigg) \\
& + \frac{iA}{\sqrt{2}} \Bigg(\overline{d}_b \left[\hat{\xi}^D_{ba} P_R - \hat{\xi}^{D*}_{ba} P_L \right] d_a + \overline{u}_b \left[-\hat{\xi}^U_{ba} P_R + \hat{\xi}^{U*}_{ba} P_L \right] u_a \Bigg) ,
\end{aligned}
\tag{4.34}
$$

where $a, b = 1, 2, 3$ are flavour indices and u_a and d_a denote the up and down quark states in the mass basis. For simplicity we have left out the leptons from the above. The derivation of this Lagrangian is presented in Appendix B. Defining

$$
g_{\overline{q}_b q_a \phi} \equiv i \left(\Gamma^{LR\,\phi}_{q_b q_a} P_R + \Gamma^{RL\,\phi}_{q_b q_a} P_L \right) , \tag{4.35}
$$

as in Ref. [46], we may read off each coupling * provided in Table 4.5. For Z_2 aligned 2HDMs the terms are given in Table 4.6. We note the relationships

$$
\begin{aligned}
\Gamma^{LR,H^\pm}_{ud} &= \kappa_d V_{ud} \Gamma^X_d , \\
\Gamma^{RL,H^\pm}_{ud} &= \kappa_u V_{ud} \Gamma^X_u , \\
\Gamma^A_{f_a f_b} &= -i \frac{\kappa_u}{\sqrt{2}} \Gamma^X_f .
\end{aligned}
\tag{4.37}
$$

The charged scalar particle and lepton interaction term appear in the Yukawa Lagrangian as $[\sqrt{2}\Gamma^X_f \bar{\mu}_L l_R H^+ + \text{H.c.}]$, the neutral scalar-lepton interactions are the same as those of the neutral Higgs-quark interactions.

Looking at the couplings for the type-I model given in Table 4.6 we see that when $\alpha = 0$ (or a half-period rotation of this), the couplings to the fermions rotate entirely towards the SM-like Higgs. If we then take $s_\beta \to 1$, we find that we recover complete SM-like behaviour within the Yukawa sector. This is only possible within the type-I model as Z_2 symmetry alignment is assigned to the same field.

Working in the type-III model without flavour alignment introduces a large number of variables into our theory (the extra Yukawa's). The in-

* Due to the Hermicity of the Lagrangian an important identity holds,

$$
\Gamma^{LR\,\phi\,*}_{q_a q_b} = \Gamma^{RL\,\phi}_{q_b q_a} . \tag{4.36}
$$

Table 4.5: Scalar-quark-quark couplings extracted from Eq. (B.13) using the convention of Eq. (4.35).

	$\Gamma^{LR\phi}_{q_b q_a}$	$\Gamma^{RL\phi}_{q_b q_a}$
$\overline{q_b} q_a h$	$\frac{\hat{M}_{q,ba}}{v} s_{\beta\alpha} + \frac{1}{\sqrt{2}} \hat{\xi}^q_{ba} c_{\beta\alpha}$	$\frac{\hat{M}_{q,ba}}{v} s_{\beta\alpha} + \frac{1}{\sqrt{2}} (\hat{\xi}^q_{ba})^* c_{\beta\alpha}$
$\overline{q_b} q_a H$	$\frac{\hat{M}_{q,ba}}{v} c_{\beta\alpha} - \frac{1}{\sqrt{2}} \hat{\xi}^q_{ba} s_{\beta\alpha}$	$\frac{\hat{M}_{q,ba}}{v} c_{\beta\alpha} - \frac{1}{\sqrt{2}} (\hat{\xi}^q_{ba})^* s_{\beta\alpha}$
$\overline{q_b} q_a A$	$\frac{i}{\sqrt{2}} \hat{\xi}^q_{ba}$	$-\frac{i}{\sqrt{2}} (\hat{\xi}^q_{ba})^*$
$\overline{u_b} d_a H^+$	$V_{\mathrm{CKM},bc}\, \hat{\xi}^D_{ca}$	$-(\hat{\xi}^U_{cb})^*\, V_{\mathrm{CKM},ca}$

Table 4.6: Scalar-fermion couplings in the convention of Eq. (4.35) for each of the Z_2 aligned 2HDMs. For the charged and pseudoscalar particles we may write couplings in terms of Γ^X_f according to the relationships given in Eq. (4.37).

Type	$\Gamma^h_u \frac{v}{M_u}$	$\Gamma^h_d \frac{v}{M_d}$	$\Gamma^h_e \frac{v}{M_e}$	$\Gamma^H_u \frac{v}{M_u}$	$\Gamma^H_d \frac{v}{M_d}$	$\Gamma^H_e \frac{v}{M_e}$	Γ^X_u	Γ^X_d	Γ^X_e
I	c_α/s_β	c_α/s_β	c_α/s_β	s_α/s_β	s_α/s_β	s_α/s_β	ct_β	$-ct_\beta$	$-ct_\beta$
II	c_α/s_β	$-s_\alpha/c_\beta$	$-s_\alpha/c_\beta$	s_α/s_β	c_α/c_β	c_α/c_β	ct_β	t_β	t_β
X (LS)	c_α/s_β	c_α/s_β	$-s_\alpha/c_\beta$	s_α/s_β	s_α/s_β	c_α/c_β	ct_β	$-ct_\beta$	t_β
Y (flipped)	c_α/s_β	$-s_\alpha/c_\beta$	c_α/s_β	s_α/s_β	c_α/c_β	s_α/s_β	ct_β	t_β	$-ct_\beta$

crease in parameters becomes computationally expensive for numerical scans. As such, we introduce two different sets below.

Yukawa Set I: Full This is the case where all extra Yukawa's are non-zero. As the Yukawa's are complex numbers this introduces 54 variables to our theory[38] , making it computationally expensive to explore

$$\hat{\xi}^U = \begin{pmatrix} \hat{\xi}^U_{11} & \hat{\xi}^U_{12} & \hat{\xi}^U_{13} \\ \hat{\xi}^U_{21} & \hat{\xi}^U_{22} & \hat{\xi}^U_{23} \\ \hat{\xi}^U_{31} & \hat{\xi}^U_{32} & \hat{\xi}^U_{33} \end{pmatrix}, \qquad \hat{\xi}^D = \begin{pmatrix} \hat{\xi}^D_{11} & \hat{\xi}^D_{12} & \hat{\xi}^D_{13} \\ \hat{\xi}^D_{21} & \hat{\xi}^D_{22} & \hat{\xi}^D_{23} \\ \hat{\xi}^D_{31} & \hat{\xi}^D_{32} & \hat{\xi}^D_{33} \end{pmatrix}, \qquad \hat{\xi}^L = \begin{pmatrix} \hat{\xi}^L_{11} & \hat{\xi}^L_{12} & \hat{\xi}^L_{13} \\ \hat{\xi}^L_{21} & \hat{\xi}^L_{22} & \hat{\xi}^L_{23} \\ \hat{\xi}^L_{31} & \hat{\xi}^L_{32} & \hat{\xi}^L_{33} \end{pmatrix}. \tag{4.38}$$

38: Here we include the Yukawa's corresponding to the leptonic terms which we have not previously included in our Lagrangian.

Yukawa Set II: Restricted With the knowledge that the couplings to the first family are very restricted we introduce the *restricted* set of Yukawa's. In this set only the most dominant Yukawa's, which are those that contain the third family, are non-trivial. We also set the leptonic Yukawa's trivial, although this restricts our analysis to flavour changing in the up and down sector we do so for the study to remain computationally viable. The *restricted* set of Yukawa's then takes the

form

$$\hat{\xi}^U = \begin{pmatrix} 0 & 0 & 0 \\ 0 & 0 & \hat{\xi}^U_{23} \\ 0 & \hat{\xi}^U_{32} & \hat{\xi}^U_{33} \end{pmatrix}, \qquad \hat{\xi}^D = \begin{pmatrix} 0 & 0 & 0 \\ 0 & 0 & \hat{\xi}^D_{23} \\ 0 & \hat{\xi}^D_{32} & \hat{\xi}^D_{33} \end{pmatrix}, \qquad \hat{\xi}^L = \begin{pmatrix} 0 & 0 & 0 \\ 0 & 0 & 0 \\ 0 & 0 & 0 \end{pmatrix}. \tag{4.39}$$

The only a priori requirement placed on the entries of $\hat{\xi}^U$ and $\hat{\xi}^D$ is that they respect perturbativity. *This is the set of Yukawa's we use for the type-III analysis.*

4.3 Decay Spectrum of the 2HDM Higgs Scalars

In section 2.5, we described the decay spectrum of the SM Higgs boson. The introduction of another doublet (new scalar states) not only brings new exotic decay channels but also alters some of the SM channels. In this section, we revisit the decays in their most general form. Throughout, vertex couplings are denoted as C_X, where X identifies the vertex interaction.

4.3.1 Modified Decays

Scalar to Fermions: $\phi \to f\overline{f}$ The scalar to fermion-fermion decay width is not altered for h^0 from the one stated in Eq. (2.5). There is, however, a new class of decays that may occur in the 2HDM, these being tree-level FC decays. If there is no protection against FC interactions, the two final fermion states may be different. For a charged Higgs scalar, the initial and final state fermions belong to different families.

$\phi \to f_1\overline{f_2}$ Decay Width

$$\Gamma(\phi \to f_1\overline{f_2}) = \frac{N_c m_\phi}{8\pi}\left[\epsilon^+|C_S|^2 + \epsilon^-|C_P|^2\right]\sqrt{\lambda(1, \epsilon^2_{f_1}, \epsilon^2_{f_2})}. \tag{4.40}$$

Above as usual

$$\begin{aligned} \epsilon^{\pm} &= 1 - (\epsilon_{f_1} \pm \epsilon_{f_2})^2, \\ \lambda(1, a, b) &= (1 - a - b)^2 - 4ab, \\ \epsilon_f &= \frac{m_f}{m_\phi}. \end{aligned} \tag{4.41}$$

The vertex couplings in this process correspond to scalar and pseudo-scalar terms respectively. We may recover the SM decay width by setting $|C_S|^2 = \sqrt{2}G_F$, $|C_P| = 0$ and $f_1 = f_2$.

Scalar to Vector Bosons: $\phi \to VV/VX$ These processes remain the same as those detailed in section 2.5. If the charged scalar particle is the initial state, then care must be taken to ensure quantum numbers are conserved.

$\phi \to VV$ Decay Width ($m_\phi > 2m_V$)

$$\Gamma(H_i \to VV) = \delta_V \frac{|C_{\phi_i VV}|^2 m_{\phi_i}^3}{128\pi m_V^4}(1 - x_V + 3x_V^2)\sqrt{1 - x_v}. \tag{4.42}$$

Above as usual

$$x_f = \frac{4m_f^2}{m_h^2}, \tag{4.43}$$

and the symmetry factor is $\delta_W = 2$ or $\delta_Z = 1$. For the case where $m_\phi < 2m_V$ we may get the state $\phi \to VX$ with an off-shell V, the numerical expression for this process is given in (15)-(17) of [47].

Scalar to Photons: $\phi \to \gamma\gamma$ Earlier we showed that this decay happened through a loop. In the 2HDM the charged Higgs scalar contributes to the loop and as such modifies the form factor for the channel in Eq. (2.108). We also note that to accommodate scalars other than the light Higgs, we need to normalise each of the factors according to their respective Yukawa's. The most general equation for the decay within the 2HDM is given below.

$\phi_i \to \gamma\gamma$ Decay Width

$$\Gamma(\phi_i \to \gamma\gamma) = \frac{\alpha^2 m_{\phi_i}^3}{256\pi^3 v^2}\left(|S^\gamma(m_{\phi_i})|^2 + |P^\gamma(m_{\phi_i})|^2\right). \tag{4.44}$$

Above, the scalar and pseudo-scalar form factors have been separated as

$$S^{\gamma}(m_{\phi_i}) = 2 \sum_{\text{fermions}} N_c Q_f^2 C^S_{\phi_i f \overline{f}} \frac{v}{m_f} F_s(x_f) - C_{\phi_i WW} \frac{v}{2m_W^2} F_W(x_W) - C_{\phi_i H^+ H^-} \frac{v}{2m_{H^\pm}^2} F_\pm(x_{H^\pm}), \tag{4.45}$$

and

$$P^{\gamma}(m_{\phi_i}) = 2 \sum_{\text{fermions}} N_c Q_f^2 C^P_{\phi_i f \overline{f}} \frac{v}{m_f} F_p(x_f). \tag{4.46}$$

F_W remains the same as in the SM case, see Eq. (2.108). We split the F_f into it's scalar and pseudo-scalar counterparts as

$$\begin{aligned} F_s(x_f) &= x_f [1 + (1 - x_f) f(x_f)], \\ F_p(x_f) &= \frac{f(x_f)}{x_f}, \end{aligned} \tag{4.47}$$

and the new charged scalar form factor contributions is

$$F_\pm(x_f) = x_f [x_f f(x_f) - 1]. \tag{4.48}$$

The function $f(x)$ is also unchanged from Eq. (2.108).

Scalar to Gluons: $\phi_i \to gg$ The $\phi_i \to gg$ decay loop remains the same; however, we may re-express it in the same general form as we did for the above.

$\phi_i \to gg$ Decay Width

$$\Gamma(\phi_i \to gg) = \frac{\alpha_s^2 m_{\phi_i}^3}{32\pi^3 v^2} K_S^g \left(|S^g(m_{\phi_i})|^2 + K_P^g |P^g(m_{\phi_i})|^2 \right). \tag{4.49}$$

In the heavy quark limit the QCD corrections are given below.

$$\begin{aligned} K_S^g &= 1 + \frac{\alpha_s(m_{\phi_i}^2)}{\pi} \left(\frac{95}{4} - \frac{7}{6} n_f \right), \\ K_P^g &= 1 + \frac{\alpha_s(m_{\phi_i}^2)}{\pi} \left(\frac{97}{4} - \frac{7}{6} n_f \right), \end{aligned} \tag{4.50}$$

where n_f is limited to the quark flavours for which $m_f < m_{\phi_i}$.

4.3.2 New Decays

Higgs to Vector Boson-Higgs Pair: $\phi_i \to V\phi_j$ The width of this new process is given below.

$\phi_i \to V\phi_j$ Decay Width

$$\Gamma(\phi_i \to V\phi_j) = \frac{|C_{\phi_i V \phi_j}|^2 m_V^2}{16\pi^2 m_\phi} \lambda\left(1, \frac{m_{\phi_i}^2}{m_V^2}, \frac{m_{\phi_j}^2}{m_V^2}\right) \lambda^{1/2}\left(1, \frac{m_V^2}{m_{\phi_i}^2}, \frac{m_{\phi_j}^2}{m_{\phi_i}^2}\right). \tag{4.51}$$

For an off-shell gauge boson we may have the decay $\phi_i \to V\phi_j \to \phi_j f_1 \overline{f}_2$. This decay width is given numerically in (21)-(22) of [47].

Higgs to Higgs-Higgs Pair: $\phi_i \to \phi_j\phi_k$ An important decay in the 2HDM is the three-point Higgs particle decay. The width is given below.

$\phi_i \to \phi_j\phi_j$ Decay Width

$$\Gamma(\phi_i \to \phi_j\phi_k) = (2 - \delta_{jk}) \frac{|C_{\phi_i\phi_j\phi_k}|^2}{32\pi} m_{\phi_i} \sqrt{\lambda(1, x_j, x_k)}. \tag{4.52}$$

Couplings for this decay can be read directly off a potential written in the Higgs basis as detailed in section 4.1.1.

4.3.3 Flavour-changing Decays

In Table 4.7 we have listed the FC decay allowed by the restricted Yukawa space and their corresponding couplings.

Due to the heavier masses of the b, s and c quarks the FC processes of the Higgs scalar that could provide a fingerprint for BSM physics are $h \to bs$ and $t \to ch$. Another interesting process is the leptonic $h \to \tau\mu$, but we do not discuss leptonic FC processes in this work.

The $h \to bs$ decay width at tree-level[39] , neglecting final state masses is given below.

39: Beyond tree-level, $h \to bs$ receives QCD corrections at NLO that may increase the rate by 10 – 20% [48].

$h \to bs$ Decay Width

$$\Gamma(h \to bs) \simeq \frac{3 m_h c_{\beta\alpha}^2}{16\pi} \left(|\hat{\varsigma}_{23}^D|^2 + |\hat{\varsigma}_{32}^D|^2\right). \tag{4.53}$$

Again, if we neglect the charm mass, the $t \to ch$ decay width at tree-level is given below.

$t \to ch$ **Decay Width**
$$\Gamma(t \to ch) \simeq \frac{m_t c_{\beta\alpha}^2}{32\pi} \left|\hat{\xi}_{32}^U\right|^2 \left(1 - \frac{m_h^2}{m_t^2}\right)^2 . \quad (4.54)$$

For the conjugate process $\bar{t} \to h\bar{c}$, $\hat{\xi}_{32}^U \mapsto \hat{\xi}_{23}^U$.

Decay	Yukawa's
$\phi^0 \to bs$	$\hat{\xi}_{23}^D, \hat{\xi}_{32}^D$
$t \to c\phi^0$	$\hat{\xi}_{32}^U$
$\phi^0 \to tc$	$\hat{\xi}_{23}^U, \hat{\xi}_{32}^U$
$t \to H^+ s$	$\hat{\xi}_{32}^{D*}, \hat{\xi}_{23}^U$
$H^+ \to \bar{b}t$	$\hat{\xi}_{33}^D, \hat{\xi}_{33}^{U*}$
$H^+ \to \bar{b}c$	$\hat{\xi}_{23}^D, \hat{\xi}_{32}^{U*}$
$H^+ \to \bar{s}t$	$\hat{\xi}_{32}^D, \hat{\xi}_{23}^{U*}$
$t \to H^+ b$	$\hat{\xi}_{33}^{D*}, \hat{\xi}_{33}^U$

Table 4.7: Notable FC processes in the general 2HDM involving $\phi^0 = h, A, A$ and H^+, with contributions from the Yukawa's of Eq. (4.39). Notice that the charged Higgs Yukawa's always appear in a pair with the CKM matrix, which we take here to be diagonal (but not in the numerical scan). For $h \to tc$ at least one of the quarks is off-shell.
40: In anticipation for the fits, detailed information about these processes as we use them is summarised in [49]

4.4 Flavour Processes in the 2HDM

Due to the suppressed nature of FC processes in the SM, the FC observables are highly sensitive to NP contributions. FC processes will depend on our Yukawa couplings, which in the Type-III are not restricted by symmetry and in the Z_2-aligned models are proportional to $\tan\beta$ as described in table 4.3. In this section we prepare our understanding of the FC processes that we include as constraints in our global fits that we are yet to speak about. The first two subsections will detail meson mixing and radiative B-decay processes. We apply the constraints from both these processes on both the type-III and Z_2-aligned models. As such we detail them significantly, and explore the available parameter space of B_s meson mixing processes in the type-III model. The third section describes leptonic processes. This is done with much more brevity and we provide references to more detailed descriptions[40] . We fit the leptonic processes just to Z_2-aligned 2HDM models. There has been much previous work done fitting flavor physics anomalies with the 2HDM, particularly the Type-II model. Some notable works include [50], [46], [51], [52].

4.4.1 Effective Field Theory for Flavour Physics Observables

We use an effective field theory approach to compute flavour observables. Section 2.6 introduces EFT methods. Flavour processes may be categorised by groups of operators known as classes [22]. Using flavour quantum numbers, it is convenient to classify operators into classes that cannot mix. These classes follow a basis structure [41] as is introduced in Ref. [53]. Each entry of the basis has the form

$$O_i = (\overline{\psi_1} P_R (X_i)_\mu \psi_2)(\overline{\psi_3} (X_i)^\mu \psi_4), \quad (4.55)$$

41: The basis consists of ten operators with another ten that are obtained by flipping chirality.

Class	Flavour Structure	Class Quantum Number
I	$\bar{s}b\bar{s}b, \bar{d}b\bar{d}b$	$\lvert\Delta B\rvert = 2$
II	$\bar{u}b\bar{l}\nu_{l'}, \bar{c}b\bar{l}\nu_{l'}$	$\lvert\Delta B\rvert = 1$
III	$\bar{s}b\bar{u}c, \bar{s}b\bar{c}u$ $\bar{d}b\bar{u}c, \bar{d}b\bar{c}u$	$\lvert\Delta B\rvert = \lvert\Delta C\rvert = 1$
IV	$\bar{s}b\bar{s}d, \bar{d}b\bar{d}s$ $\bar{b}s\bar{b}d$	$\lvert\Delta B\rvert = 1, \lvert\Delta S\rvert = 2$
V	$\bar{s}b\bar{q}q, \bar{d}b\bar{q}q$ $\bar{s}bF, \bar{d}bF$ $\bar{s}bG, \bar{d}bG$ $\bar{s}b\bar{l}, \bar{d}b\bar{l}l$	$\lvert\Delta B\rvert = 1, \lvert\Delta C\rvert = 0$

Table 4.8: Operator Classes I-V. We do not include Lepton or Baryon Number Violating operator sets (Classes VI and VII, respectively.) In class V we have $F^{\mu\nu}$ and $G^{\mu\nu}$ which construct the magnetic penguin operators.

where

$$(X_i)_\mu = (\gamma_\mu, \gamma_\mu T^A, \gamma_{\mu\nu\rho}, \gamma_{\mu\nu\rho} T^A, I, T^A, \sigma^{\mu\nu}, \sigma^{\mu\nu} T^A, \gamma_{\mu\nu\rho\sigma}, \gamma_{\mu\nu\rho\sigma} T^A). \tag{4.56}$$

The classes are identified by the various ψ_i, given in Table 4.8. The exception to this basis designation above is Class I. This class structure covers all possible operators and there is a possibility of Fierz-equivalent pairs, in which case we remove one from the pair. Calculations do not always follow the same notation as this but calculations will always be limited to the designated class.

4.4.2 Meson Mixing

Oscillations amongst the neutral mesons $M^0 - \overline{M}^0$ lead to some intriguing observables. The M^0 and barred meson $\overline{M}^0$ do not share the same mass or indeed the same width.

The down sector mesons for which the analysis is interesting are $M = B_s^0$ and B_d^0 mesons, the K^0 (Kaon) and also the D^0 meson. The latter of these two requires that we use the complete set of *extra* Yukawa couplings as the couplings always enter the process calculation with a term that is otherwise zero in the *restricted* set. As such, we focus our discussions to the B_s^0 and B_d^0 mesons; but mention the Kaon and the D^0 meson when calculations are applicable to these as well. A study with the Kaon and the D^0 meson is an interesting extension as the mixing processes yield smaller SM predictions and in turn, are more sensitive to BSM physics contributions.

4.4.2.1 Meson Mixing: Calculation of Observables

Following Refs. [54] and [55], we may define our mixed meson state

$$\psi = \begin{pmatrix} M^0 \\ \overline{M}^0 \end{pmatrix}. \tag{4.57}$$

The Schrodinger equation for meson mixing is

$$i\frac{d}{dt}\psi = (\mathbf{M} - \frac{i}{2}\blacksquare)\psi, \tag{4.58}$$

where $\mathbf{M}$ and $\blacksquare$ are Hermitian. Upon expansion of this we have

$$\begin{aligned}(\mathbf{M} - \frac{i}{2}\blacksquare)\psi = m^{(0)}_{M^0}\delta_{ij} + \frac{\langle M^0|\mathscr{H}^{|\Delta B|=2}|\overline{M}^0\rangle}{2m_{M^0}} \\ + \frac{1}{2m_{M^0}}\sum_f \frac{\langle M^0|\mathscr{H}^{|\Delta B|=2}|f\rangle\langle f|\mathscr{H}^{|\Delta B|=2}|\overline{M}^0\rangle}{m^{(0)}_{M^0} - E_f + i\epsilon},\end{aligned} \tag{4.59}$$

where $\mathscr{H}^{|\Delta B|=2}$ is the Hamiltonian for $|\Delta B| = 2$ processes. We will state it explicitly for meson-mixing later. The first term

$$m^{(0)}_{M^0}\delta_{ij}, \tag{4.60}$$

corresponds to the time evolution of the mass, and does not affect the meson oscillation. This term does not contribute to our FC processes.

The next term

$$\frac{\langle M^0|\mathscr{H}^{|\Delta B|=2}|\overline{M}^0\rangle}{2m_{M^0}}, \tag{4.61}$$

contains all of the flavour oscillation processes. These are known as short-range off-shell (dispersive) and encoded in the $\mathbf{M}$ matrix. We will be interested in the off-diagonal contributions.

The final term

$$\frac{1}{2m_{M^0}}\sum_f \frac{\langle M^0|\mathscr{H}^{|\Delta B|=2}|f\rangle\langle f|\mathscr{H}^{|\Delta B|=2}|\overline{M}^0\rangle}{m^{(0)}_{M^0} - E_f + i\epsilon}, \tag{4.62}$$

describes flavour oscillations that occur due to hadronic intermediate states, which are long-range. These are on-shell (absorptive) processes and compose the $\blacksquare$ matrix.
For B_s and B_d mixing we may ignore absorptive long-range effects as they are negligible and as such the mass splitting is derived only from $\mathbf{M}$.

The physical mass splitting is then

$$\Delta M = 2|M_{12}|. \tag{4.63}$$

where M_{12} is the off-diagonal element of M.

Consulting the EFT, it is possible to describe all meson mixing processes using the closed basis of operators of class I ($|\Delta B| = 2$), given by

$$\begin{aligned} O_1 &= (\overline{\psi}_{1\alpha}\gamma^\mu P_L \psi_{2\alpha})(\overline{\psi}_{3\beta}\gamma^\mu P_L \psi_{4\beta}), \\ O_2 &= (\overline{\psi}_{1\alpha} P_L \psi_{2\alpha})(\overline{\psi}_{3\beta} P_L \psi_{4\beta}), \\ O_3 &= (\overline{\psi}_{1\alpha} P_L \psi_{2\beta})(\overline{\psi}_{3\beta} P_L \psi_{4\alpha}), \\ O_4 &= (\overline{\psi}_{1\alpha} P_L \psi_{2\alpha})(\overline{\psi}_{3\beta} P_R \psi_{4\beta}), \\ O_5 &= (\overline{\psi}_{1\alpha} P_L \psi_{2\beta})(\overline{\psi}_{3\beta} P_R \psi_{4\alpha}), \end{aligned} \tag{4.64}$$

where we have explicitly denoted the colour indices α and β. By flipping the chirality of the operator basis $L \to R$ we construct the primed operator basis $O_i^{'}$ for $i = 1, 2, 3$. The operators O_4 and O_5 are equivalent under such a flip. Making use of the γ matrix identities, the chirality of the particles is related to the projection operators through

$$\overline{\psi} P_L \psi = \overline{\psi_R}\psi_L, \quad \overline{\psi} P_R \psi = \overline{\psi_L}\psi_R. \tag{4.65}$$

Recall that a chirality flip of ψ occurs through an interaction with a scalar particle.
The effective Hamiltonian for the class I operator may be constructed as

$$\mathscr{H}_{\text{eff}}^{|\Delta B|=2} = -\sum_{i=1}^{5} C_i(\mu)\, O_i(\mu) - \sum_{i=1}^{3} C_i'(\mu)\, O_i'(\mu). \tag{4.66}$$

Notice that in the effective Hamiltonian above we have factored out the conventional factor[42] that arises from the W boson loops. We include this factor as necessary.

42: The factor is $-\lambda_c^{ab}\frac{4G_F}{\sqrt{2}}$, where λ_c^{ab} is composed of the CKM values.

Relating the effective Hamiltonian to the off-diagonal elements of the interaction matrix

$$M_{12} = \frac{\langle M^0 | \mathscr{H}_{\text{eff}}^{|\Delta B|=2} | \overline{M}^0 \rangle}{2m_{M^0}}, \tag{4.67}$$

with the matrix element of the Hamiltonian

$$\langle M^0 | \mathscr{H}_{\text{eff}}^{|\Delta B|=2} | \overline{M}^0 \rangle = \sum_i C_i(\mu)\, \langle M_q^0 | O_i(\mu) | \overline{M_q^0} \rangle. \tag{4.68}$$

The matrix element of the operator i

$$\langle M^0 | O_i(\mu) | \overline{M}^0 \rangle \tag{4.69}$$

contains all the QCD effects [56] and is thus highly sensitive to constants derived from QCD simulations. This matrix element may be

evaluated for meson-mixing to give

$$\begin{aligned}\langle M^0|O_1(\mu)|\overline{M}^0\rangle &= b_1\, m^2_{M^0} f^2_{M^0} B_i^{M^0}(\mu),\\ \langle M^0|O_i(\mu)|\overline{M}^0\rangle &= b_i\, \chi^{M^0}\, m^2_{M^0} f^2_{M^0} B_i^{M^0}(\mu),\end{aligned} \tag{4.70}$$

with $i = 2,3,4,5$ covering class I and where

$$\begin{aligned}\vec{b} &= \{8/3,\ -5/3,\ 1/3,\ 2,\ 2/3\},\\ \chi^{M^0}(\mu) &= \frac{m^2_{M^0}}{(m_{q_1}(\mu)+m_{q_2}(\mu))^2},\end{aligned} \tag{4.71}$$

f_{M^0} are decay constants, m_{M^0} are meson masses and $B_i^{B_s}, B_i^{B_d}$ are bag factors. In the χ_{M^0} function, q_1 and q_2 are the quark constituents of the meson. All of the quantities needed for the calculation of the operator matrix element may be found in Appendix F.2.

Additionally, to the mass-splitting, we may also measure the mixing phase for meson-mixing processes. This is given as

$$\beta_q = \arg(\langle M^0|\mathscr{H}_{\text{eff}}^{|\Delta B|=2}|\overline{M}^0\rangle). \tag{4.72}$$

4.4.2.2 Meson Mixing: SM Calculation

Beginning with the contribution from the SM, we find that only the O_1 operator is present. The remaining operators require a chirality flip between quarks of the same charge Q at tree-level[43] , which is not possible in the SM. The form of C_1, as shown in Figure 2.6, for a loop with off-shell top-quarks is [57]

43: This would need to be a chirality flip mediated by a neutral particle.

$$C_1^{\text{SM}}(\mu_W) = \frac{G_F^2}{32\pi^2}(\lambda_t^{B_q^0})^2 M_W^2 \hat{\eta}_B S\left(\frac{m_t^2}{m_W^2}\right). \tag{4.73}$$

where $\hat{\eta}_B(\mu_B) = 0.8393$ is the scale-dependent QCD factor (calculated at NLO in section XIII of Ref. [58]) and S is the Inami-Lim function [59] which grasps the electroweak loop contributions. The superscript on the CKM factor λ refers to the particles within the meson (e.g. $\lambda^{B_s^0} = \lambda^{bs}$). There is no contribution to C_1' in the SM. We also ignore all diagrams with off-shell charm or up quarks as these are negligible. The resultant mass splitting is then

$$\Delta M_{B_q^0} = \frac{G_F^2}{3\pi^2}(\lambda_t^{B_q^0})^2 M_W^2 \hat{\eta}_B S\left(\frac{m_t^2}{m_W^2}\right) m_{B_q^0} f^2_{B_q^0} B_1^{B_q^0}. \tag{4.74}$$

The arising combination of $(\hat{\eta}B)$ is a scale as well as scheme independent quantity. In our calculations we will always quote the scale dependent QCD factors $\hat{\eta}$ and scale dependent bag-factors B. The Wilson coefficient in (4.73) is evaluated at the matching scale $\mu = m_W$.

Before calculating our observable matrix element we must use RG evolution to run this to the meson scale $\mu_B \sim 4.2$ GeV (the mass of the bottom quark). This is done in the $\hat{\eta}(\mu_B)$ quantity in this case, such that

$$C_1(\mu_B) = \hat{\eta}(\mu_B) C_1(\mu_W). \tag{4.75}$$

Putting this together

$$\langle B_s^0 | \mathscr{H}_{\text{eff}}^{|\Delta B|=2} | \overline{B}_s^0 \rangle_{\text{SM}} = (7.08 - 0.26i) \times 10^{-11} \text{ GeV}, \tag{4.76}$$

which gives[44]

$$\Delta M_{B_s^0} = (1.32 \pm 0.08) \times 10^{-11} \text{ GeV}, \tag{4.77}$$

44: This translates to $\Delta M_{B_s^0} = 20.06 \pm 1.22 \text{ps}^{-1}$ which aligns with the calculated value from Ref. [60].

where we have included the theoretical error from the combination of QCD errors as laid out in Table II of Ref. [60]. The matrix element for B_d meson mixing in the SM (at $\mu = \mu_B$) is

$$\langle B_d^0 | \mathscr{H}_{\text{eff}}^{|\Delta B|=2} | \overline{B}_d^0 \rangle_{\text{SM}} = (1.34 - 1.29i) \times 10^{-12} \text{ GeV}, \tag{4.78}$$

which gives

$$\Delta M_{B_d^0} = (3.36 \pm 0.34) \times 10^{-13} \text{ GeV}, \tag{4.79}$$

we choose an arbitrary theoretical error of (10%) here, which is based upon the QCD error for $\Delta M_{B_s^0}$ while being conservative.

The calculated SM meson-mixing phase for the $B_s^0 - \overline{B}_s^0$ mixing is

$$\beta_s = (1.82 \pm 0.11) \times 10^{-2} \text{rad}, \tag{4.80}$$

where the theoretical error is again from Ref. [60].

4.4.2.3 Meson Mixing: 2HDM Contributions

The new scalars $(H^0, A^0, H^\pm)$ of the 2HDM contribute to the $M_q^0 = B_s^0, B_{d'}^0, K^0$ and D^0 meson mixing processes. At tree-level, these meson mixing processes are mediated via neutral scalars, as shown in Figure 4.1 for B_s^0 meson mixing. Beyond tree-level, the meson mixing processes have contributions from neutral and charged scalar particles through box diagrams, as shown in Figure 4.2 and Figure 4.3, again for for B_s^0 meson mixing. The Wilson coefficients may be written

$$\begin{aligned}
C_1 &= C_1^{\text{SM}} + C_1^{\text{NB}} + C_1^{\text{CB}} + C_1^{\text{CGB}}, \\
C_2 &= C_2^{\text{T}} + C_2^{\text{NB}} + C_2^{\text{CB}}, \\
C_3 &= 0, \\
C_4 &= C_4^{\text{T}} + C_4^{\text{NB}} + C_4^{\text{CB}} + C_4^{\text{CGB}}, \\
C_5 &= C_5^{\text{NB}} + C_5^{\text{CB}},
\end{aligned} \tag{4.81}$$

with primed coefficients

$$\begin{aligned} C_1' &= C_1^{\mathrm{NB}'} + C_1^{\mathrm{CB}'} + C_1^{\mathrm{CGB}'}, \\ C_2' &= C_2^{\mathrm{T}'} + C_2^{\mathrm{NB}'} + C_2^{\mathrm{CB}'}, \\ C_3' &= 0, \end{aligned} \tag{4.82}$$

where the superscript T, NB, CB and CGB refer to tree-level, neutral-box, charged-box, charged-gauge-box processes respectively. Expressions for the Wilson coefficients at the matching scale μ_W are given below[46]. The Wilson coefficients have been calculated in the R_ξ-gauge.

Again the Wilson coefficients are evaluated at the matching scale $\mu = m_W$ and must be run to $\mu_B \sim 4.2$ GeV. We do this using the evolution matrix calculated according to Eq. (2.123). The numerical calculation of the evolution matrix for class I is done by DSIXTOOLS and may be found in Appendix F.2.

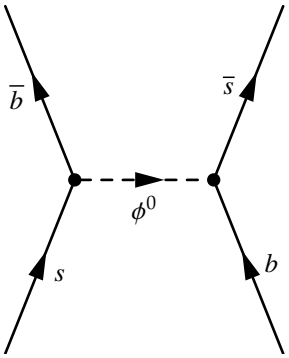

Figure 4.1: The tree-level meson mixing contribution from neutral scalars.

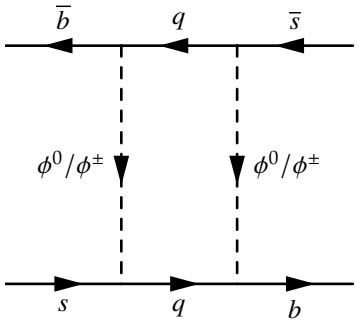

Figure 4.2: The neutral/charged scalar box meson mixing contribution.

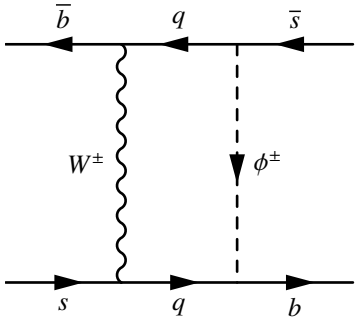

Figure 4.3: The charged scalar gauge boson box meson mixing contribution.

Tree-Level Neutral Contributions The scalar particles h^0, H^0 and A^0 contribute to the neutral contribution of the meson mixing processes of B_s^0, B_d^0, K^0 and D^0 as shown in Figure 4.1. The Wilson coefficients are

$$\begin{aligned} C_2^{\mathrm{T}}(\mu_W) &= \sum_{k=1}^{3} -\frac{1}{2m^2_{\phi_k^0}} \left(\Gamma^{LR,\phi_k^0 \star}_{q_2 q_1}\right)^2, \\ C_2^{\mathrm{T}'}(\mu_W) &= \sum_{k=1}^{3} -\frac{1}{2m^2_{\phi_k^0}} \left(\Gamma^{LR,\phi_k^0}_{q_1 q_2}\right)^2, \\ C_4^{\mathrm{T}}(\mu_W) &= \sum_{k=1}^{3} -\frac{1}{m^2_{\phi_k^0}} \Gamma^{LR,\phi_k^0}_{q_1 q_2} \Gamma^{LR,\phi_k^0 \star}_{q_2 q_1}, \end{aligned} \tag{4.83}$$

where $\phi_k^0 = (h^0, H^0, A^0)$ and $q_1 = s, q_2 = b(d)$ for $B_s^0(B_d^0)$ - mixing.

Neutral/Charged Box Contributions The neutral scalar particles h^0, H^0 and A^0 have a non-negligible contribution only to the $D^0 - \overline{D^0}$ meson mixing process. As we do not focus on D^0 meson mixing, we ignore neutral-box contributions here.

The box diagram contributions to B_s^0, B_d^0 and K^0 meson mixing processes are from the charged scalar H^+. This process is displayed in Figure 4.2, the internal quarks (labelled as q) represent the allowed states, in this case, $q = u, c, t$.

$$
\begin{aligned}
C_1^{\mathrm{CB}}(\mu_W) &= \frac{-1}{128\pi^2}\sum_{k=1}^{3}\sum_{j=1}^{3}\Gamma^{RL\,H^+\star}_{u_j d_2}\Gamma^{RL\,H^+}_{u_j d_3}\Gamma^{RL\,H^+\star}_{u_k d_2}\Gamma^{RL\,H^+}_{u_k d_3} \\
&\quad\times D_2\left(m_{u_j}^2, m_{u_k}^2, m_{H^\pm}^2, m_{H^+}^2\right), \\
C_2^{\mathrm{CB}}(\mu_W) &= \frac{-1}{32\pi^2}\sum_{k=1}^{3}\sum_{j=1}^{3} m_{u_j} m_{u_k}\Gamma^{LR\,H^+\star}_{u_j d_2}\Gamma^{RL\,H^+}_{u_j d_3}\Gamma^{LR\,H^+\star}_{u_k d_2}\Gamma^{RL\,H^+}_{u_k d_3} \\
&\quad\times D_0\left(m_{u_j}^2, m_{u_k}^2, m_{H^\pm}^2, m_{H^\pm}^2\right), \\
C_4^{\mathrm{CB}}(\mu_W) &= \frac{-1}{16\pi^2}\sum_{k=1}^{3}\sum_{j=1}^{3} m_{u_j} m_{u_k}\Gamma^{LR\,H^+\star}_{u_j d_2}\Gamma^{RL\,H^+}_{u_j d_3}\Gamma^{RL\,H^+\star}_{u_k d_2}\Gamma^{LR\,H^\pm}_{u_k d_3} \\
&\quad\times D_0\left(m_{u_j}^2, m_{u_k}^2, m_{H^\pm}^2, m_{H^\pm}^2\right), \\
C_5^{\mathrm{CB}}(\mu_W) &= \frac{1}{32\pi^2}\sum_{k=1}^{3}\sum_{j=1}^{3}\Gamma^{LR\,H^+\star}_{u_j d_2}\Gamma^{LR\,H^+}_{u_j d_3}\Gamma^{RL\,H^+\star}_{u_k d_2}\Gamma^{RL\,H^+}_{u_k d_3} \\
&\quad\times D_2\left(m_{u_j}^2, m_{u_k}^2, m_{H^\pm}^2, m_{H^\pm}^2\right),
\end{aligned}
$$

where D_0 and D_2 are loop functions given in the Appendix of Ref. [46]. For the case in which a gauge boson enters as one of the particles in the loop (Figure 4.3) we have the corresponding contributions to the Wilson coefficients

$$
\begin{aligned}
C_1^{\mathrm{CGB}}(\mu_W) &= \frac{(g')^2}{32\pi^2}\sum_{j,k=1}^{3}\left(m_{u_j} m_{u_k} V_{j2}^\star V_{k3}\Gamma^{RL\,H^+}_{u_j d_3}\Gamma^{RL\,H^+\star}_{u_k d_2}\right. \\
&\quad\left.\times\frac{4M_W^2 D_0\left(M_W^2, m_{H^\pm}^2, m_{u_j}^2, m_{u_k}^2\right) - D_2\left(M_W^2, m_{H^\pm}^2, m_{u_j}^2, m_{u_k}^2\right)}{4M_W^2}\right), \\
C_4^{\mathrm{CGB}}(\mu_W) &= \frac{(g')}{32\pi^2}\sum_{j,k=1}^{3}\left(V_{j3} V_{k2}^\star\Gamma^{LR\,H^+\star}_{u_j d_2}\Gamma^{LR\,H^+}_{u_k d_3}\right. \\
&\quad\left.\times\frac{C_2\left(\xi M_W^2, m_{H^\pm}^2, m_{u_j}^2\right) - C_2\left(m_{H^\pm}^2, m_{u_j}^2, m_{u_k}^2\right) + m_{u_k}^2 C_0\left(\xi M_W^2, m_{H^\pm}^2, m_{u_k}^2\right)}{M_W^2}\right).
\end{aligned}
\tag{4.84}
$$

Note here that $C_0(m_1^2, m_2^2, m_3^2)$ and $C_2(m_1^2, m_2^2, m_3^2)$ are loop functions which may be found in the Appendix of [46]. The gauge-dependent ξ term that appears in C_4^{CGB} is chosen to be one for simplicity (Feynman t'Hooft gauge choice).

4.4.2.4 On the Discrepancy within the Two-Higgs-Doublet Model

There is a 1.8σ deviation between the calculated SM value and the observed value for $\Delta M_{B_s^0}$. Let us look at the parameter space in the 2HDM type-III model that can explain the deviation. This argument is taken directly from our published work [61]. Notice that the 2HDM contribution can partially cancel the SM contribution, and therefore yield a better agreement with the lower observed value. For degener-

ate H and A as expected from EWPO, the tree-level contributions to the Wilson coefficients give

$$\begin{aligned}
&\Delta M_{B_s,\,\text{2HDM tree-level}} \\
&= C_2(\mu_b)\langle O_2\rangle + C_2'(\mu_b)\langle O_2\rangle + C_4'(\mu_b)\langle O_4\rangle, \\
&= -A_B\left\{\frac{1}{4}c_{\beta\alpha}^2\left[\frac{1}{m_h^2}-\frac{1}{m_H^2}\right]\left((U_{22}B_2^{B_s}b_2+U_{32}B_3^{B_s}b_3)(\hat{\xi}_{32}^{D\star 2}+\hat{\xi}_{23}^{D\,2})\right.\right. \\
&\left.\left.+2U_{44}B_4^{B_s}b_4\hat{\xi}_{23}^{D}\hat{\xi}_{32}^{D\star}\right)+\frac{1}{m_H^2}U_{44}B_4^{B_s}b_4\hat{\xi}_{23}^{D}\hat{\xi}_{32}^{D\star}\right\},
\end{aligned} \tag{4.85}$$

where we have defined $A_B \equiv f_{B_s}^2\, M_{B_s}^3/(4\,(m_b+m_s)^2) \simeq 0.105\,\text{GeV}^3$, and U_{ij} are elements of the evolution matrix are given in Appendix F.2.

We plot ΔM_{B_s} (including the 2HDM contribution both at tree and loop-level) versus $|\hat{\xi}_D^{32}|$ for different fixed values of $\hat{\xi}_D^{23}$, m_A and $s_{\beta\alpha}$. In the first two plots, we fix $m_H = m_A = 200$ GeV and $\hat{\xi}_{23}^D = (\pm 1 \pm i)\times 10^{-4}$ and plot $s_{\beta\alpha} = 0.9$ in Figure 4.4 and $s_{\beta\alpha} = 0.99$ in Figure 4.5. Under this setup we can fit the experimental observation for the intervals $|\hat{\xi}_{32}^D| \sim [2\times 10^{-4}, 5\times 10^{-3}]$ for both $s_{\beta\alpha}$. The total allowed interval is discontinuous and a second region as large as $|\hat{\xi}_{32}^D| \sim 3.5\times 10^{-2}$ is allowed for $s_{\beta\alpha} = 0.99$. We can see that $|\hat{\xi}_{32}^D| \sim 3.6\times 10^{-2}$ is the largest Yukawa we expect for $s_{\beta\alpha} \leq 0.99$. In the next two plots we fix $m_H = m_A = 2000$ GeV and a Yukawa of $\hat{\xi}_{23}^D = (\pm 1 \pm i)\times 10^{-3}$. We plot $s_{\beta\alpha} = 0.9$ in Figure 4.6 and $s_{\beta\alpha} = 0.99$ in Figure 4.7. For the case where $s_{\beta\alpha} = 0.99$ we can attain a Yukawa as large as $|\hat{\xi}_{32}^D| \sim 1.6\times 10^{-2}$. We have also checked that in these regions the 2HDM is able to satisfy the observed value of the B_s^0–$\overline{B}_s^0$ mixing phase.

The 2HDM explanation of the discrepancy in terms of the tree-level contribution, also implies a prediction of $\text{BR}(h\to bs)$. For degenerate H, A, and much heavier than the light Higgs scalar, the latter contribution to meson mixing dominates in Eq. (4.85). This is true unless $c_{\beta\alpha} \simeq 0$, for which in any case there is no contribution to $\text{BR}(h\to bs)$. Assuming a hierarchy in the off-diagonal Yukawa's (taken to be real), for example $\hat{\xi}_{32}^D \gg \hat{\xi}_{23}^D$, so that the C_2 contribution to $\Delta M_{B_s,\text{2HDM}}$ dominates (and the mixed C_4 contribution can be neglected) we get from Eqs. (4.53) and Eq. (4.85)

$$\begin{aligned}
\text{BR}(h\to bs) &\simeq \frac{3m_h^3 m_H^2}{16\pi\Gamma_h(m_H^2-m_h^2)}\,\frac{|\Delta M_{B_s,\text{2HDM}}|}{A_B\,|U_{22}B_2^{B_s}\,b_2+U_{32}B_3^{B_s}\,b_3|} \\
&\simeq 2.1\times 10^{-4},
\end{aligned} \tag{4.86}$$

where we used $\Delta M_{B_s,\text{2HDM}} = \Delta M_{B_s,\text{obs}} - \Delta M_{B_s,\text{SM}}$, and $\Gamma_h \simeq 4.07\cdot 10^{-3}$ GeV. The prediction is identical if the other Yukawa dominates, $\hat{\xi}_{32}^D \ll \hat{\xi}_{23}^D$, so that C_2' dominates. On the other hand, for equal Yukawa's $\hat{\xi}_{32}^D = \hat{\xi}_{23}^D$, the mixed C_4 contribution cannot be neglected, and there is an extra term proportional to $U_{44}B_4^{B_s}b_4$ inside the denominator of

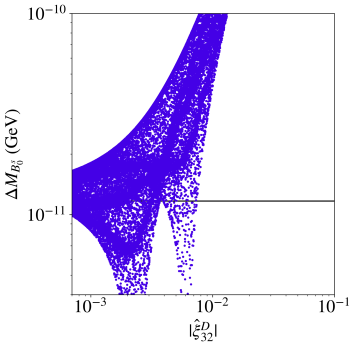

Figure 4.4: ΔM_{B_s} in the 2HDM versus $|\hat{\xi}_{32}^D|$. The horizontal line shows the observed value (the corresponding error is smaller than the width of the line itself). Here we set $s_{\beta\alpha} = 0.9$, $m_H = m_A = 200$ GeV, $\hat{\xi}_{23}^D = (\pm 1 \pm i)\times 10^{-4}$.

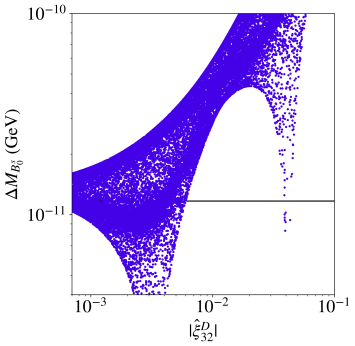

Figure 4.5: Same as Figure 4.4, however, here we set $s_{\beta\alpha} = 0.99$, $m_H = m_A = 200$ GeV, $\hat{\xi}_{23}^D = (\pm 1 \pm i)\times 10^{-4}$.

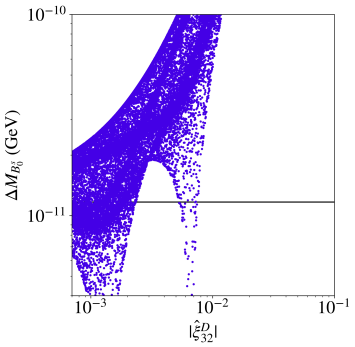

Figure 4.6: Same as Figure 4.4, however, here we set $s_{\beta\alpha} = 0.9$, $m_H = m_A = 2000$ GeV, $\hat{\xi}_{23}^D = (\pm 1 \pm i)\times 10^{-3}$.

Eq. (4.86), so that $\mathrm{BR}(h \to bs) \simeq 6.3 \times 10^{-5}$. As the angle $\beta - \alpha$ approaches $\pi/2$ this lower limit grows. We confirm these predictions in Figures 4.8 and 4.9, where we only have the SM plus the 2HDM tree-level contributions. In these figures we throw random points and see that may more easily reach lower values of $\mathrm{BR}(h \to bs)$ in the case of $\hat{\xi}^D_{23} = \hat{\xi}^D_{32}$. In case the reader is left wondering, the solid-like lines that appear on these plots are areas where corresponding values for $\mathrm{BR}(h \to bs)$ and ΔM_{B_s} were most frequently found. The horizontal solid-like line, for example, represents the value of ΔM_{B_s} as the off-diagonal Yukawa's tend to zero.

We therefore conclude, that, if the observed discrepancy is confirmed, if accommodated in a 2HDM with negligible contributions at loop-level, it implies a prediction of $\mathrm{BR}(h \to bs) \simeq 10^{-5} - 10^{-4}$. This motivates a 2HDM type-III scan to confirm the validity of our estimation and to investigate the features of a possibly accommodating parameter space.

Briefly commenting on Z_2-aligned models, there will be different behaviour depending on the model type. Taking the type-II and type-Y models into consideration we find that the process is proportional as ct^4_β and ct^2_β from the charged scalar-boxes and mixed charged scalar and W boxes, respectively. Additionally, the meson mixing process is inversely proportional to the heavy scalars masses. This combination and the fact that an enhancement to the process improves the agreement between SM and observed values means that we expect a clear best-fit somewhere along the $m_{H^{pm}}$ vs t_β plane.

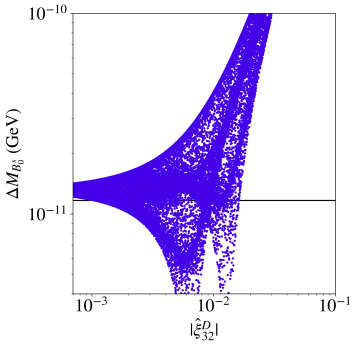

Figure 4.7: Same as Figure 4.4, however, here we set $s_{\beta\alpha} = 0.99$, $m_H = m_A = 2000$ GeV, $\hat{\xi}^D_{23} = (\pm 1 \pm i) \times 10^{-3}$.

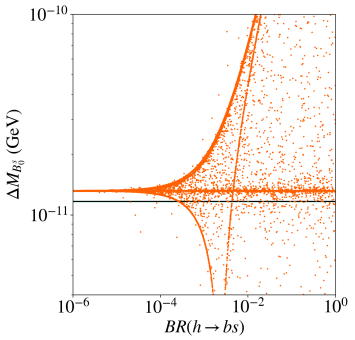

Figure 4.8: Mass splitting ΔM_{B_s} (from the SM and the 2HDM at tree-level) versus $\mathrm{BR}(h \to bs)$. We set $m_H = m_A = 2000$ GeV and $s_{\beta\alpha} = 0.9$. The horizontal line shows the observed value (the corresponding error is smaller than the width of the line itself). In this case, $\hat{\xi}^D_{23} \gg \hat{\xi}^D_{32}$, or $\hat{\xi}^D_{23} \ll \hat{\xi}^D_{32}$.

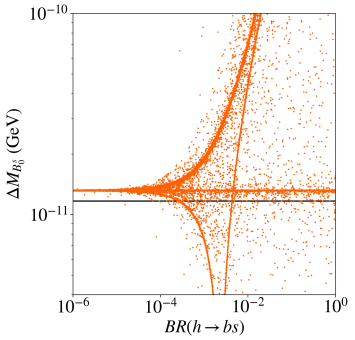

Figure 4.9: Same as Figure 4.8, but with $\hat{\xi}^D_{23} = \hat{\xi}^D_{32}$. We see lower values of $\mathrm{BR}(h \to bs)$ being more accessible for this case.

4.4.3 Radiative B Decays

A process that could provide us with clues of NP is the $b \to s\gamma$ decay channel. It is sensitive to FC currents, but more enticingly it occurs at a QCD order of α_{QCD}, resulting in a more prominent width. Other FC sensitive photon/lepton processes occur at α^2_{QCD} and as such are suppressed.

The radiative $b \to s\gamma$ decays process belongs to the class V operator set. For the calculation of radiative B decays it is common to use the

basis chosen in Ref. [62]

$$
\begin{aligned}
O_1 =& (\bar{s}_L \gamma_\mu T^a c_L)\,(\bar{c}_L \gamma^\mu T_a b_L)\,, \\
O_2 =& (\bar{s}_L \gamma_\mu c_L)\,(\bar{c}_L \gamma^\mu b_L)\,, \\
O_3 =& (\bar{s}_L \gamma_\mu b_L) \sum_{q=u,d,s,b,c} (\bar{q} \gamma^\mu q)\,, \\
O_4 =& (\bar{s}_L \gamma_\mu T^a b_L) \sum_{q=u,d,c} (\bar{q} \gamma^\mu T_a q)\,, \\
O_5 =& (\bar{s}_L \gamma_\mu \gamma_\nu \gamma_\rho b_L) \sum_{q=u,d,s,b,c} (\bar{q} \gamma^\mu \gamma^\nu \gamma^\rho q)\,, \\
O_6 =& (\bar{s}_L \gamma_\mu \gamma_\nu \gamma_\rho T^a b_L) \sum_{q=u,d,c} (\bar{q} \gamma^\mu \gamma^\nu \gamma^\rho T_a q)\,, \\
O_7 =& \frac{\alpha_s}{16\pi^2}\, \overline{m}_b(\mu)\, (\bar{s}_L \sigma^{\mu\nu} b_R)\, F_{\mu\nu}\,, \\
O_8 =& \frac{\alpha_{\mathrm{EM}}}{16\pi^2}\, \overline{m}_b(\mu)\, (\bar{s}_L \sigma^{\mu\nu} T^a b_R)\, G^a_{\mu\nu}\,,
\end{aligned}
\tag{4.87}
$$

where T^a ($a = 1, 8$) are $SU(3)$ colour generators and α_s and α_{EM} are the strong and electromagnetic coupling constants, respectively. In the occurrence of $q = s, b$ the operator O_4 is Fierz equivalent to O_3 and similarly O_6 is Fierz equivalent to O_5. As such, each Fierz equivalent pair makes only one appearance in the basis above. In this form the chiralities of the particles are explicitly stated.

In the 2HDM we also have the primed operators [63]

$$
\begin{aligned}
O_1' =& (\bar{s}_R \gamma_\mu T^a c_R)\,(\bar{c}_R \gamma^\mu T_a b_R)\,, \\
O_2' =& (\bar{s}_R \gamma_\mu c_R)\,(\bar{c}_R \gamma^\mu b_R)\,, \\
O_3' =& (\bar{s}_R \gamma_\mu b_R) \sum_{q=u,d,s,b,c} (\bar{q} \gamma^\mu q)\,, \\
O_4' =& (\bar{s}_R \gamma_\mu T^a b_R) \sum_{q=u,d,c} (\bar{q} \gamma^\mu T_a q)\,, \\
O_5' =& (\bar{s}_R \gamma_\mu \gamma_\nu \gamma_\rho b_R) \sum_{q=u,d,s,b,c} (\bar{q} \gamma^\mu \gamma^\nu \gamma^\rho q)\,, \\
O_6' =& (\bar{s}_R \gamma_\mu \gamma_\nu \gamma_\rho T^a b_R) \sum_{q=u,d,c} (\bar{q} \gamma^\mu \gamma^\nu \gamma^\rho T_a q)\,, \\
O_7' =& \frac{\alpha_s}{16\pi^2}\, \overline{m}_b(\mu)\, (\bar{s}_R \sigma^{\mu\nu} b_L)\, F_{\mu\nu}\,, \\
O_8' =& \frac{\alpha_{\text{EM}}}{16\pi^2}\, \overline{m}_b(\mu)\, (\bar{s}_R \sigma^{\mu\nu} T^a b_L)\, G^a_{\mu\nu}\,.
\end{aligned}
\tag{4.88}
$$

Where unless explicitly stated everything in the calculation applies to both the primed and unprimed operators. The effective Hamiltonian for this operator set is then given as

$$
\mathcal{H}_{\text{eff}} = \frac{4G_F}{\sqrt{2}} \lambda_t^{bs} \left(\sum_{i=1}^{8} C_i(\mu) O_i(\mu) + \sum_{i=1}^{8} C_i'(\mu) O_i'(\mu) \right). \tag{4.89}
$$

For this calculation we have included the conventional SM (W boson loop) factor and as such we will be careful to cancel it when writing BSM contributions. There exists a relationship between the tree-level matrix elements of O_i for $i = 1, ..., 6$ and the one-loop matrix elements of O_7 and O_8

$$
\begin{aligned}
\langle O_7 \rangle_{\text{loop}} &= y_i \langle O_i \rangle_{\text{tree}}, \\
\langle O_8 \rangle_{\text{loop}} &= z_i \langle O_i \rangle_{\text{tree}},
\end{aligned}
\tag{4.90}
$$

where the LHS is at loop-level, the RHS is at tree-level and the values of y_i and z_i depend on the renormalisation scheme [64].
This relationship makes it convenient for us to introduce an effective basis for our Wilson coefficients in which we may define effective Wil-

son coefficients

$$\begin{aligned} C_i^{\text{eff}}(\mu) &= C_i(\mu)\,, \quad (i=1,...,6)\,, \\ C_7^{\text{eff}}(\mu) &= C_7(\mu) + \sum_{i=1}^{6} y_i C_i(\mu)\,, \\ C_8^{\text{eff}}(\mu) &= C_8(\mu) + \sum_{i=1}^{6} z_i C_i(\mu)\,. \end{aligned} \tag{4.91}$$

Here $\vec{y} = (0, 0, -1/3, -4/9, -20/3, -80/9)$ and $\vec{z} = (0, 0, 1, -1/6, 20, -10/3)$, in the $\overline{\text{MS}}$ scheme.

The following calculation is from Ref. [62] and Table 4.9 gives the equation numbers (from this reference) of any necessary functions we introduce below.

Beginning our observable calculation, the width for radiative B decays is given by the expression

$$\Gamma(\overline{B} \to X_s\gamma) = \frac{G_F^2}{32\pi^4}|V_{ts}^* V_{tb}|^2 \alpha_{em}\, m_b^5\, (|C_7^{eff}(\mu_b)|^2). \tag{4.92}$$

This expands to

$$\begin{aligned} \Gamma(\overline{B} \to X_s\gamma) \;=\; & \frac{G_F^2}{32\pi^4}|V_{ts}^* V_{tb}|^2 \alpha_{em}\, m_b^5 \\ & \left\{ |\overline{D}|^2 + A + \frac{\delta_\gamma^{NP}}{m_b^2}|C_7^{0,\text{eff}}(\mu_b)|^2 + \right. \\ & \left. \frac{\delta_c^{NP}}{m_c^2}\text{Re}\left[\left[C_7^{0,\text{eff}}(\mu_b)\right]^*\left(C_2^{0,\text{eff}}(\mu_b) - \frac{1}{6}C_1^{0,\text{eff}}(\mu_b)\right)\right]\right\}, \end{aligned} \tag{4.93}$$

where the reduced amplitude $\overline{D}$ is

$$\overline{D} = C_7^{0,\text{eff}}(\mu_b) + \frac{\alpha_s(\mu_b)}{4\pi}\left(C_7^{1,\text{eff}}(\mu_b) + V(\mu_b)\right)\,. \tag{4.94}$$

The symbol $V(\mu_b)$ is defined as

$$V(\mu_b) = \sum_{i=1}^{8} C_i^{0,\text{eff}}(\mu_b)\left[r_i + \frac{1}{2}\gamma_{i7}^{0,\text{eff}}\ln\frac{m_b^2}{\mu_b^2}\right] - \frac{16}{3}C_7^{0,\text{eff}}(\mu_b)\,. \tag{4.95}$$

The branching ratio for $\overline{B} \to X_s\gamma$ may be calculated by taking the width $\Gamma(\overline{B} \to X_s\gamma)$ normalised to the total semi-leptonic width Γ_{SL} and scaled by the full semi-leptonic branching ratio B_{SL}

$$BR(\overline{B} \to X_s\gamma) = \frac{\Gamma(\overline{B} \to X_s\gamma)}{\Gamma_{SL}} B_{SL}. \tag{4.96}$$

The equation for the semi-leptonic width is given in Table 4.9. The

semi-leptonic branching ratio has been measured to be [65]

$$B_{SL} = 0.1091 \pm 0.0033. \tag{4.97}$$

The inclusion of the primed basis adds an extra component to the width Eq. (4.92)

$$\Gamma(\overline{B} \to X_s\gamma) = \frac{G_F^2}{32\pi^4}|V_{ts}^* V_{tb}|^2 \alpha_{em}\, m_b^5\, (|C_7^{eff}(\mu_b)|^2 + |C_7^{'eff}(\mu_b)|^2). \tag{4.98}$$

4.4.3.1 Radiative B Decays: Wilson Coefficients

Next-to-leading-order effects should not be neglected in the analysis as they may provide up to a 20% correction [66] to the process. As such, we will present our entire calculation at NLO accuracy. With the NLO term included

$$C_i^{\text{eff}}(\mu) = C_i^{0,\text{eff}}(\mu) + \frac{\alpha_s(\mu)}{4\pi} C_i^{1,\text{eff}}(\mu). \tag{4.99}$$

We may write our Wilson coefficient, separating out SM, neutral and charged contributions as

$$\begin{aligned} C_i^{0,\text{eff}} &= C_i^{0,\text{eff,SM}} + C_i^{0,\text{eff},H^\pm} + C_i^{0,\text{eff},\phi^0}, \\ C_i^{1,\text{eff}} &= C_i^{1,\text{eff,SM}} + C_i^{1,\text{eff},H^\pm}. \end{aligned} \tag{4.100}$$

At the matching scale, μ_W the leading-order SM contributions to the Wilson coefficients are

$$\begin{aligned} C_i^{0,\text{eff,SM}}(\mu_W) &= 0 \quad \text{for } i = 1,3,4,5,6\,, \\ C_2^{0,\text{eff,SM}}(\mu_W) &= -\frac{\lambda_c}{\lambda_t}, \\ C_7^{0,\text{eff,SM}}(\mu_W) &= \sum_{q=u,c,t} \frac{\lambda_q}{\lambda_t}\, C_7^{0,\text{SM}}\left(\frac{m_q^2}{m_W^2}\right), \\ C_8^{0,\text{eff,SM}}(\mu_W) &= \sum_{q=u,c,t} \frac{\lambda_q}{\lambda_t}\, C_8^{0,\text{SM}}\left(\frac{m_q^2}{m_W^2}\right). \end{aligned} \tag{4.101}$$

The NLO corrections in the SM follow

$$
\begin{aligned}
C_1^{1,\text{eff,SM}}(\mu_W) &= -\frac{\lambda_c}{\lambda_t}\left(15+6\ln\frac{\mu_W^2}{m_W^2}\right),\\
C_i^{1,\text{eff,SM}}(\mu_W) &= 0 \quad \text{for } i=2,3,5,6\,,\\
C_4^{1,\text{eff,SM}}(\mu_W) &= \left(E_0\left(\frac{m_t^2}{m_W^2}\right)+\frac{2}{3}\ln\frac{\mu_W^2}{m_W^2}\right),\\
C_7^{1,\text{eff,SM}}(\mu_W) &= C_{7,\,\text{SM}}^{1,\text{eff}}\left(\frac{m_t^2}{m_W^2},\mu_W\right),\\
C_8^{1,\text{eff,SM}}(\mu_W) &= C_{8,\text{SM}}^{1,\text{eff}}\left(\frac{m_t^2}{m_W^2},\mu_W\right).
\end{aligned}
\tag{4.102}
$$

Functions introduced are mapped in Table 4.9 and $\lambda_q = \lambda_q^{bs}$.

Function	Eq No.
Γ_{SL}	(38)
$C_7^{0,\text{SM}}$	(A1)
$C_8^{0,\text{SM}}$	(A1)
E_0	(A2)
$C_7^{1,\text{SM}}$	(18)
$C_8^{1,\text{SM}}$	(18)
C_{7YY}^0	(A3)
C_{7XY}^0	(A3)
C_{8YY}^0	(A5)
C_{8XY}^0	(A5)
C_{7YY}^1	(18)
C_{7XY}^1	(18)
C_{8YY}^1	(18)
C_{8XY}^1	(18)

Table 4.9: Locations of functions from Ref. [62] required to calculate radiative B decay processes.

The 2HDM contributions mediated by the charged scalars may be written by combining the notation and expressions for the Wilson coefficients introduced in Refs. [62] and [63]. In this notation, we introduce X which represents the term in the Yukawa Lagrangian that couples the charged Higgs and down Yukawa's and Y which couples the charged Higgs and up Yukawa's, such that

$$
\begin{aligned}
X_{ij} &= \frac{1}{\kappa_{d_j} V_{ij}}\Gamma^{LR\,H^\pm}_{u_i\,d_j},\\
Y_{ij} &= \frac{1}{\kappa_{u_i} V_{ij}}\Gamma^{RL\,H^\pm}_{u_i\,d_j}.
\end{aligned}
\tag{4.103}
$$

For our case we have the transition $b \to s$ with a FC vertex containing a sum over u family quarks. We find in this kind of transition the two combinations occur (where we have fixed the j values to 2, 3 as required)

$$
\begin{aligned}
(XY^*)_{u_i} &= \frac{1}{\kappa_{u_i}\kappa_b V^*_{u_i d_2} V_{u_i d_3}}\Gamma^{RL\,H^\pm *}_{u_i\,d_2}\Gamma^{LR\,H^\pm}_{u_i\,d_3},\\
(YY^*)_{u_i} &= \frac{1}{\kappa^2_{u_i} V^*_{u_i d_2} V_{u_i d_3}}\Gamma^{RL\,H^\pm *}_{u_i\,d_2}\Gamma^{RL\,H^\pm}_{u_i\,d_3}.
\end{aligned}
\tag{4.104}
$$

In the Z_2 aligned 2HDM models these may be identified as $X = \Gamma_d^X$ and $Y = \Gamma_u^X$, with only the diagonal $i = j$ terms non-trivial. The useful combinations are given in Table 4.10. For example, this gives then for a type-II or type-Y model Wilson coefficients that are proportional to both $1/m_{H^\pm}$ and ct_β^2.

In this notation the LO Wilson coefficients due to the charged Higgs

Type	XY^*	YY^*
I	$-ct_\beta^2$	ct_β^2
II	1	ct_β^2
X (LS)	$-ct_\beta^2$	ct_β^2
Y (flp.)	1	ct_β

Table 4.10: Functions XY and YY expanded in the Z_2 aligned 2HDM models.

Figure 4.10: Charged scalar contributions to the electromagnetic penguin operator O_7. The photon couples directly to the charged Higgs and there are three possible positions for the mass insertion (a different mass insertion shown in each diagram).

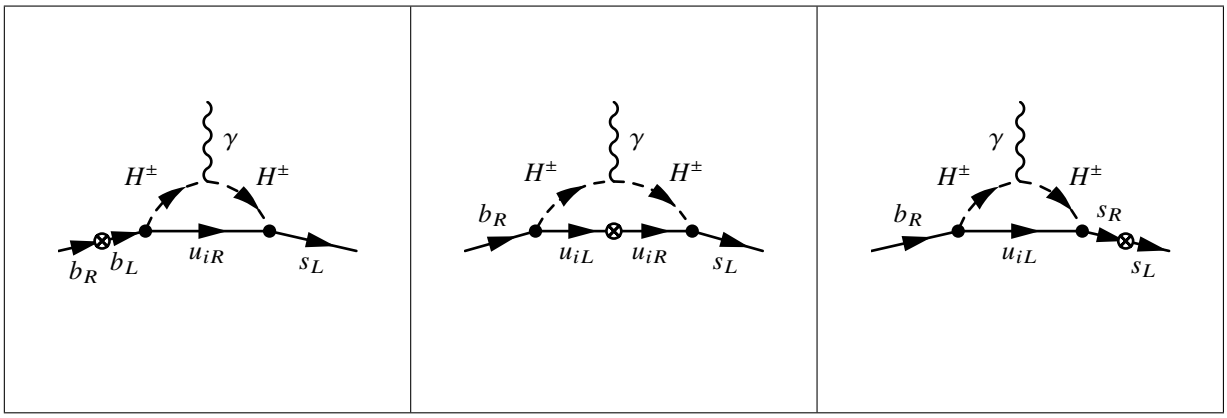

Figure 4.11: Neutral 2HDM contributions to the electromagnetic penguin operator O_7. The photon couple to the up-family fermion within the neutral Higgs loop. There are four possible positions for the mass insertion (a different mass insertion shown in each diagram).

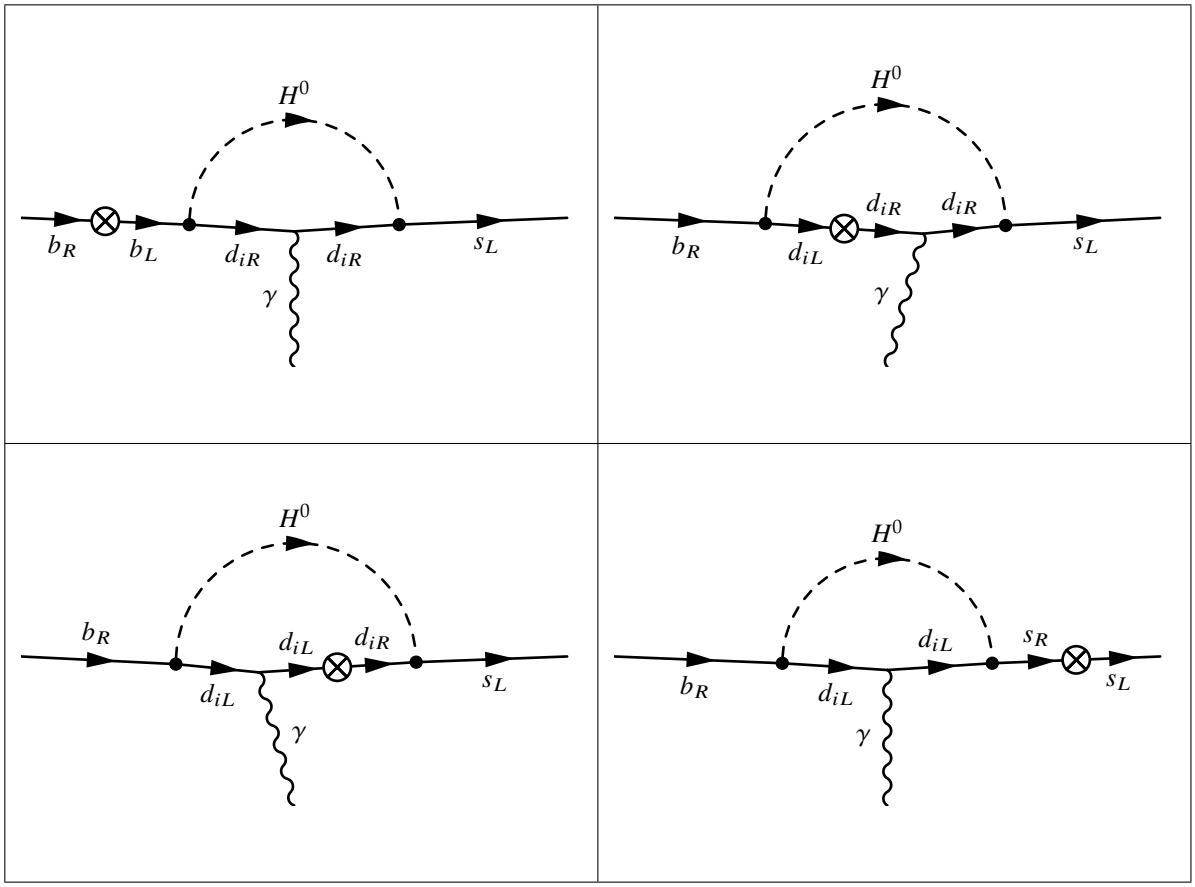

scalar at the matching scale are

$$
\begin{aligned}
C_i^{0,\text{eff},H^+}(\mu_W) &= 0 \quad \text{for} \quad i = 1,2,3,4,5,6, \\
C_7^{0,\text{eff},H^+}(\mu_W) &= \frac{\sqrt{2}}{4G_F\lambda_t} \sum_{q=u,c,t} \left[(YY^*)_q^{H^+} C_{7YY}^0\left(\frac{m_q^2}{m_{H^+}^2}\right) \right. \\
&\qquad \left. + (XY^*)_q^{H^+} C_{7XY}^0\left(\frac{m_q^2}{m_{H^+}^2}\right) \right], \\
C_8^{0,\text{eff},H^+}(\mu_W) &= \frac{\sqrt{2}}{4G_F\lambda_t} \sum_{q=u,c,t} \left[(YY^*)_q^{H^+} C_{8YY}^0\left(\frac{m_q^2}{m_{H^+}^2}\right) \right. \\
&\qquad \left. + (XY^*)_q^{H^+} C_{8XY}^0\left(\frac{m_q^2}{m_{H^+}^2}\right) \right].
\end{aligned}
\tag{4.105}
$$

The primed Wilson coefficients may be obtained by substituting the primed (YY^*) and (XY^*) couplings. NLO corrections are

$$
\begin{aligned}
C_i^{1,\text{eff},H^+}(\mu_W) &= 0 \quad \text{for}\, i = 1,2,3,5,6, \\
C_4^{1,\text{eff},H^+}(\mu_W) &= \frac{\sqrt{2}}{4G_F\lambda_t} \sum_{q=u,c,t} E_H\left(\frac{m_q^2}{m_{H^+}^2}\right) (YY^*)_q^{H^+}, \\
C_7^{1,\text{eff},H^+}(\mu_W) &= \frac{\sqrt{2}}{4G_F\lambda_t} \sum_{q=u,c,t} \left((YY^*)_q^{H^+} C_{7YY}^1\left(\frac{m_q^2}{m_{H^+}^2}, \mu_W\right) \right. \\
&\qquad \left. + (XY^*)_q^{H^+} C_{7XY}^1\left(\frac{m_q^2}{m_{H^+}^2}, \mu_W\right) \right), \\
C_8^{1,\text{eff},H^+}(\mu_W) &= \frac{\sqrt{2}}{4G_F\lambda_t} \sum_{q=u,c,t} \left((YY^*)_q^{H^+} C_{8YY}^1\left(\frac{m_q^2}{m_{H^+}^2}, \mu_W\right) \right. \\
&\qquad \left. + (XY^*)_q^{H^+} C_{8XY}^1\left(\frac{m_q^2}{m_{H^+}^2}, \mu_W\right) \right).
\end{aligned}
\tag{4.106}
$$

Again, the primed Wilson coefficients may be obtained by substitution of the primed couplings. Ref. [48] introduces a leading order contribution from the scalar particles which we include for completeness

$$
\begin{aligned}
C_7^{0,\text{eff},\phi^0} &= \frac{\sqrt{2}}{4G_F\lambda_t} \frac{1}{36 m_{\phi_k^0}^2} \sum_{k=1}^{3} \sum_{i=1}^{3} \left(\Gamma_{d_2\, d_i}^{RL,d,\phi_k^0} \Gamma_{d_3\, d_i}^{RL,d,\phi_k^0\,*} + \frac{m_s}{m_b} \Gamma_{d_i\, d_3}^{RL,d,\phi_k^0\,*} \Gamma_{d_i\, d_2}^{RL,d,\phi_k^0} \right. \\
&\quad \left. - \frac{m_{d_i}}{m_b} \Gamma_{d_2\, d_i}^{RL,d,\phi_k^0\,*} \Gamma_{d_i\, d_3}^{RL,d,\phi_k^0\,*} \left(9 + 6 \log\left(\frac{m_{d_i}^2}{m_{\phi_k^0}^2} \right) \right) \right). \\
C_8^{0,\text{eff},\phi^0} &= -3 C_7^{\phi^0}.
\end{aligned}
\tag{4.107}
$$

The charged scalar contributions to the electromagnetic penguin operator are shown in Figure 4.10, while the neutral scalar contributions are shown in Figure 4.11.

The pure SM calculation using all the above yields

$$\mathrm{BR}(\overline{B} \to X_s\gamma)_{SM} = (3.234 \pm 0.33) \times 10^{-4}. \tag{4.108}$$

where we impose a conservative theoretical error of 10% on this calculation.[45] We may compare our calculated value of the branching to the experimental value [68]

$$\mathrm{BR}(\overline{B} \to X_s\gamma) = (3.32 \pm 0.16) \times 10^{-4}. \tag{4.109}$$

45: The theoretical error depends most heavily on the scale dependence of the Wilson coefficients, such a conservative error is just above that calculated in [67].

We see our SM calculation and experimental values match closely within 1σ, so we want to avoid any significant enhancement to this value from NP contributions. Applied to the type-II or type-Y models, this would disfavour regions of low $m_{H^\pm}$ and low t_β.

4.4.4 Leptonic Flavour Processes

Operators that contribute to semi-leptonic processes do not follow the standard basis structure we have discussed earlier; rather we define new operators

$$\begin{aligned} O_9^l &= (\overline{q}\gamma_\mu P_L b)(\bar{l}\gamma^\mu l), \\ O_{10}^l &= (\overline{q}\gamma_\mu P_L b)(\bar{l}\gamma^\mu\gamma_5 l), \\ O_{AB}^l &= (\overline{q}\gamma_\mu P_A b)(\bar{l}\gamma^\mu P_B l), \end{aligned} \tag{4.110}$$

where $A, B = L, R$. We also define operators

$$\begin{aligned} O_S &= (\overline{q}P_R b)(\bar{l}l), \\ O_P &= (\overline{q}P_R b)(\bar{l}\gamma_5 l). \end{aligned} \tag{4.111}$$

All the above have primed operators created by a chirality flip. The form of the respective Wilson coefficients for the SM and generalised to the 2HDM may be found in Ref. [69].

As we have done previously, the operators may be split into their SM and NP contributions, put explicitly

$$O = O^{\mathrm{SM}} + O^{\mathrm{NP}}. \tag{4.112}$$

4.4.4.1 Electroweak Penguins: $B \to K^*\mu^+\mu^-$

The $B \to K^*\mu^+\mu^-$ decay channel with all relevant formulae is detailed in Ref. [70].

Experimentally we observe the process $B \to K^*(\to K\pi)\mu^+\mu^-$ for which the calculation of the width suffers from a large theoretical error due to large form factor uncertainties. Instead the process may be described by twelve angular functions $I_i^{(a)}$ and twelve CP-conjugate angular

functions $\overline{I_i^{(a)}}$ (see Ref. [70]). The (a) superscript and i subscript together count the twelve functions. Separating averaged CP-conserving and CP-violating angular effects we form the respective observables

$$\begin{aligned} S_i^{(a)} &= \left(\frac{d(\Gamma+\overline{\Gamma})}{dq^2}\right)^{-1}\left(I_i^{(a)} + \overline{I_i^{(a)}}\right), \\ A_i^{(a)} &= \left(\frac{d(\Gamma+\overline{\Gamma})}{dq^2}\right)^{-1}\left(I_i^{(a)} - \overline{I_i^{(a)}}\right). \end{aligned} \tag{4.113}$$

where the normalisation factor is the differential decay rate.

Additionally, the K^* longitudinal polarisation fraction F_L, forward-backward asymmetry A_{FB} and isospin asymmetry A_I are also interesting quantities. The backward asymmetry may be written as combinations of the averaged angular observables above

$$A_{FB} = \frac{3}{8}(S_6^s + S_6^c). \tag{4.114}$$

The isospin asymmetry comes from a ratio of the difference in widths [71]

$$A_I = \frac{\Gamma(B^0 \to K^{*0}\mu^+\mu^-) - \Gamma(B^+ \to K^{*+}\mu^+\mu^-)}{\Gamma(B^0 \to K^{*0}\mu^+\mu^-) + \Gamma(B^+ \to K^{*+}\mu^+\mu^-)}. \tag{4.115}$$

These variables also depend on the energy at which they are evaluated through the dependence on the dilepton invariant mass q^2. The observables are binned into ranges of $q^2 = [a, b]$, represented as $\langle x \rangle_{[a,b]}$ with x the observable in question. The integral is carried out in bin $[a, b]$ as follows

$$\langle S_i^{(a)} \rangle_{[a,b]} = \int_a^b dq^2 \left(\frac{d(\Gamma+\overline{\Gamma})}{dq^2}\right)^{-1} \int_a^b dq^2 \left(I_i^{(a)} + \overline{I_i^{(a)}}\right), \tag{4.116}$$

and similarly for $\langle A_i^{(a)} \rangle_{[a,b]}$.

Some angular observables show significant deviations from the SM [72].[46] NP contributions to the process occur in Class V operators O_7, O_9 and O_{10} (rather than the newly introduced semi-leptonic operators which we do not use here). In the type-II 2HDM, for example, C_7 plays the largest role in NP contributions - which are proportional to $1/m_{H^\pm}$ and ct_β^2.

46: The most notable are $\langle S_4 \rangle_{[14.18,16]}$ at 2.8σ, $\langle S_5 \rangle_{[1,6]}$ at 2.4σ and $\langle F_L \rangle_{[1,6]}$ at 1.9σ.

4.4.4.2 Rare Fully Leptonic B decays: $B_s^0 \to \mu^+\mu^-$

The $B_s \to \mu^+\mu^-$ decay is fully leptonic in its final state, and is rare in the SM[47] . This makes it a good candidate for probing BSM physics.

47: The decay only occurs through loop-diagrams in the SM and is also helicity-suppressed.

The branching ratio is defined as [73]

$$\mathrm{BR}(B_s \to \mu^+\mu^-) = \frac{G_F^2 \alpha^2 M_{B_s}}{16\pi^3}\sqrt{1-4\frac{m_\mu^2}{m_{B_s}^2}}|V_{tb}V_{ts}^*|^2|C_{10}^{\mu\,\mathrm{SM}}|^2\tau_{B_s} f_{B_s}^2 m_\mu^2(|P|^2+|S|^2), \tag{4.117}$$

where

$$P = \frac{C_{10}^l - C_{10}^{\mu'}}{C_{10}^{\mu\,\mathrm{SM}}} + \frac{m_{B_s}^2}{2m_\mu}\left(\frac{1}{m_b+m_s}\right)\left(\frac{C_P - C_P'}{C_{10}^{\mu\,\mathrm{SM}}}\right), \tag{4.118}$$

$$S = \sqrt{1-\frac{4m_\mu^2}{m_{m_{B_s}}^2}}\frac{m_{B_s}^2}{2m_\mu}\left(\frac{1}{m_b+m_s}\right)\left(\frac{C_S - C_S'}{C_{10}^{\mu\,\mathrm{SM}}}\right). \tag{4.119}$$

Current observations of the process show that it is consistent with the SM [74]. In the type-II and type-Y models this process is proportional to t_β^2 and $1/m_A$ specifically.

4.4.4.3 Tree-level leptonic and semi-leptonic B and D decays

As previously mentioned, the $B \to K^*\mu^+\mu^-$ decay channel is difficult to predict due to large form factor uncertainties. Another way we could frame this observable is in ratio with other semi-leptonic decays. Introducing the lepton flavour non-universal observables

$$R_K^{(*)} = \frac{\mathrm{BR}(B \to K^{(*)}\mu^+\mu^-)}{\mathrm{BR}(B \to K^{(*)}e^+e^-)}. \tag{4.120}$$

The above observables may be written [75] in terms of semi-leptonic operators with [48]

$$R_K = 1 + \Delta_+ + \Sigma_+, \tag{4.121}$$

and

$$R_{K^*} = 1 + \Delta_+ + \Sigma_+ + p(\Sigma_- - \Sigma_+ + \Delta_- - \Delta_+), \tag{4.122}$$

where as stated in [75], p is the fraction of transverse parallel and longitudinal contributions to $\mathrm{BR}(B \to K^\star ll)$. The linear term $\Delta_\pm$ is

$$\Delta_\pm = 2\mathrm{Re}\left(\frac{C_{LL}^{\mu\,\mathrm{NP}} \pm C_{RL}^\mu}{C_{LL}^{\mu\,\mathrm{SM}}} - (\mu \to e)\right), \tag{4.123}$$

and the quadratic term $\Sigma_\pm$ is

$$\Sigma\pm = \frac{|C_{LL}^{\mu\,\mathrm{NP}} \pm C_{RL}^\mu|^2 + |C_{LR}^\mu \pm C_{RR}^\mu|^2}{|C_{LL}^{\mu\,\mathrm{SM}}|^2} - (\mu \to e). \tag{4.124}$$

Here we use $(\mu \to e)$ to mean the same term but with substitution $\mu \to e$.

48: This neglects the electromagnetic dipole operator [76].

As described before, integrating over energy bins $[a, b]$, the observables $\langle R_K \rangle_{[1,6]}$, $\langle R_{K^*} \rangle_{[0.045,1.1]}$, $\langle R_{K^*} \rangle_{[1.1,6]}$ individually have reported deviations from the SM at $2.2\sigma - 2.5\sigma$ [77]. Combining these three there is motivation for potential NP.

With regards to the D decays, we may similarly define

$$R_D^{(*)} = \frac{\mathrm{BR}(\overline{B} \to D^{(*)} \tau \overline{\nu}_\tau)}{\mathrm{BR}(\overline{B} \to D^{(*)} l \overline{\nu}_l)}, \tag{4.125}$$

where $l = e$ or μ. These observables also show a deviation from the SM [78] with R_D having a deviation at 1.9σ and $R_D^{(*)}$ exhibiting a stronger deviation at 3.3σ.[49]

49: See the reference [78] for details on the calculation of these processes.

Other interesting semi-leptonic flavour decays which we will not discuss here but will be included within our analysis are for the B channels, $B \to \tau\nu, B \to D\mu\nu, B \to D^*\mu\nu$ and for the D channels, $D_s \to \tau\nu, D_s \to \mu\nu$ and $D \to \mu\nu$.

4.5 Oblique Parameters

The electroweak precision parameters/observables (EWPP/EWPO), otherwise known as the oblique parameters, are six measurable quantities that allow us to search for NP in the electroweak sector, specifically in vacuum polarisation corrections.

They are defined as benchmark parameters at a fixed reference Higgs scalar mass (SM-Higgs scalar mass) in a theory that satisfies the criteria [79]:

- The electroweak gauge group is the SM - $SU_L(2) \times U(1)$ theory and there are no new gauge bosons.
- Any NP must have suppressed couplings to light fermions in comparison to couplings to gauge bosons.

These two conditions allow us to identify and isolate the vacuum polarisation corrections (oblique corrections) from other four-fermion scattering processes such as vertex corrections and box corrections (non-oblique corrections).

Another requirement is:

- The scale of any NP is much greater than the electroweak scale.

The above means that we must work in the low-energy approximation, $q \approx 0$, at which oblique corrections may be expanded in q^2/M^2, throwing away any terms of quadratic order in q^2 or higher. Under

these circumstances, the oblique corrections may be entirely parameterised by three parameters S, T and U[50] . We start by writing out the vacuum polarisation tensor as

$$\Pi_{ab}(q^2) = \Pi^{\text{SM}}_{ab}(q^2) + \delta\Pi_{ab}(q^2), \tag{4.126}$$

with this the parameters S, T and U are

$$\begin{aligned}\frac{\alpha S}{4s_W^2 c_W^2} =& \left[\frac{\delta\Pi_{ZZ}(M_Z^2) - \delta\Pi_{ZZ}(0)}{M_Z^2}\right] - \frac{(c_W^2 - s_W^2)}{s_W c_W}\delta\Pi'_{Z\gamma}(0)|_{q^2=0} \\ &- \delta\Pi'_{\gamma\gamma}(0)|_{q^2=0},\end{aligned} \tag{4.127}$$

$$\alpha T = \frac{\delta\Pi_{WW}(0)}{M_W^2} - \frac{\delta\Pi_{ZZ}(0)}{M_Z^2}, \tag{4.128}$$

$$\begin{aligned}\frac{\alpha U}{4s_W^2} =& \left[\frac{\delta\Pi_{WW}(M_W^2) - \delta\Pi_{WW}(0)}{M_W^2}\right] - c_W^2\left[\frac{\delta\Pi_{ZZ}(M_Z^2) - \delta\Pi_{ZZ}(0)}{M_Z^2}\right] \\ &- s_W^2\delta\Pi'_{\gamma\gamma}(0)|_{q^2=0} - 2s_w c_w \delta\Pi'_{Z\gamma}(0)|_{q^2=0}.\end{aligned} \tag{4.129}$$

Corrections to the W boson mass may be written with respect to all the above oblique parameters as

$$M_W^2 = (M_W^2)_{\text{SM}}\left[1 - \frac{\alpha S}{2(c_W^2 - s_W^2)} + \frac{c_W^2\alpha T}{(c_W^2 - s_W^2)} + \frac{\alpha U}{4s_W^2}\right]. \tag{4.130}$$

In Eq. (2.52) we introduced the ρ parameter, the ratio of mixing in the neutral and charged currents. The ρ parameters is by definition unity at tree-level in the SM. Corrections to ρ are defined as the difference in vacuum polarisations of the neutral and weak current, these are given by the T term

$$\rho = \rho_{\text{SM}}(1 + \alpha T). \tag{4.131}$$

If we then no longer restrict ourselves to NP much larger than the electroweak scale, we must be able to analyse the oblique corrections at $q^2 = M_W^2$. In this case, vacuum polarisation insertions must be summed to all orders according to the Schwinger-Dyson equations. We require an extra three parameters to entirely describe the oblique corrections, these being, V, W and X, which are defined as

$$\begin{aligned}\alpha V &= \delta\Pi'_{ZZ}(M_Z^2)|_{q^2=M_Z^2} - \left[\frac{\delta\Pi_{ZZ}(M_Z^2) - \delta\Pi_{ZZ}(0)}{M_Z^2}\right], \\ \alpha W &= \delta\Pi'_{WW}(M_W^2)|_{q^2=M_W^2} - \left[\frac{\delta\Pi_{WW}(M_Z^2) - \delta\Pi_{WW}(0)}{M_W^2}\right], \\ \alpha X &= -s_W c_W\left[\frac{\delta\Pi_{Z\gamma}(M_Z^2)}{M_Z^2}\right] - \delta\Pi'_{Z\gamma}(0)|_{q^2=0}.\end{aligned} \tag{4.132}$$

50: S, T and U are known as the Peskin-Takeuchi parameters [80] [81] [82].

Contributions to the width of the W boson may be written as

$$\Gamma_W = (\Gamma_W)_{SM}\left[1 - \frac{\alpha S}{2(c_W^2 - s_W^2)} - \frac{s_W^2 \alpha T}{(c_W^2 - s_W^2)} + \frac{\alpha U}{4 s_W^2} + \alpha W\right]. \quad (4.133)$$

We may express all six parameters in just three as follows [83]

$$\begin{aligned} S' &= S + 4 s_W^2 c_W^2 V + 4(c_W^2 - s_W^2) X, \\ T' &= T + V, \\ U' &= U - 4 s_W^2 c_W^2 V + 8 s_W^2 X. \end{aligned} \quad (4.134)$$

This parameterisation allows us to include NP near the electroweak scale while keeping equations for observables invariant. Notice that as we increase the energy of our NP scale then $V, W, X \to 0$ and we recover just the set of three oblique parameters S, T, U. The W parameter is ignored, as this notation does not consider contributions to the width of the W boson in the low-energy NP limit.

Ref. [84] presents the oblique parameters generalised to a multi-Higgs-doublet model. The locations for equations giving the EWPP are given in Table 4.11 with the relationship to the 2HDM

$$\begin{aligned} m = n &= 2, \\ \mathcal{U} = \mathrm{Im}\mathcal{V} &= R^{\dagger}(\beta), \\ \mathrm{Re}\mathcal{V} &= R^{\dagger}(\alpha), \end{aligned} \quad (4.135)$$

where $R(\theta)$ are the rotation matrices introduced in section 3.4.1.

The final results for S, T and U in the 2HDM are also expanded and presented in section 5 of [85].

Parameter	Eq. No.
S	(30)
T	(28)
U	(31)
V	(35)
W	(36)
X	(32)

Table 4.11: Locations of the oblique parameters generalised to a multi-Higgs-doublet model in Ref. [84].

Global Fits and Bayesian Statistics

5

In this chapter, we discuss the setup of our global scans over the 2HDMs. The previous chapters give us the theoretical and phenomenological tools to constrain our models. We discuss how these constraints are best applied and the statistics, tools and algorithms that make it possible.

To do a global scan, we select a 2HDM and apply constraints in the form of likelihood functions to find and map out the best-fit areas of parameter space.

We carry out two sets of global scans. The first is an analysis of the parameter space of Z_2 Yukawa aligned 2HDMs, specifically the type-I, type-II, lepton-specific and flipped models. This analysis is carried out by the open-source tool `GAMBIT` [86] (Global and Modular Bayesian Inference Tool). * The second analysis is of FC currents between the second and third flavour quarks in the general (type-III) 2HDM with a *restricted* Yukawa sector as introduced in Eq. (4.39). This analysis is carried out standalone.

5.1 Global Fit Statistics

Parameters that make up the current SM are quite well known through experimental measurements. Beyond SM theories such as the 2HDM or the Minimal Supersymmetric Model (MSSM) introduce a large number of new unknown parameters. The best approach to investigating such models is a test throughout all the acceptable regions of parameter space. This is an ambitious feat as it often requires scanning over many parameters. A Z_2-aligned 2HDM, for example, has nine unknown parameters. A global fit scans over all these nine parameters in a given predefined region of parameter space. We will see that global fits allow us to make two critical predictions about our models:

1. We can compare multiple models to evaluate which model is a better fit to the data.
2. For any single model, we can map the parameter space and find which regions best fit the data.

In our case, we will be focusing on the latter of these as we map out the parameter spaces and observables of the various 2HDMs.

* We have added the 2HDMs to `GAMBIT` to carry out this analysis, and as such, sections of this chapter double as a reference for the models' implementation in `GAMBIT`.

5.1.1 Bayes Theorem

Bayesian statistics is the essence of performing our global fits. As the name suggests it is founded upon Bayes theorem

$$P(A|B) = \frac{P(B|A)P(A)}{P(B)}, \tag{5.1}$$

where $P(A|B)$ defines a conditional probability, the probability of the occurrence of A given B, requiring that $P(B) \neq 0$.[52] To make this more intuitive, consider the case at hand. We want to perform a global fit of the 2HDM. We have a set of data D which we will want to match with our theoretical model to see how well it performs. Expressing the nine free parameters in our model as θ_i, or just θ, the probability of our model given the data is

$$P(\theta|D) = \frac{P(D|\theta)P(\theta)}{P(D)}. \tag{5.3}$$

The probability distribution on the LHS is known as the posterior distribution. Each of the terms of the RHS can be separated and described as follows:

- $\mathcal{L}(\theta) = P(D|\theta)$ is known as the likelihood. It is the probability of the data given a point θ.
- $\pi(\theta) = P(\theta)$ is known as the prior. It is the probability distribution of θ with prior knowledge of the data distribution. Usually, we take a flat prior meaning each point of our model is equally probable.
- $Z = P(D)$ is known as the evidence. For simplicity here, we will say this is a normalisation factor to ensure the total volume of the posterior distribution is one.

In our newly developed language the posterior can be written as

$$P(\theta|D) = \frac{\mathcal{L}(\theta)\pi(\theta)}{Z}. \tag{5.4}$$

Integrating both sides of the equation with respect to the model points θ we get

$$\int_\theta P(\theta|D)d^D\theta = \frac{1}{Z}\int_\theta \mathcal{L}(\theta)\pi(\theta)d^D\theta, \tag{5.5}$$

which given that a probability distribution functions volume on the LHS must be one

$$Z = \int_\theta \mathcal{L}(\theta)\pi(\theta)d^D\theta. \tag{5.6}$$

It is also useful to compare two models θ and $\tilde{\theta}$ with the same data set. We can eliminate the evidence when we take the ratio

$$\frac{P(\theta|D)}{P(\tilde{\theta}|D)} = \frac{P(D|\theta)P(\theta)}{P(D|\tilde{\theta})P(\tilde{\theta})}. \tag{5.7}$$

52: Mathematically, conditional probability is written as

$$P(A|B) = \frac{P(A \cap B)}{P(B)}. \tag{5.2}$$

5.1.2 Likelihoods

The likelihood is somewhat similar to a probability density function (PDF); however, it tells us nothing about the frequency of outcomes which is a crucial feature of probability distributions. The likelihood function as described is a joint probability density[53] for our data given some point that we want to fit, as such, we have no guarantee that it will integrate to one. Care must be taken when interpreting likelihood results, and we will discuss methods in which this is done throughout this section.

53: A multivariate probability density.

A larger likelihood represents a point that better fits the model, hence, our goal is to maximise $\mathscr{L}(\theta_i)$ for θ_i. Consider that in our model $\theta_1 = \alpha$ is true, then introduce the χ^2 function as the error-squared for any point θ_1, we may define

$$\chi^2(\theta_1) = (\theta_1 - \alpha)^2. \tag{5.8}$$

Then $\chi^2 = 0$ gives the best-fit of the model. Creating a Gaussian PDF likelihood function with this knowledge

$$\mathscr{L}(\theta_1) = \frac{1}{\sqrt{2\pi\sigma^2}} \exp\left(\frac{-\chi^2(\theta_1)}{2\sigma^2}\right), \tag{5.9}$$

here σ is the error in α and this function may easily be generalised to a vector θ_i. In this function our $\mathscr{L}$ is now maximised for the best-fit point $\chi = 0$ and χ follows the normal distribution according to σ.

Optimisation is enhanced by performing a logarithmic transformation. Eq. (5.9) becomes[54]

$$\log \mathscr{L}(\theta_i) = \frac{-\chi^2(\theta_i)}{2\sigma^2} - \frac{\log(2\pi\sigma^2)}{2}. \tag{5.10}$$

54: The log-likelihood is generally known to be a negative number which is optimised at $\log \mathscr{L} = 0$. There are, however, exceptions to this rule, resulting from the arbitrary normalisation of $\mathscr{L}$.

Using Gaussian likelihoods provides a smooth map of the parameter space and aids in guiding optimisation algorithms in moving towards regions of better likelihood fits.

So far we have considered a Gaussian-centred χ^2 which is useful for a central data value we are attempting to fit. If we, however, are faced with a bound B, the most straightforward approach would be to create a so-called 'hard-cut'. In the case of an upper bound B^+, point θ_{calc} would have the log-likelihood

$$\log \mathscr{L}(\theta_{\text{calc}}) = \begin{cases} 0, & \text{if } \theta_{\text{calc}} < B^+ \\ -\chi_{\text{max}}, & \text{if } \theta_{\text{calc}} \geq B^+, \end{cases} \tag{5.11}$$

where χ_{max} is a large number, such that it is rejected by any optimisation algorithm used. The same likelihood with reversed limits applies

to a lower bound. This kind of approach is valid for our theory constraints which are not stated with any statistical confidence unlike our experimental bounds.

To improve the efficiency of the scanning algorithm, it is sometimes better to apply a half-Gaussian bound, a so-called 'soft-cutoff'. For an upper bound B^+ and point θ_{calc}, a half-Gaussian log-likelihood function would be

$$\log \mathscr{L}(\theta_{\text{calc}}) = \begin{cases} -\frac{\log(2\pi\sigma^2)}{2}, & \text{if } \theta_{\text{calc}} < B^+ \\ \frac{-\chi^2(\theta_{\text{calc}})}{2\sigma^2} - \frac{\log(2\pi\sigma^2)}{2}, & \text{if } \theta_{\text{calc}} \geq B^+. \end{cases} \tag{5.12}$$

Again we reverse the conditions if we have a lower bound.

5.1.3 Distributions

Based upon different statistical interpretations there are two ways in which we may present the final likelihood distributions that we map for our parameter space. We discuss both here.

5.1.3.1 Posterior Probability Distribution

The posterior probability distribution is the direct result of Bayes theorem (5.4), $P(\theta|D)$, the probability distribution of parameter space θ given the data D. The posterior probability distribution is normalised with respect to the evidence Z, ensuring we indeed get a probability distribution[55] . Hence, calculating the evidence is a prerequisite. The distribution may be presented as a ratio of its maximum value

55: A function that has an integrated volume of one.

$$x_{\text{posterior}}(\theta) = \frac{P(\theta|D)}{P_{\text{max}}(\theta|D)}. \tag{5.13}$$

If we only care for a single variable we may integrate out all the others, for example, if $\theta_i = (\theta_1, \theta_2)$ then we may use

$$P(\theta_1|D) = \int P(\theta_i|D) d\theta_2, \tag{5.14}$$

to integrate out θ_2. This is known as marginalising and θ_2 is known as our nuisance parameter.

5.1.3.2 Profile Likelihood Distribution

A profile likelihood distribution only involves the un-normalised likelihood values for each point in parameter space. The distribution is a

ratio of each point with respect to the point with the best-likelihood

$$x_{\text{profiled}}(\theta) = \frac{\mathscr{L}(\theta)}{\mathscr{L}_{\text{best}}(\theta)}. \tag{5.15}$$

As we work with log-likelihoods, this becomes

$$x_{\text{profiled}}(\theta) = \exp(\log \mathscr{L}(\theta) - \log \mathscr{L}_{\text{best}}(\theta)). \tag{5.16}$$

5.2 GAMBIT

The Global and Modular Beyond-Standard Model Inference Tool [86] (GAMBIT) released in 2017 is an open-source tool to perform efficient statistical analysis (in the form of global scans) of physics models. GAMBIT is built upon the paradigm of modularity, separated into so-called 'Bits' each with a different purpose. BSM models may be added or modified in GAMBIT and plugged into the physics calculations and statistical scanning tools already provided by GAMBIT.

We have worked to integrate the 2HDMs with Z_2 Yukawa aligned sectors into GAMBIT. We are also working to integrate the general type-III model with FC; however, this is a work in progress at the time of writing.

The 2HDM spectrum has been added to GAMBIT through at both tree-level and loop-level in SpecBit [87] and FlexibleSUSY [88], [89]. A new SpecBit node[56] has been added for the 2HDM and we integrated existing FlexibleSUSY 2HDM loop-level spectrum generators with some minor alterations. All theoretical spectrum calculations necessary for the analysis (e.g. unitarity of the scattering matrix, vacuum stability, scale couplings) were added to SpecBit .

56: The source file and respective headers required to generate a spectrum at both tree and loop-level, according to the GAMBIT paradigm.

2HDM decays were added to DecayBit , precision physics to PrecisionBit and flavour physics and collider physics integrations to FlavBit and ColliderBit respectively [87]. GAMBIT also integrates with backends, and we linked the shared library from 2HDMC [47] to access this programs inbuilt calculations.

Here we discuss interesting points about the implementation of the 2HDM in GAMBIT and the likelihoods added or adapted that we use for our analysis.

5.2.1 Models

Models in GAMBIT represent physics models. Each model must be unique if it has a different set of input parameters or is defined by different

physics. However, models may be related as either 'FRIEND' or 'PARENT'*, depending on a model translation hierarchy. The translation between models is done via translation functions. When required and allowed, GAMBIT will automatically trigger the necessary translation function for changes between models.

On these grounds, we need to declare separately (and in combination):

- each 2HDM Z_2 Yukawa aligned model/the general type-III model,
- each input basis,
- models with and without running parameters in the Spectrum generation.

For each 2HDM, input basis transformations and transformations between tree-level and loop-corrected spectra are FRIEND translations. Translations between Z_2 Yukawa aligned models are not allowed, and each Z_2 Yukawa aligned model, is related to the general 2HDM through a PARENT transformation.

We give the available GAMBIT models for the 2HDM type-II in Table 5.1. These are also available for type-I, lepton-specific (type-X) and flipped (type-Y) with the model name changes THDMII → THDMI, THDMII → THDMLS and THDMII → THDMflipped, respectively.

Notice, each model has two entries: the tree-level model and an 'atQ' partner model. The 'atQ' partner includes loop-corrections in the spectrum generation and requires extra parameters to specify the model. Notice also, the Z_2 hard-breaking terms λ_6 and λ_7 appear in the Z_2 Yukawa aligned models. Generally, one would fix these to zero; however, if only interested in theoretical constraints, a Z_2-breaking model is supported. The restriction here is that not all theoretical likelihoods support Z_2-breaking terms, more on this later.

Aside from the generic basis, we allow input in the Higgs basis, physical basis and two hybrid bases in which either λ_1 or λ_2 are replaced by m_h.

The basis transformations between the Higgs and generic basis are given explicitly in the (A13) - (A22) of Ref. [43] (with necessary relationships to the Higgs basis we use detailed in section 4.1.1). Transformations between the physical and generic basis may be found from the relationships described in section 3.4.2. The replaced coupling in

* PARENT relationships are created when extending a model with extra parameters and conversely allow us create child models where some parameters are fixed. FRIEND relationships are used when manipulating parameters in the same model, for example, when carrying out basis transformations.

Table 5.1: Description of 2HDM type-II models available in GAMBIT. These same models are also available for the other Yukawa aligned types.

Name	Model Description	Input Parameters (Variable Names)
THDMII [THDMIIatQ]	2HDM type-II Model - Generic Basis Input	lambda_1, lambda_2, lambda_3, lambda_4, lambda_5, lambda_6, lambda_7, m12_2, tanb [Qin, QrunTo]
THDMII_physical [THDMII_physicalatQ]	2HDM type-II Model - Physical Basis Input	lambda_6, lambda_7, m12_2, m_A, m_H, m_Hp, m_h, sba, tanb [Qin, QrunTo]
THDMII_hybrid_lambda1 [TTHDMII_hybrid_lambda1atQ]	2HDM type-II Model - Generic Basis Input with λ_1 replaced by m_h	lambda_2, lambda_3, lambda_4, lambda_5, lambda_6, lambda_7, m12_2, m_h, sba, tanb [Qin, QrunTo]
THDMII_hybrid_lambda2 [THDMII_hybrid_lambda2atQ]	2HDM type-II Model - Generic Basis Input with λ_2 replaced by m_h	lambda_1, lambda_3, lambda_4, lambda_5, lambda_6, lambda_7, m12_2, m_h, sba, tanb [Qin, QrunTo]
THDMII_higgs [THDMII_higgs_atQ]	2HDM type-II Model - Higgs Basis Input	Lambda_1, Lambda_2, Lambda_3, Lambda_4, Lambda_5, Lambda_7, M22_2, sba, tanb [Qin, QrunTo]

Table 5.2: Description of the 2HDM general model (type-III) in GAMBIT . At time of publication this model is not yet supported by all of GAMBIT

Name	Model Description	Input Parameters (Variable Names)
2HDM [THDMatQ]	2HDM General Model (type-III) - Higgs Basis Input	Lambda_1, Lambda_2, Lambda_3, Lambda_4, Lambda_5, Lambda_7, alpha, M22_2, tanb, $\sum_{ij}^{3}$(yd2_re_ij, yd2_im_ij, yu2_re_ij, yu2_im_ij, yl2_re_ij, yl2_im_ij) [Qin, QrunTo]

the hybrid bases may be recovered using

$$\begin{aligned}\lambda_1 &= \frac{1}{v^2 c_\beta^2 s_\alpha^2}\left(m_h^2(s_\alpha^4 - c_\alpha^4) + m_{12}^2(ct_\beta c_\alpha^2 - t_\beta s_\alpha^2) + \lambda_2 v^2 s_\beta^2 c_\alpha^2\right),\\ \lambda_2 &= \frac{1}{v^2 s_\beta^2 c_\alpha^2}\left(-m_h^2(s_\alpha^4 - c_\alpha^4) - m_{12}^2(ct_\beta c_\alpha^2 - t_\beta s_\alpha^2) + \lambda_1 v^2 c_\beta^2 s_\alpha^2\right).\end{aligned} \tag{5.17}$$

All models are transformed into the generic basis[57] via FRIEND translation functions before being used by GAMBIT. As such, all models, except the generic basis, exist only as a rotation to allow us better to explore different regions of the 2HDM parameter space. Each basis has its benefits and disadvantages when searching for valid points. It is often hard to satisfy perturbativity and stability in the physical basis, whereas, it is easy to satisfy a valid scalar sector with SM Higgs-like signals. The opposite is true for the generic basis. The hybrid basis allows one to fix m_h while scanning on the remainder of the couplings, sitting somewhere in between these.

57: e.g. for the type-II model the generic basis corresponds to the model THDMII or THDMIIatQ.

The relationship between different models displaying the nature of translation functions linking them is shown in Figure 5.1.

Note that the most general 2HDM (type-III) is at the time of publication included but not yet supported by GAMBIT (see Table 5.2).

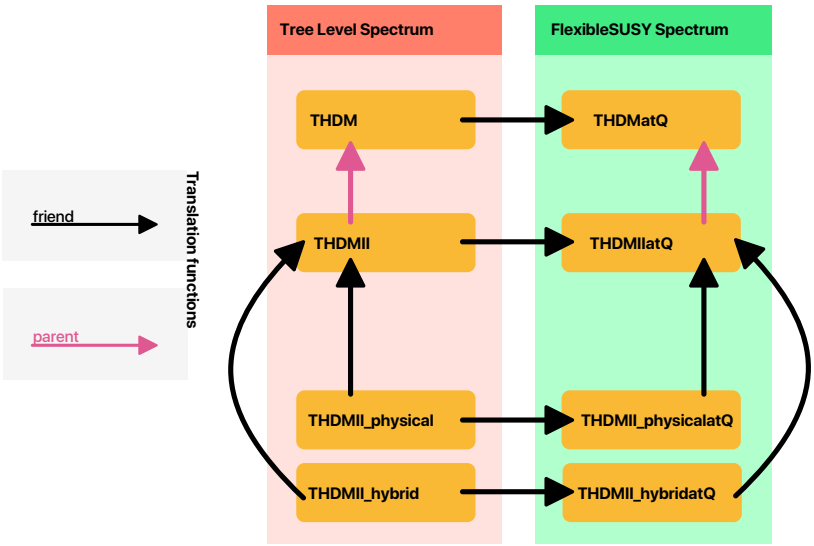

Figure 5.1: An overview of model translations for the 2HDM type-II model in GAMBIT (We have not included the Higgs basis input model here and have compressed both the hybrid models into one for simplicity).

Table 5.3: Modular-level dependencies on backends that are used in the 2HDM GAMBIT implementation.

	2HDMC [47]	SuperIso [91]	HiggsBounds HiggsSignals [92] [93] [94]
SpecBit	×		
FlavBit		×	
ColliderBit	×		×
PrecisionBit	×		
DecayBit	×		

5.2.2 Backends

GAMBIT utilises the existing physics code-base, through interfacing external source-code shared libraries (back-ending). The goal is to be able to access routines and variables provided by external codes directly within GAMBIT. The backend dependencies for the 2HDM, grouped at a modular level are given in Table 5.3. [58]

58: Since these results were generated the backend heplike [90] has also been added to aid with flavour likelihood calculations.

5.2.2.1 Two-Higgs-Doublet Model Calculator

This work has required that we backend the code Two-Higgs-Doublet Model Calculator (2HDMC). To install the 2HDMC backend one needs to run the command:

```
make THDMC
```

in the build directory. This downloads and extracts the package, applies compatibility patches, performs BOSS-ing as required and finally runs a patched make build script, which is described in the next section.

The 2HDMC provides functionality to calculate couplings and widths for 2HDM processes along with particle spectrum calculations. It also evaluates constraints from stability, unitarity, perturbativity, electroweak precision measurements and experimental constraints through integration with HiggsBounds and HiggsSignals. We use the 2HDMC to perform coupling and width calculations as well as to calculate the electroweak precision parameters. All other constraints and calculations are carried out through GAMBIT .

2HDMC and BOSS 2HDMC is written in C++ and makes use of class structure. The most notable is the THDM class which creates a correspondingly named object that holds our spectrum and gives us an entry point into the desired calculations. This class structure will need to be known to GAMBIT, and GAMBIT must be able to handle objects belonging to the 2HDMC. Under basic circumstances, we would use dlopen, a C tool that accesses functions and global variables from shared libraries. However, as 2HDMC requires the passing of objects based on a class structure, we need a different approach. The tool packaged with GAMBIT that enables us to do this is the python 'Backend on a Stick Script' (BOSS). BOSS parses the backend and creates *abstract* classes that recreate the backend class structure with *virtual* functions. [59] Each of the original classes in our backend is then demoted to a child member of each respective abstract class. Finally, an interface class is created which wraps the abstract class and can be called by GAMBIT to access the backend. As such, the interface class would contain a pointer of the abstract class type that then would point to the original class in the backend. The interface class for the 2HDMC is THDMC_1_8_0 and the pointers corresponding to each of the original backend classes of the 2HDMC program are [60] are:

59: The virtual functions in the abstract class mirror the functions within the respective original backend class.

60: The pointers are of the respective abstract class type.

```
THDMC_1_8_0::THDM*
THDMC_1_8_0::SM*
THDMC_1_8_0::DecayTableTHDM*
THDMC_1_8_0::Constraints*
```

These may be used as constructors within GAMBIT directly when the 2HDMC is stated as a dependency.

An example of usage of the 2HDMC classes would be:

```
// Create a new pointer to an object created from the 2HDMC THDM class
THDMC_1_8_0::THDM* THDM_object;
// Set the 2HDM input by calling the standard functions from the THDM object
THDM_object->set_param_gen(lambda_1, lambda_2, lambda_3, lambda_4, lambda_5, lambda_6, lambda_7, m12_2, tan_beta);
THDM_object->set_yukawas_type(2);
// Retrieve a coupling from the THDM object
THDM_object->get_coupling_hhh(h1, h2, h3, coupling);
```

Patches to 2HDMC It was necessary to modify some sections of the 2HDMC code to provide better compatibility with GAMBIT. Patches are applied to the out-of-the-box source files as part of the GAMBIT cmake scripts. Here we document each modification made.

- set_CKM function added to the SM class.
- The BOSS-ed classes have been included in the Makefile.
- In GAMBIT the class name DecayTable is protected as it belongs to DecayBit, hence, we have renamed the 2HDMC class with the same name to DecayTableTHDM and propagated this change through the source code.
- Conditional compiler directives (#ifdef) that are placed outside of functions must be moved inside such that functions are still defined regardless of directive logic. All function definitions are expected at compile time as they have virtual definitions in the abstract classes.
- Constant variable values are no longer defined in the header file but now set in the respective classes 'global scope' section. This was due to a compilation error introduced due to changing definitions of the const static double combination type in some modern C++ standards.
- Construction of a THDM object initialises an instance of the SM class as a private member. The default way to access the member SM class is to use the get_SM method which returns a copy of the SM object. We are then able modify the object and pass the copy back using the default set_SM method. As we carry out manual memory management of the THDM object (as discussed later) we create the function get_SM_pointer which allows us to access the private SM object directly. The return pointer may be assigned directly to the abstract class pointer THDMC_1_8_0::SM* type.
- The 2HDMC uses only tree-level input and in effect tree-level relations between bases. When working with a spectrum from FlexibleSUSY that includes loop-level corrections we may still

use 2HDMC acknowledging that we have input parameters at a given energy and when inputting the physical masses we need to input the pole masses. Up to this point it is acceptable to use 2HDMC in its current state. However, if for any reason we require a change of basis between a coupling basis (generic or Higgs) and the physical basis the inbuilt tree-level routines are not valid. To allow 2HDMC to access both the couplings and the physical masses in any run without transforming we create an input option that takes the entire spectrum (the couplings in the generic couplings and the physical masses).

```
1   bool THDM::set_param_full(
2   double lambda1, double lambda2, double lambda3,
3   double lambda4, double lambda5, double lambda6,
4   double lambda7, double m12_2, double tan_beta,
5   double m_h,double m_H, double m_A, double m_Hp,
6   double sba) {
7   // set couplings, set masses, calculate m22_2
8   // ...
9   params_set = true; params_full_set = true;
10  return params_set;
11  }
```

The function get_param_phys, which returns the physical mass basis, has been adjusted to check if params_full_set has been set true (this is equivalent to set_param_full completing successfully) and if so it returns the masses given to the set_param_full routine.[61]

61: The masses given to this routine are saved as private class variables.

5.2.3 SpecBit

SpecBit [87] is an integral part of GAMBIT and the 2HDM implementation. It is necessary for spectrum generation and as such, is a prerequisite to all 2HDM functionality. We detail how spectrum generation happens at tree- and loop-level and introduce the THDMSpec_basis header.

The non-standard GAMBIT header THDMSpec_basis[62] exists for code reuse and exposes THDM basis transformations.

62: The header is located at the include path of gambit/SpecBit/THDMSpec_basis.hpp and is part of the namespace Gambit::SpecBit.

The THDM_spectrum_container struct The standard GAMBIT method is to distribute the spectrum is through the Spectrum object. We respect this policy but require more flexibility as the 2HDMC also creates its own spectrum-like object. On top of this, the multitude of 2HDMs means it is convenient to store and validate basis transformations in a central location. As such, we introduce the THDM_spectrum_container struct.

Most functions involving 2HDM observable or statistical calculations make use of the `THDM_spectrum_container` struct. The struct is filled by the `2HDMC` frontend convenience function `init_THDM_spectrum_container_CONV` and hence is the `THDM_spectrum_container` struct is one of backend types the `2HDMC` reports to `GAMBIT` . It is given by the initialiser:

```
struct THDM_spectrum_container {
    std::unique_ptr<SubSpectrum> he;
    std::unique_ptr<SubSpectrum> SM;
    SMInputs sminputs;
    THDMC_1_8_0::THDM* THDM_object;
    higgs_basis_pars higgs_pars;
    int yukawa_type;
    // constructors and destructors
    THDM_spectrum_container() {
        THDM_object = new THDMC_1_8_0::THDM();
    }
    ~THDM_spectrum_container() {
        delete THDM_object;
    }
};
```

The first three objects in the struct are the extracted component of the `GAMBIT` `Spectrum` object. Storing them separately avoids having to extract the `Spectrum` object each time we need to access either or all of these (and exists purely for convenience as we already need to pass around the struct). Next is the `THDM_object`, which is a `2HDMC` backend class that holds the spectrum and can perform calculations. Many times we require our parameters in the Higgs basis and to conserve function calls we save the Higgs basis parameters to the struct `higgs_pars` with the definition:

```
struct higgs_basis_pars {
        double Lambda1, Lambda2, Lambda3, Lambda4, Lambda5, Lambda6,
        ↪  Lambda7;
        double M11_2, M22_2, M12_2;
};
```

The final member of the `THDM_spectrum_container` struct is an integer that specifies the Yukawa type.

To create a new container struct one should pass an empty container struct to its initialiser function as follows:

```
// Creates a THDM spectrum container with no running scale
inline void init_THDM_spectrum_container(THDM_spectrum_container&
↪ container, const Spectrum& spec, const int yukawa_type);

// Creates a THDM spectrum container
inline void init_THDM_spectrum_container(THDM_spectrum_container&
↪ container, const Spectrum& spec, const int yukawa_type, const
↪ double scale);
```

The initialiser function has been overloaded to allow one to input the energy scale to which the spectrum should be run. The initialiser function takes care of the necessary steps to run the spectrum if desired.

When initialising the `THDM_spectrum_container` the `THDM_object` is also initialised. This involves matching the `GAMBIT` spectrum with that the spectrum used by the `2HDMC` . The `GAMBIT` SM parameters are also matched with the SM parameters in the `2HDMC` . The light-quarks u, d, c, and s are input as $\overline{MS}$ quantities, all other SM fermion and gauge boson masses are given at their pole.

5.2.3.1 Spectrum Generation

`SpecBit` is responsible for the overall generation of the 2HDM spectrum. The spectrum is always input in the generic coupling basis. EWSB is carried out using tree-level relations or using the `FlexibleSUSY` (FS) spectrum generator (which includes loop-corrections and energy running).

FS requires the scalar basis input $\lambda_1, ..., \lambda_7$ and m_{12}^2 at the user-defined input scale Q_{in}. It also requires $\tan\beta$ at the scale of m_t. The input parameters are in the $\overline{MS}$ parameterisation. From the input FS calculates the gauge couplings as well as $v_1, v_2, m_{11}^2, m_{22}^2$ and the Yukawa's at the low-scale m_Z. Next, FS calculates the scalar mass spectrum in the $\overline{DR}$ scheme (at the energy Q_{in}), as well, as the pole masses. If we desire we may use the Q_{runTo} parameter (in conjunction with some likelihood settings) to run all the parameters to the energy Q_{runTo} and perform tests on our theory at this point.

In our scans, we set the input energy scale at which to calculate the spectrum to $Q_{\text{in}} = m_Z$.

The user may choose a `GAMBIT` model that is cast in a different basis to the generic couplings basis, however, in this case, the `THDMSpec_basis` header uses a tree-level conversion to rotate to the generic couplings

basis before starting spectrum generation. This is necessary when using the FS spectrum generator, as it has been configured to only receive input in the generic couplings basis. When using tree-level models, this process results in a closed transformation and hence is not needed.

FS has been configured to accept the four types of 2HDMs in the generic basis. Each FS model that the user chooses to use must be built and specified at the `cmake` stage. To build with all 2HDM FS models the following FS `cmake` flag is required:

```
-DBUILD_FS_MODELS="THDM_I;THDM_II;THDM_LS;
THDM_flipped"
```

These models are also automatically included when specifying the default build command for all FS models.

5.2.3.2 Perturbativity Check on Loop-Corrections

When using models with a FS-generated spectrum, we will have the running scalar masses calculated at $Q_{\text{in}} = m_Z$ as well as the pole masses. To ensure the corrections to the masses remain perturbative, we place an upper limit. The pole mass for scalar ϕ is given as

$$m_\phi = \overline{m}_\phi(m_Z) + \Sigma(m_\phi), \tag{5.18}$$

where $\overline{m}_\phi(m_Z)$ is the running mass and $\Sigma(m_\phi)$ contains the corrections. We construct an upper limit to the corrections based on the assumption that corrections remain perturbative if they are below half the size of the running mass

$$\Sigma(m_\phi) < \frac{\overline{m}_\phi(m_Z)}{2}. \tag{5.19}$$

We apply this limit to each scalar particle as a hard cut-off.

Perturbativity Check on Loop-Corrections

Usage

```
# Checks light CP-even scalar
- purpose:    LogLike
  capability: h0_loop_order_corrections
  function:   check_h0_loop_order_corrections

# Checks extra scalars
- purpose:    LogLike
  capability: THDM_scalar_loop_order_corrections
  function:   check_THDM_scalar_loop_order_corrections
```

Likelihood Type: Hard cut-off
Model Compatibility: CP-violating

5.2.3.3 Stability of the Potential

The stability of our potential is described in section 3.5.1.1. Firstly we use the `2HDMC` program to calculate the stability conditions using the radial parameterisation of the potential. This calculation returns an acceptance/rejection, which translates into a hard cut-off. It is more efficient if we have a half-Gaussian to guide the scanner for a condition of this importance. It proves difficult to convert the radial parameterisation for stability to a half-Gaussian, so instead, for points that fail the radial approach, we apply the conditions obtained from the Minkowski-space-time parameterisation (3.96), (3.97) and (3.98). These conditions are a set of simple inequalities and hence may be more easily converted to half-Gaussians. The radial parameterisation of the potential takes into account both CP- and Z_2-violating terms in the potential. The Minkowski-space-time parameterisation has only been implemented to allow for Z_2-conserving potentials. This may be easily extended beyond Z_2-conserving potentials using the method outlined in section 3.5.1.1.

Checking at different scales We check that stability remains valid up to 1 TeV[63] . Our approach assumes that if stability is valid at both m_Z and 1 TeV, then it is valid along the interval between the energies. As such, we apply the constraint as discussed above at both energies and choose the worse performing likelihood.

63: This upper limit is motivated by energies at next-generation colliders.

To enable checking at scales the following option needs to be added to the likelihood in the *Rules* section of the input YAML file:

```
check_all_scales: true
```

Stability of the Potential

Usage

```
- purpose:    LogLike
  capability: stability_likelihood_THDM
  function:   get_stability_likelihood_THDM
```

Likelihood Type: Hard cut-off and half-Gaussian
Model Compatibility: Softly-broken Z_2-conserving

We also consider the stability of the vacuum through the discriminant introduced in section 3.5.1.2. In this section, we gave a general approach; however, we provided analytic expressions only for a Z_2-conserving model. In `SpecBit`, we have implemented this form for the Z_2-conserving model. Rather than implementation as a likelihood the vacuum stability constraint has been defined as an observable which returns either true or false (1 or 0) if the discriminant condition is satisfied respectively.

Vacuum Stability

Usage

```
- purpose:    Observable
  capability: vacuum_global_minimum
  function:   check_vacuum_global_minimum
```

Likelihood Type: Hard cut-off
Model Compatibility: Softly-broken Z_2-conserving

5.2.3.4 Perturbativity of the Couplings

Initially, we may check that the generic couplings satisfy perturbativity using the limit from perturbative theory corrections of

$$|\lambda_i| < 4\pi. \tag{5.20}$$

In the generic basis, this may be guaranteed at tree-level by the prior limits. We may improve this constraint by looking into the four-Higgs scalar interactions and extracting these couplings

$$|C_{\phi_i \phi_j \phi_k \phi_l}| < 4\pi, \tag{5.21}$$

where $\phi_i = h^0, H^0, A^0, H^+, H^-$. When converting this to a set of half-Gaussian likelihoods, we get an additive effect from each combination; hence, we inevitably end up double-counting some processes. To get around this, we remove identical values from the calculation.

We check perturbativity up to 1 TeV, using the method discussed in the section above.

Perturbativity of the Couplings

Usage

```
- purpose:    LogLike
  capability: perturbativity_likelihood_THDM
  function:   get_perturbativity_likelihood_THDM
```

Likelihood Type: Half-Gaussian
Model Compatibility: CP-violating

5.2.3.5 Unitarity of the Scattering Matrix

This constraint may be calculated at LO or NLO. The leader order scattering eigenvalues are given in section 3.6, with eigenvalues a_l

$$|a_{Y\sigma\pm}^{Z_2\mathrm{LO}}| < \frac{1}{2}. \tag{5.22}$$

Notice that this constraint is not necessary when using the perturbativity constraint. This is because the LO scatterings that enter here are the same $2 \to 2$ Higgs scattering we limit in the perturbativity constraint. The LO scattering eigenvalues are calculated for a general model that may violate CP- and Z_2-symmetry. The next-to-leading-order scattering eigenvalues are also given in section 3.6 and satisfy

$$\left| a_{Y\sigma\pm}^{Z_2\mathrm{NLO}} - \frac{1}{2}i \right| \leq \frac{1}{4}. \tag{5.23}$$

We include wave function corrections to the eigenvalues as well as gauge and Yukawa corrections to the λ_i coupling beta functions. The NLO eigenvalues we use are only derived with a Z_2-symmetric model. The NLO unitarity constraint restricts the parameter space more than LO eigenvalues and, as such, if using the NLO constraint the LO eigenvalue constraint is automatically satisfied. We do however need to check perturbativity here, that is the NLO corrections are not greater than the LO values

$$R = \frac{|a_{Y\sigma\pm}^{Z_2\mathrm{NLO}}|}{|a_{Y\sigma\pm}^{Z_2\mathrm{LO}}|} < 1, \tag{5.24}$$

for each eigenvalue. As discussed in Ref. [39] we need to be careful when the leading order contribution is very small, for example, when $|a^{Z_2\mathrm{LO}}| < 1/(16\pi)$ we do not use the perturbativity check above. Each of the constraints for unitarity is an inequality; hence, it is straightforward to build half-Gaussian likelihoods from the bounds.

The perturbativity check between the LO and NLO scattering eigenvalues needs to be explicitly enabled in the YAML file by adding the following rule to the NLO unitarity likelihood:

```
check_correction_ratio: true
```

Unitarity of the Scattering Matrix

Usage

```
# LO unitarity
- purpose:    LogLike
  capability: LO_unitarity_likelihood_THDM
  function:   get_LO_unitarity_likelihood_THDM

# NLO unitarity (LO unitarity is not required in combination with
↪  this)
# Requires model to have Z2 conservation
- purpose:    LogLike
  capability: NLO_unitarity_likelihood_THDM
  function:   get_NLO_unitarity_likelihood_THDM
```

Likelihood Type: Half-Gaussian
Model Compatibility: Softly-broken Z_2-conserving

5.2.4 `PrecisionBit`

5.2.4.1 Electroweak Oblique Parameters

Section 4.5 describes how we use and calculate the electroweak precision parameters (oblique parameters) and gives references to where we can find suitable derivations for the 2HDM.

We fit the calculated values to the observed values (EWPO), which given in Appendix F.1. These values are evaluated at $m_{h,\text{ref}} = 125$ GeV.

Electroweak Oblique Parameters

Usage

```
- purpose:    LogLike
  capability: oblique_parameters_likelihood_THDM
  function:   get_oblique_parameters_likelihood_THDM
```

Likelihood Type: Gaussian
Model Compatibility: CP-violating

5.2.5 `ColliderBit`

`ColliderBit` [95] allows us to fit our model against collider physics results. We have linked the 2HDM to `HiggsBounds` 5 [92] and `HiggsSignals` 2 [93] beta versions. `HiggsSignals` tests our Higgs sector against LHC Higgs scalar decay rates and masses, while `HiggsBounds` incorporates

LEP, Tevatron and also LHC data and tests against exclusion bounds resulting from Higgs scalar searches.

Specifically the beta versions of `HiggsBounds` and `HiggsSignals` used includes experimental tables up to and including September 2018.

`HiggsBounds` and `HiggsSignals` share the same model-independent input. The input contains the masses and total widths of our the theory scalars, as well as (SM normalised) effective Higgs couplings for the neutral scalars and interesting branching ratios for the charged scalars. We input the neutral scalar properties according to the effective coupling input (described in the `HiggsBounds` 5 manual [94]) and the default charged scalars input. The programs then fit the input to data tables and provide us with a χ^2.[64]

64: We choose the peak-centred methods for the likelihood calculations.

Couplings and decay widths that enter the `HiggsBounds/HiggsSignals` input are provided by `SpecBit` and `DecayBit` respectively and use the in-built coupling and decay calculation routines of the `2HDMC`. The spectrum used in `GAMBIT` is matched with that input to `2HDMC` at the initialisation of each point. However, during the calculation of a coupling or decay, `2HDMC` carries out its own running of quark masses, and in turn Yukawa couplings, to the process energy. This sometimes creates some minor discrepancies between the final FS Yukawa's and those used by the `2HDMC`, which does not affect our results.

5.2.6 `FlavBit`

Flavour constraints are calculated within `FlavBit` [49] using `SuperIso` [91].[65] `FlavBit` fits each constraint to a Gaussian according to the experimental values, errors and correlations recorded in the `FlavBit` database.*

65: `SuperIso` is the only of the backends used in `FlavBit` needed for 2HDM flavour calculations.

`SuperIso` accepts input in the SLHA2 format[96]. SLHA2 input is filled and added to the spectrum object in the `thdm_slhahelp.cpp` helper file[66] . Currently the helper supports filling only the Z_2 Yukawa aligned models. The most important details when filling our models for flavour observables are the Yukawa couplings, which we fill according to Table 4.3. `FlavBit` comes with the following calculations and respective likelihoods built-in:

66: The location of this file is `Elements/src/thdm_slhahelp.cpp`.

- $\mathrm{BR}(\overline{B} \to X_s\gamma)$,
- $B \to K^*\mu^+\mu^-$ angular observables,
- $\mathrm{BR}(B_s^0 \to \mu^+\mu^-)$,
- R_K and R_K^*,
- $\mathrm{BR}(B^\pm \to \tau^\pm\nu)$, $\mathrm{BR}(B \to D\mu\nu)$ and $\mathrm{BR}(B \to D^*\mu\nu)$,
- R_D and R_D^*,
- $\mathrm{BR}(D_s^\pm \to \tau^\pm\nu)$, $\mathrm{BR}(D_s^\pm \to \mu^\pm\nu)$ and $\mathrm{BR}(D^\pm \to \mu^\pm\nu)$.

* The location of the flavour database within `GAMBIT` is`FlavBit/data/flav_data.yaml`.

We have extended `FlavBit` to calculate (using `SuperIso`):

- $\Delta M_{B_s^0}$ and $\Delta M_{B_d^0}$,
- BR($B \to K^* \mu^+ \mu^-$),
- $B \to K^* \mu^+ \mu^-$ isospin asymmetry.

Each of these is detailed below.

$\Delta M_{B_s^0}$ and $\Delta M_{B_d^0}$ `FlavBit` includes a likelihood template for $\Delta M_{B_s^0}$ with the observable calculation obtained from an alternative backend - FeynHiggs (not easily compatible with the 2HDM). We have extended the calculation for $\Delta M_{B_s^0}$ by using `SuperIso` (and also included the calculation for $\Delta M_{B_d^0}$ from `SuperIso`). We have then also added a likelihood function for $\Delta M_{B_d^0}$ based on the $\Delta M_{B_s^0}$ template.

$BR(B \to K^* \mu^+ \mu^-)$ Due to the significant theoretical error in the calculation of $BR(B \to K^* \mu^+ \mu^-)$[67] this calculation is not included by default and instead the angular observables are constrained. As there is a deviation from the SM here, out of interest, we have added this likelihood. We use the experimental values of $dB/(dq^2)$ given in Table 2 of Ref. [97] and then integrate them over the energy bins to get the branching ratio. We then compare this with the branching ratio calculated by `SuperIso` with a 60% theoretical error as discussed in Ref. [98].

67: Arising from form factors.

$B \to K^* \mu^+ \mu^- : A_I$ We include the likelihood for the isospin asymmetry of the process in the energy bin $q^2 = [1.0, 6.0]$ GeV^2,for interest. The experimentally measured value from Ref. [71] is used. We also include a likelihood for the isospin asymmetry zero-crossing and obtain the experimental value from the same reference.

5.2.7 `ScannerBit`

Many algorithms exist which perform Bayesian global fits and offer efficient methods of sampling a distribution. `ScannerBit` [99] is the integrated `GAMBIT` tool that takes the input parameter prior and runs a sampling algorithm. The algorithm which we choose for our `GAMBIT` analysis is `Diver` [99]. `Diver` is a global scanning tool that uses differential evolution. `Diver` does not sample the posterior and thus restricts us to present our final data-sets as profile likelihood distributions.

5.2.7.1 Differential Evolution

`Diver` invokes a method known as the differential evolution (DE) algorithm. The specific DE algorithm that `Diver` uses is known as jDE with rand/1/bin evolution [100].

Consider a sample of points in our multi-dimensional parameter space $\{\mathbf{X_i}\}$.[68] Each point within this sample is known as a target vector.

68: Initially they are randomly generated.

We want to traverse the parameter space with different sets of target vectors. This process has three steps mutation, crossover and selection.

Step One: Mutation Initially, we want to randomly combine target vectors to create what are known as donor vectors

$$\mathbf{V}_i = \mathbf{X}_{r1} + F(\mathbf{X}_{r2} - \mathbf{X}_{r3}), \tag{5.25}$$

where

- $\mathbf{V}_i$ is the donor vector.
- $\mathbf{X}_{r1}, \mathbf{X}_{r2}, \mathbf{X}_{r3}$ are random target vectors chosen from the sample of points. The randomly chosen vectors have the condition that no two are the same, and none are equal to $\mathbf{X}_i$, i being the index of the donor vector under construction.
- F is the scaling factor; it is used to determine how much we want the distance between $\mathbf{X}_{r2}$ and $\mathbf{X}_{r3}$ to affect our donor vector.

Step Two: Crossover The next step combines the target vectors with donor vectors component-wise into a sample of what we call trial vectors $\mathbf{U_i}$. We set a parameter Cr in $(0, 1)$ and then choose a random number r_k in $(0, 1)$. Then the kth component of $\mathbf{U_i}$ is

$$(\mathbf{U}_i)_k = \begin{cases} (\mathbf{V}_i)_k, & \text{if } r_k \leq Cr \\ (\mathbf{X}_i)_k, & \text{if } r_k > Cr. \end{cases} \tag{5.26}$$

To guarantee that $\mathbf{U}_i$ and $\mathbf{X}_i$ are not the same we make one final replacement $(\mathbf{U}_i)_l = (\mathbf{V}_i)_l$, with a random l for each i.[69]

69: Notice, that $\mathbf{U} = \mathbf{V}$ is possible.

Step Three: Selection The final step checks each of our newly developed trial vectors in the sample $\{\mathbf{U_i}\}$ to see if they are fit to replace their corresponding target vector. Assigning generation superscript, each point with the best likelihood is selected for the next generation[70]

$$\mathbf{X}_i^{g+1} = \max[\mathscr{L}(\mathbf{X}_i^g), \mathscr{L}(\mathbf{U}_i^g)]. \tag{5.27}$$

70: If the points have the same likelihood we accept the new point regardless.

By this method each point is always as good or better than the last. Due to this it is possible to miss the global minimum depending on the initial conditions.

To summarise, we randomly combine our sample of target vectors to form a sample of the donor vector. We then randomly combine the donor and target vectors to produce a sample of the trial vector. For our final sample of trial vectors, the likelihood of each point is compared with the likelihood of the corresponding point in the sample of target vectors (before combination), whichever has the better likelihood is kept. In this way, we are evolving towards the best likelihood points in our parameter space.

We see that the algorithm depends on three parameters. The first, although not explicitly mentioned, is the number of points that we initially (randomly) selected in our sample of target vectors. The second is the scaling factor F. The scaling factor F should be chosen between 0.1 and 0.9. It affects the size of steps between points; hence, a small scaling factor leads to slow convergence, whereas, if the scaling factor is too large convergence may not be possible. The third parameter of importance is the bound Cr, which dictates the mixing of the target and donor vectors into the trial vector. The bound Cr may be chosen anywhere between 0 and 1. A low Cr, interestingly, separates dependence between dimensions, whereas a large Cr will increase contributions from the donor vector leading to greater exploration of parameter space.

Another model available is λjDE which allows for self-adaptive optimisation of parameters.

In our study, we use the jDE algorithm with the default settings provided by `Diver`, where the F and Cr parameters are randomly selected for each trial.

5.3 Independent Type-III Global Fit

Aside from the `GAMBIT` scan, we carry out an independent global fit of the most general 2HDM (the type-III) with FC currents. Unlike the global fits for the Z_2-aligned models our goal here is not to analyse the entire parameter space of the model but instead to see if the model can accommodate the ΔM_{B_s}, ΔM_{B_d} and BR($B \to X_s\gamma$) flavour processes.

The type-III model does not conserve Z_2-symmetry and has interesting consequences on the flavour sector. These include predicted contributions to FC decays that are highly suppressed in the SM. We are interested in these FC decays as they may provide evidence for a 2HDM. The two processes we want to fit with our global scan are

$h \to bs$ and $t \to ch$. Current experimental bounds on the branching ratios of processes with a top decaying are at the 10^{-3} level (see Refs. [55, 101–103]). We have at 95% CL

$$\mathrm{BR}(t \to hq) < 7.9 \cdot 10^{-3}, \quad \mathrm{BR}(t \to ch) < 2.2 \cdot 10^{-3}, \mathrm{BR}(t \to hu) < 2.4 \cdot 10^{-3}. \tag{5.28}$$

To predict potentially large upper bounds for the $h \to bs$ process we are especially interested in investigating the B_s^0 meson-mixing deviation from the SM and fitting it onto the type-III. Radiative B decays constrain the $t \to ch$ process, which are also included in the fit.

We create an independent `C++` code to perform such a global fit. To do so, we link likelihood routines with the statistical global scanning code `MultiNest`.

We carry out this fit using tree-level relations on the spectrum generation and apply the same theoretical constraints that we did on the `GAMBIT` scan. We, however, calculate the scattering eigenvalues only at LO. Vacuum meta-stability is also not checked for this scan, as it becomes more complicated with Z_2-breaking. We check the electroweak precision parameters agree with observed values and fit the flavour observables:

- ΔM_{B_s} and ΔM_{B_d},
- β_s (meson-mixing phase),
- $\mathrm{BR}(B \to X_s \gamma)$.

The calculations of the flavour observables (for the type-III fit) have been coded up specifically for this study. To our knowledge they did not exist out-of-the-box in any package for the 2HDM without Z_2-alignment. [71]

The experimentally observed values for these processes and the electroweak precision parameters are given in Appendix F.1.

To fit the SM-like signal strengths we use a custom code snippet rather than `HiggsSignals` for this study. [72] As usual we identify SM-like scalar state with the field h, and thus the first requirement is $m_h = (125.09 \pm 0.32)$ GeV [104]. The width is also required to satisfy $\Gamma_h < 17$ MeV following the result at 2σ presented in Ref. [105]. The most relevant information for the phenomenological aspects of the 125 GeV scalar is the set of signal strengths μ_{XY} for combined production (Y) and decay (X) channels

$$\mu_{XY} = \frac{\sigma([pp]_Y \to h)_{\mathrm{2HDM}} \, \mathrm{BR}(h \to X)_{\mathrm{2HDM}}}{\sigma([pp]_Y \to h)_{\mathrm{SM}} \, \mathrm{BR}(h \to X)_{\mathrm{SM}}}, \tag{5.29}$$

which are factorised in production × decay model dependent factors

71: We are working to extend `GAMBIT` to be completely compatible with the general type-III model in the future, meaning that it will support all flavour observables previously discussed.

72: The future `GAMBIT` implementation will use `HiggsBounds` and `HiggsSignals` for collider constraints.

$$\mu_{XY} = \kappa_Y^P \kappa_X^{BR}, \qquad \kappa_Y^P = \frac{\sigma([pp]_Y \to h)_{\rm 2HDM}}{\sigma([pp]_Y \to h)_{\rm SM}}, \quad \kappa_X^{BR} = \frac{{\rm BR}(h \to X)_{\rm 2HDM}}{{\rm BR}(h \to X)_{\rm SM}}. \tag{5.30}$$

The relevant production modes are gluon-gluon fusion (ggF), vector boson fusion (VBF), Higgs-strahlung (Wh, Zh) and associated production with top quarks (tth); the corresponding factors are

$$\begin{aligned} \kappa_{ggF}^P &= \frac{\Gamma(h \to gg)_{\rm 2HDM}}{\Gamma(h \to gg)_{\rm SM}}, \\ \kappa_{tth}^P &= \frac{v^2}{2m_t^2}\left(|\Gamma_{tt}^{LRh}|^2 + |\Gamma_{tt}^{RLh}|^2\right), \\ \kappa_{VBF}^P &= \kappa_{WH}^P = \kappa_{ZH}^P = s_{\beta\alpha}^2 . \end{aligned} \tag{5.31}$$

where the couplings Γ (not to be confused with the widths with the same symbol) may be read from Table 4.5. The corresponding factors for the relevant decay channels are

$$\begin{aligned} \kappa_{\gamma\gamma}^{BR} &= \frac{\Gamma(h \to \gamma\gamma)_{\rm 2HDM}}{\Gamma(h \to \gamma\gamma)_{\rm SM}}, \\ \kappa_{bb}^{BR} &= \frac{v^2}{2m_b^2}\left(|\Gamma_{bb}^{LRh}|^2 + |\Gamma_{bb}^{RLh}|^2\right), \\ \kappa_{\tau\tau}^{BR} &= \frac{v^2}{2m_\tau^2}\left(|\Gamma_{\tau\tau}^{LRh}|^2 + |\Gamma_{\tau\tau}^{RLh}|^2\right), \\ \kappa_{WW}^{BR} &= \kappa_{ZZ}^{BR} = s_{\beta\alpha}^2 . \end{aligned} \tag{5.32}$$

Both κ_{ggF}^P and $\kappa_{\gamma\gamma}^{BR}$ arise from one-loop amplitudes: the expressions may be found, for example, in Ref. [18]. For $h \to \bar\tau\tau$, since we assume for simplicity SM-like Yukawa couplings in the lepton sector, $\kappa_{\tau\tau}^{BR} = s_{\beta\alpha}^2$ (the experimental uncertainties in that decay channel are, in any case, large).

The experimental results (values and uncertainties) from the combined ATLAS and CMS analyses of LHC Run I data [106] are given in the following matrix:

$$\mu_{XY} = \begin{pmatrix} 1.1^{+0.23}_{-0.22} & 1.3^{+0.5}_{-0.5} & 0.5^{+1.3}_{-1.2} & 0.5^{+3.0}_{-2.5} & 2.2^{+1.6}_{-1.3} \\ 1.13^{+0.23}_{-0.22} & 0.1^{+0.5}_{-0.5} & \times & \times & \times \\ 0.84^{+0.17}_{-0.17} & 1.2^{+0.4}_{-0.4} & 1.6^{+1.2}_{-1.0} & 5.9^{+2.6}_{-2.2} & 5.0^{+1.8}_{-1.7} \\ 1.0^{+0.6}_{-0.6} & 1.3^{+0.4}_{-0.4} & -1.4^{+1.4}_{-1.4} & 2.2^{+2.2}_{-1.8} & -1.9^{+3.7}_{-3.3} \\ \times & \times & 1.0^{+0.5}_{-0.5} & 0.4^{+0.4}_{-0.4} & 1.1^{+1.0}_{-1.0} \end{pmatrix}. \tag{5.33}$$

The ordering for decay channels (rows) is $\{\gamma\gamma, ZZ, WW, \tau\tau, bb\}$ and for production mechanisms (columns) {ggF, VBF, Wh, Zh, tth}. For the missing entries ($\times$) there is no measurement available in Ref. [106]. In addition to Eq. (5.33), we also include CMS and ATLAS data from LHC Run II on $h \to \bar b b$ and $h \to \bar\tau\tau$ in the analysis for $h \to \bar b b$, we consider CMS [107] and ATLAS [108] results for VBF production while

for $h \to \bar{\tau}\tau$ we combine ggF and VBF production following Ref. [109]. Notice that the analysis of Higgs signal strengths only requires the 2HDM vs. SM modifying factors in Eqs. (5.31) – (5.32).

Lastly, we require that the observed upper bounds (5.28) on the FC decays we are trying to reach are not crossed.

We do not consider any searches for extra scalars in this work, but will do so in anticipated the general type-III using `GAMBIT`.

5.3.1 Likelihoods

We need to provide likelihood functions $\mathscr{L}$ (or $\chi^2 = -2\ln\mathscr{L}$) to scan the parameter space of the model. To ensure that the masses of the scalars are positive, as well as to impose stability of the scalar potential, we use a hard cut-off: for a calculated value $\mathcal{O}_{\text{calc}}$ and lower bound B_i

$$\chi^2_{\text{bounds}} = \begin{cases} 0, & \text{if } \mathcal{O}_{\text{calc}} > B_i \\ \chi_{\text{max}} & \text{if } \mathcal{O}_{\text{calc}} \leq B_i, \end{cases} \tag{5.34}$$

where χ_{max} is large enough that the scanner effectively invalidates the point. The reverse of this may be used for an upper bound. A soft cut-off imposes unitarity and perturbativity

$$\chi^2_{\text{bounds}} = \begin{cases} 0, & \text{if } \mathcal{O}_{\text{calc}} < B_i/0.64 \\ \left(\frac{0.64\mathcal{O}_{\text{calc}}}{B_i} - 1\right)^2, & \text{if } \mathcal{O}_{\text{calc}} \geq B_i/0.64\,, \end{cases} \tag{5.35}$$

where B_i is the upper bound at 68% confidence (improving the guidance provided to the scanner). For observables that have been measured we use a centred distribution with the observed value at $\mathcal{O}_{\text{obs}}$ and error σ

$$\chi^2_{\text{observables}} = \left(\frac{\mathcal{O}_{\text{calc}} - \mathcal{O}_{\text{obs}}}{\sigma}\right)^2. \tag{5.36}$$

The final χ^2-like function is built from all M bounds and N observables

$$\chi^2 = \sum_i^M \chi^2_{\text{bounds,i}} + \sum_i^N \chi^2_{\text{observables,i}}\,. \tag{5.37}$$

For B_s^0–$\bar{B}_s^0$ mixing and BR($B \to X_s\gamma$), we sum the errors of the experimental and calculated values in quadrature.

5.3.1.1 Scanning Algorithm: Nested Sampling

To scan our parameter space and perform the global fit, we need to select a scanning algorithm. We select `MultiNest` [110] [111] [112] which uses an extension of Monte Carlo known as nested sampling. `MultiNest` calculates the Bayesian evidence and allows us to present

the final results as either posterior probability distributions or profile likelihood distributions.

The likelihood $\mathscr{L}$ is a probability distribution function in D dimensions which at each point gives a likelihood for the corresponding model parameters θ. We can define iso-contours on the likelihood distribution for different θ as $\lambda = \mathscr{L}(\theta)$. We can introduce the prior volume function X which is the volume of the prior above the iso-contour defined by θ as

$$X(\lambda) = \int_{\mathscr{L}(\theta)>\lambda} \pi(\theta) d^D\theta. \tag{5.38}$$

We may stage the likelihood as a function of the prior volume X. We do this by introducing

$$\mathscr{L}(X) = \lambda X(\lambda), \tag{5.39}$$

which is the likelihood iso-contour at $\mathscr{L}(\theta) = \lambda$ multiplied by the prior volume above this contour. Recall the evidence is defined as the total volume of the likelihood multiplied by the prior. In this notation, this is just the sum of all of the different values our iso-contour $\mathscr{L}(\theta) = \lambda$ can take

$$\begin{aligned} Z &= \int_\lambda \lambda X(\lambda) d\lambda, \\ \implies Z &= \int_0^1 \mathscr{L}(X) dX. \end{aligned} \tag{5.40}$$

The integration bounds in the second equation arise due to X being a probability distribution function, X is defined on the interval $[0, 1]$. Now, this form of expressing the evidence may be approximated by the trapezium rule, defining a particular value of X within $[0, 1]$ as X_i, and then $\mathscr{L}_i = \mathscr{L}(X_i)$ gives

$$Z = \sum_i^M \mathscr{L}_i w_i, \tag{5.41}$$

where

$$w_i = \frac{1}{2}(X_{i-1} - X_{i+1}). \tag{5.42}$$

In the summation M represents the number of points we want to calculate within our interval $[0, 1]$. With this, we are ready to describe the sampling process:

1. Starting at step $i = 0$, we select N points from the prior. As these N points can be selected from anywhere in the prior we set $X_0 = 1$, that is, the full prior volume.
2. Evaluate the likelihoods at the N points and sort them by their order of magnitude, with $\mathscr{L}_0$ being the smallest.
3. Progressing to step $i = 1$, draw a point from the prior and if $\mathscr{L} > \mathscr{L}_0$, remove $\mathscr{L}_0$ from the point set. Now, the prior volume X_1 will be less than X_0 as the new likelihood defines an iso-contour

that is more restrictive than that defined by $\mathscr{L}_0$. We set the new prior volume to $X_1 = t_1 X_0$, where t_1 must be in the interval $[0,1)$. As we are randomly selecting points, t_1 is a random variable on $[0,1)$, such a variable follows the distribution $\Pr(t) = Nt^{(N-1)}$. The knowledge of this distribution is useful as it allows us to make statistical predictions about the entire distribution.

4. We repeat step 3 until the contribution to the evidence, which is given at each step using the trapezium rule, reaches a particular tolerance. This tolerance is given by Tol $Z_i = \mathscr{L}_{\max} X_i$, with $\mathscr{L}_{\max}$ being the maximum value the likelihood attains in the current set of points.
5. From the remaining set of N points, we may add a final contribution to Z

$$\Delta Z = \sum_{j=1}^{N} \mathscr{L}_j \frac{X_M}{N}. \tag{5.43}$$

This process allows us to find the evidence Z and do a statistically meaningful scan over the entire parameter space. We keep the data for each point that is calculated, and we can recreate the posterior by assigning each point a weight

$$p_j = \frac{\mathscr{L}_j w_j}{Z}. \tag{5.44}$$

With this weighting, we can calculate statistical quantities and plot marginalised posterior distributions. `MultiNest` extends this approach by making use of an improved ellipsoidal nested sampling algorithm. See the `MultiNest` manual for an extension to this definition.

PART II: RESULTS

Global Scans of Softly-Broken Z_2 Yukawa Aligned 2HDMs

6

In this chapter, we present the *preliminary* results of our global fits of the softly-broken Z_2-symmetric models in which the Yukawa sectors are said to be aligned. We perform our scans in the generic basis and include all the likelihoods described in the previous section. The prior we use on our scans is given in Table 6.1. For t_β, we use a logarithmic prior to assist with the exploration of difficult to reach regions of the parameter space. The parameter m_{12}^2 has a vast prior region, and it is useful to break it up into a combination of flat and logarithmic regions. The form of interval given in the table, may be read as edge regions ($[-10^6, -10^4]$, $[10^4, 10^7]$) being logarithmic and the region between ($[-10^4, 10^4]$) being flat. It's notable that $\lambda_1 > 0$ and $\lambda_2 > 0$ are required for a stable potential, although not done here, in future work it is wise to set the prior to $[-0.5, 4\pi]$ for λ_1 and λ_2. Here the lower value of -0.5 is arbitrary but we choose it less than zero in case the running of the couplings allows an opening that is negative.

The global fit results are presented as one- and two-dimensional profile likelihood distributions of interest, with the best-fit point shown by a star. The data have been parsed and plotted by `pippi`. One-dimensional plots are overlaid with three dashed lines to indicate confidence levels; from the top down, the lines represent the $1\sigma(68.3\%)$, $2\sigma(95.4\%)$ and $3\sigma(99.7\%)$ regions, respectively. Likewise, the two-dimensional distributions show the same confidence intervals, with solid lines, and the shading indicates the profile likelihood ratio at any point.

We plot the results of all four Z_2-symmetric 2HDMs, but as the literature focuses generally on the type-II, results for the type-II are (during *preliminary* stages) conducted with a higher number of sample points.

The one-dimensional and two-dimensional distributions of the generic couplings in the type-I, type-II, lepton-specific and flipped models are given in Figures 6.1, 6.2, 6.3 and 6.4 respectively.

Table 6.1: Parameters scanned over in our global fits, along with the priors used. The `GAMBIT` models also accept λ_6 and λ_7. As we work with Z_2-symmetry, we have set these to zero explicitly.

Parameter	Range	Prior Type
$\lambda_{1,2,3,4,5}$	$[-4\pi, 4\pi]$	Flat
t_β	$[0.01, 100]$	Log
m_{12}^2 (GeV)^2	$[-10^6, -10^4, 10^4, 10^7]$	Log/Flat

Figure 6.1: 1D and 2D profile likelihood distributions for the potential couplings (generic basis) in the *type-I model*.

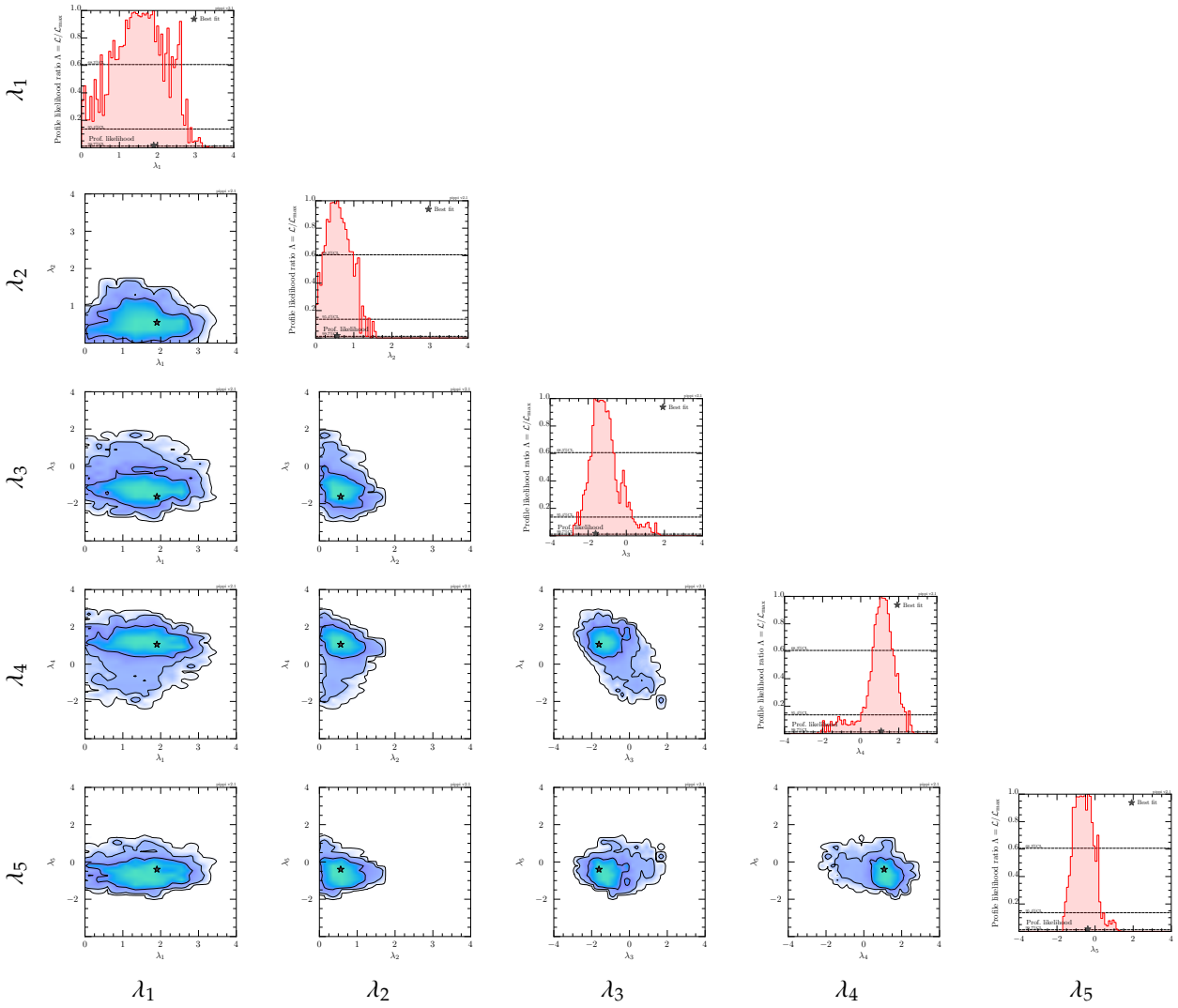

The best-fit points of each of these are given in Table 6.2. Starting at each of the best-fit points, we plot the running of the couplings up to 100 TeV; the running plots are shown in Figure 6.5.

Notice the similarities between the best-fit points, as well as the one-dimensional distributions. The type-II and flipped models display similarities and the type-I and lepton-specific models also display similarities. In fact, these similarities are easily explained by noticing that each pair of models shares a similar Yukawa structure. As such, it becomes evident that Yukawa structure significantly dictates the distributions of each of the model types. It is noteworthy to mention that Yukawa structure enters only in the experimental likelihoods.

In Figure 6.6, we plot the 2D profile likelihood distributions of the couplings with the theoretical constraints imposed exclusively. These include the stability of the potential and perturbativity of the four-point scalar couplings up to 1 TeV, the NLO unitarity bound on the scattering matrix with a perturbativity check on the NLO values, and

Figure 6.2: 1D and 2D profile likelihood distributions for the potential couplings (generic basis) in the *type-II model*.

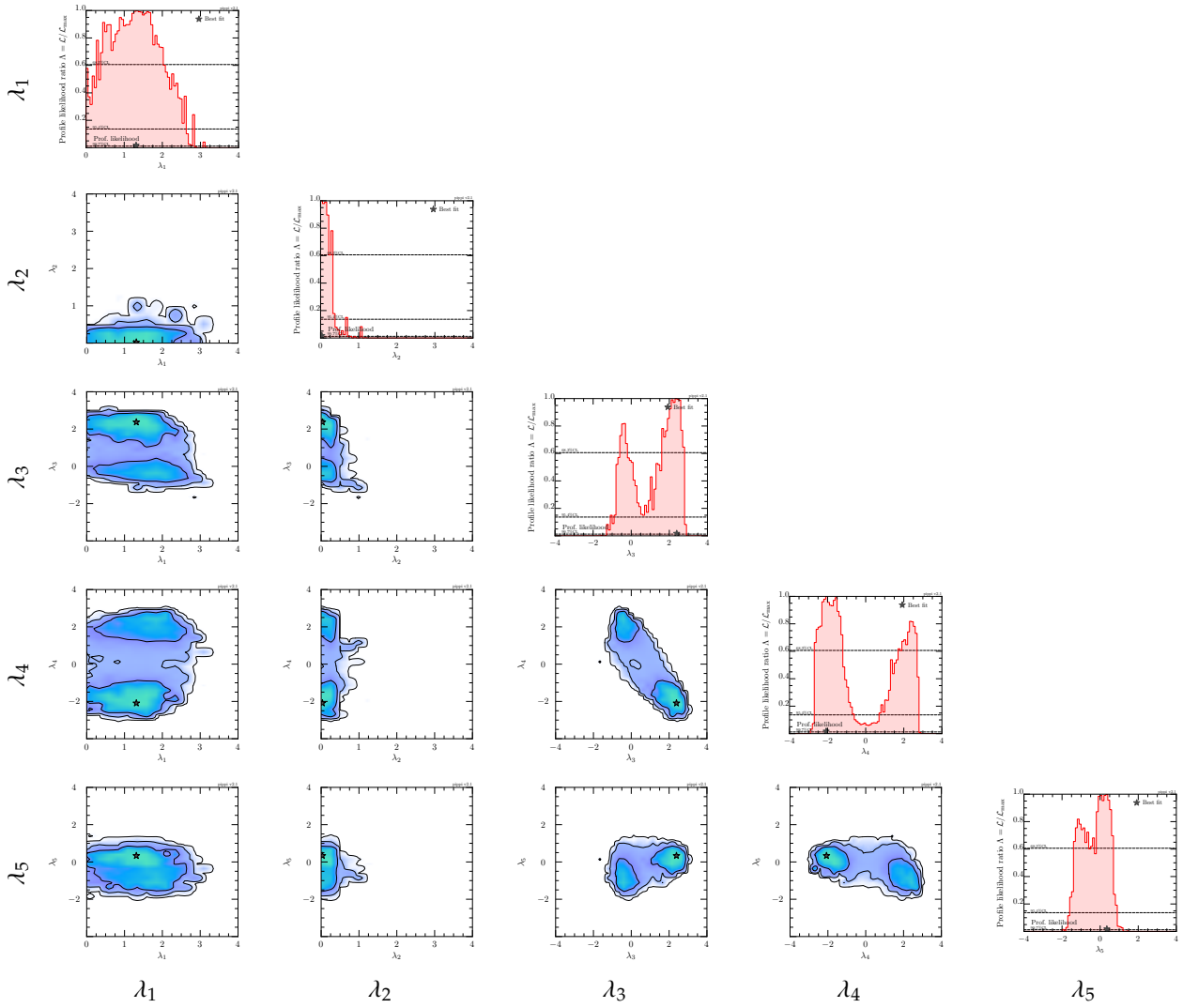

perturbativity checks on loop corrections to all scalars. The NLO scattering eigenvalues shown here are calculated without wave-function corrections or gauge and Yukawa coupling contributions to the beta functions.

As mentioned before, $\lambda_1 > 0$ and $\lambda_2 > 0$ are required for a stable potential, and as such, we only plot their positive values. The remainder of the couplings are plotted in the interval $[-4, 4]$ which encloses all of the parameter space up to 3σ. Note that all points plotted, also satisfy the vacuum meta-stability discriminant, which is to say that they correspond to a global minimum vacuum solution.

We see that λ_1 has the largest possible values within our combined fit. It proves useful to calculate the maximum value up to which λ_1 remains perturbative when running up to 1 TeV as done in our scan. Using the one-loop beta function for λ_1 given in Ref. [24] and ignoring

Figure 6.3: 1D and 2D profile likelihood distributions for the potential couplings (generic basis) in the *lepton-specific model (type-X)*.

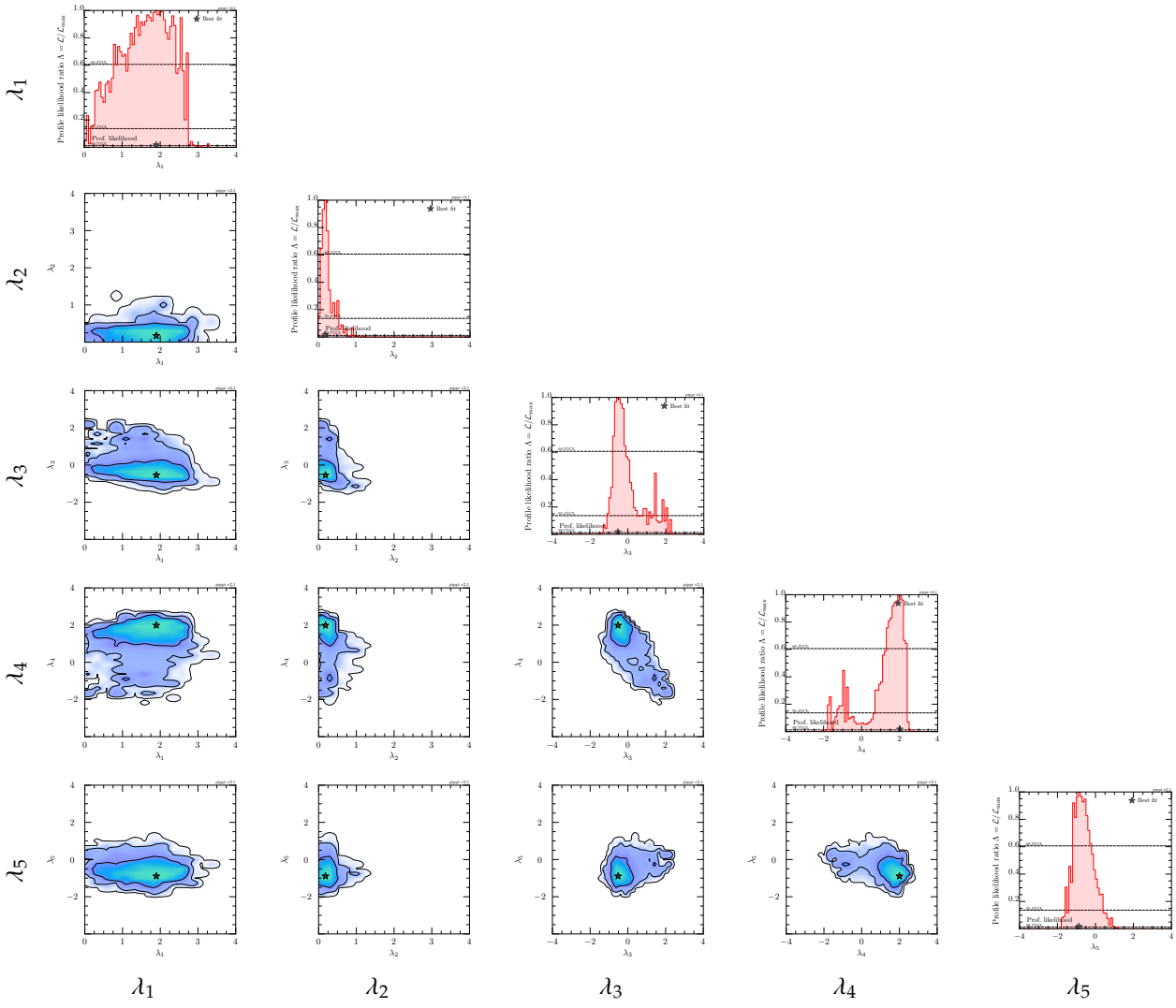

all other λ_i contributions ($i = 2, 3, 4, 5$)

$$\frac{d\lambda_1}{d\ln\mu^2} = \frac{3\lambda_1^2}{8\pi^2}. \tag{6.1}$$

Solving, we find that $\max[\lambda_1(m_Z)] \sim 5.5$ such that $\lambda_1(\mu = 1000\text{GeV}) < 4\pi$. This value is safely below the upper limit found by the scan. However, we note that we have not included other λ contributions during running. Further, we have not applied corrections beyond order-one, and we note that in our perturbativity constraint we more carefully limit $2 \to 2$ Higgs scalar couplings, not just λ_1. Hence, perturbativity up to 1 TeV may explain the upper limit on λ_1. Carrying out individual theoretical and experimental scans confirms this.

On the other hand, λ_2 has the smallest attainable values and $\lambda_2 < 1$ at 2σ for all models but the type-I where it is $\lambda_2 < 1.5$ at 2σ. The push towards low values for λ_2 may be explained by the form taken on by the CP-even scalar mass matrix. In the simple case of $\lambda_3 = \lambda_4 = \lambda_5 = 0$,

Figure 6.4: 1D and 2D profile likelihood distributions for potential couplings (generic basis) in the *flipped model (type-Y)*.

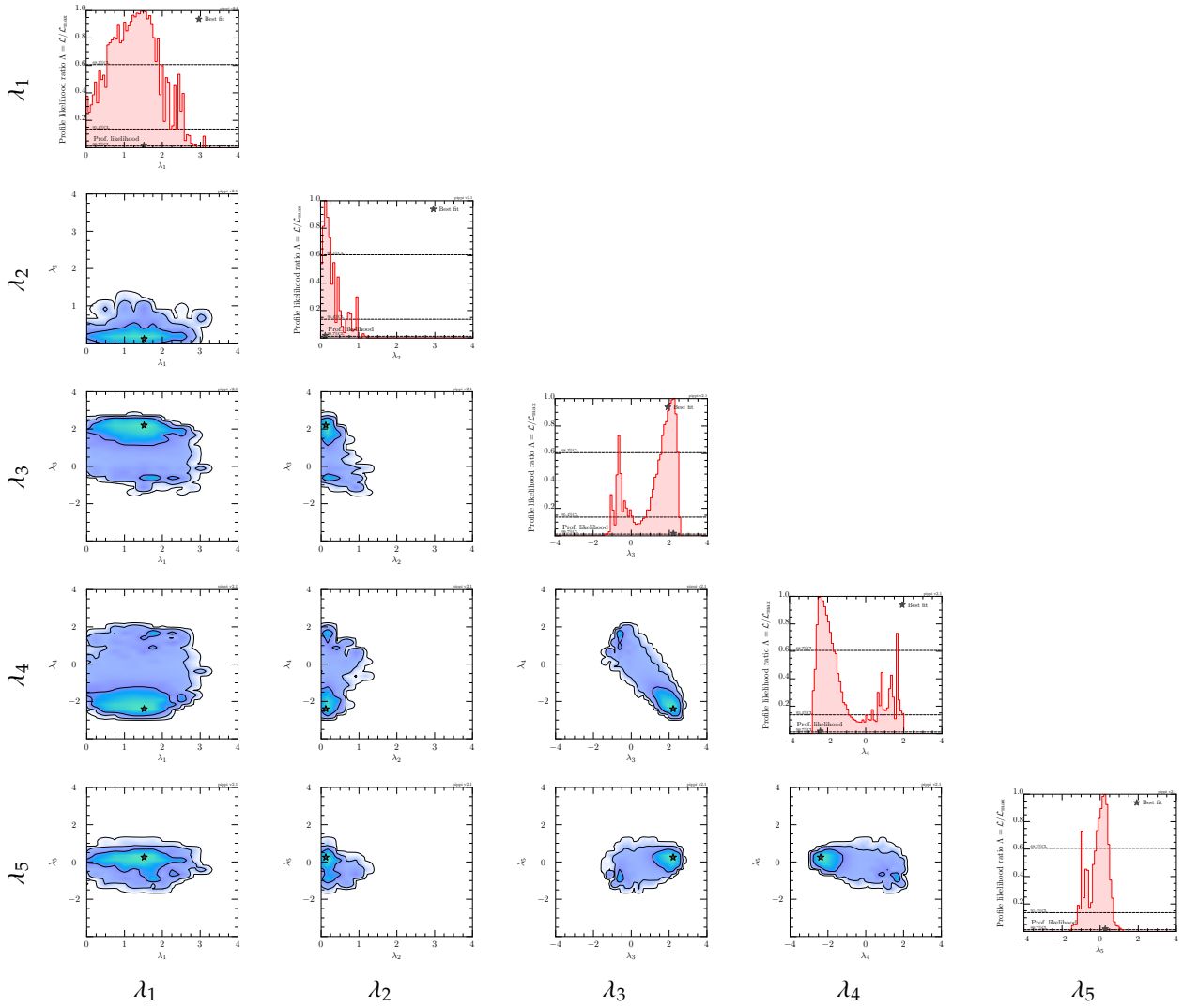

the CP-even Higgs masses are given at tree-level by Eq. (3.92). We rewrite them here for convenience

$$m_h^2 = \frac{m_{12}^2}{t_\beta} + v^2 s_\beta^2 \lambda_2, \quad m_H^2 = m_{12}^2 t_\beta + v^2 c_\beta^2 \lambda_1. \tag{6.2}$$

In an SM-like limit ($t_\beta \to \infty, s_\beta \to 1, c_\beta \to 0$) these masses become

$$m_h^2 \sim v^2 \lambda_2, \quad m_H^2 \sim m_{12}^2 t_\beta. \tag{6.3}$$

If we fix m_h to its observed value of 125 GeV in this limit then λ_2 is also fixed at $\sim$ 0.26. In the opposite case when t_β is small then m_h is approximately proportional to the m_{12}^2 term. This opens up the λ_2 value to variation away from this fixed value. This relationship may be seen in Figure 6.7, where we plot λ_2 against t_β for a tree-level model and a constraint has been placed that a CP-even scalar is fixed at the observed SM Higgs boson values.[74]

74: Here we have not applied any theoretical constraints, hence, negative values of λ_2 are open.

Table 6.2: The values of the couplings at the best-fit point.

Model Type	$\lambda_{1\text{best}}$	$\lambda_{2\text{best}}$	$\lambda_{3\text{best}}$	$\lambda_{4\text{best}}$	$\lambda_{5\text{best}}$
Type-I	1.9	0.5	-1.6	1.1	-0.5
Type-II	1.3	0.1	2.2	-2.1	0.2
Lepton-specific (X)	1.9	0.2	-0.5	2.0	-0.9
Flipped (Y)	1.5	0.2	2.2	-2.4	0.2

Figure 6.5: Running of couplings in the various 2HDMs starting at the best-fit point. Running is between m_Z and 100 TeV. *Top-left:* type-I model, *Top-right:* type-II model, *Bottom-left:* lepton-specific (type-X) model, *Bottom-right:* flipped (type-Y) model.

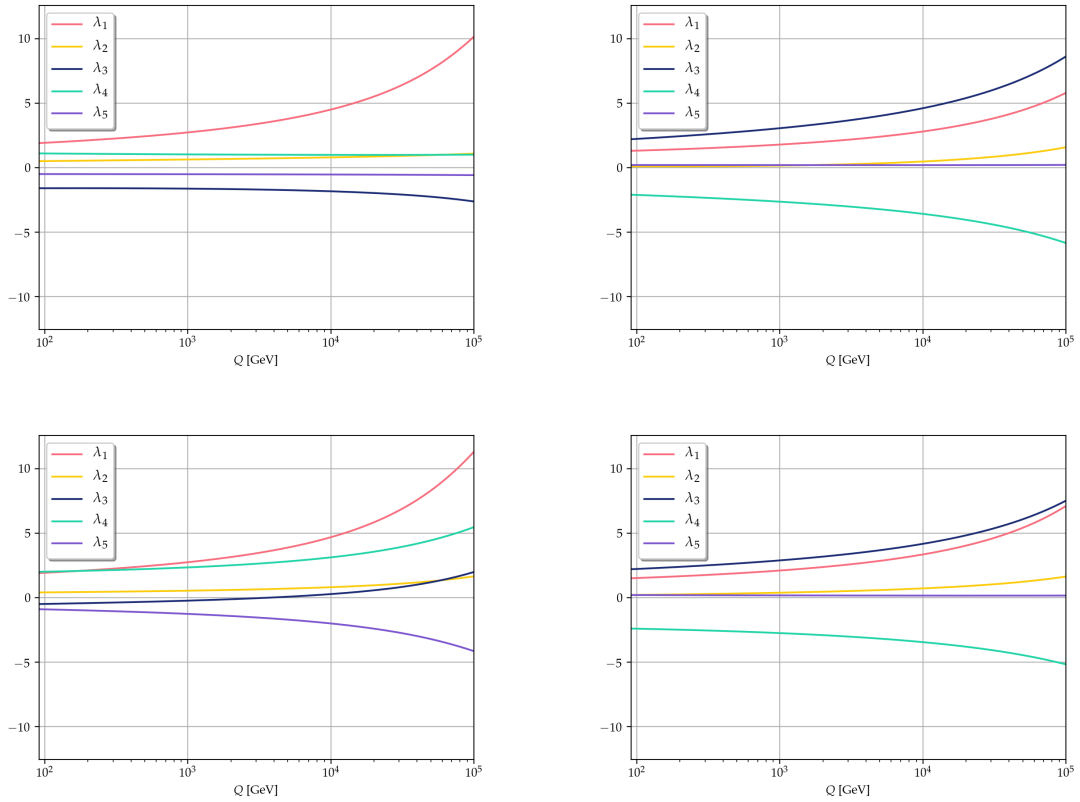

Figure 6.6: 2D profile likelihood distributions of the potential couplings (generic basis) with only the theoretical constraints of our scan imposed. We show the 3σ region.

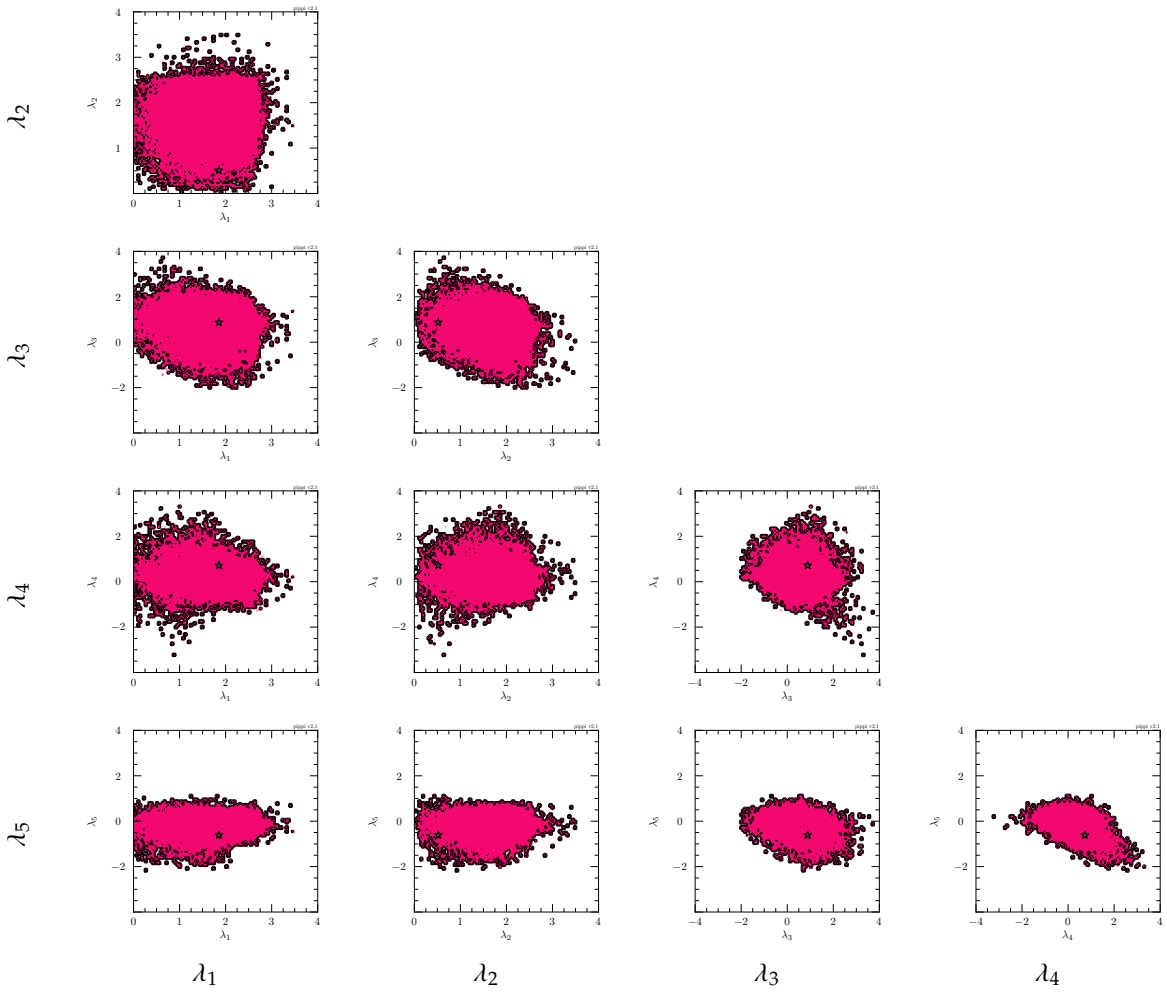

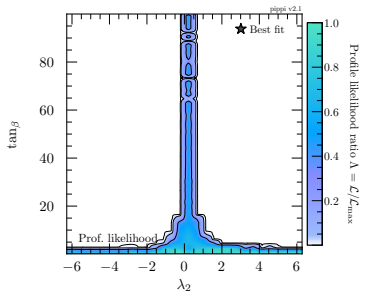

Figure 6.7: 2D profile likelihood distribution of λ_2 vs t_β with only an observed SM Higgs boson mass constraint applied to CP-even scalars via `HiggsSignals`.

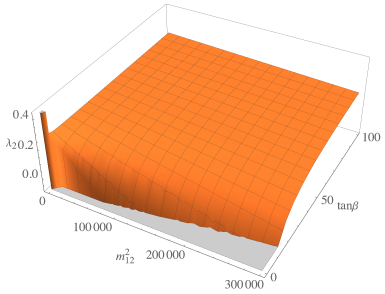

Figure 6.8: 3D plot of λ_2 vs t_β vs m_{12}^2 with $\lambda_3 = \lambda_4 = \lambda_5 = 0$. The orange plane represents the solution plane where $m_h = 125$ is realised. The grey region represents un-physical solutions.

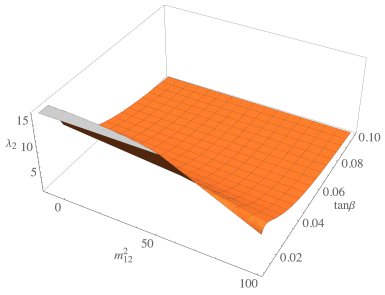

Figure 6.9: Same as 6.8 but highlighting the area with low t_β and m_{12}^2 where a large range for λ_2 is realised. The grey region here is a plotting artefact and does not represent un-physical solutions.

The implication for the relationship between λ_2 and t_β due to this constraint is that, for models with small values of t_β that are not allowed, or not easily accessible*, the value of λ_2 is fixed at ~ 0.26. We have not yet looked at the values that t_β may reach in each model but we observe from the best-fit points and distributions that the type-I and flipped models have the least constrained λ_2 parameter space and, hence, we predict for these models lower limits on t_β.

In Figure 6.8 we show this relationship in three-dimensions, adding m_{12}^2. We plot λ_2 vs t_β vs m_{12}^2 with $\lambda_3 = \lambda_4 = \lambda_5 = 0$ and add a plane (orange) that represents solutions of the three-parameters where $m_h = 125$ GeV is realised. Looking at the form of Eq. (6.2) we see that a large m_{12}^2 makes the m_{12}^2 term more significant (particularly in the lower t_β limit). To cancel contributions from a larger m_{12}^2 term we require λ_2 to be less than the ~ 0.2 solution and even go negative. A negative λ_2 is forbidden by stability of the potential so we have a region of parameter space where λ_2 cannot satisfy both the stability and Higgs mass constraints. This may be seen as the grey region in the Figure (which technically represents solutions where one or more of the scalar masses goes negative). This grey region is bounded by a proportional relationship between m_{12}^2 and t_β as they compete to keep λ_2 positive.

As expected, the majority of the figure shows that the solution plane gives $\lambda_2 \sim 0.2$. Smaller values of λ_2 may be found exclusively where m_{12}^2 is above some threshold, as explained. Interestingly, the curvature of the plane decreases as m_{12}^2 grows, meaning there are more values less than $\lambda_2 \sim 0.2$ in the larger m_{12}^2 region. Finally, near low m_{12}^2 and t_β, λ_2 may take on in theory, any value. This thin sliver of parameter space is both difficult to sample and may already be restricted by other model constraints. We plot this region in Figure 6.9 where we may see the large attainable range of λ_2.

The distributions of λ_3 and λ_4 are peaked away from zero for each of the models. More specifically, within the type-II and flipped models both λ_3 and λ_4 accommodate two peaks (at 1σ) either side of zero. In the type-I and lepton-specific models λ_3 has a single peak (at 1σ) below zero and λ_4 has a peak above zero (at 1σ) and a smaller peak below zero (at 2σ). The λ_5 distributions also share subtle similarities in the type-II and flipped models, where they exhibit roughly Gaussian peaks centred on zero.

At this point we should investigate the features as well as the collider and electroweak precision parameter constraints.

Given collider constraints there are limits that come from two locations. Firstly, we look at direct collider constraints that have searched

* Accessibility in this case refers to the scanners ability to reach these points. Accessibility may improved through educated changes to the prior.

Table 6.3: Light CP-even Higgs (h^0) to fermion 2HDM Yukawa scalings to fermions for each of the Z_2 aligned 2HDMs. We give the reference to the corresponding set of figures for each type.

Type	$\Gamma^h_u \frac{v}{M_u}$	$\Gamma^h_d \frac{v}{M_d}$	$\Gamma^h_e \frac{v}{M_e}$	Figure
I	c_α/s_β	c_α/s_β	c_α/s_β	Fig. 6.10
II	c_α/s_β	$-s_\alpha/c_\beta$	$-s_\alpha/c_\beta$	Fig. 6.11
X (LS)	c_α/s_β	c_α/s_β	$-s_\alpha/c_\beta$	Fig. 6.12
Y (flipped)	c_α/s_β	$-s_\alpha/c_\beta$	c_α/s_β	Fig. 6.13

for extra Higgs scalars. These are fit by `HiggsBounds`. Secondly, we may indirectly search for the 2HDM by looking at any modifications it imprints on the SM-like Higgs. These are fit by `HiggsSignals`.

ATLAS summary results[75] [113] [114] [115] show all observed production channels and branching channels for the light CP-even Higgs, except for $h \to ZZ$ and $h \to b\bar{b}$ (measured as $Vh \to Vb\bar{b}$) lie within 1σ of the SM prediction. Studying the combined signal strengths shows us a similar pattern, with the majority of the best fits observing signal strengths $\mu > 1$, all within 1σ of the SM prediction. The most tightly constrained signal strength is in the $h \to WW$ channel (averaged over all relevant production channels) with $\mu = 1.16^{+0.24}_{-0.21}$. Also interesting are $h \to b\bar{b}$ (it has the largest branching for h) and $h \to \gamma\gamma$ provides for a clean signature final state. The observed signal strengths for these final states (averaged over all relevant production channels) are $\mu = 0.52 \pm 0.40$ and $\mu = 1.17 \pm 0.27$, respectively.

75: We quote 2016/2018 results to match the data-sets used by our versions of `HiggsBounds` and `HiggsSignals`.

In the 2HDM we may rotate the light SM-like CP-even Higgs into heavy CP-even Higgs. This will alter from the signal strength we observe.

Looking first at $h \to f\bar{f}$ decays, we know in the 2HDM the couplings to fermions depend on the type of model we are investigating. We again show the relevant 2HDM scalings to these couplings (with respect to the SM) in table 6.3. The complete listing of coupling scaling factors may be found in table 4.6.

We plot the scaling factors in Figures 6.10, 6.11, 6.12 and 6.13 with all constraints imposed for each of the four models, respectively. It is interesting to investigate how much opening we are permitted on the Yukawa scalings in the 2HDM, as these would directly effect the amount of enhancement/suppression permitted in the production/decay channels.

There is little opening for the down coupling Γ^h_d in all four models, with a best fit point at one in all cases, except in the type-I, where the best fit and 1σ region are all below 1, weakening the process and perhaps leading to a decreased signal strength. The $h \to b\bar{b}$ channel has a large experimental error due to background noise, and, along with our channles with large noise, may not be a good candidate for 2HDM

Figure 6.10: Scaling factors for the light CP-even Higgs (h^0) to fermion couplings in the *type I* model. All constraints are included. c_α/s_β is repeated for this model. *Left:* $\Gamma^h_u \frac{v}{M_u}$, *Middle:* $\Gamma^h_d \frac{v}{M_d}$ *Right:* $\Gamma^h_e \frac{v}{M_e}$

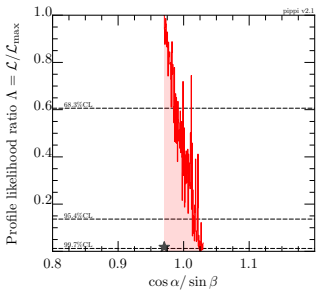

c_α/s_β c_α/s_β

Figure 6.11: Scaling factors for the light CP-even Higgs (h^0) to fermion couplings in the *type II* model. All constraints are included. $-s_\alpha/c_\beta$ is repeated for this model. *Left:* $\Gamma^h_u \frac{v}{M_u}$, *Middle:* $\Gamma^h_d \frac{v}{M_d}$ *Right:* $\Gamma^h_e \frac{v}{M_e}$

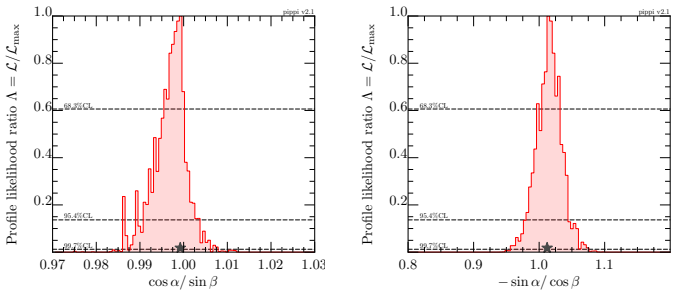

$-s_\alpha/c_\beta$

searches. In the type-II and flipped models, although the best fit is centered around one, Γ^h_u may reach $[0.975, 1.05]$ and $[0.85, 1.15]$, respectively, at 1σ. Observation of the corresponding $h \to c\bar{c}$ final state would involve reconstructing charm-jets which would, again, have large background interference. A potential probe could be via different final states such as $h \to cc\gamma$ [116]. Alternatively, we could also consider the effects of the top to Higgs coupling in tth production. Interestingly, the Γ^h_e distribution in the LS model shows a preference away from unity in both directions, but predominantly $\Gamma^h_e < 1$. The best-fit sits at Γ^h_e 0.87. The $h \to \tau\tau$ channel has the second largest branching ratio after the b. The channel is difficult to identify due to QCD-background and reconstruction of neutrinos in the final state [117] but remains interesting, especially with the behaviour discussed.

The light CP-even scalar couplings to the vector bosons are proportional to $s_{\beta\alpha}$ in all model types. We show $h \to WW$ vs $\cos_{\beta\alpha}$ for the type-II in Figure 6.14. The figure shows a 1σ opening of $[-0.15, 0.025]$, which aligns well with the SM-limit, and suggests little opening.

Figure 6.12: Scaling factors for the light CP-even Higgs (h^0) to fermion couplings in the *lepton specific* model. All constraints are included. c_α/s_β is repeated for this model. *Left:* $\Gamma^h_u \frac{v}{M_u}$, *Middle:* $\Gamma^h_d \frac{v}{M_d}$ *Right:* $\Gamma^h_e \frac{v}{M_e}$

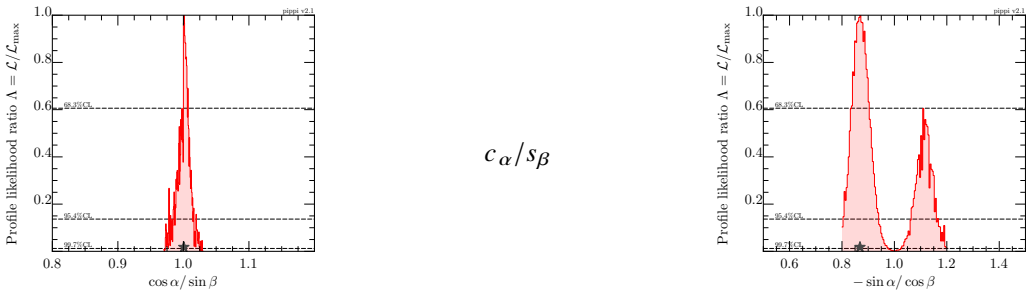

Figure 6.13: Scaling factors for the light CP-even Higgs (h^0) to fermion couplings in the *flipped* model. All constraints are included. c_α/s_β is repeated for this model. *Left:* $\Gamma^h_u \frac{v}{M_u}$, *Middle:* $\Gamma^h_d \frac{v}{M_d}$ *Right:* $\Gamma^h_e \frac{v}{M_e}$

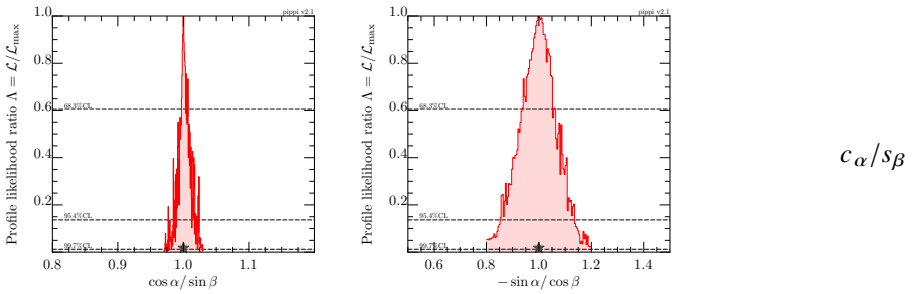

Next, we consider $h \to \gamma\gamma$. In the 2HDM, the loop via which the decay occurs will include a contribution from the charged Higgs scalar - $H^\pm$. The observed branching ratio for this channel is $(2.27 \pm 0.05) \times 10^{-3}$ [13]. We conduct an independent scan with only theoretical and collider constraints and find that $m_{H^\pm}$ fits this process up to 3000 GeV (beyond which we do not consider in this scan), see Figure 6.15. From this, NP in the 2HDM may not be visible in the $h \to \gamma\gamma$ channel.

Returning to the discussion of features, recall, to identify h_1 with h^0 then $\alpha = \pi/2 \pm n\pi$. We know from the Yukawa scalings that rotations in α and β change our signal strengths. Recall the relations

$$\begin{aligned} s_{2\alpha} &= \frac{2\mathcal{M}_{12}^2}{\sqrt{(\mathcal{M}_{11}^2 - \mathcal{M}_{22}^2)^2 + 4(\mathcal{M}_{12}^2)^2}}, \\ \mathcal{M}_{12}^2 &= -m_A^2 s_\beta c_\beta + v^2(\lambda_3 + \lambda_4), \\ &= -m_{12}^2 + v^2(\lambda_3 + \lambda_4 + s_\beta c_\beta \lambda_5), \\ m_A^2 &= \frac{m_{12}^2}{s_\beta c_\beta} - v^2\lambda_5, \end{aligned} \tag{6.4}$$

where we have set $\lambda_6 = \lambda_7 = 0$. When h^0 is aligned with h_1, and there is no mixing between CP-even scalars, $\mathcal{M}_{12}^2 = 0$. In this scenario and with $\tan\beta$ small (in the type-II) we have SM-like signal strengths. These may be maintained as α and β mix in proportion to one another. Being close to the alignment of h^0 with h_1 suggests we have limits

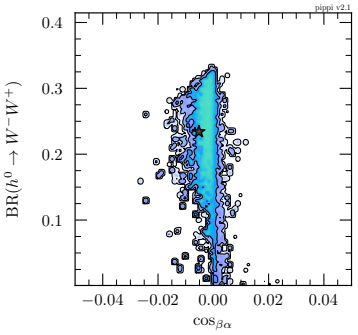

Figure 6.14: $h \to W^+W^-$ vs $\cos_(\beta\alpha)$ with collider constraints (`HiggsBounds`, `HiggsSignals`) and all theoretical constraints in the *type-II* model.

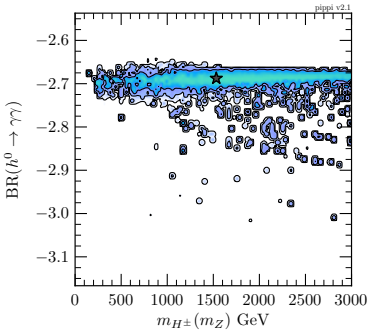

Figure 6.15: $h \to \gamma\gamma$ vs $m_{H^\pm}$ with collider constraints (`HiggsBounds`, `HiggsSignals`) and all theoretical constraints in the *type-II* model.

on the size of the couplings λ_3, λ_4 and λ_5, as here $s_{2\alpha} = 0$(subject to any cancellations between them). This also helps to explain some of the double-peaking structure of λ_3 and λ_4 throughout the models. In all models the peaks exhibit $\lambda_3 = -\lambda_4$ patterns, which help to cancel mixing between the CP-even Higgs scalars.

In the type-II and flipped models, we observe a peak in λ_3 in the interval $(-1.5, 4)$ at 1σ. In λ_4, for all models, we observe a peak in λ_4 in the interval $(-4, 0.5)$ at 1σ. The difference in distributions of λ_4 between models, unfortunately, seems to originate from lower sampling in models other than the type-II. It seems that in the flipped model, it is easier to recover the dual peak distribution for λ_4. Finally, λ_5 is mostly Gaussian about zero.

Looking explicitly to the two-dimensional distributions, similarities in the distributions are easily visible between the type-II and flipped models and between the type-I and lepton-specific models. We clearly see the λ_3 and λ_4 profile likelihood distributions peaked away from zero in the 2D profile likelihood distributions.

Contrasting these two-dimensional combined fits with the two- dimensional purely theoretical fits, we notice the most substantial difference is on the λ_2 upper limit from the SM Higgs scalar mass constraint, along with stronger bounds on λ_3 and λ_4 from collider and flavour physics processes.

Finally, it may be shown that the relations above in eq. (6.4) in combination with the requirement to keep the Yukawa scalings near one lead to a lower limit on m_A.

The masses of the extra scalars are heavy but at the lower end of the spectrum still detectable with current colliders. To detect them we would need to identify and recreate their decay products into a signature. This is notoriously difficult as processes such as those containing b-jets exhibit large amounts of background noise.

In the direct search for heavy scalars, we may implement bounds on masses and mixing angles. For example, the m_A vs $\tan\beta$ plane is most constrained by the final channels $A/H \to \tau\tau$ [118] and $H \to hh(4b)(bb\gamma\gamma/\tau\tau)$[76] [119]. Usually when searching for new scalars in this way we look for narrow widths and progress to wider width searches later. Most BSM search final channels are included in `HiggsBounds` and the dissection of global fits channel wise may be found in Ref. [120] for $H^\pm$ specifically and more generally for each model in Ref. [121]. We skip over this in the presentation of the *preliminary* results.

76: here the brackets represent two different final states.

Ref. [84] describes the electroweak precision parameters proportional to some combination of the functions. We very roughly detail how

these functions behave. The electroweak precision parameters

$$\begin{aligned} &S \propto G(m_a^2, m_b^2), \quad T \propto F(m_a^2, m_b^2), \quad U \propto G(m_a^2, m_b^2), \\ &V \propto H(m_a^2, m_b^2), \quad W \propto H(m_a^2, m_b^2), \quad X \propto G(m_a^2, m_b^2), \end{aligned} \tag{6.5}$$

where m_a and m_b are heavy scalars. These functions also include the gauge boson masses but we ignore them here as they do not change our argument. It is shown in Figures 2, 3 and 4 of [84] that $F(m_a^2, m_a^2) = 0$ while growing rapidly for $m_a \neq m_b$. Similarly $G(m_a^2, m_a^2) = 0$ for $m_a, m_b > 400$ GeV, while being slightly negative for $m_a, m_b < 400$ GeV. G then grows for $m_a \neq m_b$. Finally, $H < 0$ for $m_a, m_b < 300$ GeV, after which it is 0 for all m_a, m_b. The above information combined with the small values that we fit for the oblique parameters (given in appenix F)* and the relations in Eq. (6.5), suggest oblique parameters best fit heavy scalars with $m_a = m_b$. It also suggest that the electroweak precision constrains prefer low masses, as at these scales there is a greater potential opening to the oblique parameters. Our results fit well with these predictions, we present these in Figures 6.16 and 6.17.

Next, we are interested in distributions of the mixing angles α and β within each model. We plot the 2D profile likelihood distributions for (α vs $\log t_\beta$), ($\beta - \alpha$ vs $\log t_\beta$) and ($c_{\beta\alpha}$ vs $\log t_\beta$) in Figures 6.18, 6.19, 6.20 and 6.21.

It is more revealing to plot $c_{\beta\alpha}$ as we are close to the alignment limit $s_{\beta\alpha} = 1$ and it is difficult to read off $s_{\beta\alpha}$ values here. The best-fit points for each of the plotted angles/angle combinations are given in Table 6.4.

The calculation of the angle $\beta - \alpha$ was guaranteed between $(-\frac{\pi}{2}, \frac{\pi}{2})$, however in this scan we also required that the angle α is on the same interval $(-\frac{\pi}{2}, \frac{\pi}{2})$. To guarantee this, we impose the condition $\alpha \to \alpha - \pi$ (shifted back by half a period) when $\alpha < \frac{\pi}{2}$. The resultant shifted $\beta - \alpha$ combination no longer respects the $(-\frac{\pi}{2}, \frac{\pi}{2})$ interval. As such we observe values either side of $\frac{\pi}{2}$, in this shifted interval the sign

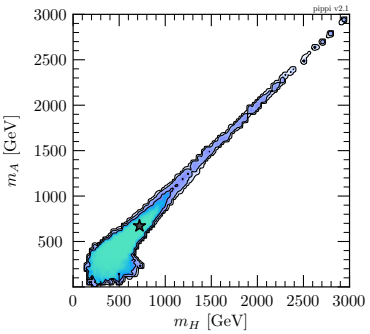

Figure 6.16: 2D Profile likelihood distribution of m_H vs m_A with only the electroweak precision parameters constraint. Note: we include all theoretical constraints here as well.

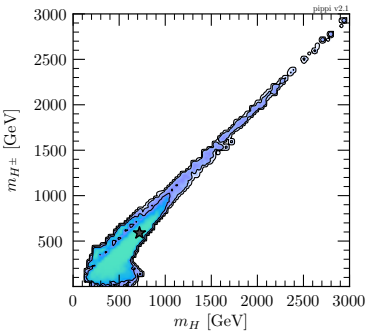

Figure 6.17: Same as above with m_H vs $m_{H^\pm}$.

Figure 6.18: 2D profile likelihood distributions of the mixing angles in the *type-I model*.

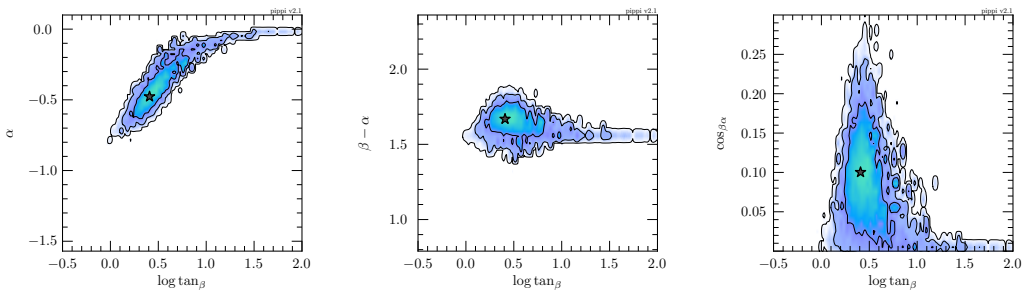

* $S = 0.04 \pm 0.11, T = 0.09 \pm 0.14$ and $U = -0.02 \pm 0.11$ [122]

Figure 6.19: 2D profile likelihood distributions of the mixing angles in the *type-II model*.

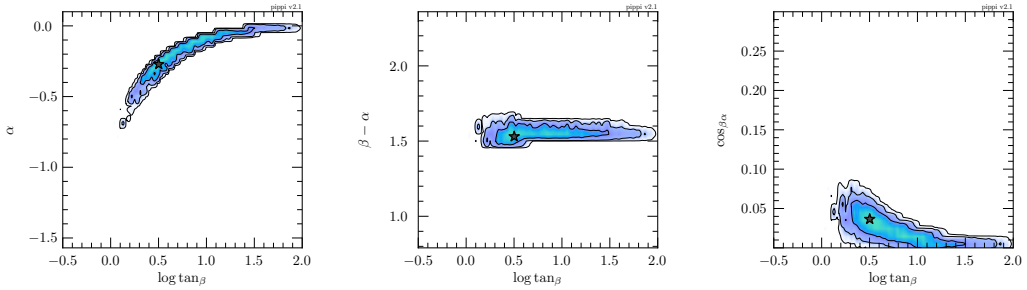

Figure 6.20: 2D profile likelihood distributions of the mixing angles in the *flipped (type-Y) model*.

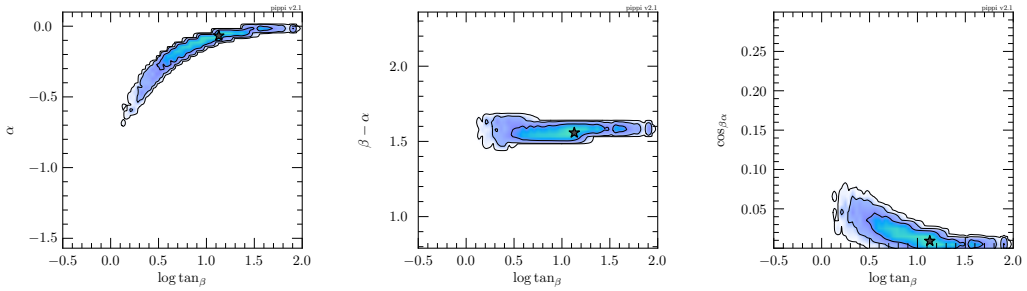

(quadrant) of $c_{\beta\alpha}$ and $s_{\beta\alpha}$ is also changed. In the plots of the running and best-fit point tables we include the shifted sign. In the 2D profile likelihood plots we plot the absolute value of $c_{\beta\alpha}$. For future scans we will be sure to only state the angle combination before the shift in α, as discussed at the closing of section 4.1.

Starting at the best-fit point we run the angles and show the energy evolution up to 100 TeV of the angles and the physical combination $s_{\beta\alpha}$ and $c_{\beta\alpha}$ for each model in Figure 6.22.

Notice that all angles begin near the alignment limit ($s_{\beta\alpha} = 1, c_{\beta\alpha} = 0$) and from this point are well-behaved. There is a small divergence from this limit at high energies.

The left-handed plots of Figure 6.21 show us the relations between α and t_β. We see that α is being pushed negative at lower values of t_β. It must do this to maintain points close to the alignment limit $\beta - \alpha = \frac{\pi}{2}$ as β shrinks.

The type-I model can replicate SM-like signal strengths; this is due to the Z_2 alignment of the Yukawa's in this model. In the case $\alpha = 0$ all the fermions couple to the SM-like Higgs scalar. The SM is recovered then as $t_\beta \to \infty$. We see that the SM-like model is ruled out at 2σ in the type-I scenario.

The central plots follow the alignment limit and show the moving of the 2HDM away from this. It is the type-I model that can reach points furthest from this limit. This behaviour again is due to the Yukawa alignment. As α diverges from zero and approaches $\pi/2$, the CP-even

Figure 6.21: 2D profile likelihood distributions of the mixing angles in the *lepton-specific (type-X) model*.

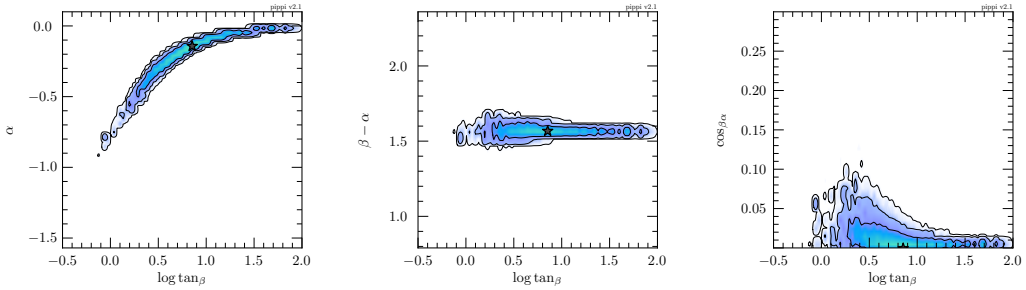

Table 6.4: The values of the angles at the best-fit point.

Model Type	t_β	$\beta - \alpha$	$c_{\beta\alpha}$
Type-I	2.63	1.67	-0.10
Type-II	3.16	1.53	0.04
Lepton-specific (X)	13.50	1.56	0.01
Flipped (Y)	7.24	1.57	0.05

Figure 6.22: Running of physical angles β and α and combinations $s_{\beta\alpha}$, $c_{\beta\alpha}$ and $\beta - \alpha$ in the various 2HDMs starting at the best-fit point. Running is between m_Z and 100 TeV. *Top-left:* type-I model, *Top-right:* type-II model, *Bottom-left:* lepton-specific (type-X) model, *Bottom-right:* flipped (type-Y) model.

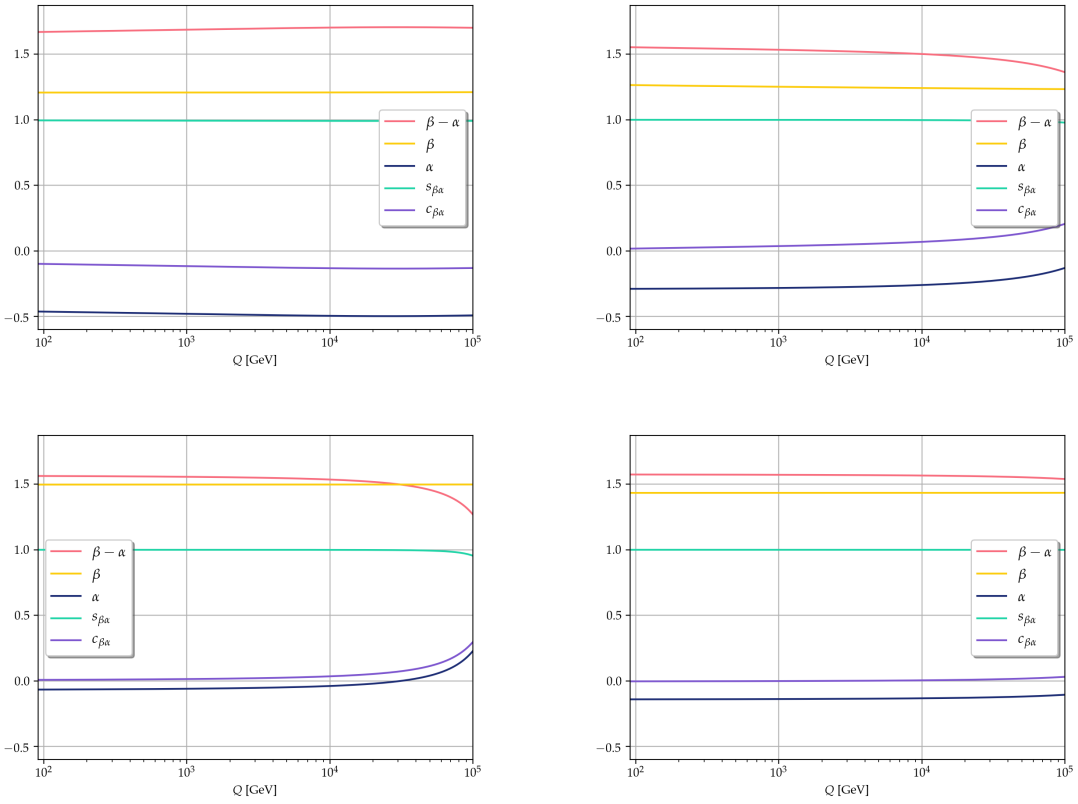

states from our fields Φ_1 and Φ_2 rotate into each other. As this happens to all our CP-even to fermion Yukawa couplings simultaneously in the type-I, we do not need strict cancellations from β. We may see the type-I divergence from the alignment limit shows a fit to anomalies in SM-like signal strengths.

The other three models show only small deviations from the alignment limit, and these are perhaps best seen in the rightmost plots where again $c_{\beta\alpha} = 0$ is the alignment condition.

Clearly, the lowest values of t_β may be reached in the type-I, with the best-fit point also pushed down in the type-II. Collider constraints push $\tan\beta$ downwards as do the leptonic flavour constraints.

When analysing the 1D profile likelihood distributions of the λ_2 coupling, we predicted a relatively low limit on t_β for the type-I and flipped models. This claim turns out to be accurate as indeed both these models reach lower t_β values than the type-II or lepton-specific models.

Perhaps the most interesting of all the results are those of the physical spectrum. We plot the interesting one- and two-dimensional profile likelihood distributions for the physical spectrum in Figures 6.23, 6.24, 6.25 and 6.26. Unfortunately the 2 and 3 σ regions for the 2D m_{12}^2 and $\log(t_\beta)$ profile likelihoods have not been sampled efficiently in the *preliminary* results and provide 'scattered' results. One may, however, make out the probability regions and we keep this binning to ensure the 1σ region features remain visible.

We plot pole masses for all our scalar particles since running masses are never much larger or smaller due to the perturbativity on the loop-correction constraint. We show the agreement between the running mass and pole mass of m_H in the type-II model in Figure 6.27. We also show the same plot for m_h in Figure 6.28. In the case of m_h, the perturbativity on loop-correction constraint is more obvious, especially at the sharp bottom limit cut-off.

Figure 6.23: 1D and 2D profile likelihood distributions for the physical spectrum in the *type-I model*.

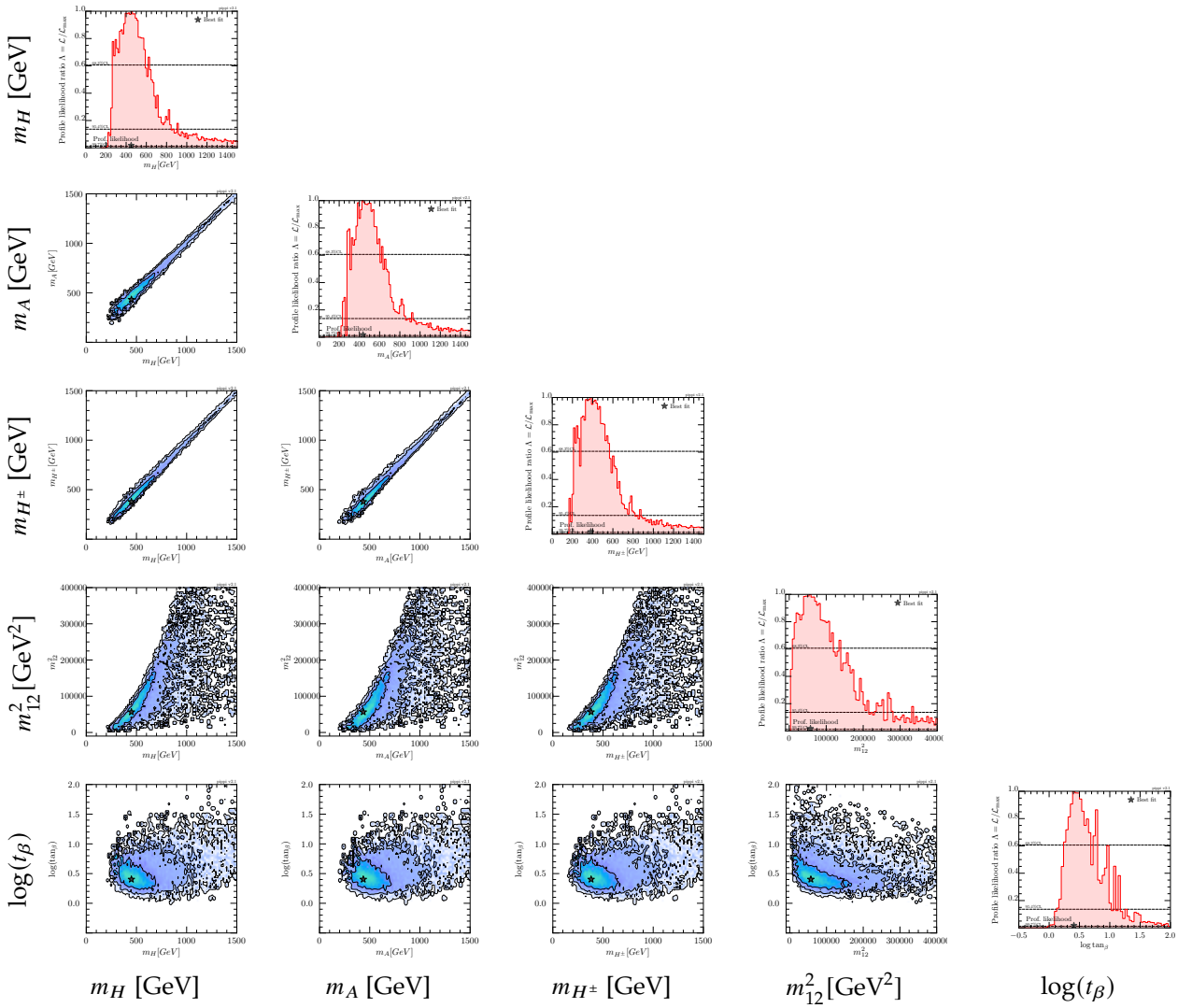

Figure 6.24: 1D and 2D profile likelihood distributions for the physical spectrum in the *type-II model*.

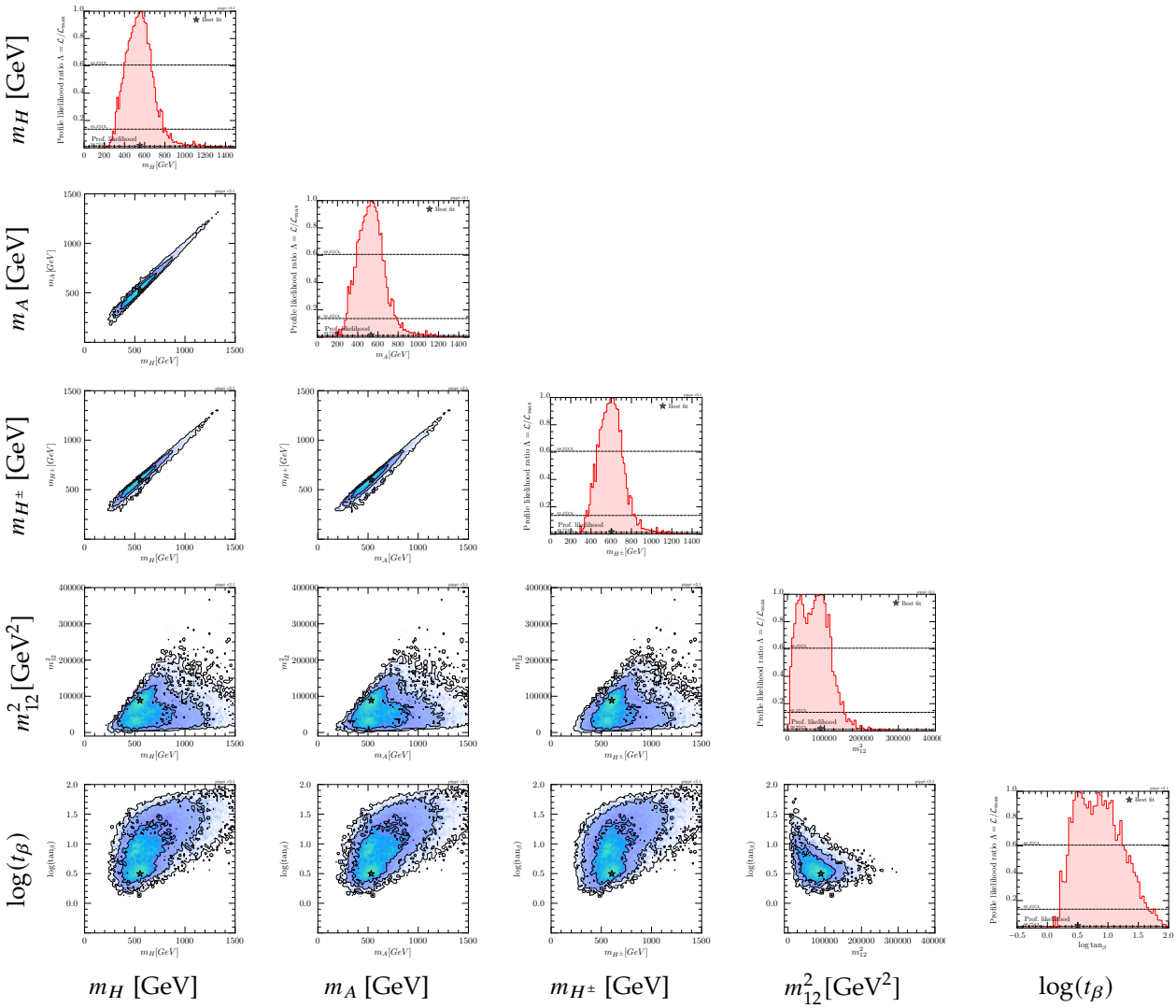

Figure 6.25: 1D and 2D profile likelihood distributions for the physical spectrum in the *lepton-specific model (type-X)*.

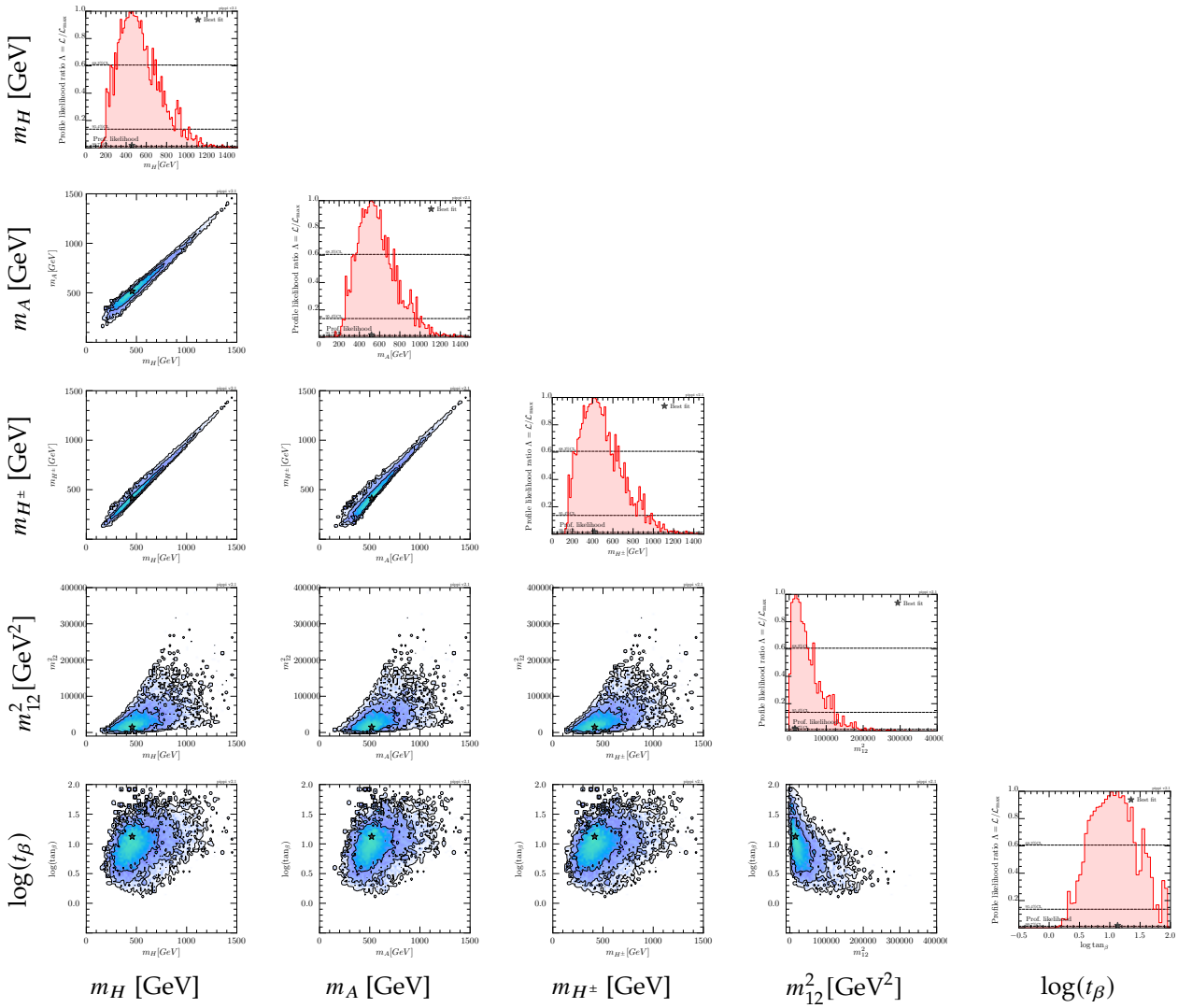

Figure 6.26: 1D and 2D profile likelihood distributions for the physical spectrum in the *flipped model (type-Y)*.

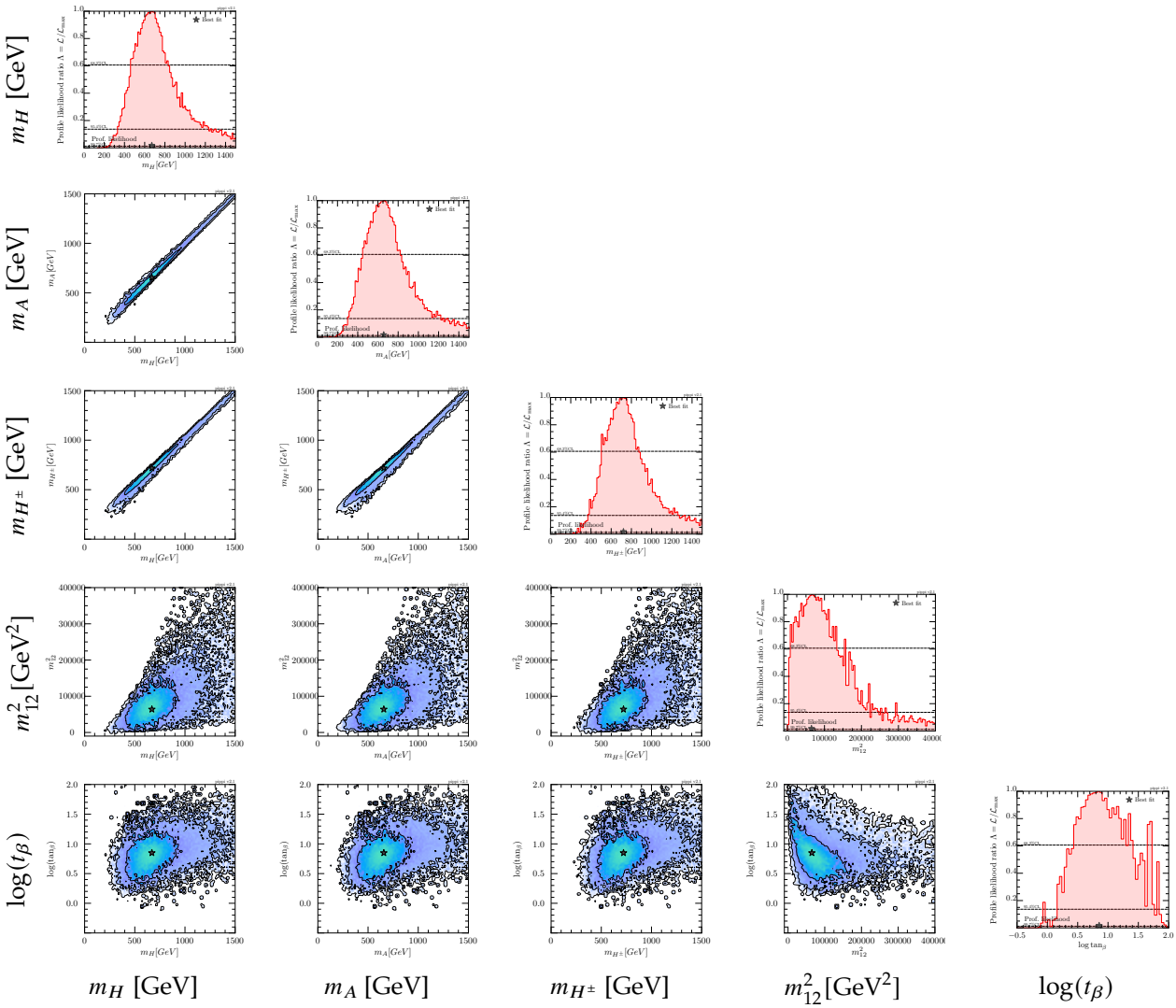

As usual, the best-fit points for the physical spectrum plots are given in Table 6.5 and the running of the scalar masses and the VEV from the best-fit points is given in Figure 6.29.

Again from our best-fit points, there is an agreement between the type-II and flipped models and the type-I and lepton-specific models due to the Yukawa sector alignment. All scalars are strongly correlated in mass as expected from the electroweak precision observables fit. We notice a distinct upper limit on all heavy scalars at around 2 TeV. This limit appears during spectrum generation with only the SM Higgs boson mass constraint imposed. Loop corrections to the light CP-even scalar are of the form $[\lambda_i m_\phi]$ where $i = 3, 4, 5$ and m_ϕ is a term proportional to the mass of the heavy scalars (indeed it does not matter which one as they are correlated in mass). This relationship implies that as heavy scalar masses grow in size, so too do the loop corrections to the light scalar (in the case that λ_i with $i = 3, 4, 5$ are not close to zero). As we have trouble sampling small values of λ_i with $i = 3, 4, 5$ in our scan, loop correction growth eventually saturates the point where we are no longer able to fit the SM Higgs scalar mass to the pole mass of the light CP-even scalar. In Figure 6.30 we present a scatter plot with the pole mass of the light CP-even Higgs scalar against that of the heavy CP-even Higgs scalar. In the scatter plot we ensure that loop corrections to both scalars remain perturbative. In turn this produces an upper bound on m_H of $\sim$ 2 TeV at $m_h = 125$ GeV. The same scatter plot is obtained for each of the heavy scalars. It is crucial to mention that this upper limit is not necessarily a limit of the theory but may arise from the inability to sample low values of λ_i with $i = 3, 4, 5$. Alternatively the upper limit may be due to the form of the loop-order calculation, specifically that there may exist cancellations to m_h at higher orders that, within the constraints of perturbativity, push down the loop-corrections and recover some of the high mass parameter space. The fit to a SM-like CP-even scalar is packaged within the `HiggsSignals` χ^2 in the combined likelihood.

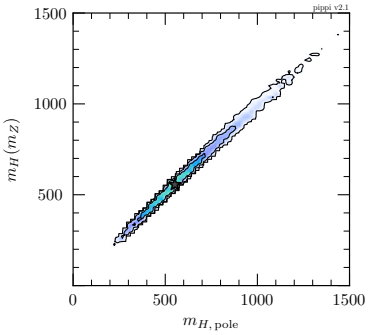

Figure 6.27: 2D Profile likelihood distribution of the running mass m_H at m_Z vs the pole mass of m_H.

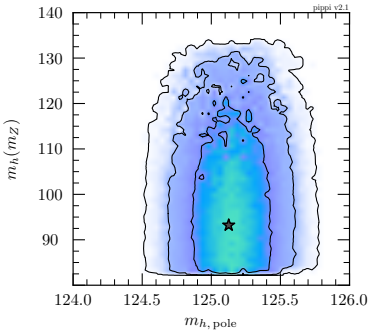

Figure 6.28: 2D Profile likelihood distribution of the running mass m_h at m_Z vs the pole mass of m_h.

Table 6.5: The values of the physical spectrum parameters at the best-fit point.

Model Type	$m_{H,\text{pole}}$ [GeV]	$m_{A,\text{pole}}$ [GeV]	$m_{H^\pm,\text{pole}}$ [GeV]	m_{12}^2 [GeV^2]
Type-I	450	430	380	58,000
Type-II	550	530	610	80,000
Lepton-specific (X)	460	520	420	10,000
Flipped (Y)	670	660	730	68,000

Figure 6.29: Running of the scalar masses and the VEV in the various 2HDMs starting at the best-fit point. Running is between m_Z and 100 TeV. The y-axis is in GeV. *Top-left:* type-I model, *Top-right:* type-II model, *Bottom-left:* lepton-specific (type-Y) model, *Bottom-right:* flipped (type-X) model.

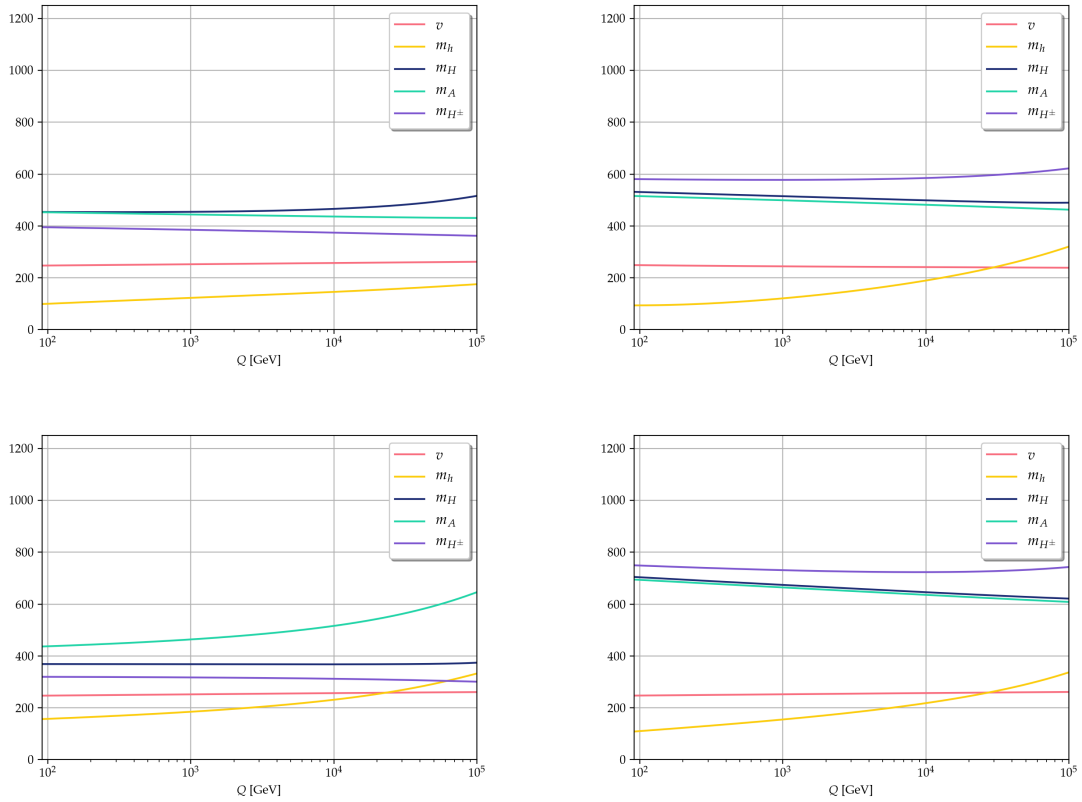

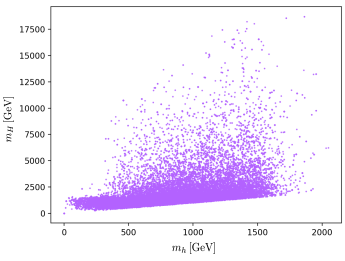

Figure 6.30: Scatter plot of CP-even scalars m_H and m_h, with perturbativity constraint on loop corrections imposed on m_h.

In the plots there seems to be an even more restrictive upper limit on the heavy scalars at ~ 2 TeV. In the type-I, type-II and lepton-specific models the upper limits fall below 1 TeV at 2σ, in the flipped models this is relaxed slightly to just over 1 TeV. The lower limit sits just over 200 GeV at 2σ for the type-I and lepton-specific models. For the type-II and flipped models, the lower limit sits just above 300 GeV at 2σ. These limits may be explained by the flavour constraints placed upon our models. The lower limit is due to the $b \to s\gamma$ branching process, whereas the upper limit is from the fit on angular observables of the $B^0 \to K^*\mu^+\mu^-$ process. These two constraints are in tension with one another, and both of them limit and shape the distributions of our scalar masses. The radial components of $B^0 \to K^*\mu^+\mu^-$ contain large anomalies to fit and have a significant downward push on our scalar masses. The $b \to s\gamma$ branching process provides stronger limits from below, especially upon the type-II and flipped models. This stronger pull not only results in a larger lower limit but also cancels the pull from the $B^0 \to K^*\mu^+\mu^-$ process and produces a Gaussian with little skew in the type-II and flipped models. On the other hand, there is a noticeable skew towards lower mass values for the type-I and lepton-specific models. The onward effects of this tension between the two

flavour constraints may also be observed in the values of the heavy scalar masses best-fit point where the type-I and lepton-specific models have lower values due to their skewed distributions.

We perform an individual study on each flavour likelihood that is switched on in our models. We plot the study for a type-II model in Figures 6.31. It is difficult to grasp the restrictions placed by all constraints on the linear scale in t_β, so we also show this logarithmically in Figure 6.32.

The flavour constraint plots for the 2HDM type-II model show exclusion regions at 2σ for each flavour likelihood. The flavour likelihoods are carried out independently, so there is no pull between each of the regions. We see all the constraints are in tension with one another. If at first we ignore the exclusion region originating from $B \to K^*\mu^+\mu^-$ angular observables (green) (see Figure 6.33), BR$(b \to s\gamma)$ (orange) disfavours masses below ~ 500 GeV as well as low t_β values. Low t_β is most strongly disfavoured by BR$(B_s \to \mu^+\mu^-)$ (yellow) with the lowest value (at 2σ) of $t_\beta = 0.4$ near masses of 1.8 TeV. Past this point the $\Delta M_{B_s^0}$ constraint drives up the lower limit on t_β. We see that near our best-fit point for the type-II model, the lower limit imposed on t_β sits at around 0.5 at 2σ. At large values of t_β tree-level leptonic and semi-leptonic B and D decays (blue) come into consideration and push up the lower mass limit on $m_{H^\pm}$.

Next, we include $B \to K^*\mu^+\mu^-$ radial components fits (green) and find no region of the 2HDM type-II model parameter space is open at 2σ. $B \to K^*\mu^+\mu^-$ radial components are anomalous over various energy bins. We show 3D scatter plots of using the 2HDM-II to fit the anomalies in the [1.1, 2.5] GeV bin in Figure 6.34.

The scatter plots show the corrections the 2HDM may provide to anomalies in each of the component fits. We plot the SM values as the pink plane and the experimentally observed values as the yellow plane. On the axes we show t_β vs $m_{H^\pm}$. We see even the type-II 2HDM struggles to fit the observed values if they are too far from the SM prediction. A similar pattern arises in the other energy bins, leading to a large likelihood pull from this constraint.

Exploring the likelihood of the calculated $B \to K^*\mu^+\mu^-$ branching ratio (rather than radial components), with a large (form factor) theoretical error in place puts virtually no limit on the parameter space. Other studies such as as [123] and [124] have shown allowed regions for the branching ratio constraint, but alas, they provide no new restrictions above what the other flavour constraints discussed above already provide in our study.

Due to the heavy anomalous pull from the measurement of the $B \to K^*\mu^+\mu^-$ radial components, we nominate to conduct scans with and

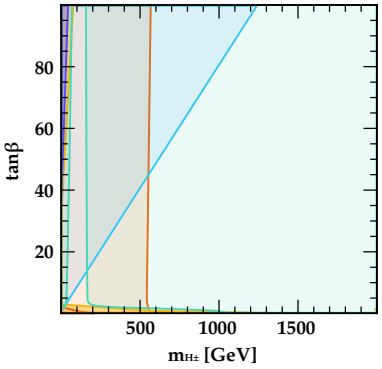

Figure 6.31: Flavour fits in the 2HDM-II model. We plot exclusion regions at 2σ with:
Green: $B \to K^*\mu^+\mu^-$ angular observables.
Yellow: BR$(B_s \to \mu^+\mu^-)$.
Orange: BR$(b \to s\gamma)$
Red: $\Delta M_{B_s^0}$.
Purple: R_K and $R_K^{(*)}$.
Blue: Tree-level leptonic and semi-leptonic B and D decays: R_D, $R_D^{(*)}$, $B \to \tau\nu, B \to D\mu\nu, B \to D^*\mu\nu$ and $D_s \to \tau\nu, D_s \to \mu\nu, D \to \mu\nu$.

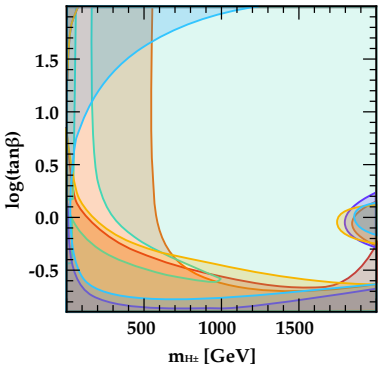

Figure 6.32: Same as Figure 6.31, with t_β plotted logarithmically.

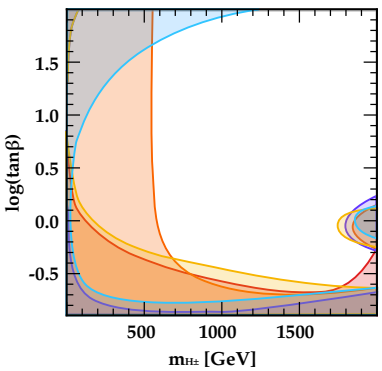

Figure 6.33: Same as Figure 6.31, but plotted without the $B \to K^*\mu^+\mu^-$ process radial component likelihood.

Figure 6.34: 3D scatter plots of the $B \to K^* \mu^+ \mu^-$ radial components in the *type-II model*. We show the components from the [1.1, 2.5] GeV bin and plot the radial component on the vertical axis, with t_β vs $m_{H^\pm}$ on the two horizontal axes. The experimentally observed (pink) and SM (yellow) values are shown as planes.

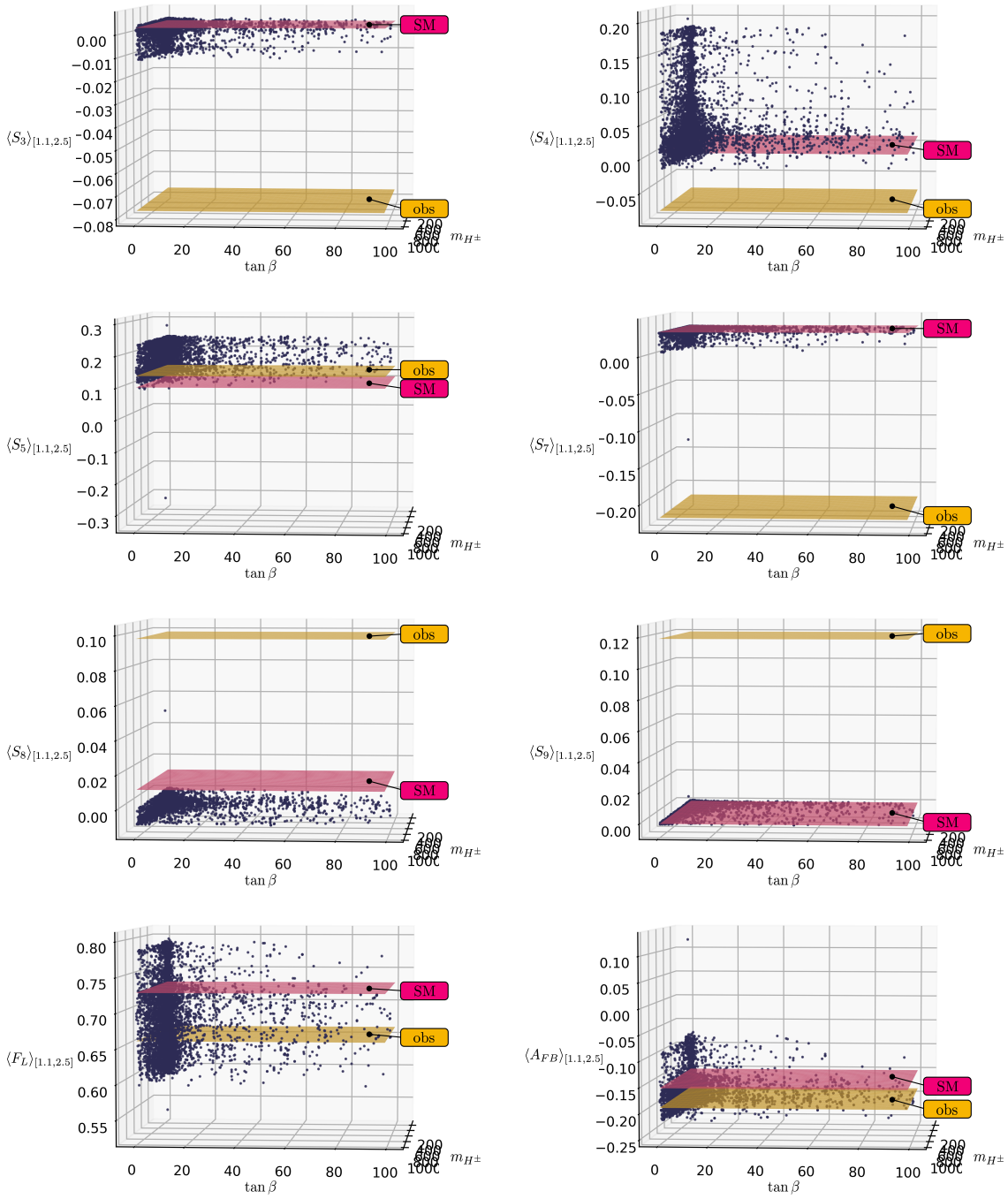

without this constraint switched on. We present a scan of the type-II model without the $B \to K^* \mu^+ \mu^-$ radial components constraint. This scan is carried out with a lower point density than the full results we have discussed up until now.

Looking at the best-fit points, in the combined type-II model $\chi^2_{\text{best-fit}} = 300.7$. While the same model without the $B \to K^* \mu^+ \mu^-$ radial components constraint has $\chi^2_{\text{best-fit}} = 104.3$. Indeed, we see the radial components constraint has a strong pull on the results.

The physical spectrum of the type-II model without the $B \to K^* \mu^+ \mu^-$ radial components constraints is presented in Figure 6.35.

Most interesting in this scan is the removal of the upper limit on the scalar masses imposed by the fit onto the radial components. Looking at the heavy scalars, we see a significant push upwards of both the distributions and the best-fit values. In this case the best-fit values are approximated to be 1070, 1080 and 1030 GeV for m_H, m_A and $m_{H^\pm}$ pole masses respectively. The significance of this upward push reveals to us that it is important to carry out future studies showing both the cases where this constraint is switched on and off.

Next, returning to the analysis of each of the model's parameter space we have yet to discuss the mixed term m^2_{12}. Our prior allows this parameter to be negative. However, we find that only the lepton-specific model finds small negative values and then only at 2σ. At 1σ the mixed term is in the interval $[0, 10^6]\,\text{GeV}^2$ for the type-I and lepton-specific models, while the type-I and flipped models allow for a greater opening up to 2×10^6. The type-I and lepton-specific models also allow us to reach value beyond $4 \times 10^6\,\text{GeV}^2$ at 3σ. The masses of all of our scalars are proportional to m^2_{12} (see Equations (3.87) and (3.88)), and in fits that do not provide tight restrictions on upper limits of masses, this term is allowed to be larger. Notice that our upper limit on m^2_{12} in the prior has been chosen so as not to cut off the scalar mass upper limit.

Finally, before we close the chapter, we comment on the invisible Higgs scenario where the mass eigenstate H^0 is identified with the SM-Higgs boson. In this case, the mass of the state h^0 is less than 125 GeV. This is a fine-tuned area in the parameter space and does not show up our combined scans. We may target this area specifically by beginning in the mass basis and setting the prior with fixed $m_H = 125$ GeV and $[10, 120]$ GeV, avoiding the scenario where we may get a composite scalar case. We present the results for a type-II model from this prior in Figures 6.36, 6.37, 6.38 and 6.39.

Figure 6.35: 1D and 2D profile likelihood distributions for the physical spectrum in the *type-II model without the* $B \to K^* \mu^+ \mu^-$ *radial components constraint*.

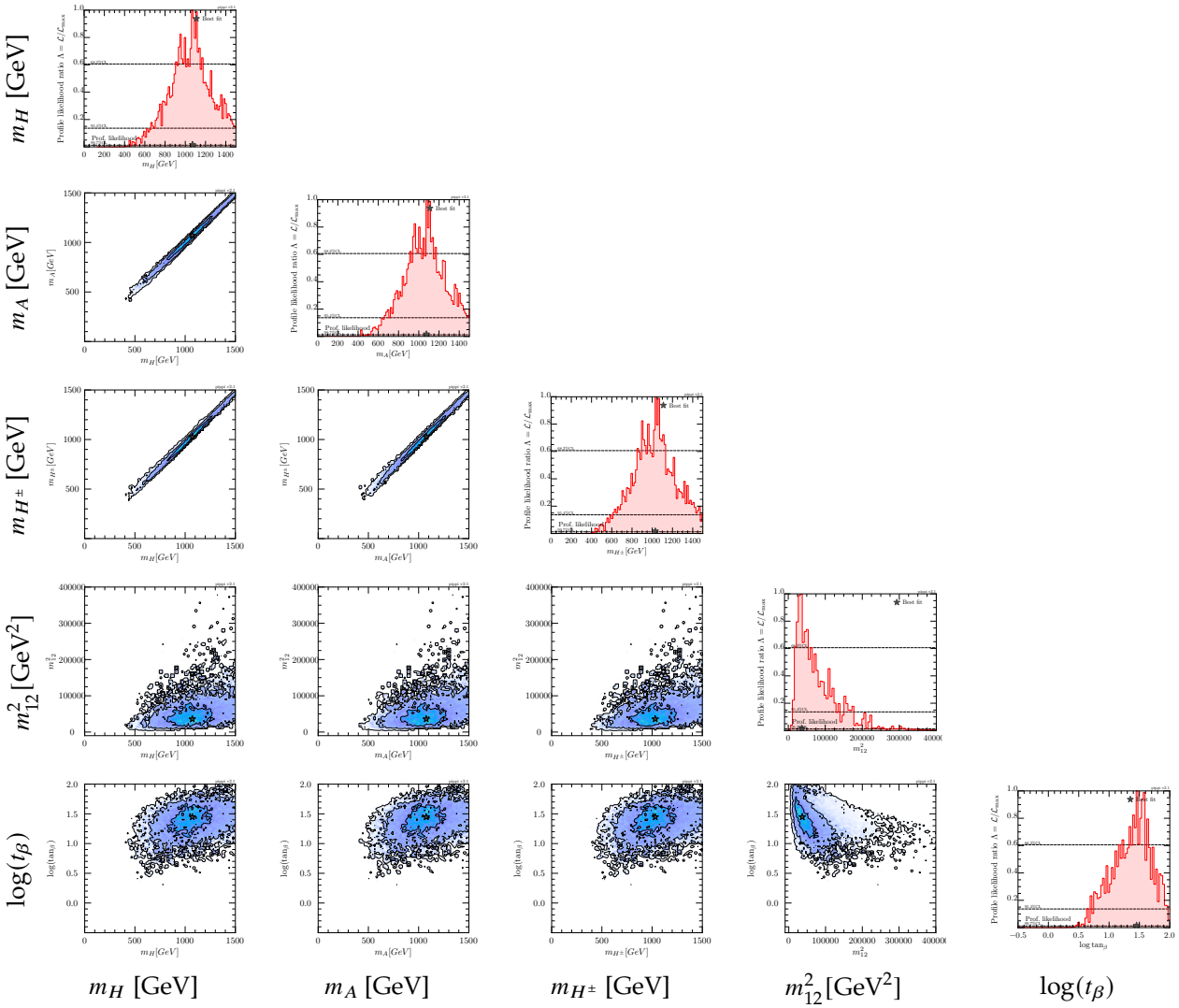

We plot the pole masses of h^0 and H^0 as well as $s_{\beta\alpha}$ and $c_{\beta\alpha}$. We see it is possible to get an invisible Higgs scenario where $m_H = 125$ GeV and $m_h < m_H$. In this case, as the identifications of the states h^0 and H^0 are flipped, the angle $\beta - \alpha$ must shift by half a period ($\frac{\pi}{2}$), this leads to $c_{\beta\alpha} \to 1$ and $s_{\beta\alpha} \to 0$, as may be seen in the distributions.

The decay products of the invisible Higgs would not be detectable by colliders and, as such, we would need to look into production channels for discovery. We would be looking for missing energy signatures in Higgs production channels. The two main channels in which we could do so at colliders are VBF and Higgs-strahlung. In VBF production we would be searching for forward b-jets, which at current colliders are difficult to separate from noise created by other processes. Higgs-strahlung is cleaner to reconstruct in this sense, however, it occurs at a low rate. Production processes are more difficult to observe and, as such, if the invisible Higgs scenario may evade detection.

As an interesting addition to this study, we present the tree-level results for the 2HDM type-II in Appendix E.

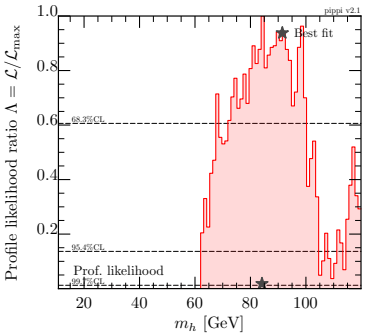

Figure 6.36: 1D Profile Likelihood of m_h in the invisible Higgs scenario.

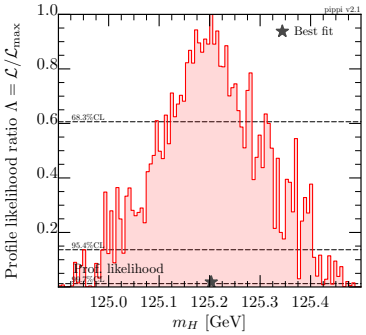

Figure 6.37: 1D Profile Likelihood of m_H in the invisible Higgs scenario.

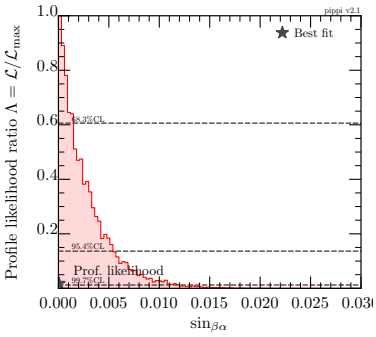

Figure 6.38: 1D Profile Likelihood of $s_{\beta\alpha}$ in the invisible Higgs scenario.

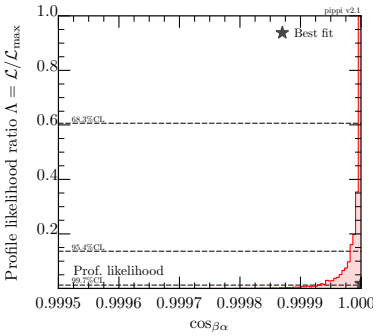

Figure 6.39: 1D Profile Likelihood of $c_{\beta\alpha}$ in the invisible Higgs scenario.

Flavour-changing Currents in the CP-conserving 2HDM Type-III

7

In this chapter, we present the results of a global fit of the general 2HDM type-III model with CP-conservation. This work has been published in Ref. [61]. We are interested in the upper limits on the $h \to bs$ and $t \to ch$ branching ratios. These branching ratios are heavily suppressed in the SM but have potentially the least suppressed Yukawa's as they depend on the off-diagonal terms between the second- and third-generation quarks. We therefore only need to work with the *restricted* Yukawa set we introduced in Eq. (4.39).

The parameters and priors scanned over are given in Table 7.1. We use the Higgs basis. To ensure that we carry out our scan over both quadrants in the physical angle, we choose $-\pi/2 \leq \beta - \alpha \leq \pi/2$.

We fix all other other parameters and they may be found in Appendix F. Note that would be beneficial to scan over some of these quantities we fix as our of the Wilson coefficients discussed in previous chapters are sensitive to them, particularly m_t and α_s for electromagnetic penguins. Any extra opening of the Wilson coefficients would expose new parameter space for the flavour processes. However, as previously discussed we have saturated the number of parameters we include. Hence, to maintain efficiency in this study we keep all the remaining parameters fixed.

To start with, we show in Figure 7.1 the experimental contributions to the total χ^2 value that we calculate in the SM limit, that is $s_{\beta\alpha} \to 1$ and $\hat{\xi}^U_{ij} = \hat{\xi}^D_{ij} = 0$. The largest pulls here come from SM Higgs scalar decays, as expected predominantly from $h \to WW$, due to the fact that the experimental values of some of the production channels are slightly off from the SM, see Eq. 5.33. LHC Run II data [125–127] gives the $h \to WW$ signal strengths by production channel (as in Table 5.33) as $(1.10^{+0.21}_{-0.21}, 0.62^{+0.36}_{-0.35}, 2.3^{+1.2}_{-1.0}, 2.9^{+1.9}_{-1.3}, 1.5^{+0.6}_{-0.6})$. This almost halves the $h \to WW$ channel $\chi^2_{\text{SM-limit}}$ contribution to ~ 7. As such, had we included

Table 7.1: Parameters scanned over. We also indicate whether the priors are flat or log. In the Yukawa sector, $i, j = 2, 3$, all other couplings are zero.

Parameter	Range	Prior
$\Lambda_{1,2,3,4,5,7}$	$\pm[10^{-15}, 4\pi]$	Log
$\beta - \alpha$	$[-\pi/2, \pi/2]$	Flat
M^2_{22} (GeV)^2	$[10^4, 10^7]$	Flat
$\text{Re}(\hat{\xi}^{D,U}_{ij})$	$\pm[10^{-15}, 4\pi]$	Log
$\text{Im}(\hat{\xi}^{D,U}_{ij})$	$\pm[10^{-15}, 4\pi]$	Log

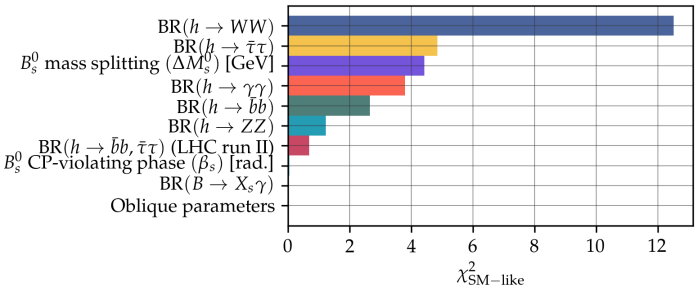

Figure 7.1: χ^2 contributions due to experimental constraints in the limit of the SM, $s_{\beta\alpha} \to 1$ and $\hat{\xi}^U_{ij} = \hat{\xi}^D_{ij} = 0$.

LHC Run II data in our fit we would improve our χ^2 from this degree of freedom. In this decay channel, the run-II data for ggF, VBF and Wh and Zh production remain within 1σ of their respective run-I result. The tth production channel, however, is more than halved and sits within 2σ of its respective run-I result. This signal strength is proportional to the top-coupling of h and $s_{\beta\alpha}$ via the production mechanism. The reduction of the signal strength would allow more opportunity to the 'invisible' Higgs decays. In any case, the SM is consistent with this data at the $\sim 2\sigma$ level.

In Figure 7.2 we show the pull from each constraint at our best fit point for the 2HDM. This occurs at heavy scalar masses ($m_H = m_A = m_{H^\pm}$) of 2450 GeV. Relative to the $\chi^2_{\text{SM-limit}}$ shown in Figure 7.1, we see that the Higgs boson decay channels are very similar, except for the decrease in the $h \to \gamma\gamma$ channel. There is a small pull from the oblique parameters. In light of the combined fit, the pull for oblique parameters is optimised at heavier masses, ~ 3 TeV, where it falls to $\chi^2 = 0.4$. Notably, flavour observables are well minimised at the best-fit point. Especially the B_s^0 meson mixing (mass splitting) discrepancy present in the SM (as discussed in section 4.4.2.4) is reduced in the 2HDM.

Examining signal strengths from (5.33)

$$\mu_{(ZZ)(VBF)} = 0.1 \pm 0.5\,, \quad \mu_{(\tau\tau)(WH)} = 5.9^{+2.6}_{-2.2}\,, \quad \mu_{(bb)(WH)} = 5.0^{+1.8}_{-1.7}\,, \quad \mu_{(\tau\tau)(tth)} = 0.4 \pm 0.4\,, \tag{7.1}$$

are anamolous at 1σ. Now, $\mu_{(ZZ)(VBF)} = s^4_{\beta\alpha}$ and the lower value will push $s_{\beta\alpha}$ away from the SM-limit of one, but due to the large power this will not be a strong effect. The anamolous signal strengths with the $\tau\tau$ final state suggest an enhancement to both $\Gamma^h_{\tau\tau}$, which in our study are not looked at. $\mu_{(bb)(WH)} = 5.0^{+1.8}_{-1.7}$ is probably the most interesting, it enhances Γ^h_{bb} which enters some Wilson coefficeints in our flavour processes. Finally, the latter processes alongside encouraging large Yukawa couplings are proportional to $s_{\beta\alpha}$ pushing this upwards.

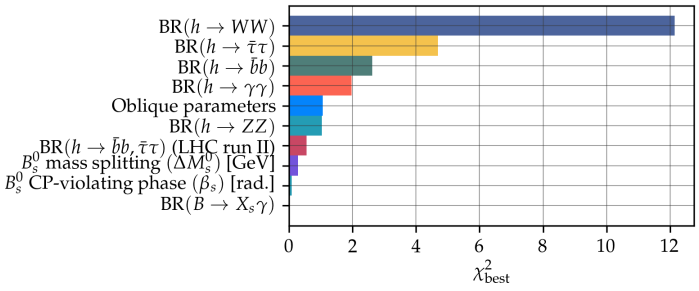

Figure 7.2: The contributions from each of the constraints to the best-fit χ^2 in our global scan of the 2HDM.

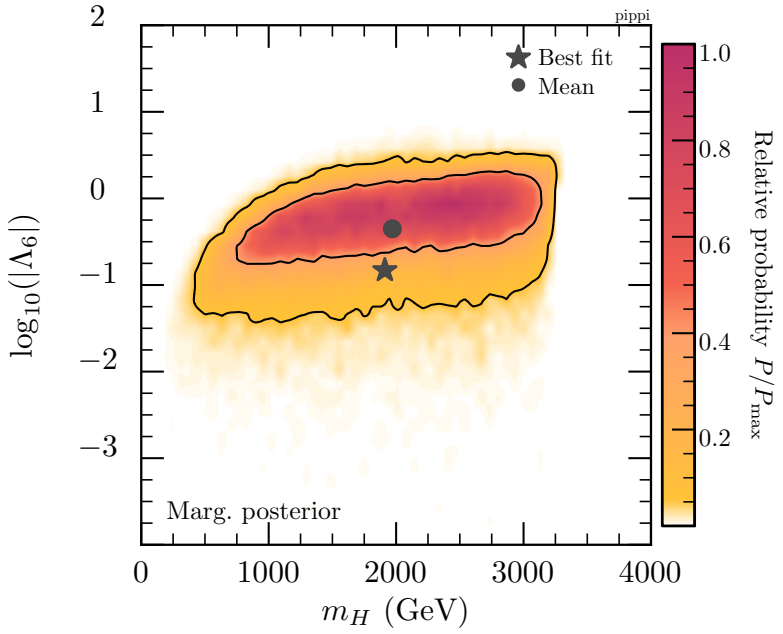

Figure 7.3: 2D posterior distribution of $\log_{10}(|\Lambda_6|)$ versus m_H.

We present our global fit results as posterior distributions with 1σ and 2σ probability regions represented by solid lines.

As mentioned we use the scanning tool `MultiNest` to carry out the scans. The setting we choose in the interest of efficiency are[78]

- $n_{\text{live}} = 2500$,
- efr = 0.90,
- tol = 0.05.

78: See the `MultiNest` manual [110] for an explanation of these quantities

In Figures 7.3 and 7.4, we plot $\log_{10}(|\Lambda_6|)$ and $\log_{10}(c_{\beta\alpha})$ versus m_H, respectively. There is a correlation between Λ_6 and m_H (as expected for a sufficiently SM-like Higgs boson, i.e., in the alignment limit $s_{\beta\alpha} \to 1$). In Figures 7.5 and 7.6 we show correlations between the extra scalars. They each obey a linear relationship imposed by the oblique parameter constraints. The size of our masses extends up to $\sim$ 3200 GeV due to the priors on M_{22} and the perturbativity limits used on the quartic couplings.

In Figure 7.8 we plot the logarithm of the absolute value of the off-

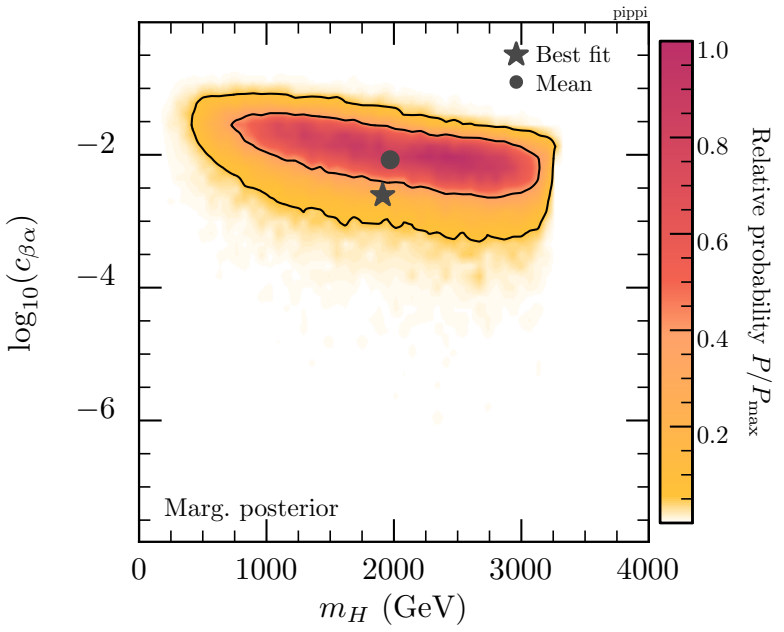

Figure 7.4: 2D posterior distribution of $\log_{10}(c_{\beta\alpha})$ versus m_H.

diagonal Yukawa combinations ($\log_{10}(|\hat{\xi}^D_{23}|)$ and $\log_{10}(|\hat{\xi}^D_{32}|)$) versus $\log_{10}[\text{BR}(h \to bs)]$. We attain an upper (lower) limit on $\text{BR}(h \to bs)$ of $\sim 10^{-3}$ ($\sim 10^{-12}$) at 1σ.

Exploring the constraints that caused these limits, we show in Figure 7.7 the posterior distributions of relevant flavour physics observables (the mass splitting ΔM_{B_s}, the CP-violating phase β_s and the radiative B-decay, $\text{BR}(B \to X_s\gamma)$) with respect to the $h \to bs$ decay. For ΔM_{B_s} we observe two solution regions, as expected from Figures 4.4, 4.5, 4.6 and 4.7. In the upper region, the predicted ΔM_{B_s} mass splitting coincides with the SM value, which is 1.8σ away from the observed value. In the lower region, the 2HDM can accommodate the observed value, and what is more interesting, this yields a upper bound $\text{BR}(h \to bs)$, at the level of $10^{-5} - 10^{-4}$ (at 1σ). This upper bound coincides well with our tree-level prediction (4.86).

In Figure 7.12 we plot the B^0_s meson mixing mass splitting and $\text{BR}(B \to X_s\gamma)$ versus $\text{BR}(t \to ch)$. For radiative B-decays, the combinations $\xi^U_{23}\,\xi^U_{33}\,m_t$ with tops and $\xi^U_{23}\,\xi^D_{33}\,m_b$ with bottoms in the loop, enter. On the other hand, Higgs scalar data favours somewhat large diagonal Yukawa contributions. This, in turn, implies some (weak) upper bounds on ξ^U_{23}. The upper limit on the $\text{BR}(t \to ch)$ comes from the LHC observed upper limit, 2.2×10^{-3} (given in Eq.(5.28)), hence, indirect constraints are weaker. As such, there is still almost an order of magnitude of precision before we may begin exploring the allowed 2HDM region at colliders. In this case, no lower bounds have been found from our scans; these are again just from the priors.

It is also interesting to investigate flavour violation in the new scalar sector, that is decays involving H, A and $H^\pm$. Figures 7.14, 7.15, 7.16

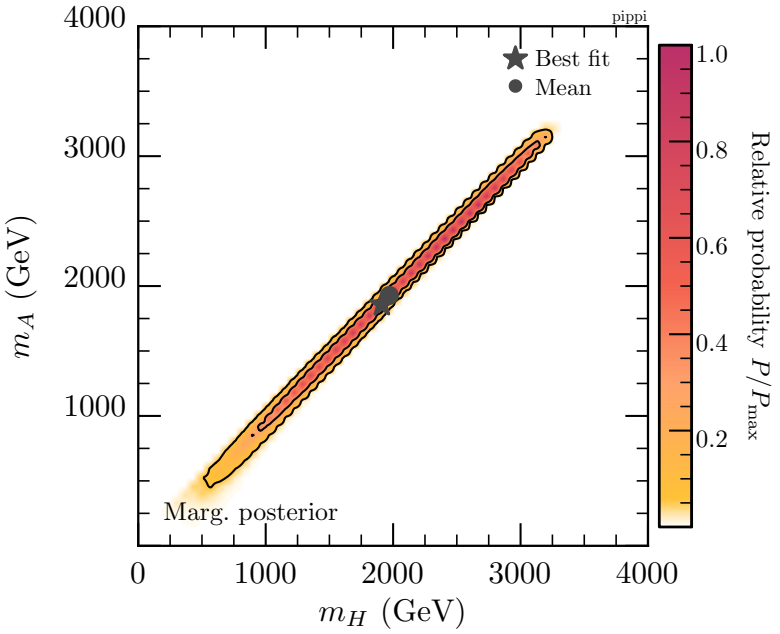

Figure 7.5: 2D posterior distribution of $m_H^{\pm}$ versus m_H.

and 7.17 display the modulus of the relevant off-diagonal Yukawa's versus BR($H \to bs$). Similar plots are obtained for $A \to bs, tc$, and $H \to tc$. Remarkably, these flavour-changing decays can saturate the decay widths of the heavy scalars. This may be relevant for direct searches. We also note that $H^+ \to tb$ has the largest lower bound.

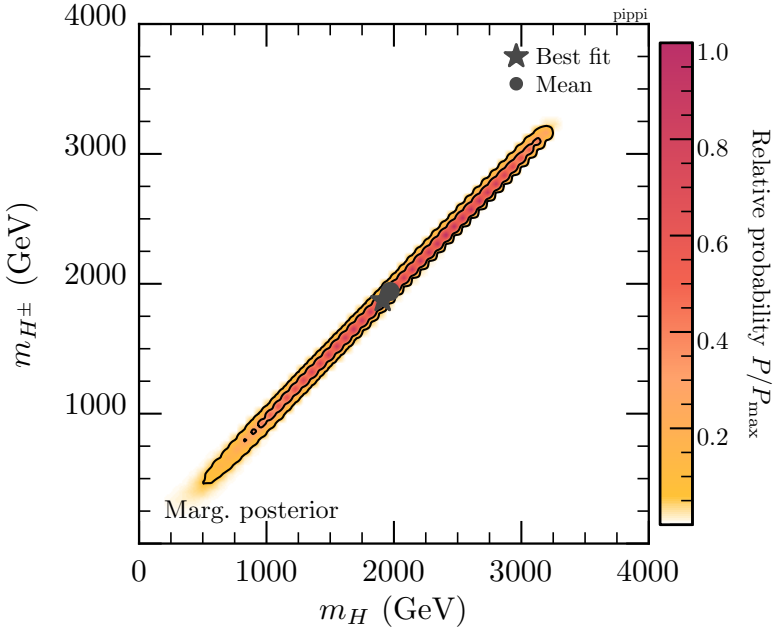

Figure 7.6: 2D posterior distribution of m_A versus m_H.

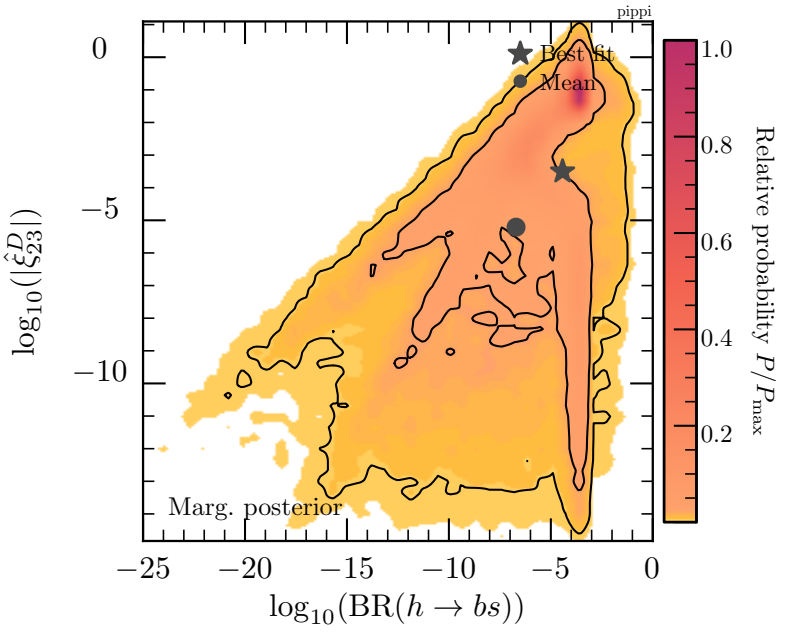

Figure 7.7: 2D posterior distribution of off-diagonal down-quark Yukawa couplings $\log_{10}(|\hat{\xi}^D_{23}|)$ versus $\log_{10}[\mathrm{BR}(h \to bs)]$.

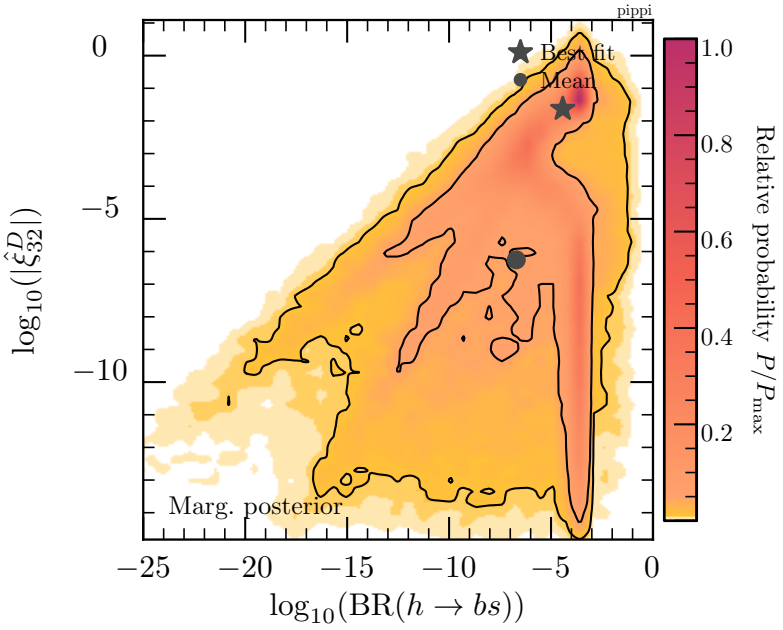

Figure 7.8: 2D posterior distribution of off-diagonal down-quark Yukawa couplings $\log_{10}(|\hat{\xi}^D_{32}|)$ versus $\log_{10}[\mathrm{BR}(h \to bs)]$.

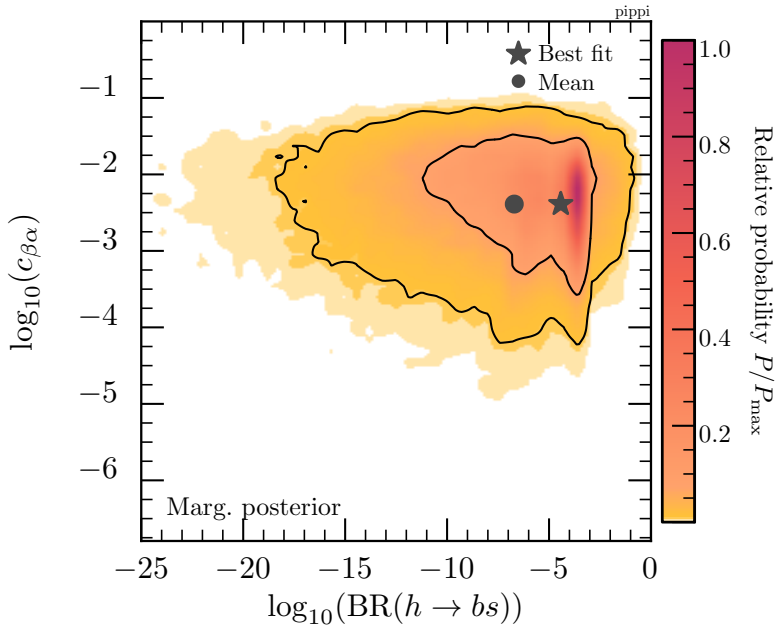

Figure 7.9: 2D posterior distribution of the logarithm of the physical angle $c_{\beta\alpha}$ versus $\log_{10}[\mathrm{BR}(h \to bs)]$.

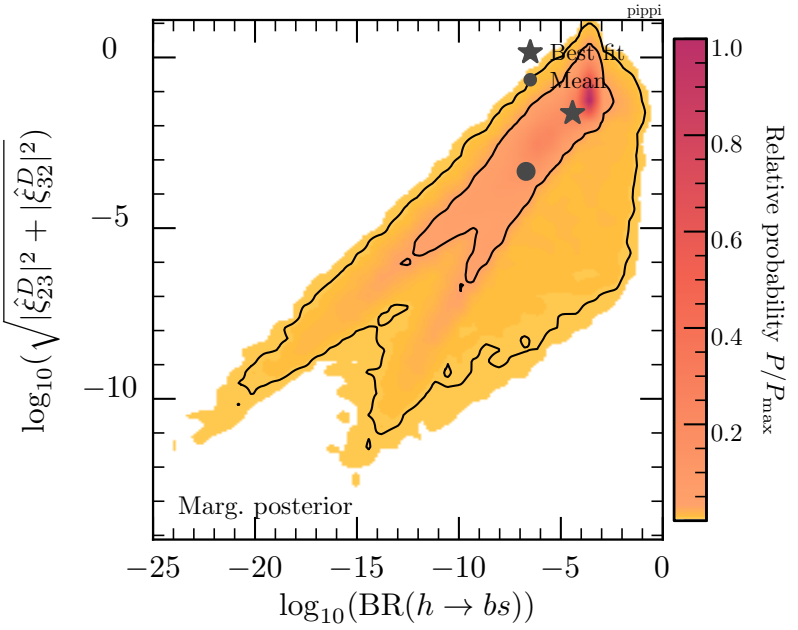

Figure 7.10: 2D posterior distribution of the modulus of the off-diagonal contributions to $\hat{\xi}^D$ versus $\log_{10}[\mathrm{BR}(h \to bs)]$.

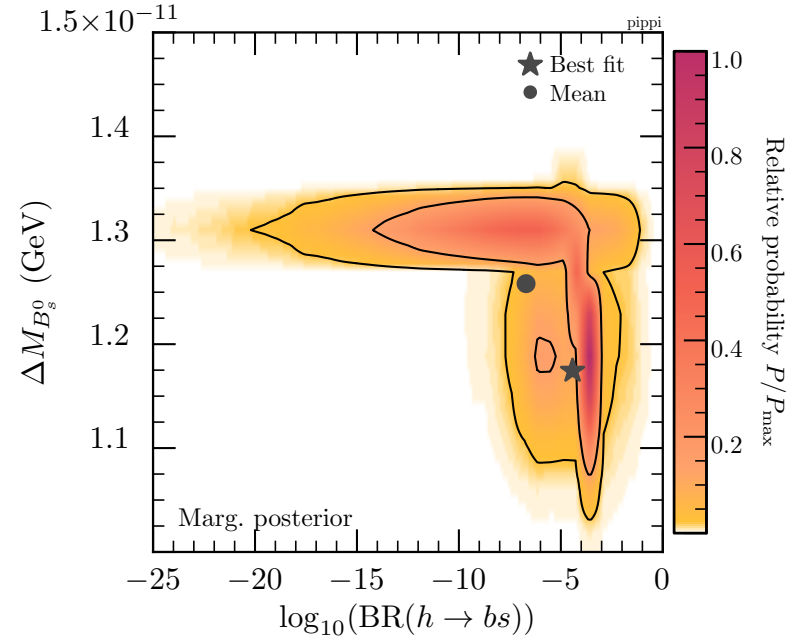

Figure 7.11: 2D posterior distribution of B^0_s meson mixing mass splitting versus $\log_{10}[\mathrm{BR}(h \to bs)]$.

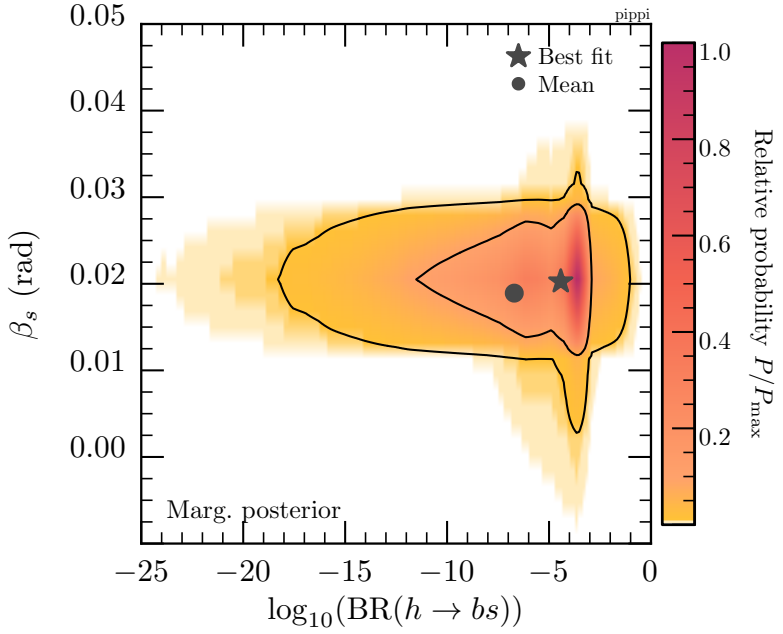

Figure 7.12: 2D posterior distribution of the B_s^0 meson CP phase versus $\log_{10}[\mathrm{BR}(h \to bs)]$.

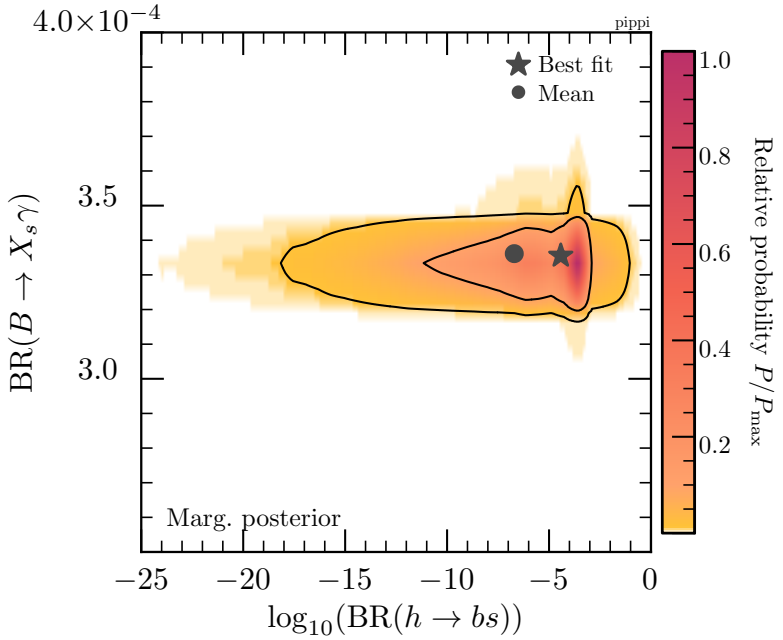

Figure 7.13: 2D posterior distribution of the radiative B decay $\mathrm{BR}(B \to X_s\gamma)$ versus $\log_{10}[\mathrm{BR}(h \to bs)]$.

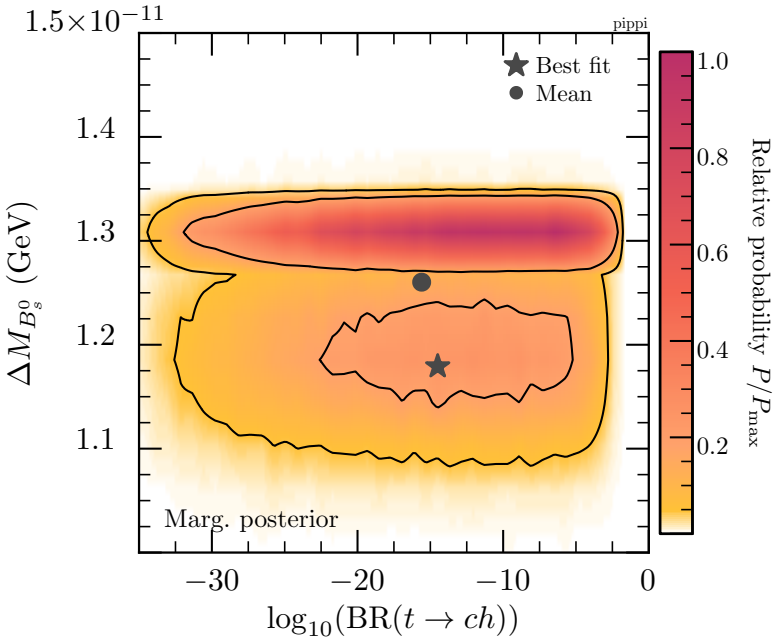

Figure 7.14: 2D posterior distribution of B_s^0 meson mixing mass splitting versus $\log_{10}[\mathrm{BR}(t \to ch)]$.

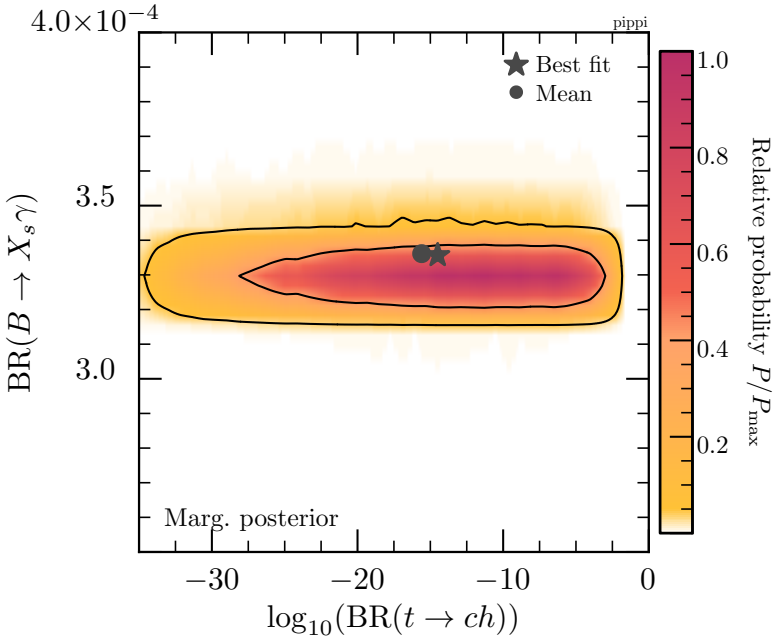

Figure 7.15: 2D posterior distribution of radiative B decays versus $\log_{10}[\mathrm{BR}(t \to ch)]$.

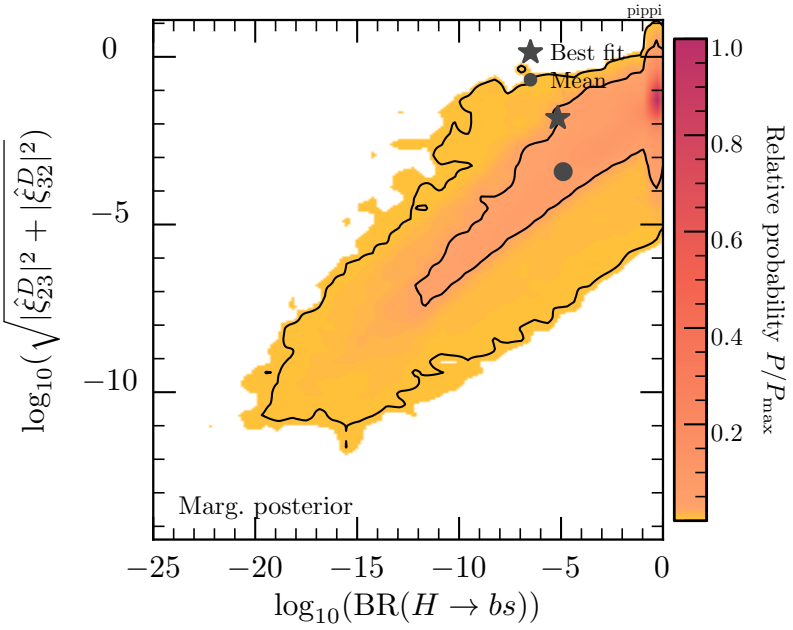

Figure 7.16: 2D posterior distribution of $\log_{10}(|\hat{\xi}^D_{23}|^2 + |\hat{\xi}^D_{32}|^2)^{1/2}$ versus $\log(\mathrm{BR}(H \to bs))$.

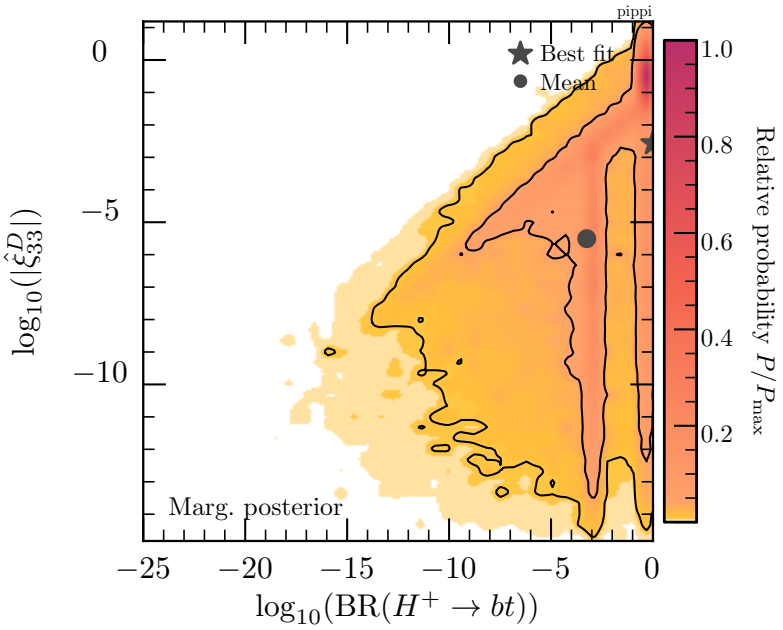

Figure 7.17: 2D posterior distribution of $\log_{10}(|\hat{\xi}^D_{33}|)$ versus $\log(\mathrm{BR}(H^+ \to tb))$.

8 Conclusions

In this thesis, we have investigated the Z_2 Yukawa aligned 2HDMs (type-I, type-II, lepton-specific and flipped models) as well as the general 2HDM (type-III) through modern global scanning techniques. Both models were taken to be CP-conserving.

For Z_2 Yukawa aligned models, we carried out our analysis up to two-loops using `GAMBIT`. We were interested in describing the accessible parameter space after the application of constraints. The theoretical constraints we applied are the stability of the tree-level potential up to 1 TeV, unitarity of the NLO scattering matrix and perturbativity of four-point scalar couplings up to 1 TeV. We also applied perturbativity constraints on both the scalars mass loop-corrections and the corrections to the scattering eigenvalues and checked that our vacuum solution was a global minimum. Experimental constraints we applied were the latest collider constraints, flavour physics process constraints and electroweak precision parameters fits.

The type-II and flipped model pair and the type-I and lepton-specific model pair each showed strong similarities between them. These similarities were expected due to the relationships in their Yukawa alignment. We found that λ_1 had an upper limit ~ 3 at 2σ set by the requirement that four-point couplings needed to remain perturbative up to 1 TeV. Meanwhile, λ_2 had the strongest upper limit at 1 set by constraining the light CP-even Higgs mass to the observed SM mass. Higher values of λ_2 are accessible for lower t_β and m_{12}^2 but this region is difficult to sample and locked out by flavour constraints pushing up t_β. Both $\lambda_1 > 0$ and $\lambda_2 > 0$ as expected by the stability of the potential. λ_3 shows double-peaked behaviour (at 1σ) about zero in the type-II and flipped models and λ_4 shows such behaviour in all models (albeit weaker in type-I and flipped, due to sampling density). This peaking behaviour is observed due to the tension between `HiggsSignals`, flavour and EWPO constraints.

The physical mixing angle combination $\beta - \alpha$ closely followed the alignment limit ($\pi/2$) for all models. In the type-I, we showed a greater opening in $\beta - \alpha$ than in the other models pushing $|c_{\beta\alpha}|$ as high as 0.19 at 1σ. The alignment may explain this opening in type-I, as all Yukawa's are coupled to the same field.

We ended our study of the Z_2 Yukawa aligned models by examining probably the most interesting sector, the physical mass spectrum. We found an upper limit on all our heavy Higgs scalars at ~ 2 TeV due to the limits on corrections to the light CP-even Higgs. When corrections to the light CP-even Higgs grow too large, we may no longer fit the observed SM Higgs mass. We do not confirm this as a limit of the theory, as it may be a limitation of the loop-order to which we carried out our analysis, and cancellations at higher loop order may suppress this. As expected, the heavy scalar masses are strongly correlated, due to the EWPO fits. We observe an upper limit on the correlated heavy scalar masses m_H, m_A and $m_{H^\pm}$ at 900, 800, 950 and 1300 GeV for the type-I, type-II, lepton-specific and flipped models, respectively at 2σ. Lower limits are shared between the model pairs, and are 200 and 300 GeV for the type-I and lepton-specific model pair, and type-II and flipped model pair, respectively, at 2σ. We found that these lower and upper limits stem from a tension between radiative B decays (BR($b \to s\gamma$)) pushing up the lower bound and $B^0 \to K^*\mu\mu$ angular observables pushing down the upper bound. These processes are associated with the alignment model type in the Yukawa's, so we see different behaviour in each case. It

is common in the 2HDM that BR($b \to s\gamma$) pushes up the scalar masses for the type-II and lepton-specific models. This effect was most apparent in the best-fit mass of the charged Higgs, which was significantly larger for the type-II and lepton-specific models. We see that $B^0 \to K^*\mu^+\mu^-$ angular observables are anomalous and we present global fits of the type-II model without this constraint. This modified scan considerably opens up our type-II scalar mass parameter space, allowing the BR($b \to s\gamma$) measurement to push up the masses, the 2σ interval for the aligned heavy scalar becomes [700, 1500] GeV.

Our second study in this thesis removed the alignment in the Yukawa sector and scanned a general tree-level type-III 2HDM using a standalone code package. The removal of the Yukawa alignment (removal of the Z_2-symmetry) allowed for FCC at tree-level. We were interested in finding upper limits on the $h \to bs$ and $t \to ch$ branching ratios as they are heavily suppressed in the SM. We applied the same theoretical and experimental constraints as used in the GAMBIT scan, and made appropriate modifications to allow for the Z_2-violating terms. We did not include NLO corrections to the scattering eigenvalues. We focused primarily on B-physics constraints coming from B_s^0 meson mixing (mass splitting and CP-violating phase) and the radiative decay $b \to s\gamma$, which impose the most significant restrictions on the non-diagonal Yukawa elements between the second and third-generation quarks. We have also observed that the $\sim 2\sigma$ mass-splitting discrepancy with respect to the SM in the B_s mass splitting can be accommodated in the 2HDM at tree-level, yielding a lower bound prediction of BR($h \to bs$) $\simeq 10^{-5} - 10^{-4}$ if loop-level and heavy Higgs contributions are not significant. The final values obtained in our full parameter scan are BR($h \to bs$) $< 10^{-3}$ (10^{-1}) and BR($t \to ch$) $< 6 \times 10^{-4}$ (10^{-2}) at 1 and 2σ (lower bounds, if present, are at the level of the one-loop SM prediction). This parameter space is already accessible and can be further examined at future colliders [128]. For example, a future 100 TeV proton-proton collider is able to constrain the $t \to ch$ channel at $O(10^{-5})$ [129]. Beyond the two hallmark decays, possibly the easiest quark-FC process to observe is $H^+ \to tb$ due to its large production cross-section and the possible large branching fraction.

Outlook This work has laid the foundations for 2HDM global scans using GAMBIT and has shown that 2HDMs are both a viable candidate for BSM physics that may be identified using FC processes. Primarily, in future work, non-preliminary GAMBIT results will be published and accompany the release of the 2HDM GAMBIT extension. It would then be desirable for all likelihoods to be extended to support Z_2-violating terms, followed by the completion of the general type-III model with FCC within GAMBIT.

Appendices

A

Decay Widths and Cross Sections

Theory allows us to calculate the amplitude $|\mathcal{M}|^2$ for a process from the scattering matrix; however, experimentally we observe only process widths leading to cross-sections and decay rates. In this Appendix, we will show how to calculate the width from the scattering amplitude. We find that one of the biggest challenges involves constructing the incoming particle kinematic state or the Lorentz invariant phase space (LIPS). We present a pedagogical introduction to LIPS and finally calculate two SM processes as an example.

This argument follows that presented in Chapter 11 of Ref [130]. *

A.1 Current Widths

Start by defining initial and final particle states for n particles $|i\rangle$, $\langle f|$, respectively. Initial state particles have a total four-momenta defined as k_{in}, final state particles have a total four momenta k_{out}. The normalised scattering probability, the probability for a particle to go from an initial to the final state, is then given by

$$P = \frac{|\langle f|i\rangle|^2}{\langle f|f\rangle\langle i|i\rangle}. \tag{A.1}$$

We may calculate the overlap

$$\begin{aligned} |\langle f|i\rangle|^2 &= [(2\pi)^4\delta^4(k_{in}-k_{out})]^2|\mathcal{M}|^2, \\ &= (2\pi)^4\delta^4(k_{in}-k_{out})\ (2\pi)^4\delta^4(0)\ |\mathcal{M}|^2, \\ &= (2\pi)^4\delta^4(k_{in}-k_{out})|\mathcal{M}|^2 \int d^4x e^{i0\cdot x}, \\ &= (2\pi)^4\delta^4(k_{in}-k_{out})|\mathcal{M}|^2 Vt, \end{aligned} \tag{A.2}$$

where $|\mathcal{M}|^2$ is the scattering amplitude squared and we assume the experiment is taking place in a box with volume V and over time t. Next, construct initial and final state overlaps.

Consider a decay process, with one incoming particle and n' outgoing particles

$$\begin{aligned} \langle i|i\rangle &= 2E_{in}V, \\ \langle f|f\rangle &= \prod_{j=1}^{n'} 2k_j^{'0}V, \end{aligned} \tag{A.3}$$

* Note in this Appendix we do not make simplifications for writing cos, sin or tan.

where, E_{in} is the incoming energy of the particle and k_j is the momentum of the j^{th} particle. Putting this all together we get an expression for the scattering probability per unit time

$$\frac{P}{t} = \frac{(2\pi)^4 \delta^4(k_{in} - k_{out})|\mathcal{M}|^2}{2E_{in} \prod_{j=1}^{n'} 2k_j'^0 V}. \tag{A.4}$$

The problem now is that this equation is defined only for precise momenta and this will be very difficult to idealise in a realistic situation. Instead we need to turn our attention to the probability over a small distribution of momenta. To achieve this, let us sum over a range of outgoing particles. We know that the three momenta must be quantised such that in a box of side length L, we can make the connection with our range in momentum space via the expression

$$\mathbf{k_j'} = \frac{2\pi \mathbf{n_j'}}{L}, \tag{A.5}$$

where $\mathbf{n_j'}$ is a three-dimensional vector of integer values that is responsible for the quantisation of the space. Summing over $\mathbf{n_j'}$ and taking $L \longrightarrow \infty$, we find that we can define the substitution

$$\sum_{\mathbf{n_j'}} \longrightarrow \frac{V}{(2\pi)^3} \int d^3 k_j', \tag{A.6}$$

which ultimately leads us to our expression

$$\sum_{\mathbf{n_j'}} \frac{P}{t} = \frac{(2\pi)^4 \delta^4(k_{in} - k_{out})|\mathcal{M}|^2}{2E_{in}} \prod_{j=1}^{n'} \int \frac{d^3 k_j'}{(2\pi)^3 2k_j'^0}. \tag{A.7}$$

This is exactly the probability of a particle going to n' particles, the expression for a decay rate. The final step is to define the Lorentz invariant phase space, it appears exactly in our decay rate formula

$$d\text{LIPS}_{n'}(k) = (2\pi)^4 \delta^4(k_{in} - \sum_{j=1}^{n'} k_{out}) \prod_{j=1}^{n'} \frac{d^3 k_j'}{(2\pi)^3 2k_j'^0}, \tag{A.8}$$

leading us to

$$\Gamma = \frac{|\mathcal{M}|^2}{2E_{in}} d\text{LIPS}_{n'}(k). \tag{A.9}$$

Next, we want to find more explicit expressions for our Lorentz invariant phase space, firstly for two-body decays and then for the more complicated case of particle decaying into three smaller particles.

A.2 About the Two-Body Phase Space

The two body phase space is fundamental to constructing multiple body extensions and, hence, writing down specific formulas for decay rates. Label our decay momenta as $P \rightarrow p_1 + p_2$, so by the general formula for LIPS (A.9)

$$d_2\Phi(P; p_1, p_2) = (2\pi)^4 \delta^4(p_1 + p_2 - P) \frac{d^3 \mathbf{p_1}}{(2\pi)^2 2p_1^0} \frac{d^3 \mathbf{p_2}}{(2\pi)^2 2p_2^0}. \tag{A.10}$$

Separating the delta function and defining the invariant mass term $s = (P_0)^2$

$$d_2\Phi(P; p_1, p_2) = (2\pi)^4\delta^3(\mathbf{p_1} + \mathbf{p_2} - \mathbf{P})\delta(E_1 + E_2 - \sqrt{s})\frac{d^3\mathbf{p_1}}{(2\pi)^2 2E_1}\frac{d^3\mathbf{p_2}}{(2\pi)^2 2E_2}. \tag{A.11}$$

Next, we place ourselves in the centre of mass frame of the decay, this is defined such that

$$\begin{aligned}\mathbf{p_1} = -\mathbf{p_2} \equiv \mathbf{p},\\ \mathbf{P} = 0.\end{aligned} \tag{A.12}$$

Here we can integrate over $\mathbf{p_2}$. Notice the condition imposed by the delta function is exactly satisfied by Eq. (A.12)

$$d_2\Phi(P; p_1, p_2) = \frac{1}{(2\pi)^2 2E_1 2E_2}\delta(E_1 + E_2 - \sqrt{s})\, d^3\mathbf{p}. \tag{A.13}$$

Using the energy-momentum relation the delta function becomes

$$\begin{aligned}&\delta(\sqrt{\mathbf{p_1} + m_1} + \sqrt{\mathbf{p_2} + m_2} - \sqrt{s}),\\ &= \delta(\sqrt{\mathbf{p} + m_1} + \sqrt{\mathbf{p} + m_2} - \sqrt{s}).\end{aligned} \tag{A.14}$$

Now introduce the useful delta function identity

$$\delta(f(\mathbf{p})) = \sum_i \frac{\delta(\mathbf{p} - p_i)}{f'(\mathbf{p})|_{\mathbf{p}=p_i}}, \tag{A.15}$$

where the sum is over the p_i roots of $f(\mathbf{p})$. In our case

$$f(\mathbf{p}) = (\sqrt{\mathbf{p} + m_1} + \sqrt{\mathbf{p} + m_2} - \sqrt{s}), \tag{A.16}$$

which has a single root when

$$|\mathbf{p}| = p_0 = \frac{1}{2\sqrt{s}}(s^2 + m_1^4 + m_2^4 - 2sm_1^2 - 2sm_2^2 - 2m_1^2m_2^2)^{1/2}. \tag{A.17}$$

After some algebraic manipulation the delta-function becomes

$$\delta(f(\mathbf{p})) = \frac{\delta(\mathbf{p} - p_0)E_1E_2}{|\mathbf{p}|(E_1 + E_2)}. \tag{A.18}$$

Returning this all to our phase space expression

$$d_2\Phi(P; p_1, p_2) = \frac{1}{(2\pi)^2 2E_1 2E_2}\frac{\delta(\mathbf{p} - p_0)E_1E_2}{|\mathbf{p}|(E_1 + E_2)}\, d^3\mathbf{p}. \tag{A.19}$$

Simplifying and redefining the integral over polar coordinates

$$d_2\Phi(P; p_1, p_2) = \frac{1}{4(2\pi)^2}\frac{\delta(\mathbf{p} - p_0)}{|\mathbf{p}|(E_1 + E_2)}|\mathbf{p}|^2 d|\mathbf{p}| d\cos\theta d\phi, \tag{A.20}$$

and finally, performing the integration over $|\mathbf{p}|$

$$d_2\Phi(P; p_1, p_2) = \frac{1}{4\pi\sqrt{s}}p_0\frac{d\cos\theta}{2}\frac{d\phi}{2\pi}, \tag{A.21}$$

where in the centre of mass $E_1 + E_2 = \sqrt{s}$. If in the final state we average over the particles spin, we have an isotropic final state, and so there is no dependence on either of the polar angles leaving us with the simplified Lorentz invariant phase space for a two-body system

$$d_2\Phi(P; p_1, p_2) = \frac{p_0}{4\pi\sqrt{s}}. \tag{A.22}$$

A.3 About the Three-Body Phase Space

Expressions for three-body decays and beyond become rapidly more complex and are best derived specifically for each decay process. We will derive a more general expression for multi-body phase spaces using the two-body phase space formula and then proceed to look at an explicit expression for the three-body phase space. Although the final expression will prove somewhat complicated, it is illuminating to construct, as many of the tricks involved in the calculation turn out to be helpful tools when calculating specific decay processes.

Begin by considering the decay with momenta $P \to p_1 + p_2 + p_3$. Again the first step will be to write out the general LIPS form

$$d_3\Phi(P; p_1, p_2, p_3) = (2\pi)^4\delta^4(p_1 + p_2 + p_3 - P)\frac{d^3\mathbf{p_1}}{(2\pi)^2 2p_1^0}\frac{d^3\mathbf{p_2}}{(2\pi)^2 2p_2^0}\frac{d^3\mathbf{p_3}}{(2\pi)^2 2p_3^0}. \tag{A.23}$$

In fact, we can think of this decay as two consecutive decay processes. Grouping the p_2 and p_3 we can write the equivalent decay processes, $\Gamma(P \to p_1 + \{p_2 + p_3\})$ followed by $\Gamma(\{p_2 + p_3\} \to p_2 + p_3)$. These are simply two body decay processes and we have already found the expression for the corresponding phase spaces. It remains to express our general result (A.23) in terms of two-body processes. The approach may at first seem abstract, but it helps to think about each equation and delta function as nothing more than a constraint set by the kinematics of the decay.

First, we take a step to the side and introduce some mathematical preliminaries. Define

$$\begin{aligned} s_{23} &= (p_2 + p_3)^2, \\ p_{23} &= p_2 + p_3. \end{aligned} \tag{A.24}$$

Then we can construct the following

$$\int \frac{d^4p_{23}}{(2\pi)^4}\theta(q_0^{23})(2\pi)^4\delta^4(p_2 + p_3 - p_{23}) = 1, \tag{A.25}$$

$$\int \frac{ds_{23}}{(2\pi)}(2\pi)\delta(s_{23} - p_{23}^2) = 1, \tag{A.26}$$

where θ is the Heaviside-step function. Combining the above two equations and expanding the first delta function gives

$$\int \frac{d^3p_{23}}{(2\pi)^3}\frac{dp_{23}^0}{(2\pi)}\frac{ds_{23}}{(2\pi)}\theta(p_{23}^0)(2\pi)^4\delta^4(p_2 + p_3 - p_{23})(2\pi)\delta(s_{23} - p_{23}^2) = 1. \tag{A.27}$$

Again we make use of the identity (A.18) on the second delta-function, making the definition

$$\begin{aligned} f(E_{23}) &= s_{23} - p_{23}^2, \\ &= s_{23} - (E_{23})^2 + \mathbf{p}_{23}^2, \end{aligned} \tag{A.28}$$

so that

$$\delta(s_{23} - p_{23}^2) = \frac{\delta(E_{23} - E_0)}{2E_{23}|_{E_0}}, \tag{A.29}$$

where

$$E_0 = \pm\sqrt{s_{23} + \mathbf{p}_{23}^2}. \tag{A.30}$$

We keep only the positive energy answers of Eq. (A.3) because of the step-function that appears in Eq. (A.27) which becomes

$$\int \frac{d^3p_{23}}{(2\pi)^3}\frac{dE_{23}}{(2\pi)}\frac{ds_{23}}{(2\pi)}\theta(E_{23})(2\pi)^4\delta^4(p_2 + p_3 - p_{23})(2\pi)\frac{\delta(E_{23} - E_0)}{2E_{23}|_{E_0}} = 1. \tag{A.31}$$

Carrying out the E_{23} integration

$$\int \frac{d^3p_{23}}{(2\pi)^3(2E_{23})}\frac{ds_{23}}{(2\pi)}(2\pi)^4\delta^4(p_2 + p_3 - p_{23}) = 1. \tag{A.32}$$

We have retained the label E_{23} here as it is exactly E_0 by the energy-momentum relation Eq. (A.3). Now, we return back to our general formula for the three-body phase space (A.23) and multiply it by the above

$$\begin{aligned} d_3\Phi(P; p_1, p_2, p_3) = &\frac{d^3\mathbf{p_1}}{(2\pi)^2 2p_1^0}\frac{d^3\mathbf{p_2}}{(2\pi)^2 2p_2^0}\frac{d^3\mathbf{p_3}}{(2\pi)^2 2p_3^0}\frac{d^3p_{23}}{(2\pi)^3(2E_{23})}\frac{ds_{23}}{(2\pi)} \\ &(2\pi)^4\delta^4(p_1 + p_2 + p_3 - P)(2\pi)^4\delta^4(p_2 + p_3 - p_{23}). \end{aligned} \tag{A.33}$$

which reduces to

$$d_3\Phi(P; p_1, p_2, p_3) = d_2\Phi(P; p_1, p_{23})\frac{ds_{23}}{(2\pi)}d_2\Phi(p_{23};, p_2, p_3). \tag{A.34}$$

This is exactly the form that we discussed. Of course, this trick is not limited to the three-body case. In fact with a bit of care and mathematical rigour any multi-particle phase-space can be reduced to a combination of two-body phase space and integrations over grouped invariant masses.

It is intuitive that next, we substitute our expression for the two-body phase space we found in section 4.4.1, that being

$$d_2\Phi(P; p_1, p_2) = \frac{|\mathbf{p}|}{4\pi\sqrt{s}}\frac{d\cos\theta}{2}\frac{d\phi}{2\pi}, \tag{A.35}$$

where

$$|\mathbf{p}| = \frac{1}{2\sqrt{s}}(s^2 + m_1^4 + m_2^4 - 2sm_1^2 - 2sm_2^2 - 2m_1^2m_2^2). \tag{A.36}$$

We obtain

$$d_3\Phi(P; p_1, p_2, p_3) = \frac{|\mathbf{p}_1|}{4\pi\sqrt{s}}\frac{d\cos\theta}{2}\frac{d\phi}{2\pi}\left[\frac{ds_{23}}{(2\pi)}\right]\frac{|\hat{\mathbf{p}}_{23}|}{4\pi\sqrt{s_{23}}}\frac{d\cos\hat{\theta}}{2}\frac{d\hat{\phi}}{2\pi}. \tag{A.37}$$

The un-hatted quantities are evaluated in the overall reference frame, while the hatted quantities are evaluated in the what we will refer to as the 'Jackson frame'. The angle θ is the angle between $-p_1$ and p_2 in the overall frame, the corresponding hatted θ, p_1, p_2 have the same relationship in the Jackson frame. The overall reference frame is the centre of mass frame for $d_2\Phi(P; p_1, q_{23})$ and has the useful

properties that

$$\begin{aligned} P = (m, 0, 0, 0) \implies \mathbf{P} = 0, \\ \mathbf{p_1} = \mathbf{q_{23}}. \end{aligned} \tag{A.38}$$

Meanwhile, the Jackson frame is the centre of mass frame for $d_2\Phi(q_{23}; p_2, p_3)$ and has useful properties

$$\begin{aligned} \mathbf{q_{23}} = 0, \\ \mathbf{p_2} = -\mathbf{p_3}, \end{aligned} \tag{A.39}$$

$$\mathbf{P} = \mathbf{p_1}. \tag{A.40}$$

Where the last property above follows from momentum conservation. In the overall reference frame we have from Eq. (A.17) that

$$|\mathbf{p}_1| = \frac{1}{2\sqrt{s}}[\lambda(s, m_1^2, s_{23})]^{1/2}, \tag{A.41}$$

$$|\mathbf{p}_{23}| = \frac{1}{2\sqrt{s_{23}}}[\lambda(s_{23}, m_2^2, m_3^2)]^{1/2}. \tag{A.42}$$

Where we have made the conventional simplification

$$\lambda(x, y, z) = x^4 + y^4 + z^4 - 2x^2y^2 - 2x^2z^2 - 2y^2z^2. \tag{A.43}$$

If we make the assumption that the decay is isotropic we can take the θ, ϕ and $\hat{\phi}$ integrals now, leaving us with

$$d_3\Phi(P; p_1, p_2, p_3) = \frac{|\mathbf{p}_1|}{4\pi\sqrt{s}}\left[\frac{ds_{23}}{(2\pi)}\right]\frac{|\hat{\mathbf{p}}_{23}|}{4\pi\sqrt{s_{23}}}\frac{d\cos\hat{\theta}}{2}, \tag{A.44}$$

simplifying

$$d_3\Phi(P; p_1, p_2, p_3) = \frac{1}{64(\pi)^3\sqrt{s}\sqrt{s_{23}}}ds_{23}|\mathbf{p}_1||\hat{\mathbf{p}}_{23}|d\cos\hat{\theta}. \tag{A.45}$$

Next we need to form a relationship between the overall frame and the Jackson frame. In the Jackson frame we have

$$\begin{aligned} s_{23} &= (\hat{p_2} + \hat{p_3})^2, \\ &= (\hat{P} - \hat{p_1})^2, \\ &= P^2 + p_1^2 - 2\hat{P}\cdot\hat{p_1}, \\ &= (P^0)^2 - \mathbf{P}^2 + (p_1^0)^2 - \mathbf{p_1}^2 - 2\hat{P}^0\hat{p_1^0} + 2\hat{\mathbf{P}}\cdot\hat{\mathbf{p}_1}, \\ &= (P^0)^2 + (p_1^0)^2 - 2\hat{P}^0\hat{p_1^0} - 2\hat{\mathbf{P}^2} + 2\hat{\mathbf{P}^2}, \\ &= (\hat{P^0} - \hat{p_1^0})^2, \\ &= (\hat{E} - \hat{E_1})^2, \end{aligned} \tag{A.46}$$

where we have made use of Eq. (A.40) in cancelling the vector quantities. Using the energy momentum relation

$$s_{23} = \left(\sqrt{s + \hat{\mathbf{p_1}^2}} - \sqrt{m_1^2 + \hat{\mathbf{p_1}^2}}\right)^2. \tag{A.47}$$

Finally solving for $|\hat{\mathbf{p}_1}|$

$$|\hat{\mathbf{p}_1}| = \frac{1}{2\sqrt{s_{23}}}[\lambda(s, m_1^2, s_{23})]^{1/2}. \tag{A.48}$$

Now, by comparing with the momentum in the overall reference frame Eq. (A.41) we can form a useful

relation

$$|\mathbf{p}_1| = \sqrt{\frac{s_{23}}{s}}|\hat{\mathbf{p}}_1|. \tag{A.49}$$

Allowing us to write

$$d_3\Phi(P; p_1, p_2, p_3) = \frac{1}{64(\pi)^3 s} ds_{23} |\hat{\mathbf{p}}_1||\hat{\mathbf{p}}_{23}| d\cos\hat{\theta}. \tag{A.50}$$

Recall, $\hat{\theta}$ is the angle between $-\hat{\mathbf{p}}_1$ and $\hat{\mathbf{p}}_2$, so we write

$$\begin{aligned} s_{12} &= (\hat{p}_1 + \hat{p}_2)^2, \\ &= m_1^2 + m_2^2 + 2\hat{E}_1\hat{E}_2 + 2|\hat{\mathbf{p}}_1||\hat{\mathbf{p}}_{23}|\cos\hat{\theta}. \end{aligned} \tag{A.51}$$

The positive sign of the last term is attributed to the fact that one of the momenta is negative. Then taking the variation of s_{12} we find that

$$ds_{12} = 2|\hat{\mathbf{p}}_1||\hat{\mathbf{p}}_{23}| d\cos\hat{\theta}. \tag{A.52}$$

This takes a slight explanation. If we solve for $|\hat{\mathbf{p}}_{23}|$ we find that it is dependent only on masses m_2, m_3 and invariant mass s_{23}

$$|\hat{\mathbf{p}}_{23}| = \frac{1}{2\sqrt{s_{23}}}[\lambda(s_{23}, m_2^2, m_3^2)]^{1/2}. \tag{A.53}$$

If we consider the invariant mass s_{23} as being fixed, then we see that the variation of Eq. (A.51) must act only on the $\cos\hat{\theta}$ term.

Reducing our phase-space expression to

$$d_3\Phi(P; p_1, p_2, p_3) = \frac{1}{128\pi^3 s} ds_{12} ds_{23}. \tag{A.54}$$

This is our final expression as appears in Eq. (A.23), however, our work is not quite done yet. Next, we need to establish the bounds over which this expression is valid, we will use the kinematics to find such bounds. Starting with limits for s_{23}, we get

$$\begin{aligned} s_{23} &= s + m_1^2 - 2\sqrt{s}E_1, \\ &= s + m_1^2 - 2\sqrt{s}\sqrt{m_1^2 + \mathbf{p}_1^2}. \end{aligned} \tag{A.55}$$

Now the maximum of this expression occurs in the case when $\mathbf{p}_1^2 = 0$

$$\begin{aligned} \max\, s_{23} &= s + m_1^2 - 2\sqrt{s}m_1^2, \\ &= (\sqrt{s} - m_1)^2. \end{aligned} \tag{A.56}$$

Finding the minimum requires us to look at the expression for s_{23} that we have in the Jackson Frame, beginning with a similar expansion as done in Eq. (A.46)

$$\begin{aligned} s_{23} &= (\hat{E}_2 + \hat{E}_3)^2, \\ &= \left(\sqrt{\hat{\mathbf{p}_2}^2 + m_2^2} + \sqrt{\hat{\mathbf{p}_2}^2 + m_3^2}\right)^2. \end{aligned} \tag{A.57}$$

Again taking the momentum equal to zero we find that this now corresponds to a minimum value

$$s_{23} \geq (m_2 + m_3)^2, \implies \min\, s_{23} = (m_2 + m_3)^2. \tag{A.58}$$

Hence, we have bounded s_{23}, but what about s_{12} can we just do the same? The answer is no, as the bound we have applied on s_{23} has affected the kinematic limits placed on s_{12} and so we must also take this into consideration. Expanding s_{12} in the Jackson frame

$$s_{12} = m_1^2 + m_2^2 + 2\big(\hat{E}_1\hat{E}_2 - |\hat{\mathbf{p}}_1||\hat{\mathbf{p}}_{23}|\cos\hat{\theta}\big). \tag{A.59}$$

The maximum and minimum values of this expression occur at $\hat{\theta} = \pi$ and $\hat{\theta} = 0$, respectively. Giving

$$s_{12\pm} = m_1^2 + m_2^2 + 2\big(\hat{E}_1\hat{E}_2 \pm |\hat{\mathbf{p}}_1||\hat{\mathbf{p}}_{23}|\cos\hat{\theta}\big), \tag{A.60}$$

where $s_{12\pm}$ denotes both maximum and minimum bounds for s_{12}. We need to solve for $\hat{E}_1$ and $\hat{E}_2$, notice that in the Jackson frame, $q_{23} = (\sqrt{s_{23}}, 0, 0, 0)$, and then

$$\begin{aligned} \hat{P} &= (\hat{p}_1 + \hat{q}_{23}), \\ &= m_1^2 + s_{23} + 2\hat{E}_1\sqrt{s_{23}}. \end{aligned} \tag{A.61}$$

Solving for $\hat{E}_1$

$$\hat{E}_1 = \frac{1}{2\sqrt{s_{23}}}(s - s_{23} - m_1^2). \tag{A.62}$$

Similarly, starting with $\hat{q}_{23} = \hat{p}_2 + \hat{p}_3$, we find

$$\hat{E}_2 = \frac{1}{2\sqrt{s_{23}}}(s_{23} + m_2^2 - m_3^2). \tag{A.63}$$

And so we deduce our kinematic bounds on s_{12} depending on masses m_2, m_3 and invariant mass s_{23}

$$s_{12\pm} = m_1^2 + m_2^2 + \frac{1}{2s_{23}}\left[(s - s_{23} - m_1^2)(s_{23} + m_2^2 - m_3^2) \pm \sqrt{\lambda(s, m_1^2, s_{23})\lambda(s_{23}, m_2^2, m_3^2)}\right]. \tag{A.64}$$

There are some important notes that we need to mention. This is a general formula and can be adapted to each case as proves mathematically simplest. Notice the method we have followed above has used the variation in s_{12}, Eq. (A.52), it would be just as valid to consider the variation in s_{13}, as this is an arbitrary change in label for the two outgoing particles that share a two-body phase space when expanded in Eq. (A.37). Mathematically, we know in the Jackson frame $\mathbf{p}_2 = -\mathbf{p}_3$, so the angle $\hat{\theta}$ needs shifting by π when considering instead the variation in s_{13}, but $\cos(\hat{\theta} + \pi) = -\cos\hat{\theta}$ and this extra negative sign is cancelled by the condition $\mathbf{p}_2 = -\mathbf{p}_3$, hence, we can rewrite Eq. (A.54) as the equivalent

$$d_3\Phi(P; p_1, p_2, p_3) = \frac{1}{128\pi^3 s} ds_{13} ds_{23}. \tag{A.65}$$

The kinematic limits would also change in correspondence. To perform the change, we simply need to relabel the particles in the expressions we have already derived. Finally, it is important to mention that the order in which we derive the bounds for the invariant mass integrals is also arbitrary. It would have been equally reasonable to begin with a bound of s_{12} and then derive the bound on s_{23} restricted by the conditions imposed by s_{12}, provided we carry out the integrations in their respectful order when applying the phase space to a given problem.

A.4 Derivation of the Higgs to Two Fermions Width: $\Gamma(h \to ff)$

We begin our calculations with the simplest case, the Higgs scalar to two fermion decay (shown in Figure 2.7). For the process to be kinematically allowed, we require $2m_f < m_h$. In the SM, both fermions must be the same due to the absence of flavour-changing and kinematically allowed decays are those where $f = d, u, s, c, b$.

The coupling of this Feynman diagram is [3]

$$\lambda_{hf\bar{f}} = \frac{-igm_f}{2m_W}. \tag{A.66}$$

Using Feynman rules we may calculate the process amplitude $\mathcal{M}$. The Feynman rules for this vertex yield

$$i\mathcal{M} = \frac{igm_f}{2m_W}\bar{u}(p,s)v(k,s')2(\pi)^4\delta^4(q-p-k). \tag{A.67}$$

The delta function is implicitly satisfied so we may cancel it. Taking the square and summing over spins s and s'

$$\begin{aligned}
|\mathcal{M}|^2 &= \frac{g^2}{4}\left(\frac{m_f}{m_W}\right)^2 \sum_{s,s'}\left|\bar{u}(p,s)v(k,s')\right|^2, \\
&= \frac{g^2}{4}\left(\frac{m_f}{m_W}\right)^2 \sum_{s,s'}\sum_{a,b}(\bar{u}(p,s)v(k,s'))_a(\bar{u}(p,s)v(k,s'))^*_b, \\
&= \frac{g^2}{4}\left(\frac{m_f}{m_W}\right)^2 \sum_{s,s'}\sum_{a,b}\bar{u}(p,s)_a u(p,s)_b v(k,s')_a \bar{v}(k,s')_b.
\end{aligned} \tag{A.68}$$

Next, we need to make use of the identities

$$\sum_s u^s\bar{u}^s = \not{p} + m, \quad \sum_s v^s\bar{v}^s = \not{p} - m. \tag{A.69}$$

Giving

$$\begin{aligned}
|\mathcal{M}|^2 &= \frac{g^2}{4}\left(\frac{m_f}{m_W}\right)^2 \sum_{a,b}(\not{p}+m)_{ba}(\not{k}-m)_{ab}, \\
&= \frac{g^2}{4}(\frac{m_f}{m_W})^2 \,\mathrm{Tr}\{(\not{p}+m)(\not{k}-m)\}.
\end{aligned} \tag{A.70}$$

Aside, Dirac matrix identities give us

$$\begin{aligned}
\mathrm{Tr}\{(\not{p}+m)(\not{k}-m)\} &= \mathrm{Tr}\{\not{p}\not{k}\} - \mathrm{Tr}\{m_f\not{p}\} + \mathrm{Tr}\{m_f\not{k}\} - \mathrm{Tr}\{m_f^2\}, \\
&= p_\mu k_\nu 4g^{\mu\nu} - 4m_f^2, \\
&= 4(p\cdot k - m_f^2).
\end{aligned} \tag{A.71}$$

Leading to the intermediate expression

$$|\mathcal{M}|^2 = \left(\frac{gm_f}{m_W}\right)^2 (p\cdot k - m_f^2). \tag{A.72}$$

To continue the calculation at this stage we need to consider the kinematics of the decay. In the centre of

mass (COM) frame for the Higgs scalar

$$\begin{aligned} q &= (m_h, \mathbf{0}), \\ p &= (E_f, \mathbf{p}), \\ k &= (E_f, -\mathbf{p}). \end{aligned} \tag{A.73}$$

Allowing us to calculate

$$\begin{aligned} p \cdot k - m_f^2 &= E_f^2 + \mathbf{p}^2 - m_f^2, \\ &= E_f^2 + (E_f^2 - m_f^2) - m_f^2, \\ &= 2\left[\left(\frac{m_h}{2}\right)^2 - m_f^2\right], \\ &= \frac{m_h^2}{2}\left[1 - \frac{4m_f^2}{m_h^2}\right], \end{aligned} \tag{A.74}$$

where we used the energy-momentum relation ($\mathbf{p}^2 = E_f^2 - m_f^2$) and conservation of momentum ($E_f = m_h/2$). Substituting Eq. (A.74) back into Eq. (A.72) we get the final process amplitude-squared

$$|\mathcal{M}|^2 = \left(\frac{g m_f}{m_W}\right)^2 \frac{m_h^2}{2}\left[1 - \frac{4m_f^2}{m_h^2}\right]. \tag{A.75}$$

Eq. (A.9) and Eq. (A.22) from Appendix A.1 for our two body system

$$\Gamma = \frac{|\mathcal{M}|^2}{2m_h} d\text{LIPS}_2(p), \tag{A.76}$$

and

$$d\text{LIPS}_2 = \frac{|\mathbf{p}|}{4\pi m_h}. \tag{A.77}$$

Combining

$$\Gamma = \frac{|\mathbf{p}|}{8\pi m_h^2} |\mathcal{M}|^2. \tag{A.78}$$

We can directly calculate $|\mathbf{p}|$ from Eq. (A.17) in Appendix A.1 or alternatively, notice that applying the energy-momentum relation differently to the first line of Eq.(A.74) we get

$$E_f^2 + \mathbf{p}^2 - m_f^2 = 2\mathbf{p}^2, \tag{A.79}$$

giving

$$|\mathbf{p}| = \frac{m_h}{2}\left[1 - \frac{4m_f^2}{m_h^2}\right]^{\frac{1}{2}}. \tag{A.80}$$

Substituting Eq. (A.75) and Eq. (A.80) into the two body width Eq. (A.78) we get the final expression for the Higgs scalar to fermion decay width

$$\Gamma(h \to f\bar{f}) = N(c) \frac{g^2 m_h}{32\pi}\left(\frac{m_f}{m_W}\right)^2 \left[1 - \frac{4m_f^2}{m_h^2}\right]^{\frac{3}{2}}, \tag{A.81}$$

where we include the colour factor $N(c) = 3$ for quarks and $N(c) = 1$ for leptons.

A.5 Derivation of the Higgs to WX width: $\Gamma(h \to WX)$

There are two couplings of interest. They are the Higgs scalar to $W^{\pm}W^{\mp}$

$$\lambda_{hWW} = igm_W g^{\mu\nu}, \tag{A.82}$$

and the $W^{\pm}$ to X. The X particle must be a fermion (see later), so we want $\lambda_{Wf\bar{f}}$, which is

$$\lambda_{Wf\bar{f}} = \frac{-ig}{\sqrt{2}}\gamma_{\mu}\frac{1-\gamma^5}{2}. \tag{A.83}$$

By evaluating the Feynman rules, in the Feynman gauge ($\xi = 1$ for the W boson propagator)

$$i\mathcal{M} = (igm_W g_{\mu\nu})\epsilon^{\mu}(k,\lambda)\frac{-g^{\nu\alpha}}{(P-p_1)^2 - m_W^2}\left(\frac{-ig}{\sqrt{2}}\right)\bar{u}(p_3,s)\gamma_{\alpha}\frac{1-\gamma^5}{2}v(p_2,s'). \tag{A.84}$$

Then, expanding the denominator of the propagator term, contracting indices and collecting terms

$$\mathcal{M} = \frac{ig^2 m_W}{\sqrt{2}}\epsilon_{\nu}(k,\lambda)\frac{1}{m_h^2 - 2(P\cdot p_1)}\bar{u}(p_3,s)\gamma^{\nu}\frac{1-\gamma^5}{2}v(p_2,s'), \tag{A.85}$$

with Hermitian conjugate

$$\mathcal{M}^* = -\frac{ig^2 m_W}{\sqrt{2}}(\epsilon_{\beta})^*(k,\lambda)\frac{1}{m_h^2 - 2(P\cdot p_1)}\bar{v}(p_2,s')\gamma^{\beta}\frac{1-\gamma^5}{2}u(p_3,s). \tag{A.86}$$

Combining then we find

$$\begin{aligned}|\mathcal{M}|^2 = &\left(\frac{g^2 m_W}{\sqrt{2}}\right)^2 \sum_{\lambda}\epsilon_{\nu}(k,\lambda)(\epsilon_{\beta})^*(k,\lambda)\frac{1}{(m_h^2 - 2P\cdot p_1)^2}\\ &\sum_{s,s'}\bar{u}(p_3,s)\gamma^{\nu}\frac{1-\gamma^5}{2}v(p_2,s')\bar{v}(p_2,s')\gamma^{\beta}\frac{1-\gamma^5}{2}u(p_3,s).\end{aligned} \tag{A.87}$$

Next, making use of the fact

$$\sum_{\lambda}\epsilon^{\mu}(k,\lambda)\epsilon^{\nu *}(k,\lambda) = -g^{\mu\nu} + \frac{k^{\mu}k^{\nu}}{k^2}, \tag{A.88}$$

and using the identities from Eq. (A.69) we find

$$\begin{aligned}|\mathcal{M}|^2 = &\left(\frac{g^2 m_W}{2\sqrt{2}}\right)^2\left(-g_{\nu\beta} + \frac{k_{\nu}k_{\beta}}{k^2}\right)\frac{1}{m_h^2 - 2(P\cdot p_1)}\\ &\mathrm{Tr}\{[\not{p}_3 + m]\gamma^{\nu}(1-\gamma^5)[\not{p}_2 - m]\gamma^{\beta}(1-\gamma^5)\}.\end{aligned} \tag{A.89}$$

We make the assumption that the fermions are massless ($m = 0$) to simplify our calculations, this is valid as $m \ll (m_W, m_h)$, which is all fermions but $m = m_t$. Aside, evaluating the trace

$$\begin{aligned}\mathrm{Tr}\{\not{p}_3\gamma^{\nu}(1-\gamma^5)\not{p}_2\gamma^{\beta}(1-\gamma^5)\} &= 2\mathrm{Tr}\{\not{p}_3\gamma^{\nu}\not{p}_2\gamma^{\beta}(1-\gamma^5)\},\\ &= 2\mathrm{Tr}\{\gamma^{\beta}\not{p}_3\gamma^{\mu}\not{p}_2\} + 8i\epsilon^{\alpha\nu\sigma\beta}p_{3\alpha}p_{2\sigma},\\ &= 8[p_3^{\beta}p_2^{\mu} + p_3^{\mu}p_2^{\beta} - g^{\beta\mu}(p_2\cdot p_3)] + 8i\epsilon^{\alpha\nu\sigma\beta}p_{3\alpha}p_{2\sigma}.\end{aligned} \tag{A.90}$$

Substituting back into Eq. (A.89)

$$|\mathcal{M}|^2 = \left(\frac{g^4 m_W^2}{(m_h^2 - 2P\cdot p_1)^2}\right)\left(-g_{\nu\beta} + \frac{k_\nu k_\beta}{k^2}\right)[p_3^\beta p_2^\mu + p_3^\mu p_2^\beta - g^{\beta\mu}(p_2\cdot p_3) + i\epsilon^{\alpha\nu\sigma\beta} p_{3\alpha} p_{2\sigma}]. \tag{A.91}$$

After expanding and some algebra

$$|\mathcal{M}|^2 = \frac{g^4 m_W^2}{(m_h^2 - 2P\cdot p_1)^2}\left[p_2\cdot p_3 + \frac{2(p_3\cdot p_1)(p_2\cdot p_1)}{m_W^2}\right]. \tag{A.92}$$

We seek to rewrite this in terms of invariant masses. To do so we need to consider the kinematics of the process. Considering the centre of momentum frame for the Higgs scalar

$$\begin{aligned} s_{23} = (P - p_1)^2 &= P^2 + p_1^2 - 2P\cdot p_1, \\ \implies P\cdot p_1 &= \frac{1}{2}(m_h^2 + m_W^2 - s_{23}), \end{aligned} \tag{A.93}$$

and

$$\begin{aligned} s_{23} = (p_2 + p_3)^2 &= p_2^2 + p_3^2 + 2p_2\cdot p_3, \\ \implies p_2\cdot p_3 &= \frac{1}{2}(s_{23}), \end{aligned} \tag{A.94}$$

and

$$\begin{aligned} s_{12} = (p_1 + p_2)^2 &= p_1^2 + p_2^2 + 2p_1\cdot p_2, \\ \implies p_1\cdot p_2 &= \frac{1}{2}(s_{12} - m_W^2), \end{aligned} \tag{A.95}$$

and finally

$$\begin{aligned} P^2 = (p_1 + p_2 + p_3)^2 &= m_W^2 + 2p_1\cdot p_2 + 2p_1\cdot p_3 + 2p_2\cdot p_3, \\ \implies p_1\cdot p_3 &= \frac{1}{2}(m_h^2 - s_{12} - s_{23}). \end{aligned} \tag{A.96}$$

We can now rewrite our amplitude squared in terms of invariant masses, a form that we are able solve in future steps when we apply our Lorentz invariant phase space formula

$$|\mathcal{M}|^2 = \frac{g^4 m_W^2}{2(s_{23} - m_W^2)^2}\left[s_{23} + \frac{(s_{12} - m_W^2)(m_h^2 - s_{12} - s_{23})}{m_W^2}\right]. \tag{A.97}$$

Expanding out terms

$$|\mathcal{M}|^2 = \frac{g^4 m_W^2}{2(s_{23} - m_W^2)^2}\left[2s_{23} + s_{12} - m_h^2 + \frac{s_{12}}{m_W^2}(s_{23} + s_{12} - m_h^2)\right]. \tag{A.98}$$

Using Eqs. (A.9) and (A.23) we construct the decay formula

$$d\Gamma(h \to WX) = \frac{|\mathcal{M}|^2}{256\pi^3 m_h^3}\, ds_{12} ds_{23}. \tag{A.99}$$

Then

$$\begin{aligned} d\Gamma(h \to WX) = \frac{g^4 m_W^2}{256\pi^3 m_h^3}\frac{1}{2(s_{23} - m_W^2)^2}\Bigg[2s_{23} + s_{12} - m_h^2 + \\ \frac{s_{12}}{m_W^2}(s_{23} + s_{12} - m_h^2)\Bigg]\, ds_{12} ds_{23}. \end{aligned} \tag{A.100}$$

The integration limits are imposed firstly on s_{12}, then on s_{23} and are given by

$$s_{12} \in [m_W^2, m_h^2], \tag{A.101}$$

and

$$s_{23} \in [0, \frac{1}{s_{12}}(s - s_{12})(s_{12} - m_W^2)]. \tag{A.102}$$

See the previous section for the derivation of these bounds. They are obtained directly from the three-body phase space general bounds (given here) with $m_2 = m_3 = m = 0$

$$s_{12} \in [(m_1 + m_2)^2, (\sqrt{s} - m_3)^2], \tag{A.103}$$

and

$$s_{23\pm} = m_2^2 + m_3^2 + \frac{1}{2s_{12}}\left[(s - s_{12} - m_2^2)(s_{12} + m_3^2 - m_1^2) \pm \sqrt{\lambda(s, m_2^2, s_{12})\lambda(s_{12}, m_3^2, m_1^2)}\right], \tag{A.104}$$

where $\lambda(x, y, z)$ is defined in Eq. (A.43). Performing the integration we get the general result [19]

$$\Gamma(h \to W^\pm X) = \frac{g^4 m_h}{3072\pi^3} F(\epsilon_W), \tag{A.105}$$

where

$$F(\epsilon) = \frac{3(1 - 8\epsilon^2 + 20\epsilon^4)}{\sqrt{4\epsilon^2 - 1}} \arccos\left(\frac{3\epsilon^2 - 1}{2\epsilon^3}\right) - (1 - \epsilon^2)\left(\frac{47}{2}\epsilon^2 - \frac{13}{2} + \frac{1}{\epsilon^2}\right) - 3(1 - 6\epsilon^2 + 4\epsilon^4)\ln\epsilon, \tag{A.106}$$

and where

$$\epsilon_W = \frac{m_W}{m_h}. \tag{A.107}$$

Finally, let us identify the possible final states X. The two final state X particles must couple to the W boson, and must also have a combined mass less than that of the W boson. The decay processes that satisfy these conditions are that of the light fermions. There are nine different decay modes for the X particle pair, $X = u, d, c, s, b, e, \mu, \tau$, additionally, we could also have either a W^+ or W^- as the other particle in the final state. We conclude that there are 18 different combinations of final state particles for this decay. As a result, we need to multiply Eq. (A.105) by a factor of 18 to account for each of these possible decays. As we have neglected the mass of X, we can assume each decay channel gives an equal contribution to Eq. (A.105). The final expression for the $h \to W^\pm X$ decay is then

$$\Gamma(h \to W^\pm X) = 3\frac{g^4 m_h}{512\pi^3} F(\epsilon_W). \tag{A.108}$$

B

The Yukawa Sector of the General Type-III 2HDM

In this Appendix, we expand the Yukawa Lagrangian of the most general 2HDM which in the generic basis reads

$$\begin{aligned} -\mathscr{L}_Y =& \overline{Q}\,(Y_u^{1\dagger}\tilde{\Phi}_1 + Y_u^{2\dagger}\tilde{\Phi}_2)u_{\mathrm{R}} + \overline{Q}\,(Y_d^{1\dagger}\Phi_1 + Y_d^{2\dagger}\Phi_2)d_{\mathrm{R}} + \\ & \overline{L}\,(Y_l^{1\dagger}\Phi_1 + Y_l^{2\dagger}\Phi_2)l_{\mathrm{R}} + [\mathrm{H.c.}]. \end{aligned} \tag{B.1}$$

We ignore leptons in this derivation. We are free to move to the Higgs basis (through a rotation of Φ_1 and Φ_2 in β) as well as the up quark mass basis

$$-\mathscr{L}_Y = \overline{Q}\left[\frac{\sqrt{2}m_D}{v}H_1 + \xi_d H_2\right]d_{\mathrm{R}} + \overline{Q}\left[\frac{\sqrt{2}\hat{m}_U}{v}\tilde{H}_1 + \hat{\xi}_u\tilde{H}_2\right]u_{\mathrm{R}} + [\mathrm{H.c.}], \tag{B.2}$$

where we defined

$$\xi_d \equiv \left(\frac{Y_{d2}^{\dagger}}{c_\beta} - \frac{\sqrt{2}m_D t_\beta}{v}\right), \qquad \hat{\xi}_u \equiv \left(\frac{Y_{u2}^{\dagger}}{c_\beta} - \frac{\sqrt{2}\hat{m}_U t_\beta}{v}\right). \tag{B.3}$$

Then we can rotate into the down quark mass basis through

$$\hat{m}_D \equiv V_{\mathrm{CKM}}^{\dagger} m_D V_{Rd}. \tag{B.4}$$

Additionally let us define

$$\hat{\xi}_d \equiv V_{\mathrm{CKM}}^{\dagger}\xi_d V_{Rd}. \tag{B.5}$$

Write the field doublets in terms of their mass eigenstates

$$H_1 = \begin{pmatrix} 0 \\ \frac{1}{\sqrt{2}}\left(s_{\beta\alpha}h + c_{\beta\alpha}H\right) \end{pmatrix}, \quad H_2 = \begin{pmatrix} H^+ \\ \frac{1}{\sqrt{2}}\left(c_{\beta\alpha}h - s_{\beta\alpha}H + iA\right) \end{pmatrix}, \tag{B.6}$$

and

$$\tilde{H}_1 = i\sigma_2 H_1^* = \begin{pmatrix} \frac{1}{\sqrt{2}}\left(s_{\beta\alpha}h + c_{\beta\alpha}H\right) \\ 0 \end{pmatrix}, \quad \tilde{H}_2 = i\sigma_2 H_2^* = \begin{pmatrix} \frac{1}{\sqrt{2}}\left(c_{\beta\alpha}h - s_{\beta\alpha}H - iA\right) \\ -H^- \end{pmatrix}.$$

Now we are ready to perform the expansion, starting from the Higgs basis and mass basis for the up quarks

$$
\begin{aligned}
-\mathscr{L}_Y &= \overline{Q}\left[\frac{\sqrt{2}m_D}{v}H_1+\xi_d H_2\right]d_{\mathrm{R}}+\overline{Q}\left[\frac{\sqrt{2}\hat{m}_U}{v}\tilde{H}_1+\hat{\xi}_u\tilde{H}_2\right]u_{\mathrm{R}}+[\mathrm{H.c.}],\\
&= \begin{pmatrix}\overline{u_L} & \overline{d_L}\end{pmatrix}\left[\frac{\sqrt{2}m_D}{v}\begin{pmatrix}0\\ \frac{1}{\sqrt{2}}\left(s_{\beta\alpha}h+c_{\beta\alpha}H\right)\end{pmatrix}+\xi_d\begin{pmatrix}H^+\\ \frac{1}{\sqrt{2}}\left(c_{\beta\alpha}h-s_{\beta\alpha}H+iA\right)\end{pmatrix}\right]d_{\mathrm{R}}\\
&+ \begin{pmatrix}\overline{u_L} & \overline{d_L}\end{pmatrix}\left[\frac{\sqrt{2}\hat{m}_U}{v}\begin{pmatrix}\frac{1}{\sqrt{2}}\left(s_{\beta\alpha}h+c_{\beta\alpha}H\right)\\ 0\end{pmatrix}+\hat{\xi}_u\begin{pmatrix}\frac{1}{\sqrt{2}}\left(c_{\beta\alpha}h-s_{\beta\alpha}H-iA\right)\\ -H^-\end{pmatrix}\right]u_{\mathrm{R}}+[\mathrm{H.c.}],\\
&= \overline{d_L}\frac{m_D}{v}\left(s_{\beta\alpha}h+c_{\beta\alpha}H\right)d_{\mathrm{R}}+\overline{u_L}\xi_d H^+ d_{\mathrm{R}}+\overline{d_L}\frac{1}{\sqrt{2}}\xi_d\left(c_{\beta\alpha}h-s_{\beta\alpha}H+iA\right)d_{\mathrm{R}}\\
&+ \overline{u_L}\frac{\hat{m}_U}{v}\left(s_{\beta\alpha}h+c_{\beta\alpha}H\right)u_{\mathrm{R}}+\overline{u_L}\frac{1}{\sqrt{2}}\hat{\xi}_u\left(c_{\beta\alpha}h-s_{\beta\alpha}H-iA\right)u_{\mathrm{R}}-\overline{d_L}\hat{\xi}_u H^- u_{\mathrm{R}}+[\mathrm{H.c.}],\\
-\mathscr{L}_Y &= \overline{u_L}\xi_d d_{\mathrm{R}}H^+-\overline{d_L}\hat{\xi}_u u_{\mathrm{R}}H^-\\
&+ \left(\overline{d_L}\left[\frac{m_D}{v}s_{\beta\alpha}+\frac{1}{\sqrt{2}}\xi_d c_{\beta\alpha}\right]d_{\mathrm{R}}+\overline{u_L}\left[\frac{\hat{m}_U}{v}s_{\beta\alpha}+\frac{1}{\sqrt{2}}\hat{\xi}_u c_{\beta\alpha}\right]u_{\mathrm{R}}\right)h\\
&+ \left(\overline{d_L}\left[\frac{m_D}{v}c_{\beta\alpha}-\frac{1}{\sqrt{2}}\xi_d s_{\beta\alpha}\right]d_{\mathrm{R}}+\overline{u_L}\left[\frac{\hat{m}_U}{v}c_{\beta\alpha}-\frac{1}{\sqrt{2}}\hat{\xi}_u s_{\beta\alpha}\right]u_{\mathrm{R}}\right)H\\
&+ i\left(\overline{d_L}\frac{1}{\sqrt{2}}\xi_d d_{\mathrm{R}}-\overline{u_L}\frac{1}{\sqrt{2}}\hat{\xi}_u u_{\mathrm{R}}\right)A+[\mathrm{H.c.}].
\end{aligned}
\tag{B.7}
$$

At this stage we perform the rotation into the mass basis for the down quarks by rotating the mass eigenstates as

$$
d_L\to V_{\mathrm{CKM}}d_L,\quad d_R\to V_{Rd}d_R,\quad \overline{d_L}\to\overline{d_L}V_{\mathrm{CKM}}^\dagger,\quad \overline{d_R}\to\overline{d_R}V_{Rd}^\dagger. \tag{B.8}
$$

Leading to

$$
\begin{aligned}
-\mathscr{L}_Y &= \overline{u_L}V_{\mathrm{CKM}}\hat{\xi}_d d_{\mathrm{R}}H^+-\overline{d_L}V_{\mathrm{CKM}}^\dagger\hat{\xi}_u u_{\mathrm{R}}H^-\\
&+ \left(\overline{d_L}\left[\frac{\hat{m}_D}{v}s_{\beta\alpha}+\frac{1}{\sqrt{2}}\hat{\xi}_d c_{\beta\alpha}\right]d_{\mathrm{R}}+\overline{u_L}\left[\frac{\hat{m}_U}{v}s_{\beta\alpha}+\frac{1}{\sqrt{2}}\hat{\xi}_u c_{\beta\alpha}\right]u_{\mathrm{R}}\right)h\\
&+ \left(\overline{d_L}\left[\frac{\hat{m}_D}{v}c_{\beta\alpha}-\frac{1}{\sqrt{2}}\hat{\xi}_d s_{\beta\alpha}\right]d_{\mathrm{R}}+\overline{u_L}\left[\frac{\hat{m}_U}{v}c_{\beta\alpha}-\frac{1}{\sqrt{2}}\hat{\xi}_u s_{\beta\alpha}\right]u_{\mathrm{R}}\right)H\\
&+ \frac{i}{\sqrt{2}}\left(\overline{d_L}\hat{\xi}_d d_{\mathrm{R}}-\overline{u_L}\hat{\xi}_u u_{\mathrm{R}}\right)A+[\mathrm{H.c.}].
\end{aligned}
\tag{B.9}
$$

Expanding out the Hermitian conjugate

$$\begin{aligned}
-\mathscr{L}_Y &= \left(\overline{u_L} V_{\mathrm{CKM}} \hat{\xi}_d d_{\mathrm{R}} - \overline{u_{\mathrm{R}}} \hat{\xi}_u^\dagger V_{\mathrm{CKM}} d_L\right) H^+ + \left(\overline{d_{\mathrm{R}}} \hat{\xi}_d^\dagger V_{\mathrm{CKM}}^\dagger u_L - \overline{d_L} V_{\mathrm{CKM}}^\dagger \hat{\xi}_u u_{\mathrm{R}}\right) H^- \\
&+ \left(\overline{d_L}\left[\frac{\hat{m}_D}{v} s_{\beta\alpha} + \frac{1}{\sqrt{2}}\hat{\xi}_d c_{\beta\alpha}\right] d_{\mathrm{R}} + \overline{d_{\mathrm{R}}}\left[\frac{\hat{m}_D}{v} s_{\beta\alpha} + \frac{1}{\sqrt{2}}\hat{\xi}_d^\dagger c_{\beta\alpha}\right] d_L\right. \\
&+ \left.\overline{u_L}\left[\frac{\hat{m}_U}{v} s_{\beta\alpha} + \frac{1}{\sqrt{2}}\hat{\xi}_u c_{\beta\alpha}\right] u_{\mathrm{R}} + \overline{u_{\mathrm{R}}}\left[\frac{\hat{m}_U}{v} s_{\beta\alpha} + \frac{1}{\sqrt{2}}\hat{\xi}_u^\dagger c_{\beta\alpha}\right] u_L\right) h \\
&+ \left(\overline{d_L}\left[\frac{\hat{m}_D}{v} c_{\beta\alpha} - \frac{1}{\sqrt{2}}\hat{\xi}_d s_{\beta\alpha}\right] d_{\mathrm{R}} + \overline{d_{\mathrm{R}}}\left[\frac{\hat{m}_D}{v} c_{\beta\alpha} - \frac{1}{\sqrt{2}}\hat{\xi}_d^\dagger s_{\beta\alpha}\right] d_L\right. \\
&+ \left.\overline{u_L}\left[\frac{\hat{m}_U}{v} c_{\beta\alpha} - \frac{1}{\sqrt{2}}\hat{\xi}_u s_{\beta\alpha}\right] u_{\mathrm{R}} + \overline{u_{\mathrm{R}}}\left[\frac{\hat{m}_U}{v} c_{\beta\alpha} - \frac{1}{\sqrt{2}}\hat{\xi}_u^\dagger s_{\beta\alpha}\right] u_L\right) H \\
&+ \frac{i}{\sqrt{2}}\left(\overline{d_L}\hat{\xi}_d d_{\mathrm{R}} - \overline{u_L}\hat{\xi}_u u_{\mathrm{R}} - \overline{d_{\mathrm{R}}}\hat{\xi}_d^\dagger d_L + \overline{u_{\mathrm{R}}}\hat{\xi}_u^\dagger u_L\right) A.
\end{aligned} \tag{B.10}$$

We may use the projection operators to expand out the left and right components and make the relations

$$\overline{q_L} q_R = \overline{q} P_R q, \tag{B.11}$$

and

$$\overline{q_R} q_L = \overline{q} P_L q. \tag{B.12}$$

Applying these to the Yukawa Lagrangian we get our desired form

$$\begin{aligned}
-\mathscr{L}_Y &= \overline{u}_b \left(V_{\mathrm{CKM},bc}\, \hat{\xi}^D_{ca} P_R - \hat{\xi}^{U*}_{cb}\, V_{\mathrm{CKM},ca} P_L\right) d_a\, H^+ \\
&+ \overline{d}_b \left(\hat{\xi}^{D*}_{cb}\, V^*_{\mathrm{CKM},ac}\, P_L - V^*_{\mathrm{CKM},cb}\, \hat{\xi}^U_{ca} P_R\right) u_a\, H^- \\
&+ \left(\overline{d}_b \left[\left\{\frac{\hat{M}_{D,ba}}{v} s_{\beta\alpha} + \frac{1}{\sqrt{2}}\hat{\xi}^D_{ba} c_{\beta\alpha}\right\} P_R + \left\{\frac{\hat{M}_{D,ba}}{v} s_{\beta\alpha} + \frac{1}{\sqrt{2}}\hat{\xi}^{D*}_{ba} c_{\beta\alpha}\right\} P_L\right] d_a\right. \\
&+ \left.\overline{u}_b \left[\left\{\frac{\hat{M}_{U,ba}}{v} s_{\beta\alpha} + \frac{1}{\sqrt{2}}\hat{\xi}^U_{ba} c_{\beta\alpha}\right\} P_R + \left\{\frac{\hat{M}_{U,ba}}{v} s_{\beta\alpha} + \frac{1}{\sqrt{2}}\hat{\xi}^{U*}_{ba} c_{\beta\alpha}\right\} P_L\right] u_a\right) h \\
&+ \left(\overline{d}_b \left[\left\{\frac{\hat{M}_{D,ba}}{v} c_{\beta\alpha} - \frac{1}{\sqrt{2}}\hat{\xi}^D_{ba} s_{\beta\alpha}\right\} P_R + \left\{\frac{\hat{M}_{D,ba}}{v} c_{\beta\alpha} - \frac{1}{\sqrt{2}}\hat{\xi}^{D*}_{ba} s_{\beta\alpha}\right\} P_L\right] d_a\right. \\
&+ \left.\overline{u}_b \left[\left\{\frac{\hat{M}_{U,ba}}{v} c_{\beta\alpha} - \frac{1}{\sqrt{2}}\hat{\xi}^U_{ba} s_{\beta\alpha}\right\} P_R + \left\{\frac{\hat{M}_{U,ba}}{v} c_{\beta\alpha} - \frac{1}{\sqrt{2}}\hat{\xi}^{U*}_{ba} s_{\beta\alpha}\right\} P_L\right] u_a\right) H \\
&+ \frac{i}{\sqrt{2}}\left(\overline{d}_b \left[\hat{\xi}^D_{ba} P_R - \hat{\xi}^{D*}_{ba} P_L\right] d_a + \overline{u}_b \left[-\hat{\xi}^U_{ba} P_R + \hat{\xi}^{U*}_{ba} P_L\right] u_a\right) A\,,
\end{aligned} \tag{B.13}$$

where $a, b = 1, 2, 3$ are flavour indices and u_a and d_a denote the up and down quark states in the mass basis. It is from the above that we may read off the couplings

$$g_{\overline{q}_b q_a \phi} \equiv i\left(\Gamma^{LR\,\phi}_{q_b q_a} P_R + \Gamma^{RL\,\phi}_{q_b q_a} P_L\right)\,. \tag{B.14}$$

Additionally, we may express this in a way that explicitly separates each of the scalar and pseudo-scalar

terms

$$
\begin{aligned}
\Rightarrow -\mathscr{L}_Y \;=\;& \overline{u}\Big(V_{\mathrm{CKM}}\hat{\xi}_d P_R - \hat{\xi}_u^\dagger V_{\mathrm{CKM}} P_L\Big) d H^+ + \overline{d}\Big(\hat{\xi}_d^\dagger V_{\mathrm{CKM}}^\dagger P_L - V_{\mathrm{CKM}}^\dagger \hat{\xi}_u P_R\Big) u H^- \\
&+ \left(\overline{d}\left[\frac{\hat{m}_D}{v} s_{\beta\alpha} + \frac{c_{\beta\alpha}}{2\sqrt{2}}\Big\{(\hat{\xi}_d + \hat{\xi}_d^\dagger) + (\hat{\xi}_d - \hat{\xi}_d^\dagger)\gamma^5\Big\}\right] d \right. \\
&+ \left. \overline{u}\left[\frac{\hat{m}_U}{v} s_{\beta\alpha} + \frac{c_{\beta\alpha}}{2\sqrt{2}}\Big\{(\hat{\xi}_u + \hat{\xi}_u^\dagger) + (\hat{\xi}_u - \hat{\xi}_u^\dagger)\gamma^5\Big\}\right] u\right) h \\
&+ \left(\overline{d}\left[\frac{\hat{m}_D}{v} c_{\beta\alpha} - \frac{s_{\beta\alpha}}{2\sqrt{2}}\Big\{(\hat{\xi}_d + \hat{\xi}_d^\dagger) + (\hat{\xi}_d - \hat{\xi}_d^\dagger)\gamma^5\Big\}\right] d \right. \\
&+ \left. \overline{u}\left[\frac{\hat{m}_U}{v} c_{\beta\alpha} - \frac{1}{2\sqrt{2}}\Big\{(\hat{\xi}_u + \hat{\xi}_u^\dagger) + (\hat{\xi}_u - \hat{\xi}_u^\dagger)\gamma^5\Big\}\right] u\right) H \\
&+ \frac{i}{2\sqrt{2}}\left(\overline{d}\Big\{(\hat{\xi}_d - \hat{\xi}_d^\dagger) + (\hat{\xi}_d + \hat{\xi}_d^\dagger)\gamma^5\Big\} d - \overline{u}\Big\{(\hat{\xi}_u - \hat{\xi}_u^\dagger) + (\hat{\xi}_u + \hat{\xi}_u^\dagger)\gamma^5\Big\} u\right) A.
\end{aligned}
\tag{B.15}
$$

C

On Higgs Family and General CP Transformations

We have a look at the application of HF and GCP transformations on the most general 2HDM potential parameters. We apply the $U(2)$ symmetry (HF) and see that it reduces the number of free parameters in the potential from 14 to 3. Further, we investigate why it is necessary to use GCP transformations rather than just CP transformations when we have more than one doublet.

This Appendix provides a guided work-through of material from [131].

C.1 Higgs Family Transformation: $U(2)$

Let us investigate the effects of the $U(2)$ symmetry by imposing it on the most general 2HDM potential of Eq. (3.2). We start with

$$\begin{aligned}(\Phi_1^\dagger\Phi_1) &\xrightarrow{HF} ((\Phi_1')^\dagger(\Phi_1')) \\ &=\Phi_1^\dagger\Phi_1 c_\theta^2 + \Phi_2^\dagger\Phi_2 s_\theta^2 + c_\theta s_\theta\left(e^{i(\xi-\psi)}\Phi_1^\dagger\Phi_2 + e^{i(\psi-\xi)}\Phi_2^\dagger\Phi_1\right),\end{aligned} \tag{C.1}$$

$$\begin{aligned}(\Phi_2^\dagger\Phi_2) &\xrightarrow{HF} ((\Phi_2')^\dagger(\Phi_2')) \\ &=\Phi_1^\dagger\Phi_1 s_\theta^2 + \Phi_2^\dagger\Phi_2 c_\theta^2 - c_\theta s_\theta\left(e^{i(\xi-\psi)}\Phi_1^\dagger\Phi_2 + e^{i(\psi-\xi)}\Phi_2^\dagger\Phi_1\right).\end{aligned} \tag{C.2}$$

We see that the bilinear mass terms are invariant under $U(2)$ when

$$m_{11} = m_{22}, \quad m_{12} = m_{21} = 0. \tag{C.3}$$

Moving onto the quartic couplings, λ, start by imposing $U(2)$ onto

$$\frac{1}{2}\lambda_1(\Phi_1^\dagger\Phi_1)^2 + \frac{1}{2}\lambda_2(\Phi_2^\dagger\Phi_2)^2 + \lambda_3(\Phi_1^\dagger\Phi_1)(\Phi_2^\dagger\Phi_2) + \lambda_4(\Phi_1^\dagger\Phi_2)(\Phi_2^\dagger\Phi_1). \tag{C.4}$$

Anticipating the solution let us set $\lambda_1 = \lambda_2$ and $\lambda_4 = \lambda_1 - \lambda_3$

$$\frac{1}{2}\lambda_1\left[(\Phi_1^\dagger\Phi_1) + (\Phi_2^\dagger\Phi_2)\right]^2 + \lambda_3\left[(\Phi_1^\dagger\Phi_1)(\Phi_2^\dagger\Phi_2) - (\Phi_1^\dagger\Phi_2)(\Phi_2^\dagger\Phi_1)\right]. \tag{C.5}$$

The λ_1 term is invariant under $U(2)$ by the same reasoning as the mass sector. Each of the λ_3 terms under a $U(2)$ transformation

$$\begin{aligned}(\Phi_1^\dagger\Phi_1)(\Phi_2^\dagger\Phi_2) &\xrightarrow{HF} ((\Phi_1')^\dagger(\Phi_1'))((\Phi_2')^\dagger(\Phi_2')) \\ &= (c_\theta^2\Phi_1^\dagger\Phi_1 + e^{i(\xi-\psi)}c_\theta s_\theta\Phi_1^\dagger\Phi_2 - e^{i(\psi-\xi)}c_\theta s_\theta\Phi_2^\dagger\Phi_1 + s_\theta^2\Phi_2^\dagger\Phi_2) \\ &\quad (s_\theta^2\Phi_1^\dagger\Phi_1 - e^{i(\xi-\psi)}c_\theta s_\theta\Phi_1^\dagger\Phi_2 + e^{i(\psi-\xi)}c_\theta s_\theta\Phi_2^\dagger\Phi_1 + c_\theta^2\Phi_2^\dagger\Phi_2),\end{aligned} \tag{C.6}$$

$$
\begin{aligned}
(\Phi_1^\dagger\Phi_2)(\Phi_2^\dagger\Phi_1) &\xrightarrow{HF} ((\Phi_1')^\dagger(\Phi_2'))((\Phi_2')^\dagger(\Phi_1')) \\
&= (-e^{i(\xi+\psi)}c_\theta s_\theta\Phi_1^\dagger\Phi_1 + e^{2i\xi}c_\theta^2\Phi_1^\dagger\Phi_2 + e^{2i\psi}s_\theta^2\Phi_2^\dagger\Phi_1 + e^{i(\psi+\xi)}c_\theta s_\theta\Phi_2^\dagger\Phi_2) \\
&(-e^{-i(\psi+\xi)}c_\theta s_\theta\Phi_1^\dagger\Phi_1 - e^{-2i\psi}s_\theta^2\Phi_1^\dagger\Phi_2 - e^{-2i\xi}c_\theta^2\Phi_2^\dagger\Phi_1 + e^{-i(\xi+\psi)}c_\theta s_\theta\Phi_2^\dagger\Phi_2).
\end{aligned} \tag{C.7}
$$

Adding the first terms of Eq. (C.6) and Eq. (C.7)

$$
(c_\theta^2\Phi_1^\dagger\Phi_1)(s_\theta^2\Phi_1^\dagger\Phi_1) - (-e^{i(\xi+\psi)}c_\theta s_\theta\Phi_1^\dagger\Phi_1)(-e^{-i(\psi+\xi)}c_\theta s_\theta\Phi_1^\dagger\Phi_1) = 0. \tag{C.8}
$$

Further

$$
\begin{aligned}
&\left[(c_\theta^2\Phi_1^\dagger\Phi_1)(c_\theta^2\Phi_2^\dagger\Phi_2) + (s_\theta^2\Phi_2^\dagger\Phi_2)(s_\theta^2\Phi_1^\dagger\Phi_1)\right] - \left[(-e^{i(\xi+\psi)}c_\theta s_\theta\Phi_1^\dagger\Phi_1)\right. \\
&\left.(e^{-i(\xi+\psi)}c_\theta s_\theta\Phi_2^\dagger\Phi_2) + (e^{i(\psi+\xi)}c_\theta s_\theta\Phi_2^\dagger\Phi_2)(-e^{-i(\psi+\xi)}c_\theta s_\theta\Phi_1^\dagger\Phi_1)\right] \\
&= (c_\theta^2 + s_\theta^2)^2(\Phi_1^\dagger\Phi_1)(\Phi_2^\dagger\Phi_2) \\
&= (\Phi_1^\dagger\Phi_1)(\Phi_2^\dagger\Phi_2).
\end{aligned} \tag{C.9}
$$

Again, we use the assumption that bi-linear field groups commute. Continuing with very similar expansions for the transformed $(\Phi_1^\dagger\Phi_2)(\Phi_2^\dagger\Phi_1)$ and $(\Phi_2^\dagger\Phi_2)(\Phi_2^\dagger\Phi_2)$ terms we find that the combination $(\Phi_1^\dagger\Phi_1)(\Phi_2^\dagger\Phi_2) - (\Phi_1^\dagger\Phi_2)(\Phi_2^\dagger\Phi_1)$ is invariant under $U(2)$.

Finally, for the terms

$$
\left[\frac{1}{2}\lambda_5(\Phi_1^\dagger\Phi_2)^2 + \lambda_6(\Phi_1^\dagger\Phi_1)(\Phi_1^\dagger\Phi_2) + \lambda_7(\Phi_1^\dagger\Phi_1)(\Phi_1^\dagger\Phi_2) + [\text{H.c}]\right], \tag{C.10}
$$

no combination (of these terms and/or their hermitian conjugates) will not be invariant under $U(2)$. To retain invariant coefficients in the potential as required under a HF transformation we set $\lambda_5 = \lambda_6 = \lambda_7 = 0$. The resultant potential that respects the strongest $U(2)$ HF symmetry has the form

$$
V \xrightarrow{HF} m_{11}^2(\Phi_1^\dagger\Phi_1 + \Phi_2^\dagger\Phi_2) + \frac{1}{2}\lambda_1\left[(\Phi_1^\dagger\Phi_1) + (\Phi_2^\dagger\Phi_2)\right]^2 + \lambda_3\left[(\Phi_1^\dagger\Phi_1)(\Phi_2^\dagger\Phi_2) - (\Phi_1^\dagger\Phi_2)(\Phi_2^\dagger\Phi_1)\right]. \tag{C.11}
$$

We have reduced the number of free parameters from 14 to 3 by restricting the potential under a $U(2)$ symmetry.

C.2 The Need for GCP Transformations

In this example, we show why it is necessary to extend CP-transformation when transforming more than a single doublet. Begin by considering the transformation

$$
U = \frac{1}{\sqrt{2}}\begin{pmatrix} 1 & e^{i\theta} \\ -e^{-i\theta} & 1 \end{pmatrix}. \tag{C.12}
$$

Such a transformation mixes the Higgs fields. The transformed fields are

$$
\begin{aligned}
\Phi_1' &= \frac{1}{\sqrt{2}}(\Phi_1 + e^{i\theta}\Phi_2), \\
\Phi_2' &= \frac{1}{\sqrt{2}}(-e^{-i\theta}\Phi_1 + \Phi_2).
\end{aligned} \tag{C.13}
$$

Under our original definition of CP Eq. (3.27) these transform as

$$\begin{aligned} \frac{1}{\sqrt{2}}(\Phi_1 + e^{i\theta}\Phi_2) &\xrightarrow{CP} \frac{1}{\sqrt{2}}(\Phi_1^* + e^{-i\theta}\Phi_2^*), \\ \frac{1}{\sqrt{2}}(-e^{-i\theta}\Phi_1 + \Phi_2) &\xrightarrow{CP} \frac{1}{\sqrt{2}}(-e^{i\theta}\Phi_1^* + \Phi_2^*). \end{aligned} \tag{C.14}$$

Multiplying the second by $e^{i\theta}$

$$\frac{1}{\sqrt{2}}(-\Phi_1 + e^{i\theta}\Phi_2) \xrightarrow{CP} \frac{1}{\sqrt{2}}(-e^{2i\theta}\Phi_1^* + e^{i\theta}\Phi_2^*). \tag{C.15}$$

Then adding and subtracting from the very first equation yields

$$\begin{aligned} \Phi_1 &\xrightarrow{CP} \frac{1}{2}\left[(1 + e^{2i\theta})\Phi_1^* + (e^{-i\theta} - e^{i\theta})\Phi_2^*\right], \\ \Phi_2 &\xrightarrow{CP} \frac{1}{2}\left[(e^{-i\theta} - e^{i\theta})\Phi_1^* + (e^{-2i\theta} + 1)\Phi_2^*\right]. \end{aligned} \tag{C.16}$$

So in our new basis the CP transformation looks different than Eq. (3.27). In this basis only $\theta = n\pi$, where n positive integer, will retain our original form of the CP transformation. All other values of θ, which of course we are free to choose, will cause mixing of the fields after the CP transformation.

Let us apply a GCP transformation instead. Define the GCP transformation matrix X as the $U(1)$ hypercharge transformation $e^{iY_i\alpha_i}$. Where Y_i is the hypercharge and α_i is an arbitrary parameter. For the two-Higgs fields we have hypercharge $Y_1 = Y_2 = 1$, giving

$$X = \begin{pmatrix} e^{i\alpha_1} & 0 \\ 0 & e^{i\alpha_2} \end{pmatrix}. \tag{C.17}$$

Our GCP transformation is

$$\begin{aligned} \Phi_1 &\xrightarrow{GCP} e^{i\alpha_1}\Phi_1^*, \\ \Phi_2 &\xrightarrow{GCP} e^{i\alpha_2}\Phi_2^*. \end{aligned} \tag{C.18}$$

In the basis U defined by Eq. (C.12) the GCP transformation becomes

$$X' = \frac{1}{2}\begin{pmatrix} e^{i\alpha_1} + e^{i(\alpha_2+2\theta)} & -e^{i(\alpha_1-\theta)} + e^{i(\alpha_2+\theta)} \\ -e^{i(\alpha_1-\theta)} + e^{i(\alpha_2+\theta)} & e^{i(\alpha_1-2\theta)} + e^{i\alpha_2} \end{pmatrix}. \tag{C.19}$$

Setting $\alpha_1 = \theta$ and $\alpha_2 = -\theta$ (we are free to choose α_i) reduces X' to

$$X' = \begin{pmatrix} e^{i\theta} & 0 \\ 0 & e^{-i\theta} \end{pmatrix}. \tag{C.20}$$

Resulting in

$$\begin{aligned} \Phi_1' &\xrightarrow{GCP} e^{i\theta}(\Phi_1')^*, \\ \Phi_2' &\xrightarrow{GCP} e^{-i\theta}(\Phi_2')^*, \end{aligned} \tag{C.21}$$

which is exactly our GCP-transformation of Eq. (3.27) for the chosen θ values.

A more intuitive approach is to apply the GCP-transformation directly to our basis relations using

$\Phi_1 \xrightarrow{GCP} e^{i\alpha_1}\Phi_1^*$ and $\Phi_2 \xrightarrow{GCP} e^{i\alpha_2}\Phi_2^*$, then

$$\begin{aligned} \frac{1}{\sqrt{2}}(\Phi_1 + e^{i\theta}\Phi_2) &\xrightarrow{GCP} \frac{e^{i\alpha_1}}{\sqrt{2}}(\Phi_1^* + e^{-i\theta}\Phi_2^*), \\ \frac{1}{\sqrt{2}}(-e^{-i\theta}\Phi_1 + \Phi_2) &\xrightarrow{GCP} \frac{e^{i\alpha_2}}{\sqrt{2}}(-e^{i\theta}\Phi_1^* + \Phi_2^*). \end{aligned} \tag{C.22}$$

Again, multiplying the second by $e^{i\theta}$ and then subtracting and adding the equations as above, we are left with

$$\Phi_1 \xrightarrow{GCP} \frac{1}{2}\left[(e^{i\alpha_1} + e^{i\alpha_2})\Phi_1^* + (e^{i(\alpha_1-\theta)} - e^{i\alpha_2+\theta})\Phi_2^*\right], \tag{C.23}$$

$$\Phi_2 \xrightarrow{GCP} \frac{1}{2}\left[(e^{i(\alpha_1-\theta)} - e^{i(\alpha_2-\theta)})\Phi_1^* + (e^{i(\alpha_1-2\theta)} + e^{i\alpha_2})\Phi_2^*\right]. \tag{C.24}$$

Setting $\alpha_1 = \theta$ and $\alpha_2 = -\theta$ as before, we are left with exactly the transformation we require.

D

EWSB In Different Vacua of the 2HDM

Beginning this Appendix, in the first section, we investigate alternative methods in which to solve the stationary conditions and extract scalar mass matrices. These methods prove useful as they may be easily generalised to each type of vacuum solution (normal, charge- and CP- breaking). Further, they allow us to compare vacuum solutions and provide the necessary framework for the 2HDM vacuum lemma proofs presented in the second section of this Appendix.

This Appendix includes a guided work-through of material from [28].

D.1 2HDM Mass Matrix Methods

D.1.1 Notation of the 2HDM Vacuum

Let us establish some notation that will become useful in future calculations. Define a function of x_k components, $\mathbf{x} \in \mathbb{R}^n$, as

$$f(\mathbf{x}) = f(x_1, x_2, ..., x_n). \tag{D.1}$$

This function attains its stationary point at

$$\mathbf{x^0} = (x_1^0, x_2^0, ..., x_n^0). \tag{D.2}$$

Giving *

$$\nabla f(\mathbf{x})\big|_{\mathbf{x}=\mathbf{x^0}} = 0. \tag{D.4}$$

Next, let us assume that there exists a basis $\mathbf{x}' = O\mathbf{x}$, O a matrix, such that in $\mathbf{x}'$, m of our stationary conditions vanish

$$(x^0)'_{n-m+1} = ... = (x^0)'_n = 0. \tag{D.5}$$

Any stationary condition may vanish without loss of generality. We assume that we have ordered the variables such that the stationary conditions vanish from the right. In this new basis, we have $n - m$ unknown stationary points required to specify these points. This set of $n - m$ conditions is given by

$$\left.\frac{\partial f}{\partial x'_i}\right|_{\mathbf{x}'=(\mathbf{x^0})'} = 0, \tag{D.6}$$

* Or component wise, we have n stationary conditions

$$\left.\frac{\partial f}{\partial x_i}\right|_{\mathbf{x}=\mathbf{x^0}} = 0, \tag{D.3}$$

for $i = 1, ..., n$.

for $i = 1, ..., n - m$.

The proof of this is given in the box below; this may be skipped without a loss in generality.

Define a function of polynomials constructed from a combination of terms x_k components of $\mathbf{x} \in \mathbb{R}^n$, as

$$f(\mathbf{x}) = f(x_1, x_2, ..., x_n). \tag{D.7}$$

Label the vector at which this function attains its stationary point as

$$\mathbf{x^0} = (x_1^0, x_2^0, ..., x_n^0). \tag{D.8}$$

The stationary conditions of this function are then given by

$$\nabla f(\mathbf{x})\big|_{\mathbf{x}=\mathbf{x^0}} = 0. \tag{D.9}$$

From this equation we may then solve for the stationary points x_i^0, we have n conditions and n unknown variables x_i^0. There will be $p \geq 1$ or a continuous number of solutions for our set of stationary points $\mathbf{x^0}$. For $p \geq 2$, the solutions are subject to constraints defined by the stationary conditions. Note, the component k of Eq. (D.9) is

$$\left(\nabla_{x_k} f(\mathbf{x})\big|_{\mathbf{x}=\mathbf{x^0}}\right)_k = \left(\frac{\partial f}{\partial x_k}\bigg|_{\mathbf{x}=\mathbf{x^0}}\right)_k. \tag{D.10}$$

We may perform a transformation on our basis in which $\mathbf{x}$ exists, such that

$$\mathbf{x^0} \to (\mathbf{x^0})' = ((x_1^0)', (x_2^0)', ..., (x_{n-1}^0)', 0). \tag{D.11}$$

In the new basis we have the relationship

$$\nabla f(\mathbf{x}')\big|_{\mathbf{x}'=(\mathbf{x^0})'} = \nabla f(\mathbf{x})\big|_{\mathbf{x}=(\mathbf{x^0})'}, \tag{D.12}$$

and

$$\nabla f(\mathbf{x}')\big|_{\mathbf{x}'=(\mathbf{x^0})'} = 0. \tag{D.13}$$

Again we get n stationary conditions, however, in this new basis there are only $n - 1$ unknown variables. This is as $(x_n^0)' = 0$. Fixing the stationary point at x_n' will either decrease the number of solutions p or weaken the constraints placed on a continuous solution. Geometrically this means fixing the set of solutions x_i^0 on the plane $X_N = 0$. In other words, we are slicing an n dimensional function into a $n - 1$ dimensional function. Our basis change extracts only the stationary points which lie on this plane. Consider the function

$$g(\mathbf{x}') = f(x_1', x_2', ..., x_{n-1}', 0). \tag{D.14}$$

This is a subset of $f(\mathbf{x}')$ with the constraint that $x_n' = 0$ everywhere. Geometrically, g is the intersection of $f(\mathbf{x}')$ with the $x_n' = 0$ plane. As it is a subset of $f(\mathbf{x}')$

$$\nabla g(\mathbf{x}')\big|_{\mathbf{x}'=(\mathbf{x^0})'} = 0. \tag{D.15}$$

The advantage of this is that now we only need to solve $n-1$ stationary conditions. Defining g as such is equivalent to applying the stationary condition $(x_n^0)' = 0$ before the differentiation is performed. There are no longer any $(x_n)'$ terms in the function g. Let us verify that f and g share the same stationary conditions, that is let us prove

$$\left(\left.\frac{\partial f}{\partial x_k'}\right|_{\mathbf{x}'=(\mathbf{x}^0)'}\right)_k = \left(\left.\frac{\partial g}{\partial x_k'}\right|_{\mathbf{x}'=(\mathbf{x}^0)'}\right)_k, \tag{D.16}$$

for $k = 1, .., n-1$. Decompose the polynomial function f into m parts

$$\begin{aligned} f(\mathbf{x}') &= f_0(x_1', x_2', ..., x_{n-1}') + (x_n') f_1(x_1', x_2', ..., x_{n-1}') + (x_n')^2 f_2(x_1', x_2', ..., x_{n-1}') \\ &\quad + ... + (x_n')^m f_m(x_1', x_2', ..., x_{n-1}'), \\ \Rightarrow f(\mathbf{x}') &= \sum_{i=0}^{m} (x_n')^i f_i(x_1', x_2', ..., x_{n-1}'), \end{aligned} \tag{D.17}$$

then

$$g(\mathbf{x}') = f_0(x_1', x_2', ..., x_{n-1}'). \tag{D.18}$$

We may solve

$$\begin{aligned} \left(\left.\frac{\partial f}{\partial x_k'}\right|_{\mathbf{x}'=(\mathbf{x}^0)'}\right)_k &= \left(\frac{\partial}{\partial x_k'}\left[\sum_{i=0}^{m} (x_n')^i f_i(x_1', x_2', ..., x_{n-1}')\right]\Bigg|_{\mathbf{x}'=(\mathbf{x}^0)'}\right)_k, \\ &= \left(\left.\frac{\partial f_0}{\partial x_k'}\right|_{\mathbf{x}'=(\mathbf{x}^0)'} + \frac{\partial}{\partial x_k'}\left[\sum_{i=1}^{m} (x_n')^i f_i(x_1', x_2', ..., x_{n-1}')\right]\Bigg|_{\mathbf{x}'=(\mathbf{x}^0)'}\right)_k, \end{aligned} \tag{D.19}$$

which for $k = n$ becomes

$$\begin{aligned} \left(\left.\frac{\partial f}{\partial x_n'}\right|_{\mathbf{x}'=(\mathbf{x}^0)'}\right)_n &= \frac{\partial}{\partial x_n'}\left[\sum_{i=1}^{m} (x_n')^i f_i(x_1', x_2', ..., x_{n-1}')\right]\Bigg|_{\mathbf{x}'=(\mathbf{x}^0)'}, \\ &= \sum_{i=1}^{m}\left[\frac{\partial (x_n')^i}{\partial x_n'} f_i(x_1', x_2', ..., x_{n-1}') + (x_n')^i \frac{\partial}{\partial x_n'} f_i(x_1', x_2', ..., x_{n-1}')\right]\Bigg|_{\mathbf{x}'=(\mathbf{x}^0)'}, \\ &= \sum_{i=1}^{m}\left[\frac{\partial (x_n')^i}{\partial x_n'} f_i(x_1', x_2', ..., x_{n-1}')\right]\Bigg|_{\mathbf{x}'=(\mathbf{x}^0)'}, \\ &= f_1(x_1', x_2', ..., x_{n-1}'). \end{aligned} \tag{D.20}$$

For $k \neq n$ this becomes

$$\begin{aligned} \left(\left.\frac{\partial f}{\partial x_k'}\right|_{\mathbf{x}'=(\mathbf{x}^0)'}\right)_k &= \left(\left.\frac{\partial f_0}{\partial x_k'}\right|_{\mathbf{x}'=(\mathbf{x}^0)'} + \left[\sum_{i=1}^{m} (x_n')^i \frac{\partial}{\partial x_k'} f_i(x_1', x_2', ..., x_{n-1}')\right]\Bigg|_{\mathbf{x}'=(\mathbf{x}^0)'}\right)_k, \\ &= \left(\left.\frac{\partial f_0}{\partial x_k'}\right|_{\mathbf{x}'=(\mathbf{x}^0)'}\right)_k, \\ &= \left(\left.\frac{\partial g}{\partial x_k'}\right|_{\mathbf{x}'=(\mathbf{x}^0)'}\right)_k. \end{aligned} \tag{D.21}$$

We have proved that $f(\mathbf{x}')$ and $g(\mathbf{x}')$ share the same stationary conditions for all values $k \neq n$. For

$k = n$, we have the extra stationary condition

$$\left(\left.\frac{\partial f}{\partial x'_n}\right|_{\mathbf{x'}=(\mathbf{x^0})'}\right)_n = f_1(x'_1, x'_2, ..., x'_{n-1}) = 0. \tag{D.22}$$

If f_1 vanishes we say that this condition is trivially satisfied, that is both the left and the right side of the equation are zero. If f_1 does not vanish, we have a non-trivial stationary condition. The function g will not include this extra stationary condition. Using the definition

$$g(\mathbf{x'}) = f_0(x'_1, x'_2, ..., x'_{n-1}), \tag{D.23}$$

we have entirely removed any dependence on x_n in g. Which means we can redefine g without loss of any generality

$$g(\mathbf{x'}) = g(x'_1, x'_2, ..., x'_{n-1}). \tag{D.24}$$

It follows that the set of stationary points of g are independent of X_N. Call this set of stationary points

$$\mathbf{x^0_{n-1}} = ((x^0_1)', (x^0_2)', ..., (x^0_{n-1})'), \tag{D.25}$$

this is a subset of $(\mathbf{x^0})'$ with identical entries but one less dimension. We have now established a function g with $n-1$ stationary conditions matching those of f with

$$\nabla g(\mathbf{x'})\big|_{\mathbf{x'}=(\mathbf{x^0_{n-1}})'} = 0. \tag{D.26}$$

We may have potentially lost a stationary condition that would have otherwise appeared in f but provided no new information is given by this stationary condition we may use g rather than f to save time. If we know that we may continue making such basis changes through until $n = l$ we may reduce our function to

$$h(x'') = (x''_1, x''_2, ..., x''_l). \tag{D.27}$$

In doing such we only need to evaluate l stationary conditions. Note that there is no restriction in the order which we make such basis changes.

We may easily generalise this argument to the 2HDM potential dependent on field operators

$$V(\phi_1, \phi_2, ..., \phi_8). \tag{D.28}$$

These field operators are each functions of space-time and are defined as components of our doublets

$$\Phi_1 = \begin{pmatrix} \phi_1 + i\phi_2 \\ \phi_5 + i\phi_7 \end{pmatrix}, \quad \Phi_2 = \begin{pmatrix} \phi_3 + i\phi_4 \\ \phi_6 + i\phi_8 \end{pmatrix}. \tag{D.29}$$

At the stationary point

$$\Phi^0_1 = \begin{pmatrix} \phi^0_1 + i\phi^0_2 \\ \phi^0_5 + i\phi^0_7 \end{pmatrix}, \quad \Phi^0_2 = \begin{pmatrix} \phi^0_3 + i\phi^0_4 \\ \phi^0_6 + i\phi^0_8 \end{pmatrix}. \tag{D.30}$$

When the stationary point corresponds to a minimum, it is a VEV and we use the notation

$$\Phi^0_a = \langle \Phi_a \rangle, \tag{D.31}$$

and

$$\phi_i^0 = \langle \phi_i \rangle. \tag{D.32}$$

Then stationary conditions of the potential are given at the VEV by the set of eight equations

$$\left.\frac{\partial V}{\partial \phi_i}\right|_{\Phi_a = \langle \Phi_a \rangle} = 0. \tag{D.33}$$

We may make certain basis and gauge transformations, which will cause the VEVs of some of the field operators to vanish, $\langle \phi_k \rangle = 0$.

In the 2HDM after all the available basis and gauge transformations have been exhausted, and we have reduced our set of VEVs to their simplest form as we have seen in the previous section, we are left with one to four VEVs. We may then proceed to relabel all the remaining fields (corresponding to non-zero field component VEVs) according to their relationship with the vacuum. Conventionally, in the 2HDM we make the following re-definitions*

$$\phi_1 = \alpha,\ \phi_5 = v_1,\ \phi_6 = v_2,\ \phi_7 = \delta. \tag{D.34}$$

These fields are still functions of space-time and only take on a particular constant value when defined directly at the VEV after EWSB. We should strictly be writing

$$\left.\frac{\partial V}{\partial \phi_i}\right|_{\phi_i = \phi_i^0} = 0, \tag{D.35}$$

where $\phi^0 = \langle \phi \rangle$. However, for simplicity we write the stationary conditions as

$$\frac{\partial V}{\partial v} = 0, \tag{D.36}$$

where v is a non-vanishing field component which acquires a particular constant value when evaluated at the VEV, (after the differentiation).

Here, we will use this notation Eq. (D.36) but it will always be made clear when we are referring to a function of the fields that is yet to be evaluated at the VEV and when we are referring to a function already evaluated at its VEV.

Stationary Conditions of a Charge Breaking VEV: An Example of Using the Notation We may expand the stationary conditions

$$\left.\frac{\partial V}{\partial \phi_i}\right|_{\Phi_a = \langle \Phi_a \rangle} = 0, \tag{D.37}$$

in terms of the x_j operators

$$\sum_j \left(\frac{\partial V}{\partial x_j} \frac{\partial x_j}{\partial \phi_i} \right)\Bigg|_{\Phi_a = \langle \Phi_a \rangle} = 0. \tag{D.38}$$

* Sometimes the meanings of ϕ_1 and ϕ_3 or ϕ_7 and ϕ_8 are swapped. Such a swap is allowed as simple field transformations relate these, and different conventions may be used.

Consider a set of VEVs that is charge breaking. After an appropriate change of basis we can write, $\phi_5 = v_1$, $\phi_6 = v_2$ and $\phi_3 = \alpha$ with all other ϕ_i vanishing. Define

$$\left.\frac{\partial V}{\partial x_j}\right|_{\Phi_a=\langle\Phi_a\rangle} = V_j'. \tag{D.39}$$

The solutions are

$$\frac{\partial V}{\partial \phi_1} = \alpha V_3', \quad \frac{\partial V}{\partial \phi_2} = 0, \quad \frac{\partial V}{\partial \phi_3} = 2\alpha V_2', \frac{\partial V}{\partial \phi_4} = 0,$$

$$\frac{\partial V}{\partial \phi_5} = 2v_1 V_1' + v_2 V_3', \quad \frac{\partial V}{\partial \phi_6} = 2v_2 V_2' + v_1 V_3', \frac{\partial V}{\partial \phi_7} = 0, \quad \frac{\partial V}{\partial \phi_8} = 0. \tag{D.40}$$

Here we have calculated all 8 derivatives. If this time we only consider the fields with non-vanishing VEVs in the transformed basis, we may rewrite the vector X (defined in Eq. (3.11)) as

$$X_{CB} = Y = \begin{pmatrix} v_1^2 \\ v_2^2 + \alpha^2 \\ v_1 v_2 \\ 0 \end{pmatrix}. \tag{D.41}$$

Now we only need to solve three equations

$$\frac{\partial V}{\partial v_1} = 2v_1 V_1' + v_2 V_3', \quad \frac{\partial V}{\partial v_2} = 2v_2 V_2' + v_1 V_3', \quad \frac{\partial V}{\partial \alpha} = 2\alpha V_2'. \tag{D.42}$$

As expected, we can see that these are exactly the three equations that we get for ϕ_3, ϕ_5 and ϕ_6 using all eight of our field variables. Finally, from the three conditions we may deduce

$$\frac{\partial V}{\partial \alpha} = 0 \Rightarrow V_2' = 0, \tag{D.43}$$

giving

$$\frac{\partial V}{\partial v_2} = 0 \Rightarrow V_3' = 0, \tag{D.44}$$

and so

$$\frac{\partial V}{\partial v_1} = 0 \Rightarrow V_1' = 0. \tag{D.45}$$

The extra condition from the full potential notation offers $V_3' = 0$ which we already know.

D.1.2 Alternative Methods for Solving Stationary Conditions

Another method that allows us to investigate the matrix structure of the potential solutions and extract masses is detailed here. This method gives us the framework to investigate the stability of the minimum solutions and extends the ability to solve mass eigenvalues for minimum solutions of different nature (normal, charge- and CP-breaking).

First derivatives tell us that we have a stationary point. Second partial derivatives determine whether the point is a minimum, maximum or a saddle point. This investigation is done by making use of the

Hessian, a matrix of second derivatives. For the function $f(x_1, x_2, .., x_n)$ the Hessian matrix would be

$$H = \begin{bmatrix} \frac{\partial^2 f}{(\partial x_1)^2} & \frac{\partial^2 f}{\partial x_1 \partial x_2} & .. & \frac{\partial^2 f}{\partial x_1 \partial x_n} \\ \frac{\partial^2 f}{\partial x_2 \partial x_1} & \frac{\partial^2 f}{(\partial x_2)^2} & .. & \frac{\partial^2 f}{\partial x_2 \partial x_n} \\ .. & .. & .. & .. \\ \frac{\partial^2 f}{\partial x_n \partial x_1} & \frac{\partial^2 f}{\partial x_n \partial x_2} & .. & \frac{\partial^2 f}{(\partial x_n)^2} \end{bmatrix}. \tag{D.46}$$

A function has a minimum at x if the Hessian is positive definite* at x.

A Hessian matrix of the potential with respect to ϕ_i is initially in the interaction basis. The process of diagonalisation takes it to the physical mass basis. The eigenvalues of the Hessian matrix are the physical mass terms for the spectra of scalar particles.

A clever method to evaluate the second derivatives of our potential exists. Making use of our field basis operators x_i introduced in Eq. (3.7), Eq. (3.10) and Eq. (3.11), we expand†

$$\frac{\partial^2 V}{\partial \phi_i \partial \phi_j} = \frac{\partial^2 V}{\partial x_m \partial x_l} \frac{\partial x_l}{\partial \phi_j} \frac{\partial x_m}{\partial \phi_i} + \frac{\partial V}{\partial x_l} \frac{\partial^2 x_l}{\partial \phi_i \partial \phi_j}. \tag{D.48}$$

Let us consider each of these two terms individually. In hindsight, we know that the mass matrix is defined as the second derivative evaluated at the VEV. Hence, each derivative above is evaluated at the VEV.

Define the 8×8 matrix

$$M_1^2 = \left(\sum_l V_l' \frac{\partial^2 x_l}{\partial \phi_i \partial \phi_j} \bigg|_{\text{VEV}} \right)_{ij}, \tag{D.49}$$

where

$$V_l' = \frac{\partial V}{\partial x_l} \bigg|_{\text{VEV}}. \tag{D.50}$$

Field combinations $\phi_i \phi_j$ with $|i - j| > 4$ never appear in x_l. As such,

$$M_1^2 = \begin{bmatrix} M_{11}^2 & 0 \\ 0 & M_{12}^2 \end{bmatrix}. \tag{D.51}$$

* A positive definite matrix has determinant and eigenvalues all greater than zero.

†
$$\begin{aligned} \frac{\partial^2 V}{\partial \phi_i \partial \phi_j} &= \frac{\partial}{\partial \phi_i} \left(\frac{\partial V}{\partial \phi_j} \right) \\ &= \frac{\partial}{\partial \phi_i} \left(\frac{\partial V}{\partial x_l} \frac{\partial x_l}{\partial \phi_j} \right) \\ &= \frac{\partial}{\partial \phi_i} \left(\frac{\partial V}{\partial x_l} \right) \frac{\partial x_l}{\partial \phi_j} + \frac{\partial V}{\partial x_l} \frac{\partial}{\partial \phi_i} \left(\frac{\partial x_l}{\partial \phi_j} \right) \\ &= \frac{\partial x_m}{\partial \phi_i} \frac{\partial}{\partial x_m} \left(\frac{\partial V}{\partial x_l} \right) \frac{\partial x_l}{\partial \phi_j} + \frac{\partial V}{\partial x_l} \frac{\partial^2 x_l}{\partial \phi_i \partial \phi_j} \\ &= \frac{\partial^2 V}{\partial x_m \partial x_l} \frac{\partial x_l}{\partial \phi_j} \frac{\partial x_m}{\partial \phi_i} + \frac{\partial V}{\partial x_l} \frac{\partial^2 x_l}{\partial \phi_i \partial \phi_j}. \end{aligned} \tag{D.47}$$

M_1^2 has two 4×4 matrices, which can be calculated to be

$$M_{11}^2 = \begin{bmatrix} 2V_1' & 0 & V_3' & V_4' \\ 0 & 2V_1' & -V_4' & V_3' \\ V_3' & -V_4' & 2V_2' & 0 \\ V_4' & V_3' & 0 & 2V_2' \end{bmatrix}, \tag{D.52}$$

$$M_{12}^2 = \begin{bmatrix} 2V_1' & V_3' & 0 & V_4' \\ V_3' & 2V_2' & -V_4' & 0 \\ 0 & -V_4' & 2V_1' & V_3' \\ V_4' & 0 & V_3' & 2V_2' \end{bmatrix}. \tag{D.53}$$

Next consider the first part which forms another 8×8 matrix, with components

$$\left(\sum_m \sum_l \left(\frac{\partial^2 V}{\partial x_m \partial x_l}\frac{\partial x_m}{\partial \phi_i}\frac{\partial x_l}{\partial \phi_j}\right)\Big|_{\text{VEV}}\right)_{ij}. \tag{D.54}$$

Conveniently, notice that using Eq. (3.11)

$$\frac{\partial^2 V}{\partial x_m \partial x_l} = B = \frac{\partial^2 V}{\partial x_m \partial x_l}\Big|_{\text{VEV}}. \tag{D.55}$$

Then, we need to calculate the matrix

$$C = \left(\frac{\partial x_i}{\partial \phi_j}\Big|_{\text{VEV}}\right)_{ij}. \tag{D.56}$$

This will be a 4×8 matrix, composed solely of ϕ_i operators. Some of these operators vanish at their VEV, at most four operators are non-zero. These non-zero VEVs correspond to those we defined in Eq. (D.34), with $\phi_1 \leftrightarrow \phi_3$.

$$C = \begin{bmatrix} 0 & 0 & 0 & 0 & 2\phi_5 & 0 & 2\phi_7 & 0 \\ 0 & 0 & 2\phi_3 & 0 & 0 & 2\phi_6 & 0 & 0 \\ \phi_3 & 0 & 0 & 0 & \phi_6 & \phi_5 & 0 & \phi_7 \\ 0 & -\phi_3 & 0 & 0 & 0 & -\phi_7 & -\phi_6 & \phi_5 \end{bmatrix}. \tag{D.57}$$

So from the definition of the mass matrix Eq. (3.66) we may then write

$$M^2 = (M_1^2 + C^T B C). \tag{D.58}$$

To proceed further with the calculation, we need to specify which vacuum we are considering.

Mass Matrix of the Normal Vacuum: Charged Scalars After suitable basis transformations the normal vacuum is identified by $\langle\phi_5\rangle = v_1$, $\langle\phi_6\rangle = v_2$ and all other $\langle\phi_i\rangle = 0$. Our C matrix (from Eq. (D.56)) reduces to

$$C = \begin{bmatrix} 0 & 0 & 0 & 0 & 2\phi_5 & 0 & 0 & 0 \\ 0 & 0 & 0 & 0 & 0 & 2\phi_6 & 0 & 0 \\ 0 & 0 & 0 & 0 & \phi_6 & \phi_5 & 0 & 0 \\ 0 & 0 & 0 & 0 & 0 & 0 & -\phi_6 & \phi_5 \end{bmatrix}. \tag{D.59}$$

The form of this C matrix means

$$C^T B C = \begin{bmatrix} 0 & 0 \\ 0 & B' \end{bmatrix}. \tag{D.60}$$

where B is defined in Eq. (3.11). Fluctuations about the fields ϕ_1 to ϕ_4 give us the charged Higgs scalar particles. The top-left 4×4 block of the mass matrix encodes the charged scalar masses

$$(M_{\varphi_1,\varphi_2,\varphi_3,\varphi_4})^2 = M_{11}^2. \tag{D.61}$$

At the normal minimum the X vector (from Eq. (3.11)) is reduced to

$$X_N = \begin{pmatrix} v_1^2 \\ v_2^2 \\ v_1 v_2 \\ 0 \end{pmatrix}. \tag{D.62}$$

At $X = X_N$ the stationary conditions may be defined

$$\left.\frac{\partial V}{\partial v_i}\right|_{\text{VEV}} = 0, \tag{D.63}$$

for $i = 1, 2$. Recall that from Eq. (D.50), $V_i' = \left.\frac{\partial V}{\partial x_i}\right|_{\text{VEV}}$. Using the stationary conditions

$$\begin{aligned} \left.\frac{\partial V}{\partial v_1}\right|_{\text{VEV}} = \left.\left(\frac{\partial V}{\partial x_1}\frac{\partial x_1}{\partial v_1}\right)\right|_{\text{VEV}} + \left.\left(\frac{\partial V}{\partial x_3}\frac{\partial x_3}{\partial v_1}\right)\right|_{\text{VEV}} = 0, \\ \Rightarrow 2V_1' v_1 + V_3' v_2 = 0. \end{aligned} \tag{D.64}$$

Similarly for v_2

$$\left.\frac{\partial V}{\partial v_2}\right|_{\text{VEV}} = 2V_2' v_2 + V_3' v_1 v_2 = 0. \tag{D.65}$$

Allowing us to write

$$V' = -\frac{V_3'}{2v_1 v_2}\begin{pmatrix} v_2^2 \\ v_1^2 \\ -2v_1 v_2 \\ 0 \end{pmatrix}. \tag{D.66}$$

From this we extract

$$V_1' = \frac{-V_3' v_2}{2v_1}, \quad V_2' = \frac{-V_3' v_1}{2v_2}. \tag{D.67}$$

Multiplying these together

$$V_3' = \pm 2\sqrt{V_1' V_2'}. \tag{D.68}$$

With prior knowledge of the outcome we select the negative solution. The normal minimum has $V_4' = 0$, so we may now proceed to calculate the mass matrix for the charged scalars*

$$(M_{\varphi_1\ldots\varphi_4})^2 = \begin{bmatrix} 2V_1' & 0 & -2\sqrt{V_1'V_2'} & 0 \\ 0 & 2V_1' & 0 & -2\sqrt{V_1'V_2'} \\ -2\sqrt{V_1'V_2'} & 0 & 2V_2' & 0 \\ 0 & -2\sqrt{V_1'V_2'} & 0 & 2V_2' \end{bmatrix}. \tag{D.71}$$

Diagonalising this matrix to bring it to the physical basis we get

$$(M_{G^\pm,H^\pm})^2 = \begin{bmatrix} 0 & 0 & 0 & 0 \\ 0 & 0 & 0 & 0 \\ 0 & 0 & 2V_1' + 2V_2' & 0 \\ 0 & 0 & 0 & 2V_1' + 2V_2' \end{bmatrix}. \tag{D.72}$$

The O_1 rotation matrix responsible for $O_1^\dagger (M_{\varphi_1\ldots\varphi_4})^2 O_1 = (M_{G^\pm,H^\pm})^2$ is given by

$$O_1 = \begin{bmatrix} \sqrt{\frac{V_2'}{V_1'}} & 0 & -\sqrt{\frac{V_1'}{V_2'}} & 0 \\ 0 & \sqrt{\frac{V_2'}{V_1'}} & 0 & -\sqrt{\frac{V_1'}{V_2'}} \\ 1 & 0 & 1 & 0 \\ 0 & 1 & 0 & 1 \end{bmatrix}. \tag{D.73}$$

We require that our rotation matrix be unitary, $O_1^\dagger O_1 = I$ by normalising each of the eigenvectors from above

$$O_1 = \frac{1}{\sqrt{V_1' + V_2'}} \begin{bmatrix} \sqrt{V_2'} & 0 & -\sqrt{V_1'} & 0 \\ 0 & \sqrt{V_2'} & 0 & -\sqrt{V_1'} \\ \sqrt{V_1'} & 0 & \sqrt{V_2'} & 0 \\ 0 & \sqrt{V_1'} & 0 & \sqrt{V_2'} \end{bmatrix}. \tag{D.74}$$

The masses for the physical particles may be identified by expanding

$$H^{\pm\dagger} (M_{G^\pm,H^\pm})^2 H^\pm, \tag{D.75}$$

with $H^\pm = (G^+, G^-, H^+, H^-)^T$. We see

$$m_{G^\pm}^2 = 0, \quad m_{H^\pm}^2 = V_1' + V_2'. \tag{D.76}$$

Had we selected the positive solution for V_3' Eq. (D.68), the mass matrix would not change; however, the first two columns of the rotation matrix would be swapped for the last two. Swapped columns correspond to different eigenvalues associated with different eigenvectors. A change in eigenvectors would correspond to massive $G^\pm$ particles and massless $H^\pm$ particles.

* Terms mixing the fields ϕ_i will appear here, as the mass matrix is not diagonal. Introducing the column vector of perturbations to the upper fields

$$\varphi_u = \begin{pmatrix} \varphi_1 \\ \varphi_2 \\ \varphi_3 \\ \varphi_4 \end{pmatrix}, \tag{D.69}$$

such that the mass term expands

$$\varphi_u^\dagger (M_{\varphi_1\ldots\varphi_4})^2 \varphi_u. \tag{D.70}$$

Now that we have defined our particles masses let us find an expression for the rotation angle by relating O_1 to O_β. O_1 rotates our field perturbations $\varphi_u = (\varphi_1, \varphi_2, \varphi_3, \varphi_4)^T$ according to

$$O_1^\dagger \varphi_u = H^\pm. \tag{D.77}$$

Recall, that for the charged Higgs bosons we have degenerate masses. So we combine the first four ϕ fields into two charged fields ϕ_1^+ and ϕ_2^+ according to Eq. (3.70) and Eq. (3.71). We may express this as a basis change according to

$$\frac{1}{\sqrt{2}}\begin{bmatrix} 1 & i & 0 & 0 \\ 0 & 0 & 1 & i \end{bmatrix}\begin{pmatrix} \varphi_1 \\ \varphi_2 \\ \varphi_3 \\ \varphi_4 \end{pmatrix} = \begin{pmatrix} \varphi_1^+ \\ \varphi_2^+ \end{pmatrix}. \tag{D.78}$$

Or more simply put

$$O_\pm \varphi_u = \varphi^+. \tag{D.79}$$

Then, using Eq. (3.73)

$$O_\beta O_\pm \varphi_u = H^+. \tag{D.80}$$

H^+ is the positive component of $H^\pm$ and may be extracted using a transformation

$$\begin{bmatrix} 1 & 0 & 0 & 0 \\ 0 & 0 & 1 & 0 \end{bmatrix}\begin{pmatrix} G^+ \\ G^- \\ H^+ \\ H^- \end{pmatrix} = \begin{pmatrix} G^+ \\ H^+ \end{pmatrix}. \tag{D.81}$$

Or more simply put

$$O_+ H^\pm = H^+. \tag{D.82}$$

Then combining Eq. (D.77), Eq. (D.80) and the above gives us

$$O_+ O_1^\dagger = O_\beta O_\pm. \tag{D.83}$$

Rearranging we get the useful formula

$$O_\beta = O_+ O_1^\dagger O_\pm^\dagger. \tag{D.84}$$

In this case

$$O_\beta = \frac{1}{\sqrt{V_1' + V_2'}}\begin{bmatrix} \sqrt{V_2'} & \sqrt{V_1'} \\ -\sqrt{V_1'} & \sqrt{V_2'} \end{bmatrix}. \tag{D.85}$$

We may finally identify our rotation angle β

$$c_\beta = \sqrt{\frac{V_2'}{V_1' + V_2'}}, \quad s_\beta = \sqrt{\frac{V_1'}{V_1' + V_2'}}, \tag{D.86}$$

and

$$t_\beta = \sqrt{\frac{V_1'}{V_2'}}. \tag{D.87}$$

Correctly defining the physics of the charged particles is the most cumbersome as it involves mixing of the original ϕ_i fields into charged fields and then again mixing of the charged fields into fields that

encode the physical particle states. Now that we have identified the process and particular relations between the states, we may save time in the future when calculating the charged mass eigenstates and associated mixing angle.

D.1.2.1 Mass Matrix of the Normal Vacuum: Neutral Scalars

There are four remaining physical particles, two real massive Higgs particles, a pseudo-scalar Higgs and a pseudo-scalar Goldstone particle. With prior anticipation of the particle spectrum, we have labelled our fields in their doublets such that the ϕ_5 and ϕ_6 fields correspond to the real scalars and the ϕ_7 and ϕ_8 fields the pseudo-scalars. In this way, the fields corresponding to each of the two groups will have rows next to one another in the full 8×8 interaction mass matrix that we have begun calculating.

Recall for the normal minimum combining the general mass matrix equation Eq. (D.58) with Eq. (D.60) we have for the bottom right 4×4 block

$$M_{12}^2 + B'. \tag{D.88}$$

This block contains the interaction state masses of ϕ_5 through ϕ_8, here

$$M_{12}^2 = \begin{bmatrix} 2V_1' & -2\sqrt{V_1'V_2'} & 0 & 0 \\ -2\sqrt{V_1'V_2'} & 2V_2' & 0 & 0 \\ 0 & 0 & 2V_1' & -2\sqrt{V_1'V_2'} \\ 0 & 0 & -2\sqrt{V_1'V_2'} & 2V_2' \end{bmatrix}, \tag{D.89}$$

and B' has a complicated form for the general potential.

It is possible to solve the eigensystem and find one zero eigenvalue corresponding to our CP-odd Goldstone Boson and three non-zero eigenvalues corresponding to our CP-odd scalar, CP-even light Higgs scalar and CP-even heavy Higgs scalar. If all the b parameters in our potential are real, we see that B' and hence the interaction mass matrix will be block diagonal. In this case, there is no mixing between the physical scalar particles and the pseudo-scalars and B' has the simpler form

$$B' = \begin{bmatrix} 2H_1 & 2H_3 & 0 & 0 \\ 2H_3 & 2H_2 & 0 & 0 \\ 0 & 0 & 2b_{44}v_2^2 & -2b_{44}v_1v_2 \\ 0 & 0 & -2b_{44}v_1v_2 & 2b_{44}v_1^2 \end{bmatrix}, \tag{D.90}$$

where

$$\begin{aligned} H_1 &= 4v_1^2 b_{11} + 2v_1v_2b_{13} + v_2^2 b_{33}, \\ H_2 &= v_1^2 b_{33} + 2v_1v_2b_{23} + 4v_2^2 b_{22}, \\ H_3 &= v_1^2 b_{13} + v_1v_2(2b_{12} + b_{33}) + v_2^2 b_{23}. \end{aligned} \tag{D.91}$$

Let us start by diagonalising the scalar mass matrix. Finding the eigenvalues gives

$$\mathrm{eig}(M_H) = H_+ \pm \sqrt{H_-^2 + 4H_3'^2}. \tag{D.92}$$

where

$$\begin{aligned} H_+ &= V_1' + V_2' + H_1 + H_2, \\ H_- &= V_1' - V_2' + H_1 - H_2, \\ H_3' &= H_3 - \sqrt{V_1' V_2'} = H_3 \pm \frac{V_3'}{2}. \end{aligned} \tag{D.93}$$

We may then rewrite the interaction mass matrix as*

$$M_{\phi_R} = \frac{1}{2}\begin{bmatrix} H_+ + H_- & 2H_3' \\ 2H_3' & H_+ - H_- \end{bmatrix}. \tag{D.95}$$

The factor of half appears as all our couplings are real.

Introduce the physical mass matrix

$$M_H = \frac{1}{2}\begin{bmatrix} H_+ + H_c & 0 \\ 0 & H_+ - H_c \end{bmatrix}, \tag{D.96}$$

with

$$H_c = \sqrt{H_-^2 + 4H_3'^2}. \tag{D.97}$$

Relating the physical and interaction state matrices we may construct the rotation matrix and find the mixing angle. Solving the eigenvalue equation $M_{\phi_R}\mathbf{v}_i = \text{eig}(M_H)_i \mathbf{v}_i$, for $i = 1, 2$ to find eigenvectors† we get the normalised rotation matrix

$$O_{H,h} = \begin{bmatrix} \frac{H_c - H_-}{\sqrt{(H_c - H_-)^2 + 4H_3'^2}} & \frac{2H_3'}{\sqrt{(H_c - H_-)^2 + 4H_3'^2}} \\ -\frac{H_c + H_-}{\sqrt{(H_c + H_-)^2 + 4H_3'^2}} & \frac{2H_3'}{\sqrt{(H_c + H_-)^2 + 4H_3'^2}} \end{bmatrix}. \tag{D.99}$$

Giving

$$c_\alpha = \frac{H_c - H_-}{\sqrt{(H_c - H_-)^2 + 4H_3'^2}} = \frac{2H_3'}{\sqrt{(H_c + H_-)^2 + 4H_3'^2}}, \tag{D.100}$$

$$s_\alpha = \frac{2H_3'}{\sqrt{(H_c - H_-)^2 + 4H_3'^2}} = \frac{H_c + H_-}{\sqrt{(H_c + H_-)^2 + 4H_3'^2}}. \tag{D.101}$$

We may express t_α in several ways

$$t_\alpha = \frac{2H_3'}{H_c - H_-} = \frac{H_c + H_-}{2H_3'}. \tag{D.102}$$

Finally, this leaves us with the pseudo-scalar sector. The interaction matrix for the pseudo-scalar sector

---

* In terms of our general potential couplings

$$\begin{aligned} H_+ + H_- &= 2\left(m_{11}^2 + 3v_1^2\lambda_1 + v_2^2(\lambda_3 + \lambda_4 + \lambda_5) + 6v_1 v_2 \lambda_6\right), \\ 2H_3' &= -2m_{12}^2 + 4v_1 v_2(\lambda_3 + \lambda_4 + \lambda_5) + 6v_1^2\lambda_6 + 6v_2^2\lambda_7, \\ H_+ - H_- &= 2\left(m_{22}^2 + 3v_2^2\lambda_2 + v_1^2(\lambda_3 + \lambda_4 + \lambda_5) + 6v_1 v_2 \lambda_7\right). \end{aligned} \tag{D.94}$$

† The eigenvectors are

$$\mathbf{v}_1 = \begin{pmatrix} \frac{1}{2H_3'}\left[H_c - H_-\right] \\ 1 \end{pmatrix}, \quad \mathbf{v}_2 = \begin{pmatrix} -\frac{1}{2H_3'}\left[H_c + H_-\right] \\ 1 \end{pmatrix}. \tag{D.98}$$

is given by

$$M_{\varphi_7,\varphi_8} = \begin{bmatrix} A_+ + A_- & -2A_3 \\ -2A_3 & A_+ - A_- \end{bmatrix}, \tag{D.103}$$

where

$$\begin{aligned} A_+ &= V_1 + V_2' + b_{44}v_2^2 + b_{44}v_1^2, \\ A_- &= V_1 - V_2' + b_{44}v_2^2 - b_{44}v_1^2, \\ A_3 &= \sqrt{V_1'V_2'} + b_{44}v_1v_2, \\ A_c &= \sqrt{A_-^2 + 4A_3^2}. \end{aligned} \tag{D.104}$$

Diagonalising, the physical mass matrix of the pseudo-scalars is

$$M_A = \begin{bmatrix} A_+ - A_c & 0 \\ 0 & A_+ + A_c \end{bmatrix}. \tag{D.105}$$

The normalised rotation matrix is then

$$O_A = \begin{bmatrix} \frac{A_c - A_-}{\sqrt{(A_c - A_-)^2 + 4A_3^2}} & \frac{2A_3}{\sqrt{(A_c - A_-)^2 + 4A_3^2}} \\ -\frac{A_c + A_-}{\sqrt{(A_c + A_-)^2 + 4A_3^2}} & \frac{2A_3}{\sqrt{(A_c + A_-)^2 + 4A_3^2}} \end{bmatrix}. \tag{D.106}$$

Giving

$$c_\beta = \frac{A_c - A_-}{\sqrt{(A_c - A_-)^2 + 4A_3^2}} = \frac{2A_3}{\sqrt{(A_c + A_-)^2 + 4A_3^2}}, \tag{D.107}$$

$$s_\beta = \frac{2A_3}{\sqrt{(A_c - A_-)^2 + 4A_3^2}} = \frac{A_c + A_-}{\sqrt{(A_c + A_-)^2 + 4A_3^2}}, \tag{D.108}$$

and so

$$t_\beta = \frac{2A_3}{A_c - A_-} = \frac{A_c + A_-}{2A_3}. \tag{D.109}$$

It is possible to show the t_β we calculated for the charged particles Eq. (D.87) agrees with the value above.

Mass Matrix of the Charge Breaking Vacuum After suitable basis changes at the charge breaking minimum, we have, $\phi_5 = v_1'$ and $\phi_6 = v_2'$, plus a charge breaking term $\phi_3 = \alpha$. Again, these are functions that when evaluated at the VEV become real numbers v_1', v_2' and α respectively. The vector X is now

$$X_{CB} = Y = \begin{pmatrix} v_1'^2 \\ v_2'^2 + \alpha^2 \\ v_1'v_2' \\ 0 \end{pmatrix}, \tag{D.110}$$

with $Y = (y_1, y_2, y_3, y_4)$.

Consider the stationary conditions for this minimum. The form of the two found at the normal minimum remain unchanged

$$\left.\frac{\partial V}{\partial v_1'}\right|_{\text{VEV}} = \left.\frac{\partial V}{\partial y_1}\right|_{\text{VEV}} 2v_1' + \left.\frac{\partial V}{\partial y_3}\right|_{\text{VEV}} v_2' = 0, \tag{D.111}$$

$$\left.\frac{\partial V}{\partial v_2'}\right|_{\text{VEV}} = \left.\frac{\partial V}{\partial y_2}\right|_{\text{VEV}} 2v_2' + \left.\frac{\partial V}{\partial y_3}\right|_{\text{VEV}} v_1' = 0. \tag{D.112}$$

However, as we have now three parameters to consider, we get an additional minimisation condition

$$\left.\frac{\partial V}{\partial \alpha}\right|_{\text{VEV}} = \left.\left(\frac{\partial V}{\partial y_2}\frac{\partial y_2}{\partial \alpha}\right)\right|_{\text{VEV}} = \left.\frac{\partial V}{\partial y_2}\right|_{\text{VEV}} 2\alpha = 0. \tag{D.113}$$

If $\alpha = 0$, we are left with precisely the two constraints we had for the normal minimum. Of course, a trivial value of α is the condition for a normal minimum, and so for a charge breaking vacuum $\alpha \neq 0$. As such we conclude, using the final constraint, that $\partial V/\partial y_2|_{\text{VEV}}$ must vanish. Then using the second constraint we are left with $(\partial V/\partial y_3)|_{\text{VEV}} v_1' = 0$, which implies that either v_1' or $\partial V/\partial y_3|_{\text{VEV}}$ must vanish. But the requirement $v_1' \neq 0$ has been made to construct the constraints. As a result, in the first constraint $\partial V/\partial y_1|_{\text{VEV}}$ will vanish. In other words, the extra constraint Eq. (D.113) allows us to write

$$\left.\frac{\partial V}{\partial y_i}\right|_{\text{VEV}} = 0. \tag{D.114}$$

Notice, that this condition is equivalent to writing

$$\left.\frac{\partial V}{\partial X}\right|_{X=Y} = 0, \tag{D.115}$$

meaning that all V_i' vanish. The general equation for the mass matrix Eq. (D.58) is

$$M^2 = (M_1^2 + C^T B C). \tag{D.116}$$

M_1^2 consists only of a combination of V_i', meaning that M_1^2 is a zero matrix. Next

$$C = \begin{bmatrix} 0 & 0 & 0 & 0 & 2v_1' & 0 & 0 & 0 \\ 0 & 0 & 2\alpha & 0 & 0 & 2v_2' & 0 & 0 \\ \alpha & 0 & 0 & 0 & v_2' & v_1' & 0 & 0 \\ 0 & -\alpha & 0 & 0 & 0 & 0 & -v_2' & v_1' \end{bmatrix}. \tag{D.117}$$

Define $B' = O(C^T B C)O^{-1}$, where O is a 8×8 orthogonal matrix. The matrices B' and B are similar and this means that they share the same eigenvalues. It is possible to find an O such that it performs suitable row and column operators on C reducing our entire mass matrix to

$$\begin{aligned} M^2 &= O(C^T B C)O^{-1}, \\ &= \begin{bmatrix} 0_{4\times4} & 0_{4\times4} \\ 0_{4\times4} & M_{12}^2 \end{bmatrix}, \end{aligned} \tag{D.118}$$

where $0_{4\times4}$ is a four-by-four zero matrix and M_{12}^2 the real and pseudo-scalar Higgs mass matrix. The first eigenvalue of M_{12}^2 is $b_{44}(v_1'^2 + v_2'^2 + \alpha^2)$. The following three are omitted here as they cannot be expressed simply. Notice that this eigenvalue implies that $b_{44} > 0$.

Mass Matrix of the CP-breaking Vacuum A CP-breaking vacuum is defined as having the definitions $\phi_5 = v_1'$, $\phi_6 = v_2'$, $\phi_7 = \delta$ and all other $\phi_i = 0$. As always, these are a result of suitable basis changes on the

most general form of the vacuum. Our X vector becomes

$$X_{CP} = \begin{pmatrix} v_1'^2 + \delta^2 \\ v_2'^2 \\ v_1' v_2' \\ -v_2 \delta \end{pmatrix}. \tag{D.119}$$

The set of stationary conditions for this are

$$\begin{aligned} 2V_1' v_1' + V_3' v_2' &= 0, \\ 2V_2' v_2' + V_3' v_1' - V_4' \delta &= 0, \\ 2V_1' \delta - V_4' v_2' &= 0. \end{aligned} \tag{D.120}$$

Combining these along with the condition from the potential

$$V_4' = 2b_{44}(-v_2' \delta), \tag{D.121}$$

we may write the vector V'

$$V' = -b_{44} \begin{pmatrix} v_2'^2 \\ \delta^2 + v_1'^2 \\ -2v_1' v_2' \\ 2\delta v_2' \end{pmatrix}. \tag{D.122}$$

From this we are able to fill in our M_1^2 matrix. The C matrix for the CP breaking case is

$$C = \begin{bmatrix} 0 & 0 & 0 & 0 & 2v_1' & 0 & 2\delta & 0 \\ 0 & 0 & 0 & 0 & 0 & 2v_2' & 0 & 0 \\ 0 & 0 & 0 & 0 & v_2' & v_1' & 0 & \delta \\ 0 & 0 & 0 & 0 & 0 & -\delta & -v_2' & v_1' \end{bmatrix}. \tag{D.123}$$

As such, the combination $C^T BC$ only contributes to uncharged scalar fields. The charged fields get their masses directly from the eigenvalues of M_{11}^2. The real and pseudo-scalar particles get their masses from the eigenvalues of M_{12}^2 added to the non-zero block of $C^T BC$. In the end, a mixed 4×4 matrix is produced. Here the charged fields have double degenerate eigenvalues of zero and $-b_{44}(v_1'^2 + v_2'^2 + \delta^2)$. The latter of these requires $b_{44} < 0$.

D.2 2HDM Vacuum Lemma Proofs

In this section, our goal is to consider each different kind of possible minimum individually and with this prove the claims from section 3.5. We approach the proofs by considering each of the minima separately. For each minimum, we formulate the expression $V_I - V_J$. V_I and V_J represent the potential evaluated at different minima; for example, V_N is the potential evaluated at the normal minimum. The sign of $V_I - V_J$ will reveal which of V_I, V_J is the global minimum.

D.2.1 Part I: The Normal Minimum

Let us begin by considering the normal minimum, given when $\phi_5 = v_1$, $\phi_6 = v_2$, all other $\phi_i = 0$. From the notation established in section D.1.1 we recall, v_1 and v_2 are functions of space-time, only at the minimum do they have a specified real value, the notation does not change, however

$$\langle v_1 \rangle = v_1, \quad \langle v_2 \rangle \quad = v_2. \tag{D.124}$$

In Eq. (D.66), we have shown

$$V' = -\frac{V_3'}{2v_1v_2}\begin{pmatrix} v_2^2 \\ v_1^2 \\ -2v_1v_2 \\ 0 \end{pmatrix}. \tag{D.125}$$

Notice that both V_1' and V_2' terms have the same sign. In Eq. (D.62) we evaluated the vector X at the normal minimum, notice that

$$X_N^T V' = 0. \tag{D.126}$$

Previously, we found the mass of the charged Higgs scalar at a normal minimum is $m_{H^\pm} = V_1' + V_2'$. This tells us that for a normal minimum to exist

$$V_1' + V_2' > 0. \tag{D.127}$$

But we know that both V_1' and V_2' have the same sign, so they must both be positive at the normal minimum. This results in

$$-\frac{V_3'}{2v_1v_2} > 0. \tag{D.128}$$

Another way to formulate the V' vector is to directly differentiate the potential with respect to x_i. We find that we may write

$$\frac{\partial V}{\partial x_i} = A + BX, \tag{D.129}$$

which evaluated at the minimum becomes

$$V' = A + BX_N. \tag{D.130}$$

We require one more useful result. Writing the potential evaluated at $X = X_N$ as

$$V_N = p_2 + p_4. \tag{D.131}$$

where $p_2 = p_2(v_1, v_2)$ contains bi-linear combinations of the functions v_1 and v_2 and $p_4 = p_4(v_1, v_2)$ are quadratic terms of the functions. Then

$$\begin{aligned} p_2 &= A^T X_N, \\ p_4 &= \frac{1}{2} X_N^T B X_N. \end{aligned} \tag{D.132}$$

At a stationary point

$$\sum_i \left(v_i \frac{\partial V_N}{\partial v_i} \right)\Bigg|_{\text{VEV}} = 0. \tag{D.133}$$

Evaluating this we find

$$\begin{aligned} 2p_2 + 4p_2 &= 0, \\ \Rightarrow p_2 &= -2p_4, \end{aligned} \tag{D.134}$$

where now p_2 and p_4 are evaluated at the VEV. Substituting this equality back into our general equation for V_N Eq. (D.131) we may write

$$V_N = \frac{1}{2} p_2 = -p_4. \tag{D.135}$$

Leaving us with the equation for the normal minimum we are searching for

$$V_N = \frac{1}{2} A^T X_N = -\frac{1}{2} X_N^T B X_N. \tag{D.136}$$

We now have all the equations corresponding to our normal minimum that we require to proceed.

D.2.2 Part II: The Charge Breaking Minimum

We strive to find an expression for $(V_{CB} - V_N)$ where V_N is the potential evaluated at the normal minimum and V_{CB} is the potential evaluated at the charge breaking minimum. We found from Eq. (D.115) that for a charge breaking minimum

$$\left.\frac{\partial V}{\partial X}\right|_{X=X_{\mathrm{CB}}=Y} = 0. \tag{D.137}$$

Exactly as in the normal vacuum situation, by differentiating the potential directly with respect to y_i and evaluating at the minimum we find

$$\left.\frac{\partial V}{\partial X}\right|_{X=Y} = A + BY. \tag{D.138}$$

Combining the two above conclusions and provided that B is an invertible matrix

$$\begin{aligned} A + BY &= 0, \\ \Rightarrow Y &= -B^{-1} A. \end{aligned} \tag{D.139}$$

We have just found a solution for the parameters in the charge breaking vacuum this will come in useful later.

As before we can write the value of the potential in terms of the functionals p_2 and p_4

$$V_{CB} = p_2 + p_4, \tag{D.140}$$

with

$$\begin{aligned} p_2 &= A^T Y, \\ p_4 &= \frac{1}{2} Y^T B Y. \end{aligned} \tag{D.141}$$

We find the useful relation

$$V_{CB} = \frac{1}{2} A^T Y = -\frac{1}{2} (Y)^T B Y. \tag{D.142}$$

Now subtracting Eq. (D.139), from Eq. (D.130)

$$V' = A + B X_N - (A + BY) = B X_N - BY. \tag{D.143}$$

Then pre-multiplying through by X_N^T and using the fact that $X_N^T V' = 0$

$$X_N^T B X_N = X_N^T B Y = -2V_N. \tag{D.144}$$

The last equality comes from our final useful equation in the normal vacuum analysis (D.136). Lastly, let us this time pre-multiply Eq. (D.143) by $(Y)^T$

$$\begin{aligned} V' &= BX_N - BY, \\ \Rightarrow Y^T V' &= Y^T B X_N - Y^T B Y. \end{aligned} \tag{D.145}$$

Using the useful equations (D.142) and Eq. (D.144) and the fact that B is symmetric ($Y^T B X_N = X_N^T B Y$)

$$\begin{aligned} (Y)^T V' &= (-2V_N) - (-2V_{CB}), \\ \Rightarrow V_{CB} - V_N &= \frac{1}{2} Y^T V'. \end{aligned} \tag{D.146}$$

This is exactly the equation we set out to find. Next, we need to determine the sign. Calculating the RHS of the above

$$\begin{aligned} Y^T V' &= -\frac{V_3'}{2v_1 v_2}\left[v_1'^2 v_2^2 + (v_2'^2 + \alpha^2) v_1^2 + (v_1' v_2')(-2v_1 v_2) \right], \\ &= -\frac{V_3'}{2v_1 v_2}\left[(v_1' v_2 - v_1 v_2')^2 + (\alpha v_1)^2 \right]. \end{aligned} \tag{D.147}$$

Using Eq. (D.128) it is easy to see the above must be positive

$$(V_{CB} - V_N) > 0. \tag{D.148}$$

If there is a normal minimum, its value is always less than that of the charge breaking minimum; hence, the normal minimum is always a global minimum. Returning to Eq. (D.145) and multiplying both sides to the left by $V'^T B^{-1}$ we are left with

$$V'^T B^{-1} V' = V'^T (X_N - Y). \tag{D.149}$$

After explicitly calculating $V'^T (X_N - Y)$, we find that

$$V'^T B^{-1} V' = -Y^T V'. \tag{D.150}$$

So if a normal minimum exists then $Y^T V' > 0$ which implies by the above that $V'^T B^{-1} V' < 0$. This result then must mean B is not a positive definite matrix. This fact will come in useful soon.

D.2.3 Part III: The CP-Breaking Minimum

We need to perform this analysis once again, this time for the CP-breaking vacuum. This vacuum has the re-definitions $\phi_5 = v_1'$, $\phi_6 = v_2'$, $\phi_7 = \delta$ and all other $\phi_i = 0$. With these parameters our X vector becomes

$$X_{CP} = \begin{pmatrix} v_1'^2 + \delta^2 \\ v_2'^2 \\ v_1' v_2' \\ -v_2 \delta \end{pmatrix}. \tag{D.151}$$

We find that at the CP-breaking minimum the relation $x_4^2 = x_1 x_2 - x_3^2$ holds. Let us make this substitution in the most general potential Eq. (3.10)

$$\begin{aligned} V = {} & a_1 x_1 + a_2 x_2 + a_3 x_3 + \\ & b_{11} x_1^2 + b_{22} x_2^2 + (b_{33} - b_{44}) x_3^2 + (b_{12} + b_{44}) x_1 x_2 + b_{13} x_1 x_3 + b_{23} x_2 x_3. \end{aligned} \tag{D.152}$$

We can retain the same forms of the equations we have used up until now by defining

$$Z = \begin{pmatrix} v_1'^2 + \delta^2 \\ v_2'^2 \\ v_1' v_2' \\ 0 \end{pmatrix}, \quad B_{CP} = \begin{pmatrix} 2b_{11} & b_{12} + b_{44} & b_{13} & 0 \\ b_{12} + b_{44} & 2b_{22} & b_{23} & 0 \\ b_{13} & b_{23} & 2(b_{33} - b_{44}) & 0 \\ 0 & 0 & 0 & 0 \end{pmatrix}, \tag{D.153}$$

with $Z = (z_1, z_2, z_3, z_4)$. We can write

$$V = A^T Z + \frac{1}{2} Z^T B_{CP} Z. \tag{D.154}$$

Again, Z is a vector of functions which at the VEV becomes a vector of real numbers. We have three stationary constraints, the first two identical to those from the charged minimum, the third gives

$$\left.\frac{\partial V}{\partial \delta}\right|_{\text{VEV}} = \left.\left(\frac{\partial V}{\partial z_1}\frac{\partial z_1}{\partial \delta}\right)\right|_{\text{VEV}} = \left.\frac{\partial V}{\partial z_1}\right|_{\text{VEV}} 2\delta = 0. \tag{D.155}$$

When $\delta = 0$ this constraint adds no extra information to the theory, and we are left with the same constraint as the normal minimum. This of course, corresponds to a trivial ϕ_7 which gives us the normal minimum to begin with. For a non-zero δ we retain the CP-breaking minimum and the constraint implies that $\left.\frac{\partial V}{\partial z_1}\right|_{\text{VEV}} = 0$. This fact combined with the first two constraints tells us that at the minimum

$$\left.\frac{\partial V}{\partial z_i}\right|_{\text{VEV}} = 0. \tag{D.156}$$

If we differentiate the potential directly with respect to x_i and evaluating at $X = Z$ (the minimum) we find

$$\left.\frac{\partial V}{\partial X}\right|_{X=Z} = A + B_{CB} Z. \tag{D.157}$$

Leading us to the direct solution for Z

$$\begin{aligned} & A + B_{CP} Z = 0, \\ & \quad \Rightarrow Z = -B_{CP}^T A, \end{aligned} \tag{D.158}$$

providing B_{CP} is invertible. Writing $V_{CP} = p_2 + p_4$, where p_2 and p_4 are functions of v_1, v_2 and α

$$\begin{aligned} p_2 &= A^T Z, \\ p_4 &= \frac{1}{2} Z^T B_{CP} Z. \end{aligned} \tag{D.159}$$

We get the familiar relation at the VEV

$$V_{CP} = \frac{1}{2} A^T Z = -\frac{1}{2} Z^T B_{CP} Z. \tag{D.160}$$

Similar to the charge breaking section, subtract Eq. (D.158) from Eq. (D.130)

$$V' = BX_N - B_{CP}Z. \tag{D.161}$$

Pre-multiplying by X_N^T

$$X_N^T BX_N - X_N^T B_{CP} Z = 0. \tag{D.162}$$

Alternatively, pre-multiplying by Z^T

$$Z^T BX_N - Z^T B_{CP} Z = Z^T V'. \tag{D.163}$$

Adding the two above equations together and using the symmetry of B_{CP} we get

$$X_N^T BX_N - Z^T B_{CP} Z + Z^T BX_N - Z^T B_{CP} X_N = Z^T V'. \tag{D.164}$$

Then using Eq. (D.136) and Eq. (D.160)

$$(-2V_N) - (-2V_{CP}) + Z^T BX_N - Z^T B_{CP} X_N = Z^T V'. \tag{D.165}$$

Which simplifies to

$$(V_{CP} - V_N) = \frac{1}{2}[Z^T V' + Z^T (B_{CP} - B)X_N]. \tag{D.166}$$

But

$$Z^T V' + Z^T (B_{CP} - B)X_N = \left(-\frac{V_3'}{2v_1 v_2} + b_{44}\right)\left[(v_1' v_2 - v_1 v_2')^2 + (\delta v_2)^2\right]. \tag{D.167}$$

We have found above that $b_{44} < 0$ for a CP minimum to exist and Eq. (D.122) gives us $V_3' = 2b_{44} v_1' v_2'$. Combining these we have the condition

$$v_1' v_2' > v_1 v_2, \tag{D.168}$$

for the $-\frac{V_3'}{2v_1 v_2} + b_{44}$ to be positive. Hence

$$(V_{CP} - V_N) > 0, \tag{D.169}$$

and our normal minimum if it exists is always 'deeper' than the CP-breaking minimum iff $v_1' v_2' > v_1 v_2$.

D.2.4 Classification of the Mass Matrices

A stationary point is a minimum if the mass matrix is positive definite. Likewise, it is a maximum if it is negative definite and a saddle point if it is neither. A $n \times n$ positive definite matrix M satisfies

$$z^T Mz > 0, \tag{D.170}$$

for every possible z a n component column vector. A negative definite classification is given if $z^T Mz < 0$ for all z. We know that the mass matrices of both the charge breaking and CP breaking are proportional to B. That is the classification of B determines the nature of the stationary points. Let us expand

$$z^T Bz = 2(b_{11}z_1^2 + b_{12}z_1 z_2 + b_{22}z_2^2 + b_{13}z_1 z_3 + b_{23}z_2 z_3 + b_{33}z_3^2 + b_{44}z_4^2). \tag{D.171}$$

Our stationary points are classified in Table D.1.

Table D.1: Classification of the potential B vector values corresponding to stationary points, where CPB stands for CP-breaking.

The condition that $b_{11} > 0$ for both the stationary points comes from requiring that the potential is bounded from below. This is explained in the Appendix of Ref. [30]. As $b_{11} > 0$ for both the CB and CP-breaking stationary points they both have a solution $z^T M z > 0$ for $z = (z_1, 0, 0, 0)^T$ (for example). As this is a solution, they cannot be negative definite. Previously we proved that if a normal minimum exists B cannot be positive definite. As such, the CB and CP-breaking stationary points must be saddle points if they are to coexist with a normal minimum. Next, as the value of b_{44} is required to be positive for the CB stationary point to be a minimum and negative for a CP-breaking stationary point to be a minimum we see that they can both never coexist as minima of the same potential.

E

Tree-Level 2HDM Type-II Global Fits

In this Appendix we extend the results given for the GAMBIT Z_2 global fits by including the tree-level spectrum results for the (softly-broken Z_2-symmetric) type-II. The constraints on the tree-level model remain the same except we only check unitarity constraints up to leading order.

We show the two-dimensional profile likelihood distributions of the mixing angles in Figure E.1, the one-dimensional profile likelihood distributions of parameters/observables in the physical spectrum in Figure E.2 and the two-dimensional profile likelihood distributions of the couplings of the potential (in the generic basis) in Figure E.3.

The tree-level model has a much greater opening for the couplings and scalar masses. The reason for this includes the omission of the most restrictive theoretical likelihood, unitarity of the scattering matrix at NLO as well as the disappearance of the heavy scalar mass cut-off coming from limits from loop-corrections when fixing the SM Higgs scalar mass.

Figure E.1: 2D profile likelihood distributions of the mixing angles in the *tree-level type-II model*.

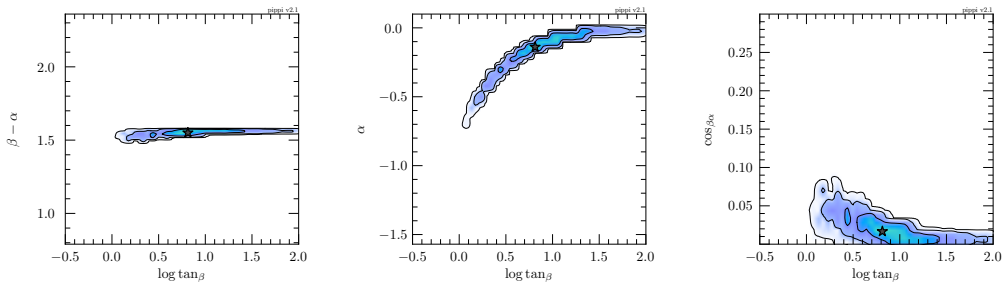

Figure E.2: 1D profile likelihood distributions for the physical spectrum in the *tree-level type-II model*.

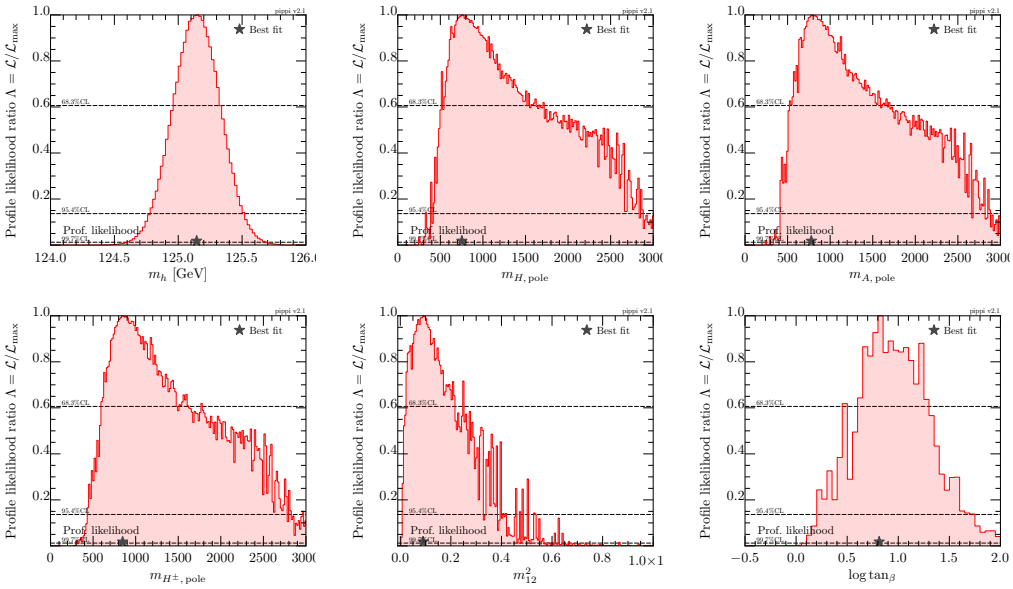

Figure E.3: 2D profile likelihood distributions for the potential couplings (generic basis) in the *tree-level type-II model*.

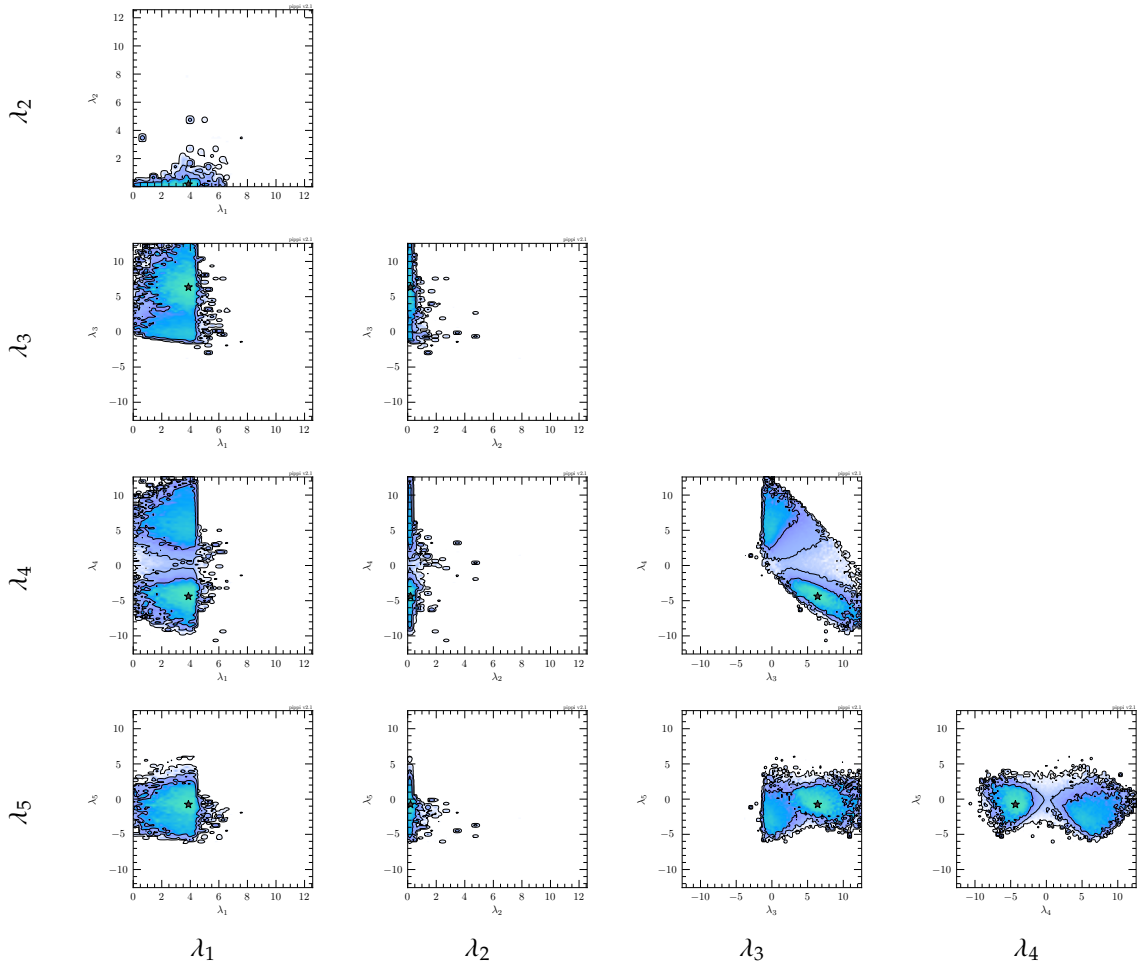

F

Physical Quantities

F.1 GAMBIT Z_2 Yukawa Aligned 2HDM Fit

Name	Symbol	Value	Reference
B_s^0-Meson Mass Splitting	$\Delta m_{B_s^0}$	$(17.757 \pm 0.021 \pm 6\%_{\text{th.}})$ ps^{-1}	[68], [132]
B_d^0-Meson Mass Splitting	$\Delta m_{B_d^0}$	$(0.507 \pm 0.005 \pm 15\%_{\text{th.}})$ ps^{-1}	[133], [132]
B Decays	$\text{BR}(B_s^0 \to \mu^+\mu^-)$	$(2.9 \pm 0.7 \pm 0.2 \pm 10\%_{\text{th.}}) \times 10^{-9}$	[134], [135]
	$\text{BR}(B^0 \to \mu^+\mu^-)$	$(0.8 \pm 1.4 \pm 10\%_{\text{th.}}) \times 10^{-10}$	[134], [135]
	$\text{BR}(B^\pm \to \tau^\pm\nu)$	$(1.09 \pm 0.2 \pm 19\%_{\text{th.}}) \times 10^{-4}$	[55]
	$\text{BR}(B \to D\mu\nu)$	$(2.19 \pm 0.12 \pm 9.1\%_{\text{th.}}) \times 10^{-2}$	[55]
	$\text{BR}(B \to D^*\mu\nu)$	$(4.93 \pm 0.11 \pm 10.55\%_{\text{th.}}) \times 10^{-2}$	[55]
D Decays	$\text{BR}(D_s^\pm \to \tau^\pm\nu)$	$(5.5 \pm 0.24 \pm 2\%_{\text{th.}}) \times 10^{-2}$	[55] [136]
	$\text{BR}(D_s^\pm \to \mu^\pm\nu)$	$(5.56 \pm 0.25 \pm 2\%_{\text{th.}}) \times 10^{-3}$	[55] [136]
	$\text{BR}(D^\pm \to \mu^\pm\nu)$	$(3.74 \pm 0.17 \pm 3\%_{\text{th.}}) \times 10^{-2}$	[55] [136]
$B \to D$ Decay Ratios	R_D	$(0.306 \pm 0.013 \pm 0.007 \pm 3.7\%_{\text{th.}})$	[68], [137]
	R_D^*	$(0.407 \pm 0.039 \pm 0.024 \pm 0.1\%_{\text{th.}})$	[68], [138]
$B \to K$ Decay Ratios	R_K	$(0.846 \pm 0.060 \pm 0.016 \pm 1\%_{\text{th.}})$	[139], [140]
	$\langle R_K^* \rangle_{[0.0454,1.1]}$	$(0.66 \pm 0.09 \pm 0.03 \pm 1\%_{\text{th.}})$	[141], [140]
	$\langle R_K^* \rangle_{[1.1,6.0]}$	$(0.69 \pm 0.09 \pm 0.05 \pm 1\%_{\text{th.}})$	[141], [140]
Isospin asymmetry of B to $K^*\mu^+\mu^-$	$\langle A_I \rangle_{[1.0,6.0]}$	(-0.15 ± 0.16)	[71]
Isospin asymmetry zero-crossing	$(A_I)_0$	(1.3 ± 1.0)	[71]
Radiative B Decay	$\text{BR}(b \to s\gamma)$	$(3.32 \pm 0.15 \pm 7\%_{\text{th.}}) \times 10^{-4}$	[68], [142]
Wolfenstein CKM Parameters	λ	0.22537	
	A	0.814	
	ρ	0.117	
	η	0.353	
Electroweak Precision Parameters	S	0.04 ± 0.11	[122]
	T	0.09 ± 0.14	[122]
	U	-0.02 ± 0.11	[122]

Name	Symbol	Value	Reference
Up Quark Running Mass (at 2 GeV)	$\overline{m_u}(2\,\text{GeV})$	2.20×10^{-3} GeV	[55]
Up Quark Pole Mass	m_u	2.2×10^{-3} GeV	[55]
Charm Quark Running Mass (at c pole)	$\overline{m_c}(m_c)$	1.280 GeV	[55]
Top Quark Pole Mass	m_t	173.34 GeV	[55]
Strange Quark Running Mass (at 2 GeV)	$\overline{m_s}(2\,\text{GeV})$	9.60×10^{-2} GeV	[55]
Bottom Quark Running Mass (at b pole)	$\overline{m_b}(m_b)$	4.18 GeV	[55]
Tau Pole Mass	m_τ	1.7769 GeV	[55]
Electron Pole Mass	m_e	5.1200×10^{-4} GeV	[55]
Muon Pole Mass	m_μ	1.0566×10^{-1} GeV	[55]
Fermi Constant	G_F	$1.16638 \times 10^{-5}\,\text{GeV}^{-2}$	[55]
Fine Structure Constant (at m_Z)	$\alpha_\text{em}(m_Z)$	1/127.95	[55]
Fine Structure Constant (at zero energy)	α^0	1/137.036	[55]
Strong Coupling (at m_Z)	$\alpha_s(m_Z)$	0.1181	[55]

Electroweak precision parameters correlation matrix [122]

$$\Sigma = \begin{pmatrix} 1.0 & 0.92 & -0.68 \\ 0.92 & 1.0 & -0.87 \\ -0.68 & -0.87 & 1.0 \end{pmatrix}. \tag{F.1}$$

Angular observables for the $B^0 \to K^{*0}\mu^+\mu^-$ decay are found in Ref. [143]. Branching fraction for $B^0 \to K^{*0}\mu^+\mu^-$ decay is found in Ref. [97] with theoretical error of 60% given in Ref. [98]. Parameters used to calculate flavour observables are not given here, we use `SuperIso` routines for these calculations. We have also ignored the correlations between flavour observables here, but they may be found within the `FlavBit` source YAML database.

F.2 Stand-alone General Type-III 2HDM Fit

Name	Symbol	Value	Reference
Observed B-Meson Mass Splitting	$\Delta m_{B_s^0,\text{obs}}$	$(1.1688 \pm 0.0014) \times 10^{-11}$ GeV	[55]
Calculated B-Meson Mass Splitting (SM)	$\Delta m_{B_s^0,\text{SM}}$	$(1.32 \pm 0.08_{\text{th.}}) \times 10^{-11}$ GeV	-
Observed B-Meson CP Phase	β_{obs}	$(1.5 \pm 1.6) \times 10^{-2}$ rad	[55]
Calculated B-Meson CP Phase (SM)	β_{SM}	$(1.86 \pm 0.11_{\text{th.}}) \times 10^{-2}$ rad	-
Observed Radiative B Decay	$\text{BR}(b \to s\gamma)_{\text{obs}}$	$(3.32 \pm 0.16) \times 10^{-4}$	[68]
Calculated Radiative B Decay (SM)	$\text{BR}(b \to s\gamma)_{\text{SM}}$	$(3.34 \pm 0.33_{\text{th.}}) \times 10^{-4}$	-
Electroweak Precision Parameters	S	0.05 ± 0.11	[144]
	T	0.09 ± 0.13	[144]
	U	0.01 ± 0.11	[144]
Up Quark Pole Mass	m_u	2.2×10^{-3} GeV	[55]
Charm Quark Pole Mass	m_c	1.67 GeV	[55]
Charm Quark Running Mass (at c pole)	$\overline{m_c}(m_c)$	1.273 GeV	[145]
Top Quark Pole Mass	m_t	173.5 GeV	[55]
Top Quark Running Mass (at t pole)	$\overline{m_t}(m_t)$	(173.5 – 10.38) GeV	[146]
Down Quark Pole Mass	m_d	4.7×10^{-3} GeV	[55]
Strange Quark Pole Mass	m_s	0.096 GeV	[55]
Bottom Quark Pole Mass	m_b	4.78 GeV	[55]
Bottom Quark Running Mass (at b pole)	$\overline{m_b}(m_b)$	4.197 GeV	[145]
$W^\pm$ Boson Pole Mass	m_W	80.385 GeV	[55]
Z Boson Pole Mass	m_Z	91.1876 GeV	[55]
Fine Structure Constant (at m_Z)	$\alpha_{\text{em}}(m_Z)$	1/127.934	[55]
Fine Structure Constant (at zero energy)	α^0	1/137.036	[55]
Fermi Constant	G_{F}	1.16638×10^{-5} GeV^{-2}	[55]
Strong Coupling (at m_Z)	$\alpha_s(m_Z)$	0.1182	[55]
B_s^0 Mass	$M_{B_s^0}$	5.36689 GeV	[145]
B_s^0 Decay Constant	$f_{B_s^0}$	0.224 GeV	[145]
B_s^0 Bag Parameters	$B_1^{B_s^0}(\mu_b)$	0.87 GeV	[147]
	$B_2^{B_s^0}(\mu_b)$	0.80 GeV	[147]
	$B_3^{B_s^0}(\mu_b)$	0.93 GeV	[147]
	$B_4^{B_s^0}(\mu_b)$	1.16 GeV	[147]
	$B_5^{B_s^0}(\mu_b)$	1.75 GeV	[147]

CKM-matrix [148]

$$V_{\text{CKM}} = \begin{pmatrix} 0.97431 & 0.22512 & 0.00365e^{-65.88i} \\ -0.22497e^{0.0352i} & 0.97344e^{-0.001877i} & 0.04255 \\ 0.00869e^{-22.0i} & -0.04156e^{1.040i} & 0.999097 \end{pmatrix}. \tag{F.2}$$

Electroweak precision parameters correlation matrix [144]

$$\Sigma = \begin{pmatrix} 1.0 & 0.9 & -0.59 \\ 0.9 & 1.0 & -0.83 \\ -0.59 & -0.83 & 1.0 \end{pmatrix}. \tag{F.3}$$

Evolution matrix ($\mu_i = m_W$ *to* $\mu_f = m_B$) *for meson mixing basis*

$$U(m_B, m_W) = \begin{pmatrix} 0.862096 & 0 & 0 & 0 & 0 & 0 & 0 & 0 \\ 0 & 1.41304 & -0.197994 & 0 & 0 & 0 & 0 & 0 \\ 0 & -0.0516513 & 0.682309 & 0 & 0 & 0 & 0 & 0 \\ 0 & 0 & 0 & 1.79804 & 0.288788 & 0 & 0 & 0 \\ 0 & 0 & 0 & 0 & 0.931673 & 0 & 0 & 0 \\ 0 & 0 & 0 & 0 & 0 & 0.862096 & 0 & 0 \\ 0 & 0 & 0 & 0 & 0 & 0 & 1.41304 & -0.197994 \\ 0 & 0 & 0 & 0 & 0 & 0 & -0.0516513 & 0.682309 \end{pmatrix} \tag{F.4}$$

Bibliography

[1] J. Beringer et al. 'Review of Particle Physics'. In: *Phys. Rev. D* 86 (1 July 2012), p. 010001. DOI: 10.1103/PhysRevD.86.010001 (cited on page 5).

[2] Benjamin W. Lee, C. Quigg, and H. B. Thacker. 'Weak interactions at very high energies: The role of the Higgs-boson mass'. In: *Phys. Rev. D* 16 (5 Sept. 1977), pp. 1519–1531. DOI: 10.1103/PhysRevD.16.1519 (cited on page 9).

[3] A.J.G. Hey I.J.R. Aitchison. *Gauge Theories in Particle Physics*. Third. Vol. 2. IOP Publishing, 2004 (cited on pages 9, 11, 185).

[4] E. Merzbacher. *Quantum Mechanics*. Third. Wiley, 1997 (cited on page 10).

[5] David Griffiths. 'Gauge Theories'. In: *Introduction to Elementary Particles*. Wiley-VCH Verlag GmbH, 2008, pp. 343–371. DOI: 10.1002/9783527618460.ch11 (cited on page 11).

[6] Xianhao Xin. 'Glashow-Weinberg-Salam Model: An Example of Electroweak Symmetry Breaking'. In: (2007) (cited on page 11).

[7] S.M. Bilenky and J. Hoek. 'Glashow-Weinberg-Salam theory of electroweak interactions and the neutral currents'. In: *Physics Reports* 90.2 (1982), pp. 73–157. DOI: http://dx.doi.org/10.1016/0370-1573(82)90016-3 (cited on page 14).

[8] R. A. Millikan. 'On the Elementary Electrical Charge and the Avogadro Constant'. In: *Phys. Rev.* 2 (2 Aug. 1913), pp. 109–143. DOI: 10.1103/PhysRev.2.109 (cited on page 17).

[9] C. S. Wu et al. 'Experimental Test of Parity Conservation in Beta Decay'. In: *Phys. Rev.* 105 (4 Feb. 1957), pp. 1413–1415. DOI: 10.1103/PhysRev.105.1413 (cited on page 18).

[10] T. D. Lee and C. N. Yang. 'Question of Parity Conservation in Weak Interactions'. In: *Phys. Rev.* 104 (1 Oct. 1956), pp. 254–258. DOI: 10.1103/PhysRev.104.254 (cited on page 18).

[11] Takaaki Kajita. 'Discovery of neutrino oscillations'. In: *Reports on Progress in Physics* 69.6 (May 2006), pp. 1607–1635. DOI: 10.1088/0034-4885/69/6/r01 (cited on page 19).

[12] T.N. Pham. 'CKM Matrix Elements'. In: (2011) (cited on page 22).

[13] M. Tanabashi et al. 'Review of Particle Physics'. In: *Phys. Rev. D* 98 (3 Aug. 2018), p. 030001. DOI: 10.1103/PhysRevD.98.030001 (cited on pages 23–25, 143).

[14] Peter J. Mohr, David B. Newell, and Barry N. Taylor. 'CODATA Recommended Values of the Fundamental Physical Constants: 2014'. In: *Rev. Mod. Phys.* 88.3 (2016), p. 035009. DOI: 10.1103/RevModPhys.88.035009 (cited on page 24).

[15] Steven Weinberg. 'New Approach to the Renormalization Group'. In: *Phys. Rev. D* 8 (10 Nov. 1973), pp. 3497–3509. DOI: 10.1103/PhysRevD.8.3497 (cited on page 24).

[16] G. 't Hooft. 'Dimensional regularization and the renormalization group'. In: *Nuclear Physics B* 61 (1973), pp. 455–468. DOI: https://doi.org/10.1016/0550-3213(73)90376-3 (cited on page 24).

[17] Timo van Ritbergen and Robin G. Stuart. 'On the precise determination of the Fermi coupling constant from the muon lifetime'. In: *Nucl. Phys.* B564 (2000), pp. 343–390. DOI: 10.1016/S0550-3213(99)00572-6 (cited on page 24).

[18] John F. Gunion et al. 'The Higgs Hunter's Guide'. In: *Front. Phys.* 80 (2000), pp. 1–404 (cited on pages 27, 126).

[19] Wai-Yee Keung and William J. Marciano. 'HIGGS SCALAR DECAYS: H —>; W+- X'. In: *Phys.Rev.* D30 (1984), p. 248. DOI: 10.1103/PhysRevD.30.248 (cited on pages 28, 189).

[20] Michael Spira. 'Higgs Boson Production and Decay at Hadron Colliders'. In: *Prog. Part. Nucl. Phys.* 95 (2017), pp. 98–159. DOI: 10.1016/j.ppnp.2017.04.001 (cited on page 29).

[21] C. P. Burgess. 'Introduction to Effective Field Theory'. In: *Ann. Rev. Nucl. Part. Sci.* 57 (2007), pp. 329–362. DOI: 10.1146/annurev.nucl.56.080805.140508 (cited on page 33).

[22] Jason Aebischer et al. 'B physics Beyond the Standard Model at One Loop: Complete Renormalization Group Evolution below the Electroweak Scale'. In: *arXiv.org* (Apr. 2017) (cited on pages 34, 35, 80).

[23] Alejandro Celis et al. 'DsixTools: The Standard Model Effective Field Theory Toolkit'. In: *arXiv.org* 6 (Apr. 2017), p. 621 (cited on page 35).

[24] A. V. Bednyakov. 'On three-loop RGE for the Higgs sector of 2HDM'. In: *Journal of High Energy Physics* 2018.11 (Nov. 2018), p. 154. DOI: 10.1007/JHEP11(2018)154 (cited on pages 42, 135).

[25] P.M. Ferreira and Joao P. Silva. 'Discrete and continuous symmetries in multi-Higgs-doublet models'. In: *Phys. Rev. D* 78 (2008), p. 116007. DOI: 10.1103/PhysRevD.78.116007 (cited on page 43).

[26] I. P. Ivanov. 'Minkowski space structure of the Higgs potential in 2HDM'. In: *Phys. Rev.* D75 (2007). [Erratum: Phys. Rev.D76,039902(2007)], p. 035001. DOI: 10.1103/PhysRevD.76.039902,10.1103/PhysRevD.75.035001 (cited on pages 45, 58, 59).

[27] P. M. Ferreira, Howard E. Haber, and Joao P. Silva. 'Generalized CP symmetries and special regions of parameter space in the two-Higgs-doublet model'. In: *Phys. Rev.* D79 (2009), p. 116004. DOI: 10.1103/PhysRevD.79.116004 (cited on page 46).

[28] A. Barroso et al. 'Stability of the normal vacuum in multi-Higgs-doublet models'. In: *Phys. Rev.* D74 (2006), p. 085016. DOI: 10.1103/PhysRevD.74.085016 (cited on pages 48, 199).

[29] Dr. Chao Cheng Huang. *Linear Algebra Lecture 11: Eigenvalues and Eigenvectors*. http://www.wright.edu/~chaocheng.huang/lecture/mth255/mth255lect11.pdf (cited on page 54).

[30] P. M. Ferreira, R. Santos, and A. Barroso. 'Stability of the tree-level vacuum in two Higgs doublet models against charge or CP spontaneous violation'. In: *Phys. Lett.* B603 (2004). [Erratum: Phys. Lett.B629,114(2005)], pp. 219–229. DOI: 10.1016/j.physletb.2004.10.022 (cited on pages 57, 220).

[31] Abdul Wahab El Kaffas et al. 'Consistency of the two Higgs doublet model and CP violation in top production at the LHC'. In: *Nucl. Phys.* B775 (2007), pp. 45–77. DOI: 10.1016/j.nuclphysb.2007.03.041 (cited on page 58).

[32] A Barroso et al. 'Metastability bounds on the two Higgs doublet model'. In: *arXiv.org* 6 (Mar. 2013), p. 45 (cited on pages 59–61).

[33] Igor P. Ivanov. 'Minkowski space structure of the Higgs potential in 2HDM. II. Minima, symmetries, and topology'. In: *Phys. Rev.* D77 (2008), p. 015017. DOI: 10.1103/PhysRevD.77.015017 (cited on page 59).

[34] Abdesslam Arhrib. 'Unitarity constraints on scalar parameters of the standard and two Higgs doublets model'. In: *Workshop on Noncommutative Geometry, Superstrings and Particle Physics Rabat, Morocco, June 16-17, 2000*. 2000 (cited on pages 62, 63).

[35] I. F. Ginzburg and I. P. Ivanov. 'Tree-level unitarity constraints in the most general 2HDM'. In: *Phys. Rev.* D72 (2005), p. 115010. DOI: 10.1103/PhysRevD.72.115010 (cited on pages 63, 64).

[36] I F Ginzburg and I P Ivanov. 'Tree-level unitarity constraints in the 2HDM with CP-violation'. In: *arXiv.org* (Dec. 2003) (cited on page 63).

[37] H. Huffel and G. Pocsik. 'Unitarity Bounds on Higgs Boson Masses in the Weinberg-Salam Model With Two Higgs Doublets'. In: *Z. Phys.* C8 (1981), p. 13. DOI: 10.1007/BF01429824 (cited on page 64).

[38] Shinya Kanemura and Kei Yagyu. 'Unitarity bound in the most general two Higgs doublet model'. In: *Phys. Lett.* B751 (2015), pp. 289–296. DOI: 10.1016/j.physletb.2015.10.047 (cited on page 64).

[39] Vincenzo Cacchio et al. 'Next-to-leading order unitarity fits in Two-Higgs-Doublet models with soft $\mathbb{Z}_2$ breaking'. In: *JHEP* 11 (2016), p. 026. DOI: 10.1007/JHEP11(2016)026 (cited on pages 65, 119).

[40] Benjamín Grinstein, Christopher W. Murphy, and Patipan Uttayarat. 'One-loop corrections to the perturbative unitarity bounds in the CP-conserving two-Higgs doublet model with a softly broken $\mathbb{Z}_2$ symmetry'. In: *JHEP* 06 (2016), p. 070. DOI: 10.1007/JHEP06(2016)070 (cited on page 65).

[41] Debtosh Chowdhury and Otto Eberhardt. 'Global fits of the two-loop renormalized Two-Higgs-Doublet model with soft Z_2 breaking'. In: *JHEP* 11 (2015), p. 052. DOI: 10.1007/JHEP11(2015)052 (cited on page 66).

[42] Christopher T. Hill, Chung Ngoc Leung, and Sumathi Rao. 'Renormalization group fixed points and the Higgs boson spectrum'. In: *Nuclear Physics B* 262.3 (1985), pp. 517–537. DOI: https://doi.org/10.1016/0550-3213(85)90328-1 (cited on page 66).

[43] Sacha Davidson and Howard E. Haber. 'Basis-independent methods for the two-Higgs-doublet model'. In: *Phys. Rev.* D72 (2005). [Erratum: Phys. Rev.D72,099902(2005)], p. 035004. DOI: 10.1103/PhysRevD.72.099902,10.1103/PhysRevD.72.035004 (cited on pages 67, 68, 108).

[44] Howard E. Haber and Deva O'Neil. 'Basis-independent methods for the two-Higgs-doublet model. II. The Significance of tanβ'. In: *Phys. Rev.* D74 (2006). [Erratum: Phys. Rev.D74,no.5,059905(2006)], p. 015018. DOI: 10.1103/PhysRevD.74.015018,10.1103/PhysRevD.74.059905 (cited on pages 69–71).

[45] John F. Gunion and Howard E. Haber. 'The CP conserving two Higgs doublet model: The Approach to the decoupling limit'. In: *Phys. Rev.* D67 (2003), p. 075019. DOI: 10.1103/PhysRevD.67.075019 (cited on page 69).

[46] Andreas Crivellin, Ahmet Kokulu, and Christoph Greub. 'Flavor-phenomenology of two-Higgs-doublet models with generic Yukawa structure'. In: *arXiv.org* 9 (Mar. 2013), p. 094031 (cited on pages 74, 80, 86, 87).

[47] David Eriksson, Johan Rathsman, and Oscar Stal. '2HDMC: Two-Higgs-Doublet Model Calculator Physics and Manual'. In: *Comput. Phys. Commun.* 181 (2010), pp. 189–205. DOI: 10.1016/j.cpc.2009.09.011 (cited on pages 77, 79, 107, 110).

[48] Andreas Crivellin, Julian Heeck, and Dario Mueller. 'Large $h \to bs$ in generic two-Higgs-doublet models'. In: (2017) (cited on pages 79, 96).

[49] Florian U. Bernlochner et al. 'FlavBit: A GAMBIT module for computing flavour observables and likelihoods'. In: *Eur. Phys. J.* C77.11 (2017), p. 786. DOI: 10.1140/epjc/s10052-017-5157-2 (cited on pages 80, 121).

[50] F. Mahmoudi and O. Stål. 'Flavor constraints on two-Higgs-doublet models with general diagonal Yukawa couplings'. In: *Physical Review D* 81.3 (Feb. 2010). DOI: 10.1103/physrevd.81.035016 (cited on page 80).

[51] Andreas Crivellin. *Higgs mediated Flavour Violation in 2HDMs and the MSSM – An Overview*. 2014 (cited on page 80).

[52] Andreas Crivellin, Christoph Greub, and Ahmet Kokulu. *Flavour-violation in two-Higgs-doublet models*. 2013 (cited on page 80).

[53] Konstantin G. Chetyrkin, Mikolaj Misiak, and Manfred Munz. '$|\Delta F| = 1$ nonleptonic effective Hamiltonian in a simpler scheme'. In: *Nucl. Phys.* B520 (1998), pp. 279–297. DOI: 10.1016/S0550-3213(98)00131-X (cited on page 80).

[54] K Anikeev et al. 'B Physics at the Tevatron: Run II and Beyond'. In: *arXiv.org* (Jan. 2002), arXiv:hep–ph–0201071 (cited on page 82).

[55] C. Patrignani et al. 'Review of Particle Physics'. In: *Chin. Phys.* C40.10 (2016), p. 100001. DOI: 10.1088/1674-1137/40/10/100001 (cited on pages 82, 125, 223–225).

[56] D. Becirevic et al. 'Combined relativistic and static analysis for all Delta B=2 operators'. In: *Nucl. Phys. Proc. Suppl.* 106 (2002), pp. 385–387. DOI: 10.1016/S0920-5632(01)01722-4 (cited on page 83).

[57] A Lenz et al. ‘Anatomy of New Physics in B-Bbar mixing’. In: *arXiv.org* 3 (Aug. 2010), p. 332 (cited on page 84).

[58] Gerhard Buchalla, Andrzej J Buras, and Markus E Lautenbacher. ‘Weak Decays Beyond Leading Logarithms’. In: *arXiv.org* 4 (Dec. 1995), pp. 1125–1244 (cited on page 84).

[59] Takeo Inami and C. S. Lim. ‘Effects of Superheavy Quarks and Leptons in Low-Energy Weak Processes KLţţ, K++ and K0K0’. In: *Progress of Theoretical Physics* 65.1 (1981), pp. 297–314. DOI: 10.1143/PTP.65.297 (cited on page 84).

[60] Luca Di Luzio, Matthew Kirk, and Alexander Lenz. ‘Updated B_s-mixing constraints on new physics models for $b \to s\ell^+\ell^-$ anomalies’. In: *Phys. Rev.* D97.9 (2018), p. 095035. DOI: 10.1103/PhysRevD.97.095035 (cited on page 85).

[61] Juan Herrero-Garcia et al. *Higgs Quark Flavor Violation: Simplified Models and Status of General Two-Higgs-Doublet Model*. 2019 (cited on pages 87, 161).

[62] F Borzumati and C Greub. ‘2HDMs predictions for B X_s γ in NLO QCD’. In: *arXiv.org* 7 (Feb. 1998), p. 074004 (cited on pages 90, 92, 94).

[63] T M Aliev and E O Iltan. ‘b -> s γdecay in the two Higgs doublet model with flavor changing neutral currents’. In: *arXiv.org* 5 (Mar. 1998), pp. 989–999 (cited on pages 91, 94).

[64] A J Buras et al. ‘Theoretical Uncertainties and Phenomenological Aspects of B X_s γ Decay’. In: *arXiv.org* 2 (Nov. 1993), pp. 374–398 (cited on page 91).

[65] A. H. Mahmood et al. ‘Measurement of the B-meson inclusive semileptonic branching fraction and electron energy moments’. In: *Phys. Rev.* D70 (2004), p. 032003. DOI: 10.1103/PhysRevD.70.032003 (cited on page 93).

[66] M Ciuchini et al. ‘Next-to-Leading Order QCD Corrections to ΔF =2 effective Hamiltonians’. In: *arXiv.org* 3 (Nov. 1997), pp. 501–525 (cited on page 93).

[67] Paolo Gambino and Mikoaj Misiak. ‘Quark mass effects in’. In: *Nuclear Physics B* 611.1-3 (Sept. 2001), pp. 338–366. DOI: 10.1016/s0550-3213(01)00347-9 (cited on page 97).

[68] Y. Amhis et al. ‘Averages of b-hadron, c-hadron, and τ-lepton properties as of summer 2016’. In: *Eur. Phys. J.* C77.12 (2017), p. 895. DOI: 10.1140/epjc/s10052-017-5058-4 (cited on pages 97, 223, 225).

[69] Andrzej J. Buras et al. ‘The Anatomy of Neutral Scalars with FCNCs in the Flavour Precision Era’. In: *JHEP* 06 (2013), p. 111. DOI: 10.1007/JHEP06(2013)111 (cited on page 97).

[70] Wolfgang Altmannshofer et al. ‘Symmetries and Asymmetries of $B \to K^*\mu^+\mu^-$ Decays in the Standard Model and Beyond’. In: *JHEP* 01 (2009), p. 019. DOI: 10.1088/1126-6708/2009/01/019 (cited on pages 97, 98).

[71] R Aaij et al. ‘Measurement of the isospin asymmetry in $B \to K^{(*)}\mu^+\mu^-$ decays’. In: *JHEP* 07 (2012), p. 133. DOI: 10.1007/JHEP07(2012)133 (cited on pages 98, 122, 223).

[72] Wolfgang Altmannshofer and David M. Straub. ‘New Physics in $B \to K^*\mu\mu$?’ In: *Eur. Phys. J.* C73 (2013), p. 2646. DOI: 10.1140/epjc/s10052-013-2646-9 (cited on page 98).

[73] Robert Knegjens. ‘Theory overview of $B_{s,d} \to \mu^+\mu^-$ decays’. In: *PoS* DIS2014 (2014), p. 194. DOI: 10.22323/1.203.0194 (cited on page 99).

[74] Roel Aaij et al. ‘Measurement of the $B_s^0 \to \mu^+\mu^-$ branching fraction and effective lifetime and search for $B^0 \to \mu^+\mu^-$ decays’. In: *Phys. Rev. Lett.* 118.19 (2017), p. 191801. DOI: 10.1103/PhysRevLett.118.191801 (cited on page 99).

[75] Gudrun Hiller and Ivan Nisandzic. ‘R_K and R_{K^*} beyond the standard model’. In: *Phys. Rev.* D96.3 (2017), p. 035003. DOI: 10.1103/PhysRevD.96.035003 (cited on page 99).

[76] Gudrun Hiller and Martin Schmaltz. ‘Diagnosing lepton-nonuniversality in $b \to s\ell\ell$’. In: *JHEP* 02 (2015), p. 055. DOI: 10.1007/JHEP02(2015)055 (cited on page 99).

[77] Diptimoy Ghosh. 'Explaining the R_K and R_{K^*} anomalies'. In: *Eur. Phys. J.* C77.10 (2017), p. 694. DOI: 10.1140/epjc/s10052-017-5282-y (cited on page 100).

[78] Debjyoti Bardhan, Pritibhajan Byakti, and Diptimoy Ghosh. 'A closer look at the R_D and R_{D^*} anomalies'. In: *JHEP* 01 (2017), p. 125. DOI: 10.1007/JHEP01(2017)125 (cited on page 100).

[79] I. Maksymyk, C. P. Burgess, and David London. 'Beyond S, T and U'. In: *Phys. Rev.* D50 (1994), pp. 529–535. DOI: 10.1103/PhysRevD.50.529 (cited on page 100).

[80] Michael E. Peskin and Tatsu Takeuchi. 'A New constraint on a strongly interacting Higgs sector'. In: *Phys. Rev. Lett.* 65 (1990), pp. 964–967. DOI: 10.1103/PhysRevLett.65.964 (cited on page 101).

[81] Guido Altarelli and Riccardo Barbieri. 'Vacuum polarization effects of new physics on electroweak processes'. In: *Phys. Lett.* B253 (1991), pp. 161–167. DOI: 10.1016/0370-2693(91)91378-9 (cited on page 101).

[82] Michael E. Peskin and Tatsu Takeuchi. 'Estimation of oblique electroweak corrections'. In: *Phys. Rev.* D46 (1992), pp. 381–409. DOI: 10.1103/PhysRevD.46.381 (cited on page 101).

[83] P. Bamert and C. P. Burgess. 'Negative S and light new physics'. In: *Z. Phys.* C66 (1995), pp. 495–502. DOI: 10.1007/BF01556377 (cited on page 102).

[84] W. Grimus et al. 'The Oblique parameters in multi-Higgs-doublet models'. In: *Nucl. Phys.* B801 (2008), pp. 81–96. DOI: 10.1016/j.nuclphysb.2008.04.019 (cited on pages 102, 144, 145).

[85] Howard E. Haber and Deva O'Neil. 'Basis-independent methods for the two-Higgs-doublet model III: The CP-conserving limit, custodial symmetry, and the oblique parameters S, T, U'. In: *Phys. Rev.* D83 (2011), p. 055017. DOI: 10.1103/PhysRevD.83.055017 (cited on page 102).

[86] Peter Athron et al. 'GAMBIT: the global and modular beyond-the-standard-model inference tool'. In: *The European Physical Journal C* 77.11 (Nov. 2017). DOI: 10.1140/epjc/s10052-017-5321-8 (cited on pages 103, 107).

[87] Peter Athron et al. 'SpecBit, DecayBit and PrecisionBit: GAMBIT modules for computing mass spectra, particle decay rates and precision observables'. In: *Eur. Phys. J.* C78.1 (2018), p. 22. DOI: 10.1140/epjc/s10052-017-5390-8 (cited on pages 107, 113).

[88] Peter Athron et al. 'FlexibleSUSYA spectrum generator generator for supersymmetric models'. In: *Computer Physics Communications* 190 (May 2015), pp. 139–172. DOI: 10.1016/j.cpc.2014.12.020 (cited on page 107).

[89] Peter Athron et al. 'FlexibleSUSY 2.0: Extensions to investigate the phenomenology of SUSY and non-SUSY models'. In: *Computer Physics Communications* 230 (Sept. 2018), pp. 145–217. DOI: 10.1016/j.cpc.2018.04.016 (cited on page 107).

[90] Jihyun Bhom and Marcin Chrzaszcz. 'HEPLike: An open source framework for experimental likelihood evaluation'. In: *Computer Physics Communications* 254 (Sept. 2020), p. 107235. DOI: 10.1016/j.cpc.2020.107235 (cited on page 110).

[91] F. Mahmoudi. 'SuperIso v2.3: A Program for calculating flavor physics observables in Supersymmetry'. In: *Comput. Phys. Commun.* 180 (2009), pp. 1579–1613. DOI: 10.1016/j.cpc.2009.02.017 (cited on pages 110, 121).

[92] Philip Bechtle et al. 'HiggsBounds – 4: Improved Tests of Extended Higgs Sectors against Exclusion Bounds from LEP, the Tevatron and the LHC'. In: *Eur. Phys. J.* C74.3 (2014), p. 2693. DOI: 10.1140/epjc/s10052-013-2693-2 (cited on pages 110, 120).

[93] Philip Bechtle et al. '*HiggsSignals*: Confronting arbitrary Higgs sectors with measurements at the Tevatron and the LHC'. In: *Eur. Phys. J.* C74.2 (2014), p. 2711. DOI: 10.1140/epjc/s10052-013-2711-4 (cited on pages 110, 120).

[94] Philip Bechtle et al. *HiggsBounds-5: Testing Higgs Sectors in the LHC 13 TeV Era*. 2020 (cited on pages 110, 121).

[95] Csaba Balázs et al. 'ColliderBit: a GAMBIT module for the calculation of high-energy collider observables and likelihoods'. In: *Eur. Phys. J.* C77.11 (2017), p. 795. DOI: 10.1140/epjc/s10052-017-5285-8 (cited on page 120).

[96] B. C. Allanach et al. 'SUSY Les Houches Accord 2'. In: *Comput. Phys. Commun.* 180 (2009), pp. 8–25. DOI: 10.1016/j.cpc.2008.08.004 (cited on page 121).

[97] Roel Aaij et al. 'Measurements of the S-wave fraction in $B^0 \to K^+\pi^-\mu^+\mu^-$ decays and the $B^0 \to K^*(892)^0\mu^+\mu^-$ differential branching fraction'. In: *JHEP* 11 (2016). [Erratum: JHEP04,142(2017)], p. 047. DOI: 10.1007/JHEP11(2016)047,10.1007/JHEP04(2017)142 (cited on pages 122, 224).

[98] F. Mahmoudi, S. Neshatpour, and J. Orloff. 'Supersymmetric constraints from $B_s - > \mu^+\mu^-$ and $B - > K * \mu^+\mu^-$ observables'. In: *JHEP* 08 (2012), p. 092. DOI: 10.1007/JHEP08(2012)092 (cited on pages 122, 224).

[99] Gregory D. Martinez et al. 'Comparison of statistical sampling methods with ScannerBit, the GAMBIT scanning module'. In: *Eur. Phys. J.* C77.11 (2017), p. 761. DOI: 10.1140/epjc/s10052-017-5274-y (cited on page 122).

[100] Rainer Storn and Kenneth Price. 'Differential Evolution - A Simple and Efficient Heuristic for global Optimization over Continuous Spaces'. In: *Journal of Global Optimization* 11.4 (1997), pp. 341–359. DOI: 10.1023/A:1008202821328 (cited on page 123).

[101] Morad Aaboud et al. 'Search for top quark decays $t \to qH$, with $H \to \gamma\gamma$, in $\sqrt{s}$ = 13 TeV pp collisions using the ATLAS detector'. In: *JHEP* 10 (2017), p. 129. DOI: 10.1007/JHEP10(2017)129 (cited on page 125).

[102] Albert M Sirunyan et al. 'Search for the flavor-changing neutral current interactions of the top quark and the Higgs boson which decays into a pair of b quarks at $\sqrt{s}$ = 13 TeV'. In: *JHEP* 06 (2018), p. 102. DOI: 10.1007/JHEP06(2018)102 (cited on page 125).

[103] Morad Aaboud et al. 'Search for flavor-changing neutral currents in top quark decays $t \to Hc$ and $t \to Hu$ in multilepton final states in proton-proton collisions at $\sqrt{s}$ = 13 TeV with the ATLAS detector'. In: *Phys. Rev.* D98.3 (2018), p. 032002. DOI: 10.1103/PhysRevD.98.032002 (cited on page 125).

[104] Georges Aad et al. 'Combined Measurement of the Higgs Boson Mass in pp Collisions at $\sqrt{s}$ = 7 and 8 TeV with the ATLAS and CMS Experiments'. In: *Phys. Rev. Lett.* 114 (2015), p. 191803. DOI: 10.1103/PhysRevLett.114.191803 (cited on page 125).

[105] Vardan Khachatryan et al. 'Search for Higgs boson off-shell production in proton-proton collisions at 7 and 8 TeV and derivation of constraints on its total decay width'. In: *JHEP* 09 (2016), p. 051. DOI: 10.1007/JHEP09(2016)051 (cited on page 125).

[106] Georges Aad et al. 'Measurements of the Higgs boson production and decay rates and constraints on its couplings from a combined ATLAS and CMS analysis of the LHC pp collision data at $\sqrt{s}$ = 7 and 8 TeV'. In: *JHEP* 08 (2016), p. 045. DOI: 10.1007/JHEP08(2016)045 (cited on page 126).

[107] Albert M Sirunyan et al. 'Evidence for the Higgs boson decay to a bottom quark–antiquark pair'. In: *Phys. Lett.* B780 (2018), pp. 501–532. DOI: 10.1016/j.physletb.2018.02.050 (cited on page 126).

[108] M. Aaboud et al. 'Evidence for the $H \to b\bar{b}$ decay with the ATLAS detector'. In: *JHEP* 12 (2017), p. 024. DOI: 10.1007/JHEP12(2017)024 (cited on page 126).

[109] Albert M Sirunyan et al. 'Observation of the Higgs boson decay to a pair of τ leptons with the CMS detector'. In: *Phys. Lett.* B779 (2018), pp. 283–316. DOI: 10.1016/j.physletb.2018.02.004 (cited on page 127).

[110] F. Feroz, M. P. Hobson, and M. Bridges. 'MultiNest: an efficient and robust Bayesian inference tool for cosmology and particle physics'. In: *Mon. Not. Roy. Astron. Soc.* 398 (2009), pp. 1601–1614. DOI: 10.1111/j.1365-2966.2009.14548.x (cited on pages 127, 163).

[111] F. Feroz et al. 'Importance Nested Sampling and the MultiNest Algorithm'. In: (2013). DOI: 10.21105/astro.1306.2144 (cited on page 127).

[112] Farhan Feroz and M. P. Hobson. 'Multimodal nested sampling: an efficient and robust alternative to MCMC methods for astronomical data analysis'. In: *Mon. Not. Roy. Astron. Soc.* 384 (2008), p. 449. DOI: 10.1111/j.1365-2966.2007.12353.x (cited on page 127).

[113] G. Aad et al. 'Measurements of the Higgs boson production and decay rates and coupling strengths using pp collision data at

$$\sqrt{s} = 7$$

s = 7 and 8ăTeV in the ATLAS experiment'. In: *The European Physical Journal C* 76.1 (Jan. 2016). DOI: 10.1140/epjc/s10052-015-3769-y (cited on page 141).

[114] M. Aaboud et al. 'Measurement of the Higgs boson mass in the HZZ4 and H channels with s=13 TeV pp collisions using the ATLAS detector'. In: *Physics Letters B* 784 (Sept. 2018), pp. 345–366. DOI: 10.1016/j.physletb.2018.07.050 (cited on page 141).

[115] G. Aad et al. 'Combined measurements of Higgs boson production and decay using up to 80fb1 of proton-proton collision data at s=13TeV collected with the ATLAS experiment'. In: *Physical Review D* 101.1 (Jan. 2020). DOI: 10.1103/physrevd.101.012002 (cited on page 141).

[116] Tao Han, Benjamin Nachman, and Xing Wang. 'Charm-quark Yukawa coupling in hccŕ at LHC'. In: *Physics Letters B* 793 (2019), pp. 90–96. DOI: https://doi.org/10.1016/j.physletb.2019.04.031 (cited on page 142).

[117] A.M. Sirunyan et al. 'Observation of the Higgs boson decay to a pair of leptons with the CMS detector'. In: *Physics Letters B* 779 (2018), pp. 283–316. DOI: https://doi.org/10.1016/j.physletb.2018.02.004 (cited on page 142).

[118] G. Aad et al. 'Search for Heavy Higgs Bosons Decaying into Two Tau Leptons with the ATLAS Detector Using pp Collisions at s=13TeV'. In: *Physical Review Letters* 125.5 (July 2020). DOI: 10.1103/physrevlett.125.051801 (cited on page 144).

[119] G. Aad et al. 'Combination of searches for Higgs boson pairs in pp collisions at s=13TeV with the ATLAS detector'. In: *Physics Letters B* 800 (Jan. 2020), p. 135103. DOI: 10.1016/j.physletb.2019.135103 (cited on page 144).

[120] A. Arbey et al. 'Status of the charged Higgs boson in two Higgs doublet models'. In: *The European Physical Journal C* 78.3 (Mar. 2018). DOI: 10.1140/epjc/s10052-018-5651-1 (cited on page 144).

[121] Debtosh Chowdhury and Otto Eberhardt. 'Update of global Two-Higgs-Doublet model fits'. In: *Journal of High Energy Physics* 2018.5 (May 2018). DOI: 10.1007/jhep05(2018)161 (cited on page 144).

[122] Johannes Haller et al. 'Update of the global electroweak fit and constraints on two-Higgs-doublet models'. In: *Eur. Phys. J.* C78.8 (2018), p. 675. DOI: 10.1140/epjc/s10052-018-6131-3 (cited on pages 145, 223, 224).

[123] A. Arbey et al. *Status of the Charged Higgs Boson in Two Higgs Doublet Models*. 2017 (cited on page 155).

[124] Quan-Yi Hu, Xin-Qiang Li, and Ya-Dong Yang. $B^0 \to K^{*0+-}$ *Decay in the Aligned Two-Higgs-Doublet Model*. 2016 (cited on page 155).

[125] Georges Aad et al. 'Measurement of the production cross section for a Higgs boson in association with a vector boson in the $H \to WW^* \to \ell\nu\ell\nu$ channel in pp collisions at $\sqrt{s}$ = 13 TeV with the ATLAS detector'. In: (2019) (cited on page 161).

[126] Morad Aaboud et al. 'Measurements of gluon-gluon fusion and vector-boson fusion Higgs boson production cross-sections in the $H \to WW^* \to e\nu\mu\nu$ decay channel in pp collisions at $\sqrt{s}$ = 13 TeV with the ATLAS detector'. In: *Phys. Lett.* B789 (2019), pp. 508–529. DOI: 10.1016/j.physletb.2018.11.064 (cited on page 161).

[127] Morad Aaboud et al. 'Evidence for the associated production of the Higgs boson and a top quark pair with the ATLAS detector'. In: *Phys. Rev.* D97.7 (2018), p. 072003. DOI: 10.1103/PhysRevD.97.072003 (cited on page 161).

[128] M. A. Arroyo-Ureña et al. 'Search for the $t \to ch$ decay at hadron colliders'. In: *JHEP* 07 (2019), p. 041. DOI: 10.1007/JHEP07(2019)041 (cited on page 174).

[129] Andreas Papaefstathiou and Gilberto Tetlalmatzi-Xolocotzi. 'Rare top quark decays at a 100 TeV protonproton collider: $t \to bWZ$ and $t \to hc$'. In: *Eur. Phys. J.* C78.3 (2018), p. 214. DOI: 10.1140/epjc/s10052-018-5701-8 (cited on page 174).

[130] Mark Srednicki. *Quantum Field Theory*. Cambridge, 2006 (cited on page 177).

[131] G. C. Branco et al. 'Theory and phenomenology of two-Higgs-doublet models'. In: *Phys. Rept.* 516 (2012), pp. 1–102. DOI: 10.1016/j.physrep.2012.02.002 (cited on page 195).

[132] Marina Artuso, Guennadi Borissov, and Alexander Lenz. 'CP violation in the B_s^0 system'. In: *Rev. Mod. Phys.* 88.4 (2016). [Addendum: Rev. Mod. Phys.91,no.4,049901(2019)], p. 045002. DOI: 10.1103/RevModPhys.88.045002,10.1103/RevModPhys.91.049901 (cited on page 223).

[133] Claude Amsler et al. 'Review of Particle Physics'. In: *Phys. Lett.* B667 (2008), pp. 1–1340. DOI: 10.1016/j.physletb.2008.07.018 (cited on page 223).

[134] *Measurement of properties of Bs0 to mu+mu- decays and search for B0 to mu+mu- with the CMS experiment*. Tech. rep. CMS-PAS-BPH-16-004. Geneva: CERN, 2019 (cited on page 223).

[135] Andrzej J. Buras et al. 'On the Standard Model prediction for BR(Bs,d to mu+ mu-)'. In: *Eur. Phys. J.* C72 (2012), p. 2172. DOI: 10.1140/epjc/s10052-012-2172-1 (cited on page 223).

[136] A. G. Akeroyd and F. Mahmoudi. 'Constraints on charged Higgs bosons from D(s)+- —> mu+- nu and D(s)+- —> tau+- nu'. In: *JHEP* 04 (2009), p. 121. DOI: 10.1088/1126-6708/2009/04/121 (cited on page 223).

[137] Jon A. Bailey et al. '$B \to D\ell\nu$ form factors at nonzero recoil and $|V_{cb}|$ from $2+1$-flavor lattice QCD'. In: *Phys. Rev. D* 92 (3 Aug. 2015), p. 034506. DOI: 10.1103/PhysRevD.92.034506 (cited on page 223).

[138] Svjetlana Fajfer, Jernej F. Kamenik, and Ivan Ni and i. '$B \to D^*\tau\bar{\nu}_\tau$ sensitivity to new physics'. In: *Phys. Rev. D* 85 (9 May 2012), p. 094025. DOI: 10.1103/PhysRevD.85.094025 (cited on page 223).

[139] Roel Aaij et al. 'Search for lepton-universality violation in $B^+ \to K^+\ell^+\ell^-$ decays'. In: *Phys. Rev. Lett.* 122.19 (2019), p. 191801. DOI: 10.1103/PhysRevLett.122.191801 (cited on page 223).

[140] Marzia Bordone, Gino Isidori, and Andrea Pattori. 'On the Standard Model predictions for R_K and R_{K^*}'. In: *Eur. Phys. J.* C76.8 (2016), p. 440. DOI: 10.1140/epjc/s10052-016-4274-7 (cited on page 223).

[141] R. Aaij et al. 'Test of lepton universality with $B^0 \to K^{*0}\ell^+\ell^-$ decays'. In: *JHEP* 08 (2017), p. 055. DOI: 10.1007/JHEP08(2017)055 (cited on page 223).

[142] Micha Czakon et al. 'The $(Q_7, Q_{1,2})$ contribution to $\overline{B} \to X_s\gamma$ at $\mathcal{O}(\alpha_s^2)$'. In: *JHEP* 04 (2015), p. 168. DOI: 10.1007/JHEP04(2015)168 (cited on page 223).

[143] The LHCb Collaboration. 'Angular analysis of the $B^0 \to K^{*0}\mu^+\mu^-$ decay'. In: (2015) (cited on page 224).

[144] M. Baak et al. 'The global electroweak fit at NNLO and prospects for the LHC and ILC'. In: *Eur. Phys. J.* C74 (2014), p. 3046. DOI: 10.1140/epjc/s10052-014-3046-5 (cited on pages 225, 226).

[145] A. Bazavov et al. 'Up-, down-, strange-, charm-, and bottom-quark masses from four-flavor lattice QCD'. In: (2018) (cited on page 225).

[146] Fred Jegerlehner, Mikhail Yu. Kalmykov, and Bernd A. Kniehl. 'On the difference between the pole and the $\overline{MS}$ masses of the top quark at the electroweak scale'. In: *Phys. Lett.* B722 (2013), pp. 123–129. DOI: 10.1016/j.physletb.2013.04.012 (cited on page 225).

[147] Vittorio Lubicz and Cecilia Tarantino. 'Flavour physics and Lattice QCD: Averages of lattice inputs for the Unitarity Triangle Analysis'. In: *Nuovo Cim.* B123 (2008), pp. 674–688. DOI: 10.1393/ncb/i2008-10650-3 (cited on page 225).

[148] M. Bona et al. 'The Unitarity Triangle Fit in the Standard Model and Hadronic Parameters from Lattice QCD: A Reappraisal after the Measurements of Delta m(s) and BR(B —> tau nu(tau))'. In: *JHEP* 10 (2006), p. 081. DOI: 10.1088/1126-6708/2006/10/081 (cited on page 225).

Abbreviations

Abbreviation	Meaning
2HDM	Two-Higgs-Doublet Model
LS	Lepton-Specific
FC	Flavour-Changing
FCCC	Flavour-Changing Charged Current
FCNC	Flavour-Changing Neutral Current
SM	Standard Model
BSM	Beyond Standard Model
CP	Charge-Parity
CB	Charge-Breaking
VEV	Vacuum Expectation Value
EWSB	Electroweak Symmetry Breaking
EWPO	Electroweak Precision Observables
NP	New Physics
FS	`FlexibleSUSY`